DEVELOPMENT OF THE DISPERSING COMPONENT FOR A CRYOGENIC POST-DISPERSED POLARIZING FOURIER TRANSFORM SPECTROMETER

ALICIA ANDERSON
Bachelor of Science with Honours, University of Lethbridge, 2020

A thesis submitted
in partial fulfillment of the requirements for the degree of

MASTER OF SCIENCE

in

PHYSICS

Department of Physics and Astronomy
University of Lethbridge
LETHBRIDGE, ALBERTA, CANADA

DEVELOPMENT OF THE DISPERSING COMPONENT FOR A CRYOGENIC POST-DISPERSED POLARIZING FOURIER TRANSFORM SPECTROMETER

ALICIA ANDERSON

Date of Defence: April 19, 2022

Dr. D. Naylor Supervisor	Professor	Ph.D.
Dr. L. Spencer Committee Member	Associate Professor	Ph.D.
Dr. C. Povey Committee Member	Instructor	Ph.D.
Dr. K. Vos Chair, Thesis Examination Committee	Professor	Ph.D.

Dedication

To my late mother, Lisa, for your endless support and encourangement. I miss you deeply.

Abstract

Recent advances in far-infrared detector technology have led to increases in raw sensitivity of more than an order of magnitude over previous state-of-the-art detectors. With such sensitivity, photon noise becomes the dominant noise component, even when using cryogenically cooled optics, unless a method of restricting the spectral bandpass is employed. The leading instrument concept features reflecting diffraction gratings to post-disperse the light that has been modulated by a polarizing Fourier transform spectrometer (FTS) onto a detector array, thereby reducing the photon noise on each detector. This thesis discusses the development of a cryogenic (4 K) diffraction grating spectrometer which operates over the wavelength range from 285 - 500 μm and was used to post-disperse the output from a room-temperature polarizing FTS. Measurements of the grating spectral response and diffraction efficiency are presented as a function of both wavelength and polarization to characterize the instrumental performance.

Acknowledgments

Firstly, I would like to thank my supervisor Professor David Naylor for all of the support and encouragement you have given me over the last 5 years. You have been an incredible mentor to me and I am grateful to have been taught by someone who brings so much passion and inspiration into your work. Thank you for believing in me and for accepting me into your group when I was just in the second year of my undergraduate degree. I am grateful that I never had to spend another summer as a "sandwich artist." You have left a permanent impact on my life and I know that wherever my career takes me I will always rememeber my time working in your group.

I would like to thank all the members of the Astronomical Instrumentation Group, AIG, at the University of Lethbridge for supporting me through this research project. I'm grateful for the mentorship provided by Ian Veenendaal who did a lot of ground work for this project. Also, thank you Ian for your work in developing the test facility cryostat which was integral to my thesis. Thank you to everyone else who's expertise has paved the way for the work done in this thesis: Jacob Groeneveld, Pawal Kapusta, Steve Zimmerman, and to many of David's previous students. I am especially appreciative of Greg Tompkins who sadly passed away years ago, but who's work on the detector and photomixer electronics has made my thesis possible. Thank you to Matthew Buchan for your work in discovering the best method to apply the epoxy-carborundum mixture to components of the instrument. Lastly, I owe a lot of thanks to Brad Gom for all of the time he spent helping me with mechanical design, software, and electronics work associated with my research. Thank you for your willingness to teach me and for being patient when I didn't understand something right away. None of this work would have been possible without you and for that I am incredibly grateful.

Thank you to Rebecca Sirota for your electronics expertise and for your willingness to help me troubleshoot when things weren't working as expected. I am also very grateful for Anthony Huber who spent several evenings with me collecting data and for always helping me out when I was stuck on a project. More than the research aspect, you and Rebecca have been great friends to me and I was lucky to have you two around to look out for me when I would get too stressed. You are both extremely caring, passionate people and I know you will do great things in your lives. Thank you also to Adam Christiansen for proofreading some of my thesis and for your attention to detail. I appreciate you taking the time to teach me proper programming techniques and for sharing your knowledge in photonics.

I have been lucky to have been supported by Blue Sky Spectroscopy Inc. through my MSc where I have met several incredible scientists. Thank you to Trevor Fulton who spent hours helping me to collect data and sharing his expertise in computer programming. Trevor, you were a great mentor when I first joined the AIG and I appreciate your patience with me as an undergraduate student. Thank you to Sughakar Gunuganti for your help in running the experiments and for being my supervisor at Blue Sky Spectroscopy Inc. who funded a significant portion of my research. Sudhakar, you are an incredibly caring person with a contagious positive attitude and you have shown me how to be a meticulous experimental scientist. I wish you the best in life as that is what you deserve. Thank you to Ben Louwerse for your engineering expertise and your friendship.

I would also like to thank my committee members, Dr. Chad Povey and Professor Locke Spencer. Thank you for making time to attend my thesis meetings and for sharing your expertise with me. I appreciate your patience with me throughout my thesis submission process. I am very grateful for all of the professors in my undergraduate courses who have inspired me to continue my studies and pursue a post-graduate degree in experimental physics. I have learnt from some extremely knowledgeable and passionate people who have instilled in me a broad background in physics. Thank you to all the professors who put up with my incessant questions and for always being available outside of class hours to talk

about physics.

I am very thankful for my amazing family who have stood by my side throughout my life and who always pretend to listen when I talk about my research. Thank you to my grandparents Allan and Fran who have always supported me and offered their home to me so I could share a home-cooked meal during busy times. Your encouragement has got me through the toughest times. Thank you to my baba, Marie, and my late grandad, John, for always believing in me and encouraging me to pursue my education. Your continued support has kept me moving forward even when I've felt defeated. I am incredibly grateful for the support of my father, Garret and my late mother, Lisa. Dad, you have shown me the true meaning of hardwork and you have taught me to be firm in my beliefs (almost to a fault). Mom, I am grateful for the 21 years I got to spend with you as my biggest supporter and my best friend. I know you've been by my side this entire journey cheering me on. Thank you to my little brother, Zach, for being a source of joy in our small family.

I would like to acknowledge financial support from the NSERC Canadian graduate scholarship - Master's award, the NSERC CREATE new technologies for Canadian observatories (NTCO) award, and contributions from the U of L, Indspire and the Metis education foundation. This research was funded by ARIF, Blue Sky Spectroscopy Inc., CFI, CMC, CSA, NSERC and the U of L. I would especially like to acknowledge Blue Sky for providing many of the instrumental components necessary for the experimental work in this thesis. Furthermore, Blue Sky acted as my industrial partner for my NTCO award which provided me with financial support. I am very grateful for the generosity of Blue Sky and to the many other foundations listed above who supported my research.

Contents

List of Tables

List of Figures

Chapter 1

Introduction to Far-infrared Astronomy

> Astronomy is perhaps the science whose discoveries owe least to chance, in which human understanding appears in its whole magnitude, and through which man can best learn how small he is.
>
> GEORG C. LICHTENBERG

For thousands of years, humans have been observing the night sky wondering what lies beyond our planet. Curiosity leads to innovation and the earliest example in astronomy was the development of the first telescope by Lippershey (1570–1619) in 1608. The modest 3X magnification realized in his design was enough to inspire other astronomers who believed they could improve it. Italian astronomer Galileo (1564–1642) crafted a telescope design of his own in 1609 which modified Lippershey's design to achieve over 20X magnification [1]. Galileo made many observations of valleys on the moon, phases of Venus, and the "Galilean moons", the four largest moons of Jupiter. Many further improvements to the telescope were made over hundreds of years and in the late 1700s, Sir William Herschel (1738–1822) became a common name among world-renowned astronomers. Herschel was a British astronomer who is credited with the discovery of Uranus in 1781 and in 1789, he led the construction of a 40-foot-long wooden telescope shown in figure 1.1. Herschel's telescope was the largest in the world at the time and allowed him to image small objects including the moons orbiting Saturn. Perhaps even more integral to the advancement of modern astronomy was Herschel's work related to astronomical spectroscopy. In 1800, Herschel used a thermometer to measure the temperature in the different colours of light as they were dispersed by a prism, noting that the temperature increased from the violet to the

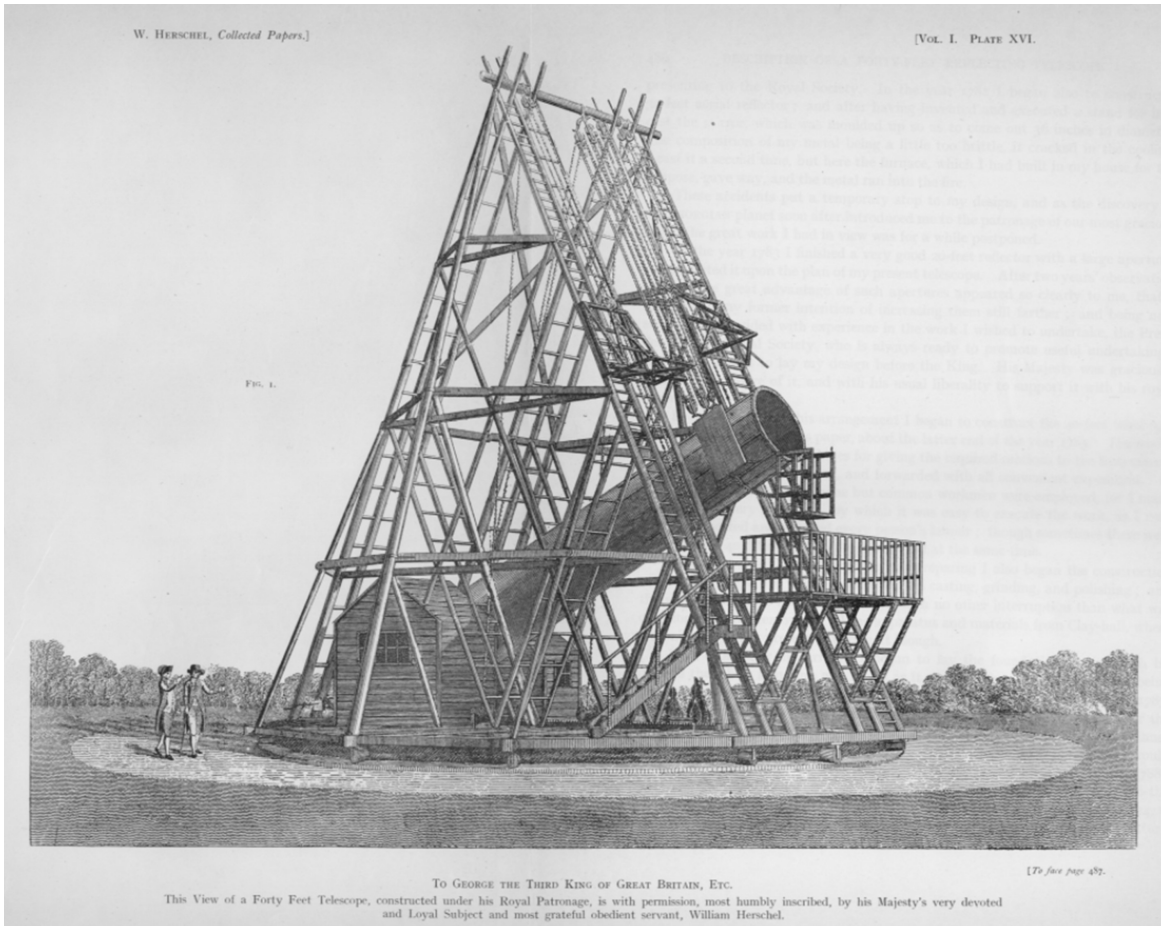

Figure 1.1: Image taken from [2] which shows the wooden telescope constructed for Herschel. The mirror itself was 48 inches in diameter and the telescope tube was 40 feet long.

red end of the spectrum [3]. Curiosity led him to measure the region just adjacent to the red light where there was no visible light and, to his surprise, this region had the highest temperature. He named the mysterious invisible radiation,"calorific rays", known today as infrared radiation. Around the same time, Fraunhofer (1787–1826) invented the modern spectroscope and used it to study the spectrum of the sun [4]. Fraunhofer noticed many dark thin lines which were later attributed to transitions between the quantized energy levels of atoms and molecules. The presence of certain atomic or molecular transitions yields information about the chemical composition of the source. Thus, modern spectroscopy was born and has evolved into the primary tool for determining the composition and physical conditions in astronomical sources.

1.1 Blackbody Radiation

Until recently with the first observation of gravitational waves, electromagnetic radiation was the only way for astronomers to study distant objects in the universe. Thus, it became critical to understand how this radiation is emitted by a source and how it interacts with matter along its path to the detector. The latter is known as radiative transfer and requires knowledge of interactions between atoms and photons [5]. This discussion begins by considering radiation emitted by condensed matter in a homogeneous and isotropic manner, known as blackbody radiation, which is governed by Planck's equation [6]:

$$B_\nu(T) = \frac{2h\nu^3}{c^2}\frac{1}{e^{\frac{h\nu}{k_B T}} - 1}, \qquad [\mathrm{W\,m^{-2}\,Hz^{-1}\,sr^{-1}}] \quad (1.1)$$

where ν is the radiation frequency, h is the Planck constant, c is the speed of light, k_B is the Boltzmann constant, and T is the temperature of the blackbody. In general, the matter encountered by radiation along its path of travel is not isotropic and directional information must be specified. Consider an energy density of radiation $\mathrm{d}E_\nu \mathrm{d}\nu$ in a frequency range between ν and $\nu + \mathrm{d}\nu$ passing through an area $\mathrm{d}A$ in time t from a direction specified by the solid angle $\mathrm{d}\Omega$ [5]:

$$\mathrm{d}E_\nu \mathrm{d}\nu = I_\nu(\vec{r}, t, \hat{n}) \cos\theta \mathrm{d}A \mathrm{d}\Omega \mathrm{d}\nu, \qquad [\mathrm{J\,Hz}] \quad (1.2)$$

where $I_\nu(\vec{r}, t, \hat{n})$ is the specific intensity in the direction of $\hat{n}$. These quantities are illustrated in figure 1.2. The flux is defined as the total energy of radiation per unit area per unit time:

$$F_\nu = \int I_\nu \cos\theta \mathrm{d}\Omega. \qquad [\mathrm{W\,m^{-2}\,Hz^{-1}}] \quad (1.3)$$

The energy density, U_ν, can be calculated by assuming the radiation travels along a cylinder with area dA and axis length cdt such that the volume which the radiation travels is

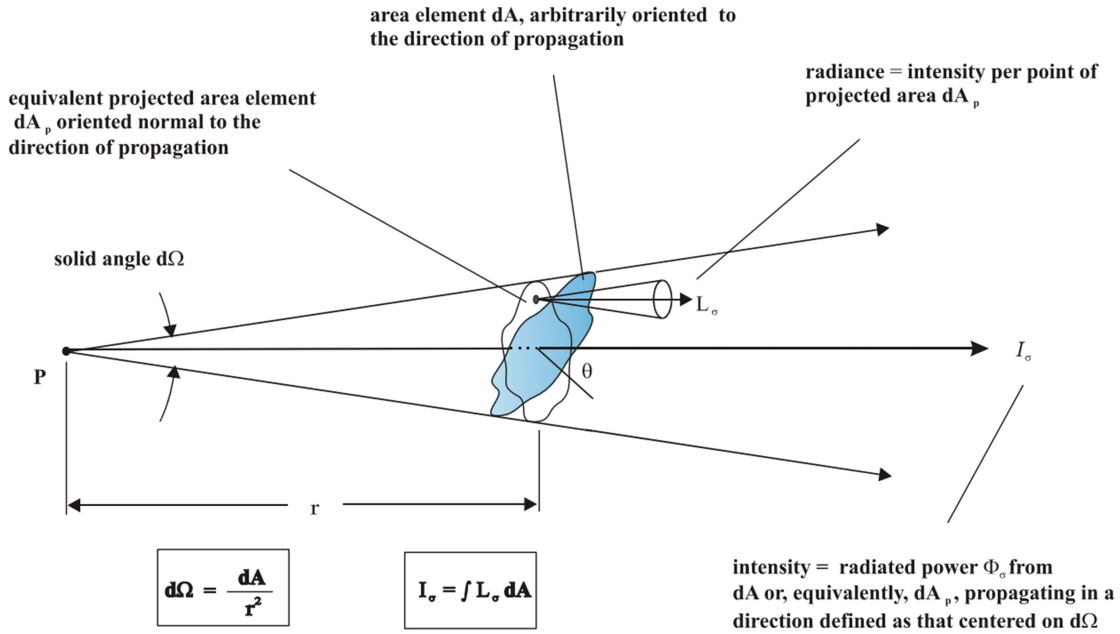

Figure 1.2: Diagram taken from [7] illustrating radiometric quantities. The spectral intensity, I_σ, which is denoted as I_ν in the text, describes the emission of a source at point P measured at a distance r. $\sigma = \frac{\nu}{c}$ is the wavenumber of the light.

$\cos\theta dAcdt$:

$$\begin{aligned} U_\nu &= \frac{\mathrm{d}E_\nu}{\mathrm{d}V} \\ &= \frac{\mathrm{d}E_\nu}{c\mathrm{d}t}\frac{1}{\cos\theta \mathrm{d}A} \\ &= \frac{I_\nu}{c}\mathrm{d}\Omega \qquad [\mathrm{J\,m^{-3}\,Hz^{-1}}] \quad (1.4) \\ &= \int \frac{I_\nu}{c}\mathrm{d}\Omega \\ &= \frac{4\pi}{c}B_\nu(T) \end{aligned}$$

The last simplification is relevant because the specific intensity of blackbody radiation is independent of direction so the integral evaluates to 4π [5]. Substituting equation 1.1 for $B_\nu(T)$, the energy density becomes:

$$U_\nu = \frac{8\pi h}{c^3}\frac{\nu^3}{e^{\frac{h\nu}{k_B T}} - 1}, \qquad [\mathrm{J\,m^{-3}\,Hz^{-1}}] \quad (1.5)$$

for a blackbody with temperature T.

As the radiation passes from the source towards the observer through space, it will interact with particles that lie along its path. The specific intensity of radiation at a given frequency will vary due to contributions from emission from the particles within the ray path and there will be losses due to photons being absorbed by particles. The contribution due to emission is represented by, j_ν, and the losses are represented by the absorption coefficient, α_ν, multiplied by the intensity. The radiative transfer equation states that the specific intensity, I_ν, of radiation at a frequency ν varies along the path of travel, s, as [5]:

$$\frac{\mathrm{d}I_\nu}{\mathrm{d}s} = j_\nu - \alpha_\nu I_\nu. \qquad [\mathrm{J\,m^{-3}\,sr^{-1}\,Hz^{-1}}] \quad (1.6)$$

If all of the radiation is absorbed, i.e. $j_\nu = 0$, the solution to the previous equation becomes:

$$I_\nu(s) = I_\nu(s_o) e^{-\int_{s_o}^{s} \alpha_\nu(s')\mathrm{d}s'}, \qquad [\mathrm{J\,m^{-2}\,sr^{-1}\,Hz^{-1}}] \quad (1.7)$$

where $\tau_\nu = \int_{s_o}^{s} \alpha_\nu(s')\mathrm{d}s'$ is the optical depth along the path [5].

Equation 1.6 for radiative transfer can be written in terms of $\frac{dI_\nu}{d\tau_\nu}$ by noting that $d\tau_\nu = \alpha_\nu ds$:

$$\frac{\mathrm{d}I_\nu}{\mathrm{d}\tau_\nu} = \frac{j_\nu}{\alpha_\nu} - I_\nu, \qquad [\mathrm{J\,m^{-2}\,sr^{-1}\,Hz^{-1}}] \quad (1.8)$$

where $S_\nu \equiv j_\nu/\alpha_\nu$ is the source function. Multiplying both side of equation 1.8 by e^{τ_ν} and integrating from 0 to τ_ν (s_o to s) the result is [5]:

$$I_\nu(\tau_\nu) = I_\nu(0) + S_\nu(1 - e^{-\tau_\nu}). \qquad [\mathrm{J\,m^{-2}\,sr^{-1}\,Hz^{-1}}] \quad (1.9)$$

In the interest of studying an object without an external source, i.e. $I_\nu(0) = 0$, the specific

intensity is then given by:

$$I_\nu(\tau_\nu) = S_\nu(1 - e^{-\tau_\nu}). \qquad [\mathrm{J\,m^{-2}\,sr^{-1}\,Hz^{-1}}] \quad (1.10)$$

For an optically thin medium, $\tau_\nu \ll 1$, the above equation simplifies to $I_\nu \approx j_\nu L$ where $L = s - s_o$ is the length of the path. For an optically thick medium, $\tau_\nu \gg 1$, and the equation simplifies to $I_\nu \approx S_\nu$ [5]. In 1860, Kirchhoff (1824–1887) proposed that matter in thermal equilibrium with its immediate environment will emit as a blackbody and predicted a relation for light passing through an optically thick medium [8]:

$$j_\nu = \alpha_\nu B_\nu(T). \qquad [\mathrm{J\,m^{-3}\,sr^{-1}\,Hz^{-1}}] \quad (1.11)$$

This relationship is known as Kirchhoff's law of thermal radiation. Optically thin astronomical sources, such as a sparse nebula, emit almost solely in spectral line features while stars are generally optically thick and their emission resembles a blackbody. The next section describes specific examples of astronomical sources which are best studied at infrared wavelengths.

1.2 The Case for Far Infrared Astronomy

In 2005, the European Space Agency (ESA) released a decadal cosmic vision that outlined the four most important questions to be answered by modern astronomy in the decade 2015 - 2025 [9]:

1. What are the conditions for planet formation and the emergence of life?

2. How does the Solar System work?

3. What are the fundamental physical laws of the Universe?

4. How did the Universe originate and what is it made out of?

Observations in the far-infrared provide critical information needed to answer questions 1, 2, and 4 [10]. Spectroscopy at these wavelengths gives insight into the evolution of stars, planetary systems, and galaxies. By detecting metallic content in cold, young, star forming regions, it is possible to infer the physical processes happening when a star is evolving. Furthermore, these observations will help scientists understand the complex conditions necessary for planets of different types to form within a protoplanetary disk. Additionally, due to cosmological expansion which will be discussed below, observations at far-infrared wavelengths are required to probe the formation and evolution of galaxies over cosmic time.

Between 2017-2019, a series of papers related to the development of a far-infrared space-based observatory were submitted and published in the Publications of the Astronomical Society of Australia. These papers outlined the specific scientific goals that are expected to be achieved with far-infrared spectroscopic observations [11–17]. Kaneda et. al. [11] describe the potential to create large-scale galactic surveys to study how star formation and black hole accretion evolves over time. Mid and far-infrared wavelengths are rich in atomic and molecular transitions which act as chemical indicators of the physical processes within the region being probed. These wavelengths are also key to detect polycyclic aromatic hydrocarbons (PAH) and understand their role in star formation [11]. Spectral identification of dust and ice features will give insight into the composition and physical properties of the interstellar medium (ISM) and into the baryonic cycling of matter between stars and gas in star forming galaxies [12]. Spignolio *et al.* [13] describes the importance of mid- and far-infrared spectroscopic observations which will allow scientists to directly measure star formation rates and the metallicity of galaxies with increasing redshift. Observations at longer wavelengths are also used to probe star forming galaxies back to the reionization epoch and see through the dusty ISM that would otherwise obscure these galaxies at shorter wavelengths [14]. The last two articles reference the use of high-resolution spectroscopic measurements to determine the outflow inflow of gas in galaxies [16] and the chemical composition of a large number of galaxies both near and far [17].

1.2.1 Star Formation

Stars are some of the most fundamental astronomical objects. Observations of stars have led them to being well classified by their physical properties including: mass, temperature, luminosity, and chemical composition. Spectroscopy is the main tool for determining these properties. The diversity in the physical characteristics of stars is mainly determined by the birth weight and, at a secondary level, the chemical composition of the protostellar nebula in which it forms. The main property to determine in a star is its mass. Stars form due to gravitational collapse in dense regions of the ISM. However, there are significant forces opposing this gravitational collapse and each opposing force varies in importance depending on the scale of interest [18]. On a large, galactic scale, the main opposing forces to gravity are the galactic tidal forces which are lowest in the spiral arms of a galaxy causing these areas to be rich in star formation [18]. On an intermediate scale, star forming regions consist of dense molecular clouds and the most important opposing forces to gravity are turbulence and magnetic fields. On the smallest scales of interest, thermal pressure dominates as the main opposing force to gravity [18]. There is a delicate balance between the forces at play and if gravity does not sufficiently counteract the opposing forces, a star will not form. The majority of visible light is absorbed by the dust and observations of the interior can only be inferred through thermal emission of interstellar dust which occurs at infrared wavelengths [18]. Thus, observations at infrared wavelengths are required to probe into regions of star formation which are enshrouded in dust.

From studying the spectra of the ISM over a range of wavelengths, dust grains are estimated to be ≈ 1 μm in diameter, close to the wavelength of visible light. Visible and shorter wavelength radiation entering through regions of interstellar dust will be scattered and re-emitted in longer wavelengths. This process is known as 'reddening' and is portrayed in figure 1.3. The diagram shows the emitted radiation is reduced in intensity at shorter wavelengths while radiation emitted in the infrared suffers less from extinction. The dust particles within the ISM are key in the early stages of star formation because they help to

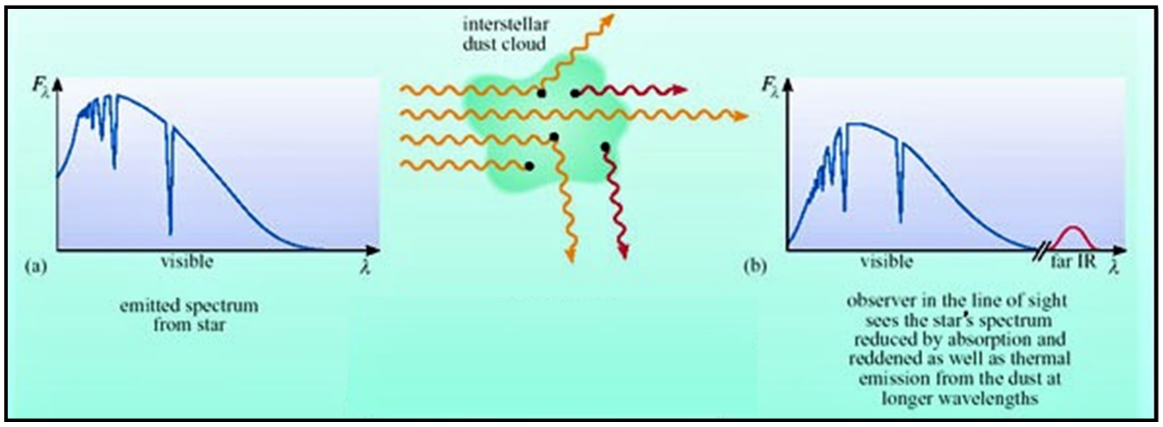

Figure 1.3: Image taken from [21] that depicts how shorter wavelength radiation is scattered and absorbed when it travels through dust clouds. The dust particles themselves emit radiation at far-infrared wavelengths.

cool the cloud as it contracts by absorbing energy from the stellar photosphere and reemitting infrared radiation [19]. Additionally, in the molecular star formation clouds, cooling is achieved by far-infrared emission from molecules such as carbon monoxide (CO) [18]. Dust particles are integral in the formation of complex molecules, including CO, within the ISM because they provide a surface for which individual atoms can meet and combine through surface reactions. Since the ISM is extremely dilute with a density of 1 atom per cm^3 on average, dust grains are critical to facilitating interactions between atoms [20]. Dust particles typically have a temperature around 20 - 40 K which means they emit radiation that peaks in the far-infrared, further necessitating observations at these wavelengths [20].

The next stages of star formation for a main-sequence star (similar in size and temperature to the sun) begin when the dense core of the cloud fragment starts to accumulate surrounding matter. As this matter is accreted into the core, the cloud spins faster to conserve angular momentum until it flattens into a protostellar disk that surrounds the dense core, or protostar [20]. From this protostar stage, the star begins to form, eventually accreting enough matter to reach core temperatures upwards of 10 000 000 K permitting the fusion of hydrogen to helium. Stars can take between 1 and 100 million years to form, thus, it is not possible to observe the evolution of a star from an interstellar cloud to a protostar and finally a mature star. However, given the 100 billion stars in the Milky Way galaxy alone

[20], astronomers can employ statistical methods to establish stellar evolutionary paths. These statistics require observations at far-infrared wavelengths which are key to studying the conditions of early star formation as mentioned above. Within the protostellar disk of a forming star lies the protoplanetary disk(s); the birthplace of planets. Infrared astronomy will provide insight into the key physical processes involved in planetary formation as described in the following section.

1.2.2 Planetary Formation

While the processes of star formation are relatively well understood, this is not the case for planets. Astronomers have discovered properties of planets from studying our solar system and nearby extrasolar planetary systems. The thousands of extrasolar planets detected to date are widely diverse and it is unknown how the properties of the planet are related to those of its parent star [22]. From the observations that have been made, planets are thought to form around young protostars in disks of interstellar dust called protoplanetary disks. Dust grains facilitate the build-up of icy mantles from sub-mm dust grains to the formation of km-sized planetesimals [23]. Spectroscopic data of several protoplanetary sources have revealed an abundance of water and ice which appears to be a key component of the accretion process. However, the chemical and physical properties of each planet depend greatly on its location relative to the parent star. Each planetary system has a defined distance from the star beyond which simple molecules such as water, can condense. This distance is known as the snowline and separates the terrestrial planets from the jovian planets [24]. The condensation of water on dust grains has a significant role in planet formation because it increases the sticking ability of the dust facilitating the accumulation of mass. Thus, outside of this snowline, the cores of these planets are able to accrete more matter and form large, jovian planets. Current astronomical observatories do not have sufficient sensitivity to determine the location of the snowline in large surveys of protoplanetary disks [23]. A need exists to develop technology for a high-sensitivity far-infrared observatory to

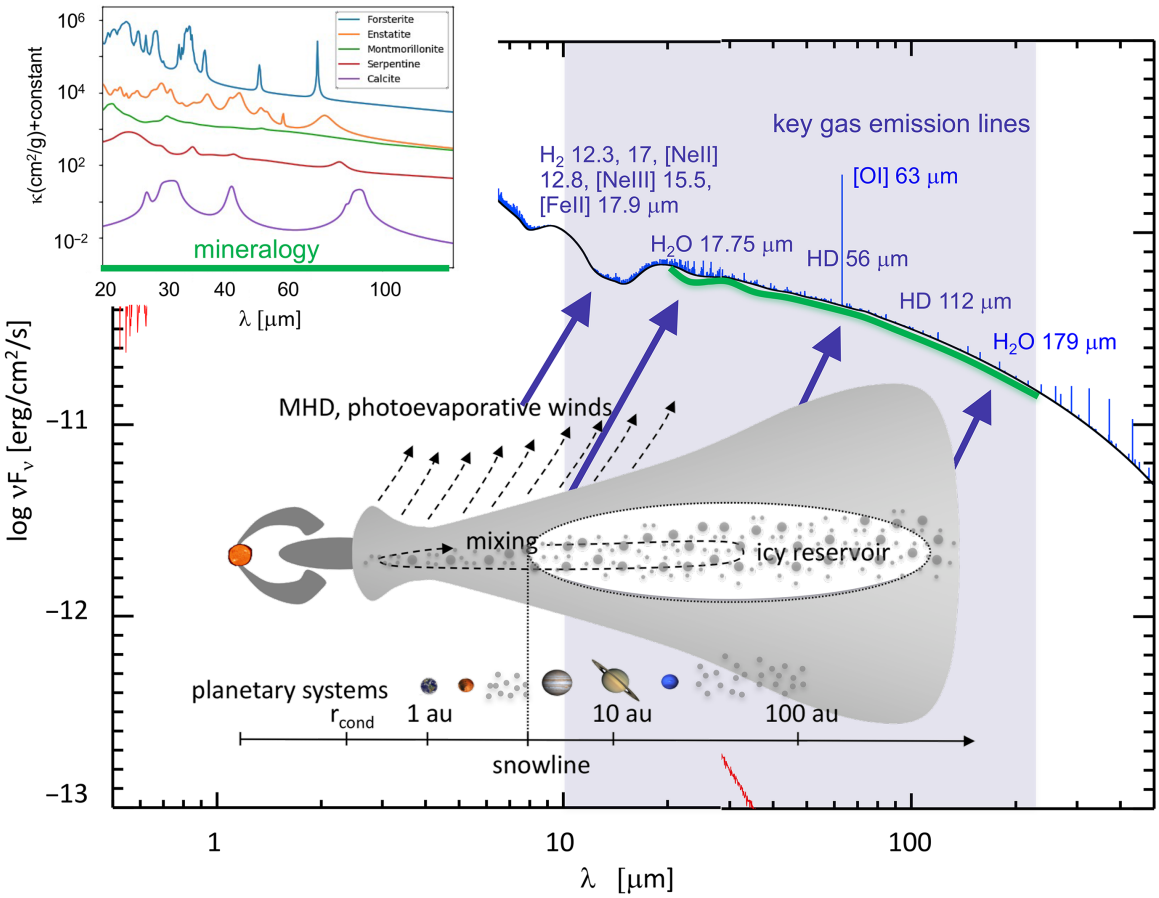

Figure 1.4: Image taken from [23] that depicts far-infrared spectral features that may appear in a protoplanetary disk.

probe protoplanetary systems.

As can be seen in figure 1.4, the measured infrared continuum and line emission allows one to probe the composition and physical state of different components within a protoplanetary disk. Astronomical facilities operating at near- to mid-infrared wavelengths cannot measure dust grains larger than several microns, which are more relevant to the planet formation process, because they emit at far-infrared wavelengths [23]. Furthermore, thermal emission from water and ice is uniquely present at far-infrared wavelengths revealing key insights into the evolution of water throughout the planet forming process [23]. Water is considered a key element in the existence of life, so understanding the role that water plays in forming planets may assist in discovering habitable worlds. Figure 1.4 shows the plethora of information that can be gained by taking high-resolution far-infrared spectro-

scopic measurements of a protoplanetary disk. Emission from neutral oxygen (OI) at 63 μm can be combined with carbon monoxide (CO) sub-mm emission to indirectly determine the disk temperature and mass [23]. Hydrogen deuteride (HD) at 56 and 112 μm is used to determine the mass of the inner disk where most planets are formed. As can be seen from figure 1.4, many diagnostic molecular and atomic lines such as hydrogen (H_2) rotational at 12.3 and 17 μm, HD, H_2O, and hydroxide (OH) fall into the far-infrared region [23]. Molecular tracers of high-energy processes include [NeII] 12.8 μm, [NeIII] 15.6 μm, [FeII] 17.9 μm, and [SI] 17.43 μm [23]. Thus, far-infrared spectroscopic measurements of protoplanetary disks are seen to provide unique diagnostic information necessary to study the formation of planets.

1.2.3 Evolution of Galaxies

Another key motivation for infrared astronomy arises from the discovery of the expanding universe. In 1929, Edwin Hubble measured the recessional velocity of 46 galaxies and used the period-luminosity relationship for Cepheid variable stars to determine the distance of each galaxy [25]. From these observations, he concluded that galaxies further away from us were moving faster away from us thus, the universe is expanding. Furthermore, he quantified this relationship between distance and velocity as being linear:

$$v = H_o r, \qquad [\mathrm{m\,s^{-1}}] \quad (1.12)$$

where H_o is the Hubble constant [25]. Hubble initially found the value of this constant to be $\approx$ 500 km s^{-1} Mpc^{-1}. However, modern methods have determined the constant to be around 70 km s^{-1} Mpc^{-1}. Hubble's measurement was inconsistent with the modern determination because he was unaware that there were two types of Cepheids with different luminosities which caused some of his distance measurements to be inaccurate [25]. These distances are on the scales of thousands of megaparsecs (1 Mpc = 3.26 million light-years) so it was still remarkable that he was able to determine this relationship to the accuracy that

he did.

Hubble's Law in equation 1.12 states that the galaxies around us are receding at velocities that increase with distance. As the light from these galaxies travels towards an observer near Earth, the wavelength becomes stretched due to cosmological expansion. For a galaxy moving away from the observer, the light is shifted into longer wavelengths and the observed wavelength depends on the relative speed of the galaxy compared to the observer. This effect is known as the Doppler shift and the relationship between the wavelength of light emitted, $\lambda_{emitted}$, to the wavelength observed, $\lambda_{observed}$, is given by [5]:

$$\frac{\lambda_{\text{observed}}}{\lambda_{\text{emitted}}} = 1 + \frac{v}{c}, \qquad [1] \quad (1.13)$$

where v is the relative speed of the source compared to the observer and c is the speed of light which is the same for all observers. Equation 1.13 is valid for galaxies with non-relativistic recessional velocities, $v/c \ll 1$. When the source is moving towards the observer, v is negative and when it is moving away, v is positive. The redshift, z, for $z < 0.2$ (non-relativistic) can be expressed as [5]:

$$z = \frac{\lambda_{\text{observed}} - \lambda_{\text{emitted}}}{\lambda_{\text{emitted}}}. \qquad [1] \quad (1.14)$$

The most distant galaxies will have their emission shifted into longer wavelengths. Thus, infrared astronomy is a powerful tool in studying the furthest reaches of the universe.

The current uniform expansion of the universe indicates there was a past time when all the matter in the universe was concentrated into a point with infinite density [5]. From this singular state, a "big bang" occurred which led to inflation and formation of the first particles. An illustration of the expansion from the beginning of the universe to present day is shown in figure 1.5. The first stars and galaxies began to form at ~ 400 million years after the Big Bang which corresponds to a redshift of $\sim$11. The transition from the dark ages to the first stars forming is known as the epoch of reionization where galactic matter

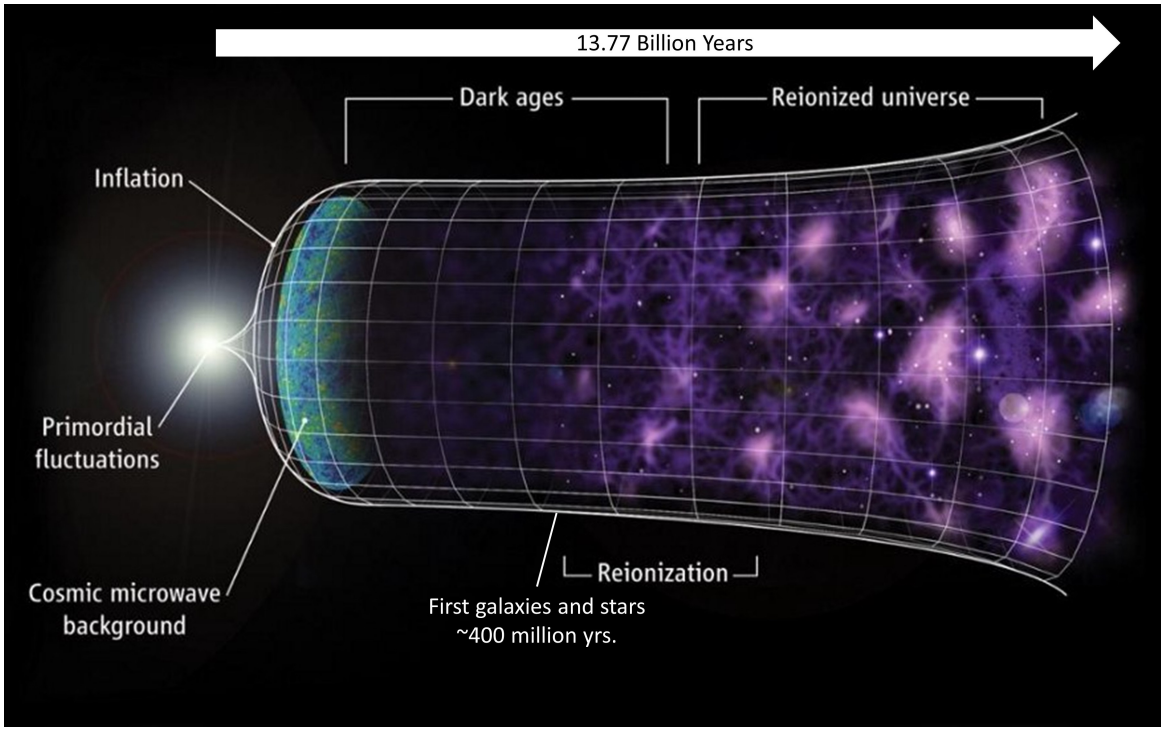

Figure 1.5: Image taken from [26] that illustrates the cosmic expansion of the universe. Gravitational instability leads to the development of the first stars and galaxies known as the transition between the ”dark ages” and the epoch of reionization.

began to emit ionized radiation [5]. Equation 1.14 gave the relationship for the redshift of an astronomical source in terms of the observed shift in wavelength of its spectral features allowing astronomers to estimate extremely far distances. Recently, astronomers have used spectroscopy to discover dozens of dust-obscured galaxies emitting with a peak luminosity in the infrared with a high star formation rate (SFR) at $z > 5$ [14]. Far-infrared observations are a unique tool to study the formation of the first galaxies which are embedded in dust and will have their emission shifted to longer wavelengths due to cosmological expansion.

Many galaxies emit radiation with a peak in the visible spectrum [20]. However, some extremely luminous sources have been found to exhibit a peculiar emission spectrum, even peaking at infrared wavelengths in the case of ultra-luminous infrared galaxies. These active galaxies have been categorized by four main species: Seyfert galaxies, radio galaxies, quasars, and blazars. All of these objects are characterized by a powerful, high-energy source located at their galactic nucleus, believed to be an active supermassive black hole

[20]. Seyfert galaxies emit most of their radiation in the infrared and resemble a similar structure to a spiral galaxy, however, their luminosity can vary by a factor of two within a period of less than a year [20]. Quasars are the most luminous of these active galaxies and usually have broad emission lines characteristic of rapid thermal motion within its core. This active galactic nucleus (AGN) is thought to be a supermassive black hole billions of times more massive than the star which is surrounded by an accretion disk of hot interstellar matter [20]. There is an intimate relationship between the increase of star formation (SF) in an active galaxy and the growth of the AGN. High-resolution spectroscopic measurements are needed to separate the spectral contributions from accretion and SF within the same source. However, the accretion disk is usually surrounded by a thick region of interstellar dust which absorbs all of the inner radiation (often with a peak in ultraviolet or optical wavelengths) and re-emits at longer wavelengths [15]. Measurements of the dust re-emission in the infrared allows astronomers to indirectly measure the primary radiation produced during the main stages of galactic evolution, and provide insight into the transition from the dark ages to the epoch of reionization [15]. With the motivation for far-infrared astronomy outlined in the above section, it is important to discuss previous infrared observatories which have paved the way for the next generation of observatories.

1.3 Infrared Observatories

1.3.1 Earth-Based Telescopes

Through centuries of technological advancements astronomers have been constantly building larger and more sensitive telescopes and instrumentation. Observing infrared radiation from ground-based telescopes is not a simple task because of the absorption by water vapour and carbon dioxide in the atmosphere. The transmission of the electromagnetic spectrum through the atmosphere is shown in figure 1.6 and it is seen that the best place to observe infrared wavelengths is from space. With the significant cost associated with sending a telescope into space, the next-best alternative is to operate the telescope in an airborne

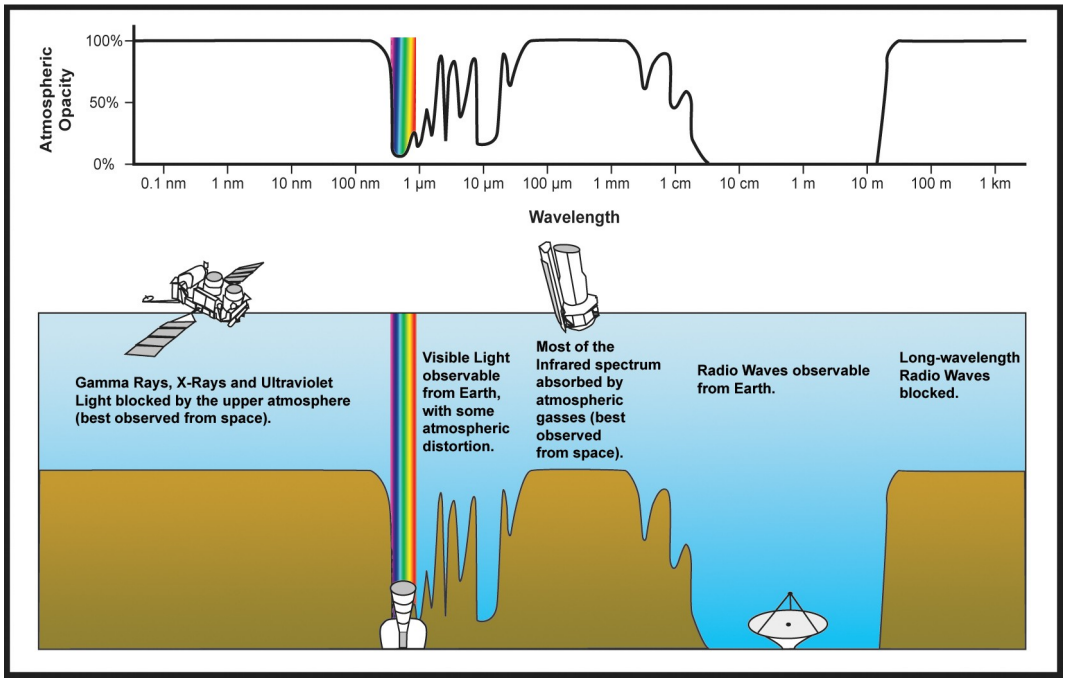

Figure 1.6: Image taken from [28] which shows the atmospheric transmission of all wavelengths of radiation. Infrared radiation is almost completely absorbed as it travels into the Earth.

facility or at the peak of a tall mountain. One observatory which operates at the top of a dormant volcano is the Mauna Kea observatory (MKO) located on the summit of Mauna Kea in Hawaii, U.S.A. MKO was built at an elevation of 4.2 km which was above most of the atmospheric water vapour; ideal conditions for infrared observations [27]. One successful infrared telescope at MKO was the James Clerk Maxwell Telescope (JCMT) which saw first light in 1987. Two of the instruments which have operated at JCMT were the submillimetre common-user bolometer array (SCUBA) and its successor SCUBA-2. The SCUBA instruments were sensitive to radiation from 450-850 µm which allowed them to make observations of distant interstellar dust sources [27].

The Llano de Chajnantor Observatory hosts a collection of observatories in the highest altitudes ($\sim$5000 m) of the Atacama Desert in Chile. The Atacama Large Millimeter Array (ALMA) is one observatory at this location which includes an array of 54 12-meter and 12 7-meter dish antennas and operates over wavelengths from 0.3 - 10 mm [29]. A new observatory aiming to see first light in 2023 is the Fred Young Submillimeter Telescope

(FYST), formerly known as CCAT-prime, which targets wavelengths between 0.2 - 3 mm and incorporates a 6-meter aperture [30]. While these high-altitude facilities experience a much lower atmospheric absorption than at sea-level, they are still ultimately limited by atmospheric emission. The Earth's atmosphere is comprised of a combination of gases: nitrogen, oxygen, argon, water vapour, etc. As the gas molecules are heated by radiation from the sun and radiation reflected from Earth's surface, they re-emit photons with energies equal to the rotational-vibrational transitions they undergo. The resulting atmospheric radiation dominates the background limiting noise generated (BLING) [31].

Another method to escape atmospheric absorption is to operate a telescope on an airborne facility. One such facility which was able to operate at an altitude of $\sim$14 km was the National Aeronautics and Space Administration (NASA) Kuiper airborne observatory (KAO) flown on a Lockheed C-141A Starlifter jet transport aircraft. KAO flew from 1974-1995 and was able to make observations in the 1 - 500 μm range using a 91.5 cm telescope [32]. The successor to the KAO was the stratospheric observatory for infrared astronomy (SOFIA) which was commissioned by NASA and the German Aerospace Center (DLR) and was flown on a Boeing 747 SP jet. The capabilities of SOFIA include high-resolution spectroscopy at wavelengths between 5-600 μm using a 2.5 m telescope with optics kept at a temperature of $\sim$ 230 K [33]. These flight missions are limited because they still experience $\sim$ 1% absorption from the atmosphere and because it is increasingly difficult to cryogenically cool the telescope within the jet interior. Ultimately, the thermal emission from the mirror of the airborne observatories dominates the BLING in the far-infrared unless the observatory is cooled to $\lesssim$ 30 K [31]. Even then, the airborne observatory is still limited by atmospheric absorption and emission. Therefore, in order to achieve a BLING which is dominated by the background of the astronomical source, the telescope must be deployed into space and cooled to cryogenic temperatures [31].

1.3.2 Spaced-Based Telescopes

Modern infrared astronomy has seen such dramatic improvements in detector sensitivity and instrument concepts that ground based telescopes are limited in sensitivity by the atmospheric emission, even at high altitudes. Even more of a limiting factor is the background radiation emitted by the intrinsic thermal emission of the telescopes, requiring them to be cooled to cryogenic temperatures. Consequently, the need for a space-based cryogenically cooled infrared observatory was established. The Infrared Astronomical Satellite (IRAS) was a collaborative effort between NASA, the Netherlands Agency for Aerospace Programmes (NIVR) and the United Kingdom's Science and Engineering Research Council (SERC). In 1983, IRAS was launched as the first space-based infrared observatory with detector bands centered around 12, 25, 60 and 100 μm [34]. IRAS featured a 57 cm telescope with mirrors cryogenically cooled to < 10 K and instrumentation cooled to < 3 K. In 1995, ESA launched the infrared space observatory (ISO) which operated in the 2.5-240 μm wavelength range and featured a 60 cm primary mirror cooled to ~ 8 K. One of the instruments on ISO was the long wavelength spectrometer (LWS) which featured optical components cooled to ~ 3 K detectors at 1.85 K allowing it to observe the long infrared wavelengths, 45-180 μm [35]. The Spitzer space telescope was launched by NASA in 2003 with a 85 cm telescope cooled to 5.5 K. The three principal instruments aboard Spitzer include the infrared array camera (IRAC) which operates in four bands from 3.6 - 8 μm, the infrared spectrometer (IRS) with four modules spanning wavelengths from 5.5-38 μm, and the multiband imaging photometer for Spitzer (MIPS) which is imaged in three bands from 24-160 μm [36]. Another infrared space mission, Akari, was launched in 2006 by the Japanese Space Agency, JAXA. Akari was specialized for the detection of wavelengths in the span of 50-180 μm and featured a 68.5 cm telescope cooled to ~ 6 K [37]. While these missions were all successful, the point source sensitivity was limited by the diameter of the primary mirror so the next step for infrared astronomy was a space-based cryogenically cooled large telescope.

The Herschel Space Observatory (Herschel) launched in 2009, was the most successful far-infrared astronomy space mission to date [38]. The instrument suite was able observe obscured regions and measure the emission of galaxies at high redshift [39]. Out of the space missions discussed, Herschel was the largest and most sensitive having a mirror with a diameter of 3.5 m and a mixture of low- and high-resolution spectroscopic instruments [40]. The instruments onboard Herschel include: the heterodyne instrument for far infrared (HIFI), the photodetector array camera and spectrometer (PACS), and the spectral and photometric imaging receiver (SPIRE). With its high sensitivity, Herschel was able to study some of the coldest and furthest objects in the universe providing invaluable information on the structure of stars, galaxies and interstellar regions.

The James Webb Space Telescope (JWST) is an infrared space observatory launched in December of 2021. The telescope features 4 instruments one of those being the Mid Infrared Instrument (MIRI) which will image and take spectral data between 5 - 29 μm. Its 6.6 m primary mirror will be passively cooled below 50 K and the telescope will be launched into the L2 orbit [41]. MIRI will provide low (R $\sim$ 100) and medium (R $\sim$ 1500 – 3000) resolution spectroscopic observations and will be the coldest instrument on the observatory at $<$ 6.7 K [42]. MIRI is expected to produce observations of the evolution of stars and planets at unprecedented sensitivities. However, it will not address the wide gap in background limited observations at far-infrared wavelengths. Figure 1.7 illustrates the spectral range and sensitivity of some current and proposed infrared missions and shows a gap between the spectral range of JWST (5 - 29 μm) and ALMA (300 μm - 10 mm) [29]. A space-based far-infrared observatory with an actively cooled, large mirror (increasing sensitivity from Herschel) is necessary to bridge this gap. Figure 1.7 illustrates how a far-infrared spaced-based mission, discussed in the next section, is the next logical step to study the infrared universe.

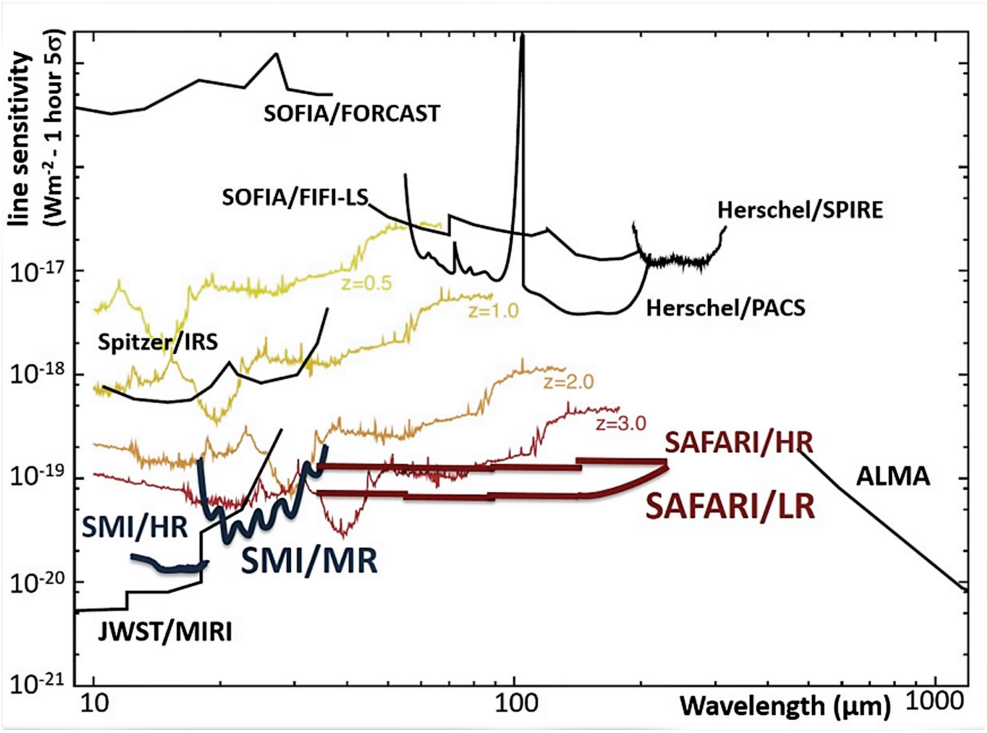

Figure 1.7: Image taken from [10] which shows a comparison of the sensitivity of current and past infrared missions. SPICA SMI and SAFARI complement the JWST and ALMA observatories.

1.4 SPICA SAFARI

Despite its success, the sensitivity of Herschel was limited by the fact that the telescope was passively cooled and could only reach temperatures of around 85 K [43]. Recognizing the potential immense improvement that could be gained with an actively cooled telescope, even before the launch of Herschel, JAXA and ESA began studying a single aperture cryogenic telescope as a future mission concept. The Space Infrared telescope for Cosmology and Astrophysics (SPICA) was selected as one of three finalists for the M5 call of the ESA [10, 44]. In October, 2020, a decision was made by the ESA and JAXA to no longer consider SPICA as a candidate mission. However, with SPICA being quite far along in the selection process, the technology developed will be useful for any future far-infrared space observatory.

The SpicA FAR-infrared Instrument (SAFARI) one of three scientific instruments on SPICA shares several features with the SPIRE instrument on Herschel [45]. New develop-

ments in detector technology utilizing superconducting transition edge sensor bolometers have yielded noise equivalent power (NEP) measurements on the order of $10^{-19}\mathrm{W}/\sqrt{\mathrm{Hz}}$; an increase of sensitivity of two orders of magnitude over the detectors used on Herschel [46]. The total NEP for a bolometer detector comes from several sources including: thermal fluctuation noise, Johnson noise in the resistance, noise in the load resistor and amplifier, excess electrical noise composed of shot noise and $1/f$ noise, and photon noise [47]. With most sources of noise coming from the composition and fabrication methods of the detector itself, advancements in technology have reduced these contributions significantly. Photon noise, however, is a fundamental source that comes from the source itself due to the discrete nature of photons. For a bolometer detector the NEP for photon noise is given by [47]:

$$\mathrm{NEP}^2_{\mathrm{photon}} = 4\frac{A\Omega}{c^2}\frac{(k_B T_s)^5}{h^3}\int \frac{x^4 \mathrm{d}x}{e^x - 1}(1 + \frac{\alpha\varepsilon f}{e^x - 1})\alpha\varepsilon f, \quad [\mathrm{W}^2\,\mathrm{Hz}^{-1}] \quad (1.15)$$

where $A\Omega$ is the optical throughput, $x = h\nu/k_B T_s$, h is Planck's constant, k_B is Boltzmann's constant, c is the speed of light, α is the absorptivity of the detector, and T_s, ε, and f are the temperature, emissivity, and transmissivity of the source. The derivative, dx, is proportional to the spectral bandwidth, dν. A Fourier transform spectrometer (FTS) observes a broad spectral band, large dν (dx), and because of this, photon noise will dominate the sensitivity of the detector unless the bandwidth of radiation falling on the detector is reduced. Restricting the bandwidth is the only meaningful way to reduce the photon noise since the throughput should be maximized and every other parameter has been optimized. A dispersive element is needed and for the SAFARI instrument this was chosen to be a reflection diffraction grating spectrometer.

The instrument concept that has been adopted for SAFARI is a Post-Dispersed Polarizing Fourier Transform Spectrometer (PDPFTS) [48]. While the principles underlying the operation of the PDPFTS are well understood, to date an integrated system has never been assembled and tested under cryogenic conditions. Our group is currently developing a PDPFTS, an analog of SAFARI, to better understand the challenges that will be presented

by this novel instrument. The results obtained from this system will be used to both inform the design of SAFARI and investigate the challenges that arise. The PDPFTS incorporates four modules: a source module consisting of a narrow line whose intensity and wavelength can be superimposed on a variable continuum, a high-resolution polarizing FTS, a low-resolution dispersing grating spectrometer, and a sensitive cryogenic bolometer detector. In this thesis I will present the results from the testing and development of a cryogenic grating spectrometer to be used as the post-dispersing module of the PDPFTS.

NASA's 2020 Decadal Survey on Astronomy and Astrophysics recognized the observational gap occurring at far-infrared wavelengths between the spectral range of JWST and ALMA [49]. In Chapter 7, section 7.5.3.3 titled: "A Far Infrared Imaging or Spectroscopy Mission" the survey acknowledges the importance of a far-infrared probe mission to answer many current questions in modern astrophysics. Furthermore, with SPICA being so far along in the selection process, the path has already been laid out to achieving major scientific advancements over the already successful Herschel. For these reasons, the survey identifies a far-infrared space probe as one of the priority missions for the next decade. With goals matching that of SPICA, a probe class mission will likely employ a similar instrument concept to the PDPFTS. This gives the work in this thesis, and throughout our group, a new sense of importance.

Chapter 2

Diffraction Grating Theory

> If you wish to make an apple pie from scratch, you must first invent the universe.
>
> *Cosmos*
> CARL SAGAN

It was shown in the previous chapter that the sensitivity of modern infrared bolometer detectors is limited by photon noise from the astronomical source when observing over a broad spectral band. From equation 1.15, the only practical way to reduce the photon noise incident on the detector is to restrict the spectral bandwidth of the radiation falling on the ultra-sensitive detectors via some form of dispersion mechanism. The concept that was developed for the SPICA far-infrared instrument (SAFARI) utilizes a diffraction grating spectrometer to post-disperse the signal from a polarizing Fourier transform spectrometer (FTS). This thesis describes the design, development, and verification of a diffraction grating spectrometer that was used to post disperse the signal from a room temperature polarizing FTS. In this chapter, the key equations that describe interference and diffraction will be introduced and subsequently used in the design of the diffraction grating spectrometer.

2.1 Interference of Light

It is now understood from quantum mechanics that light behaves both as a wave and a particle; the properties arising from the wave-nature of light will be discussed in this chapter. The first observation of interference was in the form of Newton rings discovered independently by Boyle (1627–1691) and Hooke (1635–1703) [50]. Hooke advocated the

wave theory of light and believed that light consisted of rapid variations which travelled with a great speed and over large distances. Newton (1642–1727) went on to discover the dispersion of white light through a prism into its constituent colours. Newton was devoted to proving a corpuscular theory of light, however, he was never able to do this definitively due to the dual nature of light. Huygens (1629–1695) had opposing beliefs as he believed light behaved as a wave and argued that light propagated in the same way as water waves on the surface of a pond or sound waves through air. He extended the wave theory of light by postulating a principle named after him which states that every point through which light propagates can be considered a separate source of a spherical wave. These wavelets combine to compose the overall wavefront observed. Following these theoretical descriptions, Young (1773–1829) demonstrated interference in 1801 through the famous double slit experiment. Fresnel (1788–1827) took Young's result and combined it with Huygen's principle of wavefront construction to consider the deviations that occurred when wavelets interfered with each other. These deviations are due to diffraction effects within the propagating wavefront after encountering an obstacle. Fresnel studied the effects of diffraction when light is incident on a straight edge and small apertures of different geometries [50]. Much of what he discovered forms the basis of the modern theoretical description of diffraction.

Light has been shown to exhibit interference effects when two or more coherent sources of electromagnetic radiation are superimposed on one another. A physical source produces radiation which has a phase that varies rapidly with time, and in general, any source will produce radiation that is completely uncorrelated and incoherent with another source. Therefore, in order to observe interference effects, it is necessary to consider multiple beams of light originating from the same source, ensuring that each beam is somewhat correlated with the other beam(s). A higher degree of correlation leads to a more distinct interference pattern being observed. Consider a completely monochromatic beam where the intensity (time average of the energy per unit time per unit area) perpendicular to the

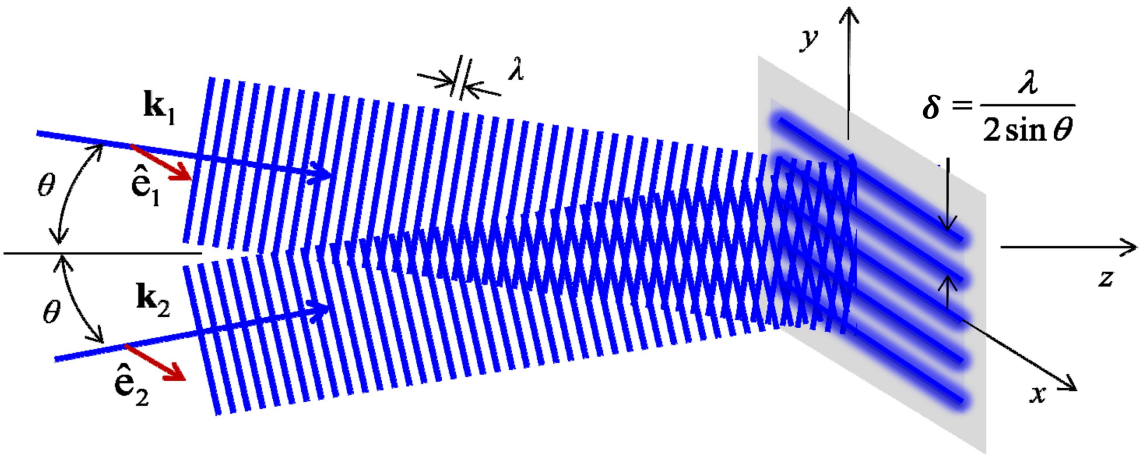

Figure 2.1: Image taken from [51] depicting the interference between two monochromatic plane waves with a wavelength of λ. The spacing between adjacent interference maxima is given by $\delta = \lambda/2\sin\theta$, where 2θ is the angle between the two beams.

direction of energy flow is given by [50]:

$$I(t) = \frac{c}{4\pi}\sqrt{\frac{\varepsilon}{\mu}}\langle E(t)^2\rangle, \qquad [\mathrm{W\,m^{-2}}] \quad (2.1)$$

where ε and μ are the electric permittivity and magnetic permeability of the medium through which the wave propagates, and $\langle E(t)^2\rangle$ is the time average of the electric field squared:

$$\vec{E}_i(\vec{r},t) = \frac{1}{2}\left[\vec{A}_i(\vec{r})e^{-i\omega t} + \overline{\vec{A}}_i(\vec{r})e^{i\omega t}\right]. \qquad [\mathrm{V\,m^{-1}}] \quad (2.2)$$

The index, i, identifies the individual components of the interfering beams. $\vec{A}_i(\vec{r})$ is a complex vector, $\overline{\vec{A}}_i$ denotes the complex conjugate, and $\omega = \frac{2\pi c}{\lambda}$ is the angular frequency of the wave. In Cartesian coordinates:

$$\vec{A}_i(\vec{r}) = \hat{e}_i\left[a_{x,i}(\vec{r}) + a_{y,i}(\vec{r}) + a_{z,i}(\vec{r})\right]e^{i\vec{k}_i\cdot\vec{r}} \qquad [\mathrm{V\,m^{-1}}] \quad (2.3)$$

where $a_{(x,y,z),i}$ are the amplitude coefficients, $\vec{k}_i = 2\pi/\lambda_i$ is the wave propagation vector, $\vec{r}$ is the position vector, and $\hat{e}_i$ is the polarization vector.

Consider two monochromatic coherent beams with propagating vectors $\vec{k}_1$ and $\vec{k}_2$, and

polarization vectors $\hat{e}_1$ and $\hat{e}_2$ as shown in figure 2.1. When these two beams with intensity I_1 and I_2 are combined the resulting intensity becomes [50]:

$$\begin{aligned} I &= I_1 + I_2 + 2\sqrt{I_{12}} \\ &= \langle E_1^2 \rangle + \langle E_2^2 \rangle + 2\langle E_1 E_2 \rangle \end{aligned} \qquad [\mathrm{W\,m^{-2}}] \quad (2.4)$$

where $\sqrt{I_{12}} = \langle E_1 E_2 \rangle$ is the interference term. For two beams which have complex amplitudes $A_1(\vec{r})$ and $A_2(\vec{r})$ [50]:

$$\begin{aligned} \vec{E}_1 \cdot \vec{E}_2 &= \frac{1}{4}\hat{e}_1 \left(A_1(\vec{r})e^{-i\omega t} + \overline{A}_1(\vec{r})e^{i\omega t}\right) \cdot \hat{e}_2 \left(A_2(\vec{r})e^{-i\omega t} + \overline{A}_2(\vec{r})e^{i\omega t}\right) \\ &= \frac{1}{4}\hat{e}_1 \cdot \hat{e}_2 \left(A_1 A_2 e^{-2i\omega t} + \overline{A}_1 \overline{A}_2 e^{2i\omega t} + \overline{A}_1 A_2 + A_1 \overline{A}_2\right) \end{aligned} \qquad [\mathrm{V^2\,m^{-2}}] \quad (2.5)$$

Taking the time average of the above expression causes the exponential terms to vanish and the resulting interference term is [50]:

$$\begin{aligned} 2\sqrt{I_{12}} = 2\langle E_1 E_2 \rangle &= \frac{1}{2}\langle \hat{e}_1 \cdot \hat{e}_2 \rangle \left(A_1 \cdot \overline{A}_2 + \overline{A}_1 \cdot A_2\right) \\ &= \langle \hat{e}_1 \cdot \hat{e}_2 \rangle (a_{x,1}a_{x,2} + a_{y,1}a_{y,2} + a_{z,1}a_{z,2}) \cos\delta \end{aligned} \qquad [\mathrm{W\,m^{-2}}] \quad (2.6)$$

where δ describes the overall phase difference between the two waves. This final expression shows the dependence of interference on both the amplitude and phase of the combined beams. For two monochromatic coherent beams linearly polarized in the $\hat{x}$ direction, $\langle \hat{e}_1 \cdot \hat{e}_2 \rangle = 1$, and traveling in the $\hat{z}$ direction [50]:

$$I = \frac{1}{2}a_{x,1}^2 + \frac{1}{2}a_{x,2}^2 + a_{x,1}a_{x,2}\cos\delta, \qquad [\mathrm{W\,m^{-2}}] \quad (2.7)$$

which has a maximum amplitude when $\delta = |2n\pi|, n \in \mathbb{Z}$, and minimum amplitude whenever $\delta = |(2n+1)\pi|$. The observation of successive maxima and minima as δ is varied is called an interference pattern. The resulting interference pattern is shown in figure 2.1.

2.2 Diffraction Theory

Considering the principles of interference, diffraction is a straightforward extension. in 1965, Richard Feynman pointed out that "no one has ever been able to define the difference between interference and diffraction satisfactorily. It is just a question of usage, and there is no specific, important physical difference between them" [52]. Usually when distinguishing between the two, one talks about diffraction when many sources interact, whereas interference is usually only a few. Nonetheless, the theory of diffraction will be discussed separately in this section utilizing the methods of Classical Electrodynamics by Jackson [53].

2.2.1 Scalar Diffraction Theory

Early diffraction theories developed by Huygen's, Young, and Fresnel relied on observations to drive approximations which described physical systems well. However, Kirchhoff (1824–1887) attempted a more rigorous approach deriving diffraction theory from first principles [8]. The scalar approach starts by taking Green's theorem for a scalar field within a closed volume, V, that is bounded by a surface, S [53]:

$$\int_V (\phi\nabla^2\psi - \psi\nabla^2\phi)d^3\vec{x} = \oint_S \left[\phi\frac{\partial\psi}{\partial n} - \psi\frac{\partial\phi}{\partial n}\right] da, \qquad [\mathrm{W}] \quad (2.8)$$

where $\frac{\partial}{\partial n}$ is the partial derivative with respect to the outward normal of the surface. $\psi(\vec{x})$ is the scalar field with a harmonic time dependence, $e^{i\omega t}$, that must satisfy the homogeneous Helmholtz wave equation:

$$\nabla^2\psi(\vec{x})e^{i\omega t} - \frac{1}{c^2}\psi(\vec{x})\frac{\partial^2 e^{i\omega t}}{\partial t^2} = 0 \quad (2.9)$$

$$(\nabla^2 + k^2)\psi(\vec{x}) = 0 \qquad [\sqrt{W}\ /\mathrm{m}^3] \quad (2.10)$$

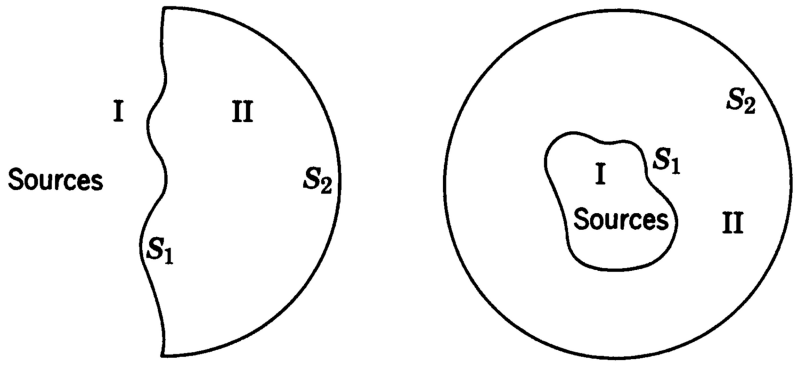

Figure 2.2: Sketch taken from [53] portraying different diffraction geometries in which region I contains the radiation sources and region II is where diffraction occurs.

where $k = \omega/c$. The other function in equation 2.8 is denoted by $\phi \equiv G(\vec{x},\vec{x}')$ which is the Green's function that satisfies the inhomogeneous Helmholtz' wave equation:

$$(\nabla^2 + k^2)G(\vec{x},\vec{x}') = -\delta(\vec{x},\vec{x}'). \qquad [\mathrm{m}^{-3}] \quad (2.11)$$

Using these definitions, the LHS of Green's theorem (equation 2.8) becomes:

$$\begin{aligned} &\int_V (G(\vec{x},\vec{x}')\nabla^2\psi(\vec{x}') - \psi(\vec{x}')\nabla^2 G(\vec{x},\vec{x}'))d^3\vec{x}' \\ =&\int_V [G(-k^2\psi(\vec{x})') - \psi(\vec{x}')(-\delta(\vec{x},\vec{x}') - k^2 G)]d^3\vec{x}' \\ =&\int_V \psi(\vec{x}')\delta(\vec{x},\vec{x}')d^3\vec{x}' \\ =&\psi(\vec{x}) \end{aligned} \qquad [\sqrt{W}\ /\mathrm{m}] \quad (2.12)$$

Combining this with the RHS of the same equation and defining $\hat{n}'$ as the normal inward to the surface, S, the expression for the scalar field is [53]:

$$\psi(\vec{x}) = \oint_S \left[\psi(\vec{x}')\hat{n}'\cdot\vec{\nabla}'G(\vec{x},\vec{x}') - G(\vec{x},\vec{x}')\hat{n}'\cdot\vec{\nabla}'\psi(\vec{x}')\right] da'. \ [\sqrt{W}\ /\mathrm{m}] \quad (2.13)$$

The Kirchoff diffraction integral can be derived from the last equation by considering the physical conditions. First, the Green's function is taken to be $G(\vec{x},\vec{x}') = \frac{e^{ik\mathcal{R}}}{4\pi\mathcal{R}}$ where $\mathcal{R} = |\vec{x}-\vec{x}'|$. This represents an outgoing wave of radiation over infinite-space [53]. The

normal derivative of this Green's function is:

$$\begin{aligned}\vec{\nabla}'G(\vec{x},\vec{x}') &= \frac{\partial G(\vec{x},\vec{x}')}{\partial \mathcal{R}}\frac{\hat{n}'\cdot\vec{\mathcal{R}}}{\mathcal{R}} \\ &= \frac{\partial}{\partial \mathcal{R}}\frac{e^{ik\mathcal{R}}}{4\pi\mathcal{R}}\frac{\hat{n}'\cdot\vec{\mathcal{R}}}{\mathcal{R}} = \frac{e^{ik\mathcal{R}}}{4\pi\mathcal{R}}(ik-1/\mathcal{R})\frac{\hat{n}'\cdot\vec{\mathcal{R}}}{\mathcal{R}} \qquad [\mathrm{m}^{-2}] \quad (2.14)\\ &= \frac{e^{ik\mathcal{R}}}{4\pi\mathcal{R}}ik\left(1+\frac{i}{k\mathcal{R}}\right)\frac{\hat{n}'\cdot\vec{\mathcal{R}}}{\mathcal{R}}\end{aligned}$$

Next, the surface S is divided into two sections, S_1 includes the screen and its apertures, and S_2 which extends to infinity outside of S_1. Figure 2.2 shows possible configurations where region I contains radiation sources and region II contains the diffracted fields. In S_2, radiation is outgoing from S_1 and therefore, in region II, $\psi(\vec{x})$ must satisfy the general condition of radiation: "the sources must be sources, not sinks, of energy. The energy which is radiated from the sources must scatter to infinity; no energy may be radiated from infinity into the prescribed singularities of the field" [54]. From this condition, the field is of the form: $\psi(\vec{x}) \equiv C\frac{e^{ikr}}{r}$, and the radiation condition gives:

$$\lim_{r\to\infty} r\left(\frac{\partial\psi}{\partial r} - ik\psi\right) = 0, \qquad [\sqrt{W}\,/\mathrm{m}^2] \quad (2.15)$$

therefore, as $r \to \infty$, the integral in equation 2.13 goes to 0, and the contribution from S_2 will vanish. The Kirchoff scalar diffraction integral is:

$$\psi(\vec{x}) = -\int_{S_1}\frac{e^{ik\mathcal{R}}}{4\pi\mathcal{R}}\hat{n}'\cdot\left[\vec{\nabla}'\psi + ik\left(1+\frac{i}{k\mathcal{R}}\right)\frac{\vec{\mathcal{R}}}{\mathcal{R}}\psi\right]da', \quad [\sqrt{W}\,/\mathrm{m}] \quad (2.16)$$

which is integrated only over the surface, S_1, which includes the screen and its apertures.

2.2.2 Approximations

Equation 2.16 requires one to know the values of the scalar field and its normal derivative on S_1 which, in general, is not straightforward. Kirchoff formulated approximations to these functions where he assumed $\psi(\vec{x})$ and $\frac{\partial\psi}{\partial n}$ vanish on S_1 except at the apertures.

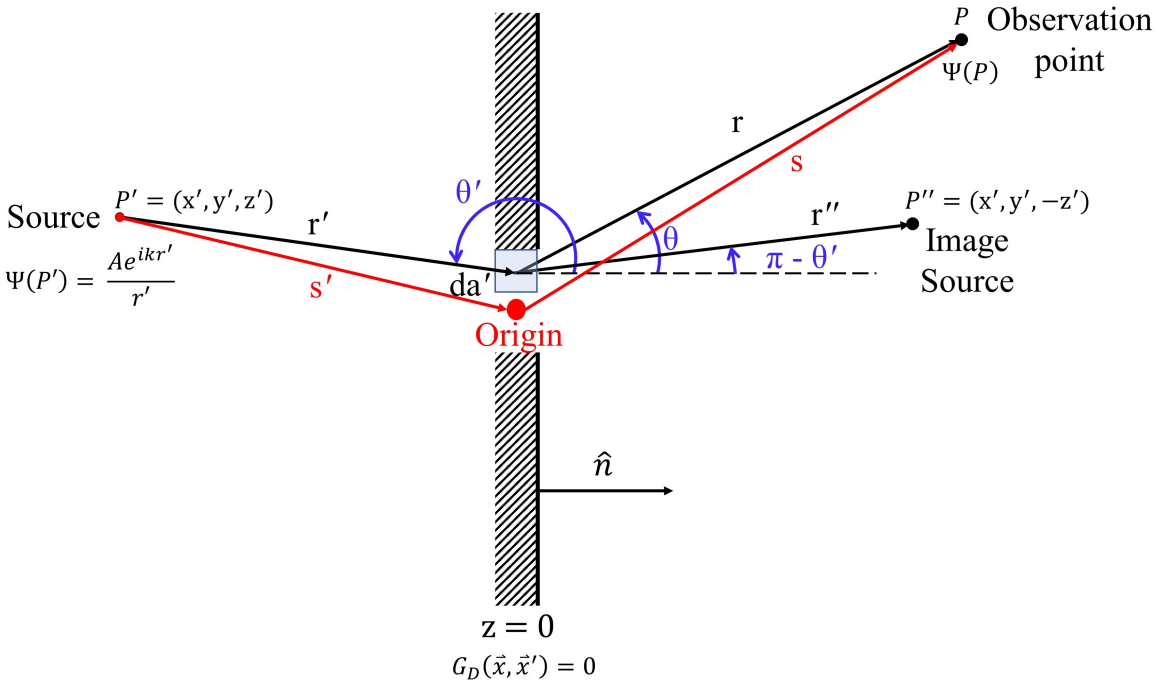

Figure 2.3: Diffraction geometry for a source incident on an infinite plane at $z = 0$ with a small aperture.

Furthermore, he postulated that the field and its derivative are equal to the values of the incident wave. While these assumptions make the calculation much easier, they have been found to be mathematically inconsistent. This stems from the Helmholtz and Laplace equations where if the scalar field vanishes for any finite surface on S_1, it must vanish everywhere, i.e. $\psi(\vec{x}) = 0$ at the apertures which directly contradicts the second assumption [53]. Proper Dirichlet or Neumann boundary conditions on the Green's function can preserve the consistency of Kirchoff's scalar diffraction theory.

An important result arises when the screen is taken as an infinite xy-plane at $z = 0$ and a point source is incident on its aperture as shown in figure 2.3. r' represents the length of source vector: $\vec{x}' = (x', y', z')$, r'' is the length of the image source vector which is placed at: $\vec{x}'' = (x', y', -z')$ in order to have $G_D(\vec{x}, \vec{x}')$ vanish at $z = 0$. For a point source described by $\psi(P') = \frac{Ae^{ikr'}}{r'}$, the scalar field at the observation point (P) is given by:

$$\begin{aligned}\psi(P) &= -\int_{S_1} \frac{e^{ikr}}{4\pi r}\hat{n}' \cdot \left[\vec{\nabla}'\psi + ik\left(1+\frac{i}{kr}\right)\frac{\vec{r}}{r}\psi\right] \mathrm{da}' \\ &= -\frac{1}{4\pi}\int_{S_1} \frac{e^{ikr}}{r}\frac{\partial\psi}{\partial r'}\frac{\hat{n}'\cdot\vec{r}'}{r'}\mathrm{da}' - \frac{1}{4\pi}\int_{S_1}\psi\frac{e^{ikr}}{r}ik\left(1+\frac{i}{kr}\right)\frac{\hat{n}'\cdot\vec{r}}{r}\mathrm{da}'\end{aligned} \tag{2.17}$$

$$= -\frac{A}{4\pi}\int_{S_1}\frac{e^{ikr}}{r}\frac{e^{ikr'}}{r'}ik\left(1+\frac{i}{kr'}\right)\frac{\hat{n}'\cdot\vec{r}'}{r'}\mathrm{da}' - \frac{A}{4\pi}\int_{S_1}\frac{e^{ikr'}}{r'}\frac{e^{ikr}}{r}ik\left(1+\frac{i}{kr}\right)\frac{\hat{n}'\cdot\vec{r}}{r}\mathrm{da}' \quad [\sqrt{W}\text{ /m}] \tag{2.18}$$

From figure 2.3, the directions of the surface normal vector can be redefined. Recall $\hat{n}'$ is the inward normal to the surface, S_1, making it equal to $-\hat{n}$. Therefore, $\hat{n}'\cdot\vec{r} = |r|\cos(\pi-\theta) = -\cos\theta$ and $\hat{n}'\cdot\vec{r}' = |r'|\cos\theta'$. Incorporating this into the previous equation the result is:

$$\psi(P) = -\frac{iAk}{4\pi}\int_{S_1}\frac{e^{ikr}}{r}\frac{e^{ikr'}}{r'}\left[\left(1+\frac{i}{kr'}\right)\cos\theta' - \left(1+\frac{i}{kr}\right)\cos\theta\right]\mathrm{da}'. \quad [\sqrt{W}\text{ /m}] \tag{2.19}$$

When the source length, r', and observational length, r, are large compared to the wavelength of light; i.e. $r' \gg \lambda$ and $r \gg \lambda$, this equation can be further simplified. If the $1/r^2$ and $1/r'^2$ terms are ignored this becomes the Fresnel-Kirchoff diffraction formula:

$$\psi(P) = -\frac{iAk}{4\pi}\int_{S_1}\frac{e^{ikr}}{r}\frac{e^{ikr'}}{r'}\left(\cos\theta' - \cos\theta\right)\mathrm{da}'. \qquad [\sqrt{W}\text{ /m}] \tag{2.20}$$

2.3 Fraunhofer Diffraction

Approximations of the scalar field and its normal derivative are necessary to solve the complicated Kirchoff diffraction integral in equation 2.16. The Fresnel-Kirchoff diffraction formula in equation 2.20 can be simplified further by taking a closer look at the terms inside of the integral. This will be done using the methods outlined in Chapter 8 of Principles of Optics by Born and Wolf [50]. The simplified diffraction theory will be applied to the study of light passing through a rectangular aperture in this section.

2.3.1 Fraunhofer Diffraction Integral

From equation 2.20, as the integration over da$'$ is computed, $r + r'$, will change by a large amount compared to the wavelength causing the phase factors e^{ikr} and $e^{ikr'}$ to oscillate rapidly. These oscillations will happen much more quickly than the change in θ or θ' so the term: $(\cos\theta' - \cos\theta)$ in the integral can be approximated as constant over the aperture. Furthermore, the distances r and r' are much larger than the dimensions of the aperture and will not vary appreciably as the integral is computed. They can be treated as constants and are replaced by s and s' where the source and observation points are now measured relative to the origin of the aperture. Refer back to figure 2.3 for a visual representation of these distances. With the distances constant, $(\cos\theta' - \cos\theta)$ can be replaced by $2\cos\delta$ where δ is the angle between the normal of the aperture screen and the line connecting the source and observation point. Under these approximations, the Fresnel-Kirchoff diffraction equation becomes:

$$\psi(P) \approx -\frac{iAk}{2\pi}\frac{\cos\delta}{ss'}\int_{S_1} e^{ik(r+r')}\mathrm{da}'. \qquad [\sqrt{W}\ /\mathrm{m}] \quad (2.21)$$

Assuming the source point has coordinates: (x_o, y_o, z_o), and the observation point is at: (x, y, z), for a point on the aperture with coordinates: $(\xi, \eta, 0)$ the two distances r and r' are given by:

$$\begin{aligned} r^2 &= (x-\xi)^2 + (y-\eta)^2 + z^2 \\ r'^2 &= (x_o-\xi)^2 + (y_o-\eta)^2 + z_o^2 \end{aligned} \qquad [\mathrm{m}^2] \quad (2.22)$$

Additionally, the distances s and s' are expressed as:

$$\begin{aligned} s^2 &= x^2 + y^2 + z^2 \\ s'^2 &= x_o^2 + y_o^2 + z_o^2 \end{aligned} \qquad [\mathrm{m}^2] \quad (2.23)$$

such that:

$$\begin{aligned} r^2 &= s^2 - 2(x\xi + y\eta) + \eta^2 + \xi^2 \\ r'^2 &= s'^2 - 2(x_o\xi + y_o\eta) + \eta^2 + \xi^2 \end{aligned} \qquad [\mathrm{m}^2] \quad (2.24)$$

η and ξ are both within the dimensions of the aperture which is assumed to be much smaller than the distances from the source and observation points to the aperture screen. Equation 2.24 can be computed as a power series in ξ/s, η/s, ξ/s', and η/s':

$$\begin{aligned} r &\approx s - \frac{x\xi + y\eta}{s} + \frac{\xi^2+\eta^2}{2s} - \frac{(x\xi+y\eta)^2}{2s^3} + \cdots \\ r' &\approx s' - \frac{x_o\xi + y_o\eta}{s'} + \frac{\xi^2+\eta^2}{2s'} - \frac{(x_o\xi+y_o\eta)^2}{2s'^3} + \cdots \end{aligned} \qquad [\mathrm{m}] \quad (2.25)$$

Substituting this back into the integral from equation 2.21 the result is:

$$\psi(P) \approx -\frac{iAke^{ik(s+s')}}{2\pi}\frac{\cos\delta}{ss'}\int_{S_1} e^{ik(-\frac{x\xi+y\eta}{s} - \frac{x_o\xi+y_o\eta}{s'} + \frac{\xi^2+\eta^2}{2s} + \frac{\xi^2+\eta^2}{2s'} - \frac{(x\xi+y\eta)^2}{2s^3} - \frac{(x_o\xi+y_o\eta)^2}{2s'^3} + \cdots)}\mathrm{da}'.$$

$$[\sqrt{W}\ /\mathrm{m}] \quad (2.26)$$

Defining the directional cosines as: $l_o = -x_o/s'$, $l = x/s$, $m_o = -y_o/s'$, and $m = y/s$ the argument of the exponential becomes:

$$\frac{x\xi + y\eta}{s} - \frac{x_o\xi + y_o\eta}{s'} + \frac{\xi^2+\eta^2}{2s} + \frac{\xi^2+\eta^2}{2s'} - \frac{(x\xi+y\eta)^2}{2s^3} - \frac{(x_o\xi+y_o\eta)^2}{2s'^3} + \cdots \quad (2.27)$$

$$= (l_o - l)\xi + (m_o - m)\eta + \frac{1}{2}\left[\left(\frac{1}{s} + \frac{1}{s'}\right)(\xi^2+\eta^2) - \frac{(l_o\xi + m_o\eta)^2}{s'} - \frac{(l\xi+m\eta)^2}{s}\right]\cdots \quad [\mathrm{m}] \quad (2.28)$$

These relationships make the integral in equation 2.26 much more straightforward to solve. Two cases naturally come about from the power series: where quadratic terms can be neglected this is known as Fraunhofer diffraction; when they cannot be neglected this is called Fresnel diffraction. Fraunhofer diffraction is applicable when the source and observation

points tend to infinity. It is shown in Optics by Born and Wolf [50] that the Fraunhofer condition applies also when the plane that incorporates the point of observation is parallel to the plane of the aperture. The final form of the Fraunhofer diffraction integral is given by:

$$\psi(P) = C \int_{S_1} e^{-ik(p\xi+q\eta)} \mathrm{d}\xi \mathrm{d}\eta, \qquad [\sqrt{W}/\mathrm{m}] \quad (2.29)$$

where $p = l - l_o$ and $q = m - m_o$.

Appendix A presents experimental results of diffraction taken with near-infrared (1550 nm) light through various aperture geometries. The measured diffraction fields showed a strong agreement with the field predicted by the Fraunhofer diffraction integral in equation 2.29. The next section below will use equation 2.29 to compute the diffraction through a rectangular slit.

2.3.2 Single Slit

Fraunhofer studied apertures of different geometries and this section focuses on rectangular apertures and the slit. The Fraunhofer diffraction integral for light passing through a rectangular aperture is given by [50]:

$$\psi(P) = C \int_{-a}^{a} e^{-ikp\xi} d\xi \int_{-b}^{b} e^{-ikp\eta} d\eta, \qquad [\sqrt{W}/\mathrm{m}] \quad (2.30)$$

where the dimensions of the slit are $2a \times 2b$ and the slit is centered about the origin, $(\xi, \eta) = (0,0)$. The slit geometry is illustrated in figure 2.4 (a). C is the amplitude determined by the position of the source and observation point, $k = \omega/c$ for the wave, and p and q are specified by directional cosines. l, m, n and l_o, m_o, n_o are the directional cosines for the observation point and incident ray; $p = 1 - l_o$ and $q = m - m_o$ for Fraunhofer diffraction [50]. The

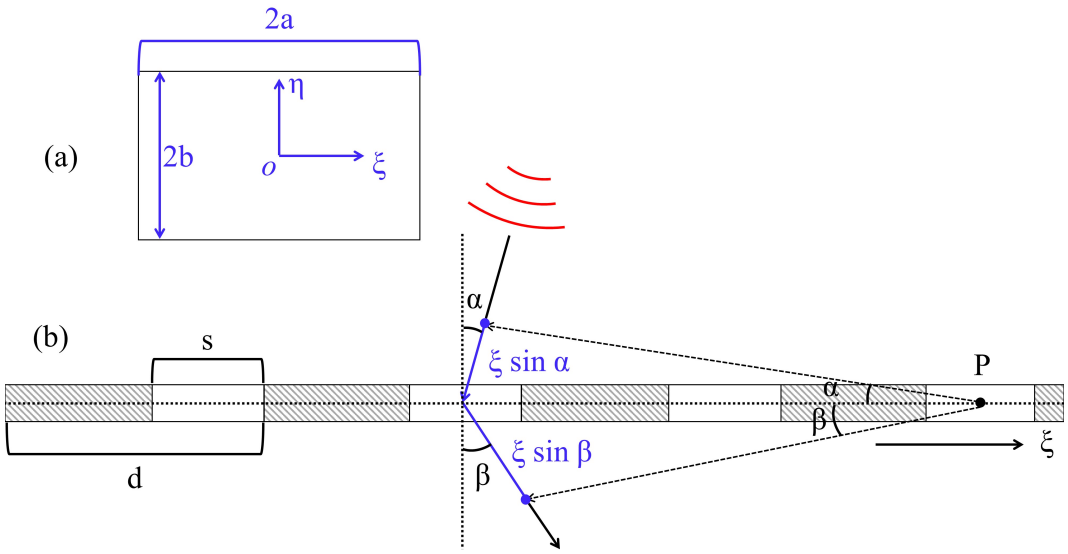

Figure 2.4: Geometry for a single rectangular aperture (a) and a wavefront incident on a transmission diffraction grating comprised of successive rectangular slits (b).

integral in the above equation can be evaluated as:

$$\begin{aligned}\int_{-a}^{a} e^{-ikp\xi} d\xi &= \frac{-1}{ikp} e^{-ikp\xi}\Big|_{-a}^{a} \\ &= \frac{1}{ikp}\left[-e^{-ikpa} + e^{ikpa}\right] \\ &= \frac{1}{ikp} 2i\sin(kpa) \\ &= \frac{2\sin(kpa)}{kp}\end{aligned} \quad \text{[m]} \quad (2.31)$$

A similar result is obtained for the second integral and the 2-D intensity distribution can be expressed as [50]:

$$I(p) = |\psi(p)|^2 = \frac{ED}{\lambda^2 \mathcal{R}^2}\left(\frac{\sin(kpa)}{kpa}\right)^2\left(\frac{\sin(kpb)}{kpb}\right)^2, \quad [\mathrm{W\,m^{-2}}] \quad (2.32)$$

where E is the total power incident on the aperture, $D = 4ab$ is the aperture area, and $\mathcal{R}$ is the observation distance. The intensity equation is the $\mathrm{sinc}(x) = \frac{\sin x}{x}$ function squared which is illustrated in figure 2.5. It is seen that the intensity produces minima, or dark

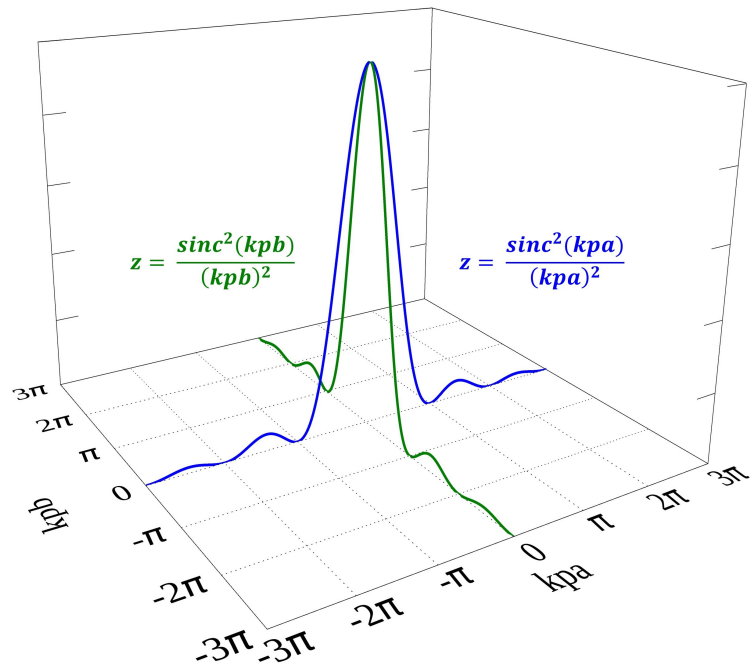

Figure 2.5: Fraunhofer diffraction through a rectangular aperture as described in equation 2.32. The intensity function is governed by the $\text{sinc}^2(x)$ function which has minima at $x = n\pi$, $n \in \mathbb{Z}$.

fringes, when $kpa = n\pi$ and $kpb = m\pi$, $(m,n = 1,2,3...)$. The intensity distribution has a principal maximum at $kpa = 0$.

2.3.3 Multiple Slits

The procedure for calculating the intensity distribution due to diffraction through a single aperture, or slit, can be generalized to a system with many slits. Consider a screen of N similar apertures of arbitrary geometry aligned parallel to each other and spaced evenly in 1 dimension. This system is illustrated in figure 2.4 (b) for a few slits. The Fraunhofer diffraction integral becomes:

$$\begin{aligned} \psi(P) &= \psi_0(p) \sum_{n=0}^{N} e^{-ikndp} \\ &= \psi_0(p) \frac{1 - e^{-ikNdp}}{1 - e^{-ikdp}} \end{aligned} \qquad [\sqrt{W}\ /\text{m}] \quad (2.33)$$

where d is the spacing between each aperture and

$$\psi_0(p) = C\int_{S_1} F(\xi)e^{-ikp\xi}d\xi. \qquad [\sqrt{W}\ /\mathrm{m}] \quad (2.34)$$

S_1 is the geometry of the aperture. The intensity can be calculated in the same way as in equation 2.32:

$$\begin{aligned} I(p) &= |U(p)|^2 = |U_0(p)|^2 \frac{(1-e^{-ikNdp})(1-e^{ikNdp})}{(1-e^{-ikdp})(1-e^{ikdp})} \\ &= I_0(p)\frac{1-\cos(Nkdp)}{1-\cos(kdp)} \qquad [\mathrm{W\,m^{-2}}] \quad (2.35) \\ &= I_0(p)\left(\frac{\sin(Nkdp/2)}{\sin(kdp/2)}\right)^2 \end{aligned}$$

$I_0(p)$ is the effect of diffraction from a single slit while the term on the RHS is the effect of interference from many slits. Substituting in equation 2.32 for $I_0(p)$ the result can be written as:

$$I(p) = \frac{sE}{\lambda\mathcal{R}^2}\left(\frac{\sin(ksp/2)}{ksp/2}\right)^2\left(\frac{\sin(Nkdp/2)}{\sin(kdp/2)}\right)^2, \qquad [\mathrm{W\,m^{-2}}] \quad (2.36)$$

which represents the intensity distribution for a 1-dimensional transmission diffraction grating. Section 2.5 will discuss how this relationship can be easily derived by using a Fourier transform to compute the transmission through the grating. Figure 2.6 shows the two functions plotted separately and the resultant distribution due to both effects. The minima of the function plotted in (c) are observed when $kdp/2 = m$, where $p = l - l_o = \sin\beta - \sin\alpha$. α is the angle that the incident ray makes with the normal of the screen and β is the angle measured from the surface normal of the ray after it passes through the aperture. The conditions of maximum interference occur when:

$$\sin\beta - \sin\alpha = \frac{m\lambda}{d}, \qquad [1] \quad (2.37)$$

where m is an integer. The above expression is known as the diffraction grating equation and is used extensively in the design of the grating module.

2.4 Diffraction Grating

A diffraction grating is an optical structure that consists of an array of reflecting or transmitting diffracting elements that are separated by a distance comparable to the wavelength of incident light [50]. The principle of the grating was discovered in 1785 by Rittenhouse (1732–1796) and was later rediscovered by Fraunhofer in 1819 who used a diamond ruling point to cut periodic grooves onto a glass surface. Rowland (1848–1901) improved this method and was able to rule 140,000 grooves/inch to create a grating structure with a resolving power of $\sim 150,000$. Michelson (1852–1931) was able to construct gratings with resolving powers around 400,000 [50]. Modern gratings continue to be manufactured using diamond ruling points to cut grooves and reflection gratings often use an aluminum substrate. Aluminum has high reflectivity and provides less wear on the diamond point since it is a softer metal. Furthermore, aluminum has well-known properties at cryogenic temperatures and is used in many other optical components and their mounts. Therefore, fabricating the grating out of aluminum also helps to minimize differential contraction of the grating module.

Used alone, a grating provides low-resolution spectroscopic capability. When used in conjunction with a high-resolution spectrometer (e.g. Fabry-Pérot, FTS) the grating serves to restrict the spectral bandwidth falling on the detector. Consider a grating composed of N uniformly placed slits each with a width of s, length of L, and separated by a distance of d, the Fraunhofer diffraction intensity distribution is given by [50]:

$$I(p) = \frac{sE}{\lambda \mathcal{R}^2} \left(\frac{\sin(Nkdp/2)}{\sin(kdp/2)} \right)^2 \left(\frac{\sin(ksp/2)}{ksp/2} \right)^2. \qquad [\mathrm{W\,m^{-2}}] \quad (2.38)$$

The maxima of this function are observed when $p = \sin\alpha - \sin\beta = \frac{m\lambda}{d}$, $(m = 0, \pm 1, \pm 2, ...)$.

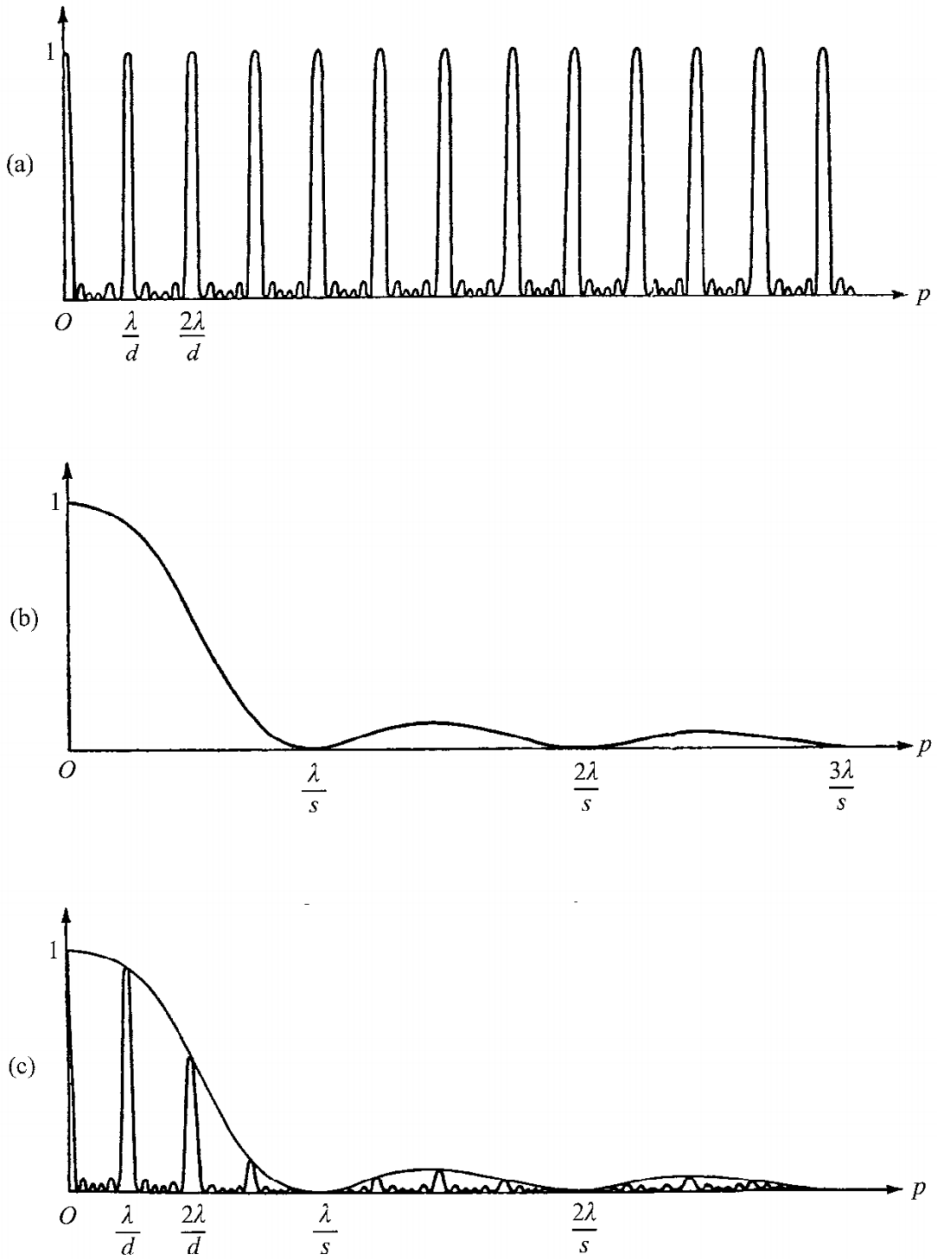

Figure 2.6: Figure (a) is the RHS term of equation 2.35 describing the effect of interference from multiple slits. Figure (b) is the intensity distribution due to the light diffraction through a single slit; the $\text{sinc}^2(x)$ function. Figure (c) shows the entirety of equation 2.35 which is the combination of (a) and (b). All functions have been normalized [50].

In a diffraction grating spectrometer, d, is not configurable after fabrication and m is determined to avoid spectral overlap. When a broadband source is incident at an angle α, the light will be diffracted at different angles, β, depending on the wavelength.

Conditions of maximum interference for the diffraction grating occur when:

$$m\lambda = d(\sin\alpha + \sin\beta), \qquad \text{[m]} \quad (2.39)$$

where m is the order of diffraction. This is the well-known diffraction grating equation which is central to the grating design. The sign difference between equation 2.37 and equation 2.39 occurs because equation 2.39 applies to a reflection grating whereas equation 2.37 corresponds to the light transmitting through the diffraction elements. The path difference between the light reflecting from adjacent grooves of the grating can be expressed as [55]:

$$d\sin\alpha + d\sin\beta, \qquad \text{[m]} \quad (2.40)$$

where α is the angle of incident light measured from the grating's normal, d is the spacing between adjacent grooves and β is the angle that the diffracted light makes with the grating normal. As was mentioned above, for a reflection grating, β is measured in the opposite direction to the normal of the grating, i.e. β is negative. This relationship is evident from figure 2.7.

Gratings are often coupled with auxiliary optics forming imaging systems. Several grating configurations exist including the Littrow mount, double and triple monochromators, etc. The configuration adopted for the grating spectrometer in this thesis was the Czerny-Turner monochromator which is illustrated in figure 2.7. In this configuration, the grating equation can be written as:

$$m\lambda = 2d(\sin(\theta - \phi)\cos\phi), \qquad \text{[m]} \quad (2.41)$$

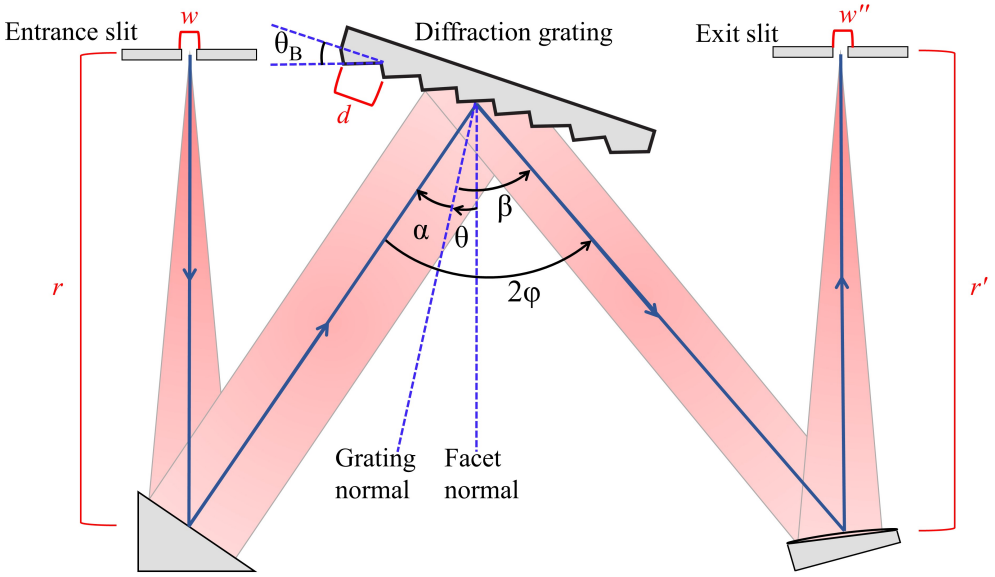

Figure 2.7: The Czerny-Turner monochromator configuration [4]. α is the incident angle, β is the diffracted angle, M_1 and M_2 are mirrors with focal lengths r and r'. w & w'' are the widths of the entrance and exit slits [57].

where ϕ is the deviation angle and θ is the angle of incidence minus the deviation angle [56]. The relationship between the angles α, β, θ, and ϕ is:

$$\begin{aligned} \alpha &= \theta + \phi \\ \beta &= \theta - \phi \end{aligned} \qquad \text{[rad]} \quad (2.42)$$

When a collimated broadband source is incident on the grating, light of wavelength λ is diffracted at an angle β in the first order, $m = 1$. However, there will also be light with a wavelength $\lambda/2$ which is diffracted at the same angle β in the second order, $m = 2$, and light with wavelength $\lambda/3$ diffracted at β in the third order, etc. This is an example of overlapping spectra, as shown in figure 2.8, and can be an issue if the free spectral range (FSR) of the grating allows overlap of these diffraction orders. The FSR is the minimum wavelength range that can be achieved such that the superposition of light from adjacent

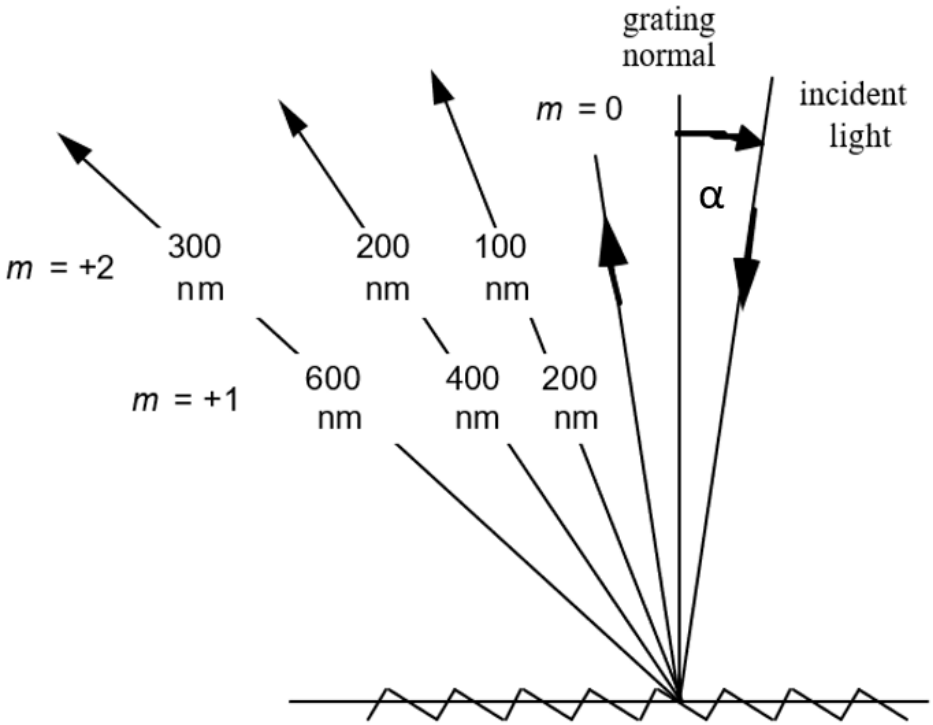

Figure 2.8: Overlapping of wavelengths of light that are diffracted at different orders. An order sorting mechanism is needed because the detector cannot distinguish between multiple wavelengths of light [55].

orders is not observed, FSR is expressed as:

$$F_\lambda = \Delta\lambda_{FSR} = \frac{\lambda_L}{m}. \qquad \text{[m]} \quad (2.43)$$

where λ_L is the lowest wavelength the system is interested in and $\Delta\lambda_{FSR}$ is the minimum wavelength range to avoid observing overlapping spectral orders.

An important property of the diffraction grating is the dispersion which describes the change in diffracted angle per unit wavelength:

$$D = \frac{d\theta}{d\lambda} = \frac{m}{d}\frac{1}{\cos\beta}, \qquad \text{[rad m}^{-1}\text{]} \quad (2.44)$$

where D is the angular dispersion of the diffracted light [55]. The linear dispersion can be

found by taking the product of the angular dispersion and the exit focal length, r':

$$L = \frac{mr'}{d}\frac{1}{\cos\beta}, \qquad [1] \quad (2.45)$$

which describes the change in distance at the observation plane as the wavelength varies.

2.4.1 Resolving Power

One of the most important performance considerations for the grating spectrometer developed in this thesis is the ability of the spectrometer to spectrally resolve an incident source. The chromatic resolving power of a grating is given by:

$$R = \frac{\lambda}{\Delta\lambda}, \qquad [1] \quad (2.46)$$

where $\Delta\lambda$ is the limit of resolution, or resolution. While there are several definitions of spectral resolution, the one used in this thesis is Rayleigh's criterion. Rayleigh stated that for two adjacent fringes of equal intensity to be resolved, the maximum of one coincides with the minimum of the other [58]. For a diffraction grating, the resolution depends on the size and positions of the entrance and exit slits as well as image magnification from the optical components.

The imaging properties of the grating system can be characterized by comparing the convolution of the image of the entrance slit with the exit slit. The resolution is optimized when the image width of the entrance slit is equal to the width of the exit slit [55]. As light passes through an entrance slit, it forms an image of the slit that will be magnified differently in the horizontal and vertical directions. The vertical magnification is known as anamorphic magnification. In this thesis, the rectangular slits are over-sized in the vertical direction to avoid excessive anamorphic magnification. The tangential magnification of the

width of the entrance slit is given by:

$$\chi_T = \frac{w'}{w} = \frac{r'}{r}\frac{\cos\alpha}{\cos\beta}, \qquad [1] \quad (2.47)$$

where w' is the width of the image of the entrance slit, w, is the width of the entrance slit, and r is the entrance focal length [55]. This equation can be used to determine the width of the image, w' and tangential magnification is illustrated in figure 2.9. The resolution is optimized when w'' and w' are equal. When w'' is less than w', the exit aperture blocks light from reaching the grating. Contrariwise, when w'' is greater than w', the exit slit is too wide and the resolution is not optimized. The instrumental bandpass of the spectrometer can then be defined as:

$$\Delta\lambda = \frac{\max(w'', w')}{L} = \frac{d\,w\cos\alpha}{m\,r} \qquad [\text{m}] \quad (2.48)$$

where L is the linear dispersion from equation 2.45, however, equation 2.47 was used to express L in terms of $\cos\alpha$ and r instead of $\cos\beta$ and r'. $\max(w'', w')$ refers to the maximum between w'' and w'.

The bandpass defined in equation 2.48 can be used to model the resolving power limited by the exit and entrance slit widths:

$$\begin{aligned} R &= \frac{\lambda}{B} = \frac{\lambda\,L}{\max(w'', w')} \\ &= \frac{\lambda\,m\,r'}{d\cos\beta\ \max(w'', w')} \end{aligned} \qquad [1] \quad (2.49)$$

This definition will be used to model the theoretical resolving power of the diffraction grating. For the grating designed in this thesis, the exit slit width was chosen to match the image of the entrance slit width at the center of the band. Therefore, the resolving power

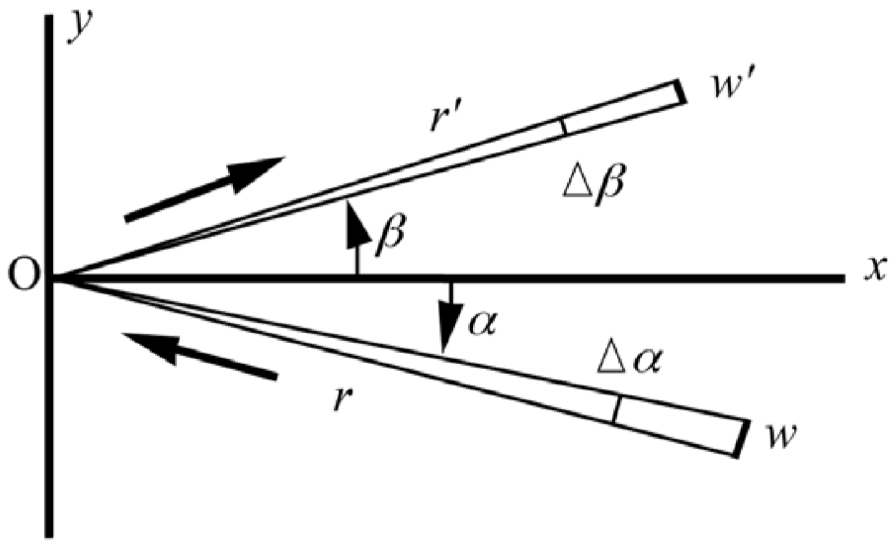

Figure 2.9: Diagram showing tangential magnification from a source that is diffracted by a slit of width, w. The magnification can lead to a reduction in the width of the image as shown in the picture but it can also lead to an enlargement in certain cases. Taken from [55].

will be split up into two cases:

$$R = \begin{cases} \frac{\lambda m r}{d w \cos\alpha} & \text{for } w' < w'' \\ \frac{\lambda m r'}{d \cos\beta w'} & \text{for } w' > w'' \end{cases} \quad [1] \quad (2.50)$$

2.5 Grating Efficiency

When observing faint sources, such as in infrared astronomy, it is important that as much light as possible is diffracted into the order of interest. The shape and orientation of the grooves of a grating have a significant impact on its efficiency. Most of the energy in a diffraction pattern is concentrated in the zeroth order of interference. This is the case when the incident angle is equal to the diffracted angle and the light follows the laws of reflection; no diffraction occurs. This order is not useful for spectroscopy because there is no dispersion of wavelengths so it is advantageous to shift light from the zeroth order and concentrate it into the order of interest. The grooves can be shaped to maximize the

efficiency of a reflection grating through a process known as blazing. The blaze angle of the grooves can be determined by solving the blaze condition:

$$m\lambda = 2dsin\theta_B, \qquad \text{[m]} \quad (2.51)$$

where θ_B is the blaze angle measured between the grating plane and the face of the groove which is labeled in figure 2.7. The grating grooves are machined into a sawtooth profile with the identified blaze angle. The grating in this thesis was designed with a blaze angle to achieve a maximum efficiency at the band center.

Recall the intensity distribution for light passing through a single slit:

$$I(p) = \frac{ED}{\lambda^2 R^2}\left(\frac{\sin(kpa)}{kpa}\right)^2\left(\frac{\sin(kpb)}{kpb}\right)^2. \qquad [\mathrm{W\,m^{-2}}] \quad (2.52)$$

The intensity is proportional to the area of the slit, D, because a larger slit allows more light to pass through. It was shown above that the slit-limited resolving power is inversely proportional to the width of the slits. Thus, increased resolving power comes at the cost of a decrease in efficiency. In my design, the target resolving power was $R \sim 100$ at the center of the band and the slit widths were chosen to maximize the throughput while achieving this target. The next sections derive a physically accurate intensity distribution for a blazed reflection grating to better understand the efficiency trade-offs.

2.5.1 Intensity Distribution for a Blazed Reflection Grating

As was mentioned at the beginning of this section, the method of blazing a grating is commonly employed to concentrate more light into the diffraction order of interest. Therefore, it is useful to have a theoretical model for the diffracted intensity distribution of a blazed reflection grating. This section will use the methods outlined in: On the Intensity Distribution Function of Blazed Reflective Diffraction Gratings by Casini and Nelson [59] who expand on the methods outlined by Gray [60] which are discussed in Appendix B.

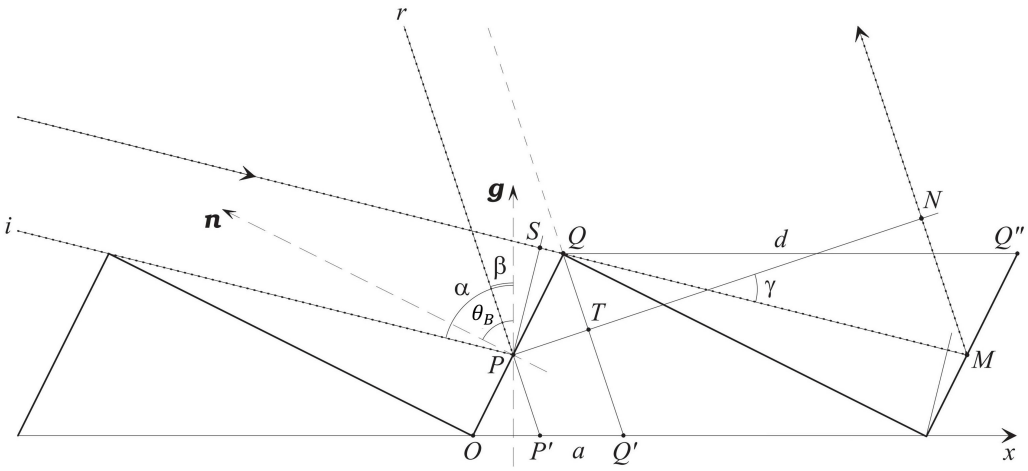

Figure 2.10: Diagram showing the profile of the diffraction grating grooves and the geometry of the incident and diffracted light. Image taken from [59].

Casini and Nelson remark on the difficulty of defining the proper illumination of the slit which is not a simple function of the slit width and slit spacing as in the case for the transmission grating. Consider a grating blazed at an angle θ_B with light incident at an angle α and diffracted at an angle β as shown in figure 2.10. The illumination of the triangular slit is given by the distance $a = \mathrm{P'Q'}$ which is found by using the Law of Sines:

$$\begin{aligned} \frac{\mathrm{PQ}}{\sin(90-\beta)} &= \frac{\mathrm{P'Q'}}{\sin(90-\theta_B+\beta)} \\ \mathrm{P'Q'} &= \frac{\mathrm{PQ}\sin(90-\beta)}{\sin(90-\theta_B+\beta)} \\ a &= \mathrm{PQ}\frac{\cos(\beta)}{\cos(\beta-\theta_B)} \end{aligned} \qquad [\mathrm{m}] \quad (2.53)$$

The distance PQ is found in a similar way:

$$\begin{aligned} \frac{\mathrm{PQ}}{\sin(90-\alpha)} &= \frac{d}{\sin(90-\theta_B+\alpha)} \\ \mathrm{PQ} &= \frac{\cos(\alpha)}{\cos(\alpha-\theta_B)} \end{aligned} \qquad [\mathrm{m}] \quad (2.54)$$

The path differences between the incident and diffracted rays are shown in figure 2.10

as $\mathrm{SQ}-\mathrm{TQ}$ which are defined by:

$$\begin{aligned}\mathrm{SQ}-\mathrm{TQ} &= \mathrm{PQ}\sin(\alpha-\theta_B)-\mathrm{PQ}\sin(\theta_B-\beta)\\ &= d\frac{\cos(\alpha)}{\cos(\alpha-\theta_B)}\left[\sin(\alpha-\theta_B)-\sin(\theta_B-\beta)\right]\end{aligned} \qquad [\mathrm{m}] \quad (2.55)$$

Thus, the overall phase difference for light with wavelength λ incident between points T and P is:

$$\phi(\theta_B) = \frac{2\pi d}{\lambda}\frac{\cos(\alpha)}{\cos(\alpha-\theta_B)}\left[\sin(\alpha-\theta_B)-\sin(\theta_B-\beta)\right] \qquad [\mathrm{rad}] \quad (2.56)$$

The phase difference vanishes when $\alpha-\theta_B=\theta_B-\beta$, or: $\alpha+\beta=2\theta_B$, which is just another way to define the blaze condition of maximum efficiency. This phase difference describes the dephasing of a ray being diffracted from the origin of a single slit. Each additional slit adds a phase retardance equal to:

$$\Theta = \frac{2\pi}{\lambda}(\mathrm{SQ}+\mathrm{QM}+\mathrm{MN}) \qquad [\mathrm{rad}] \quad (2.57)$$

Again, using the Law of Sines to determine the distance QM, the result is:

$$\begin{aligned}\frac{\mathrm{QM}}{\sin(\theta_B)} &= \frac{d}{\sin(90-\theta_B+\alpha)}\\ \mathrm{QM} &= \frac{d\sin(\theta_B)}{\cos(\alpha-\theta_B)}\end{aligned} \qquad [\mathrm{m}] \quad (2.58)$$

From the geometry in figure 2.10 an expression for MN can be found:

$$\mathrm{MN}+\mathrm{TQ} = \mathrm{QM}\cos(\alpha-\beta) \quad (2.59)$$

$$[\mathrm{m}] \quad (2.60)$$

Substituting all of the above relationships into equation 2.57 the expression becomes:

$$\begin{aligned}\Theta &= \frac{2\pi}{\lambda}\left[(\mathrm{SQ}-\mathrm{TQ})+\frac{d\sin(\theta_B)}{\cos(\alpha-\theta_B)}+\mathrm{QM}\cos(\alpha-\beta)\right] \\ &= \frac{2\pi}{\lambda}\left[d\frac{\cos(\alpha)}{\cos(\alpha-\theta_B)}\left[\sin(\alpha-\theta_B)-\sin(\theta_B-\beta)\right]+\frac{d\sin(\theta_B)}{\cos(\alpha-\theta_B)}\left[1+\cos(\alpha-\beta)\right]\right] \\ &= \frac{2\pi d}{\lambda\cos(\alpha-\beta)}\left[\cos\alpha\sin\alpha\cos\theta_B+\sin^2\alpha\sin\theta_B+\cos\alpha\sin\beta\cos\theta_B+\sin\alpha\sin\beta\sin\theta_B\right] \\ &= \frac{2\pi d}{\lambda\cos(\alpha-\beta)}\left[\cos(\alpha-\beta)(\sin\alpha+\sin\beta)\right] \\ &= \frac{2\pi d}{\lambda}(\sin\alpha+\sin\beta)\end{aligned}$$

[rad] (2.61)

The final result is the grating equation which was derived earlier in equation 2.39.

Now that the geometrical approach has been shown to return the expected result in terms of the phase retardance predicted by the grating equation, the theory can be extended to determine the efficiency of the grating. Appendix B discusses the derivation of the transmission function for a simple line grating, which is given in equation B.5. A similar derivation can be used to determine the "transmission" function for a blazed reflection grating where the diffracted light is reflected rather than transmitted. Additionally, the geometry is complicated so it is important to define the actual illumination of each slit accounting for shadowing of the grooves. For the blazed diffraction grating the transmission function, $G(\xi)$, is given by [59]:

$$G(\xi) = a(\xi) * III_d(\xi) B_L(\xi), \qquad [1] \quad (2.62)$$

where $a(\xi)$ is the window function associated with the illumination of each groove having a width a as defined in equation 2.53. $III_d(\xi)$ is the periodic sampling function associated with the groove spacing, d, and $B_L(\xi)$ is the unit box function defining the total length of the grating, L.

For a blazed grating, the function $a(\xi)$ will be complex because of the dephasing intro-

duced by the slope of the grooves. This overall dephasing term is given by [59]:

$$\Delta\theta(\xi) \equiv \left[\frac{\phi(\theta_B)}{a} - \frac{\Theta}{d}\right](\xi - \overline{\xi}), \qquad \text{[rad]} \quad (2.63)$$

where $\phi(\theta_B)$ is the phase difference across the diffracted wave, defined in equation 2.56, and Θ is the phase retardance due to each slit as give in equation 2.61. Taking this phase shift into account, the window function becomes: $a(\xi) = B_a(\xi)e^{i\Delta\theta(\xi)}$, where $B_a(\xi)$ is the unit box function of width a and the phase term appears in the exponential.

The next step is to take the Fourier transform of the transmission function which yields the spectral response of the grating:

$$\mathcal{F}\left(e^{i\Delta\theta(\xi)}B_a * III_d B_L\right) = \mathcal{F}\left(e^{i\Delta\theta(\xi)}B_a\right) \times \left[\mathcal{F}\left(III_d\right) * \mathcal{F}\left(B_L\right)\right] \quad [1] \quad (2.64)$$

The symbol, $*$, denotes the convolution operator which quantifies the overlap between two functions. Casini *et al.* derives the Fourier transform in equation 2.64 and note that the intensity distribution function is proportional to $|\mathcal{F}(G(\xi))|^2$ [59] . The intensity envelope of the diffracted wavefront is determined by the transform of the first term squared which is found to be [59]:

$$\begin{aligned} I(\beta) &\propto |\mathcal{F}\left(e^{i\Delta\theta(\xi)}B_a\right)|^2 \\ &= \mathrm{sinc}^2\left(\frac{\phi(\theta_B)}{2}\right) \end{aligned} \qquad [1] \quad (2.65)$$

Substituting equation 2.56 for $\phi(\theta_B)$:

$$I(\beta) = \mathrm{sinc}^2\left(\frac{\pi d\cos(\alpha)}{\lambda\cos(\alpha-\theta_B)}\left[\sin(\alpha-\theta_B) - \sin(\theta_B-\beta)\right]\right) \qquad [1] \quad (2.66)$$

This intensity corresponds to constructive interference only when the grating equation, $\Theta = \frac{2\pi d}{\lambda}(\sin\alpha + \sin\beta) = 2\pi m$, where m is the integer representing the order of diffraction.

Substituting this relationship into the above equation yields:

$$\begin{aligned} I(\beta) &= \mathrm{sinc}^2\left(\frac{m\pi}{\sin\alpha+\sin\beta}\frac{\cos\alpha}{\cos(\alpha-\theta_B)}\left[\sin(\alpha-\theta_B)-\sin(\theta_B-\beta)\right]\right) \\ &= \mathrm{sinc}^2\left(\frac{m\pi\cos\alpha}{\cos(\alpha-\theta_B)}\left[\cos\theta_B-\sin\theta_B\cot\frac{\alpha+\beta}{2}\right]\right) \end{aligned} \quad [1] \quad (2.67)$$

The final expression is the normalized intensity distribution function of the diffracted wavefront. This expression returns a normalized function which depends on the incident and diffracted angle of the light.

The intensity distribution function in equation 2.67 is a scalar approach to modelling the efficiency response of a diffraction grating. However, this model does not consider the effects of polarization which is a vectorial property of the electromagnetic field. In general, the diffraction efficiency of a blazed grating will depend strongly on the polarization state of the incident light [55]. When the incident light is linearly polarized parallel to the grooves on the grating (p-polarized), the diffracted power is expected to be lower than when the light is polarized perpendicular (s-polarized) to the grooves [55]. When coupled to a polarizing FTS, it is thus favourable to orient the output to be s-polarized to exploit the polarization sensitivity of the grating. To better understand the relationship between polarization and diffraction efficiency, it was necessary to construct a theoretical model. In 2020, Germer developed an interface written in Python3 [61] called pySCATMECH which utilizes a C++ class library called SCATMECH [62]. pySCATMECH can be applied to model the interaction of light with a blazed diffraction grating using rigorous coupled wave, RCW, analysis. The program computes the diffraction efficiency of a blazed grating for p-polarized and s-polarized light separately.

Figure 2.11 shows the polarization sensitive efficiency models compared with the scalar model from equation 2.67 which was normalized to equal the maximum of the s-polarized curve. All three models use the groove spacing (312 μm), blaze angle (39.4°), and wavelength range (285 - 500 μm) of the grating designed for this study, which is described in

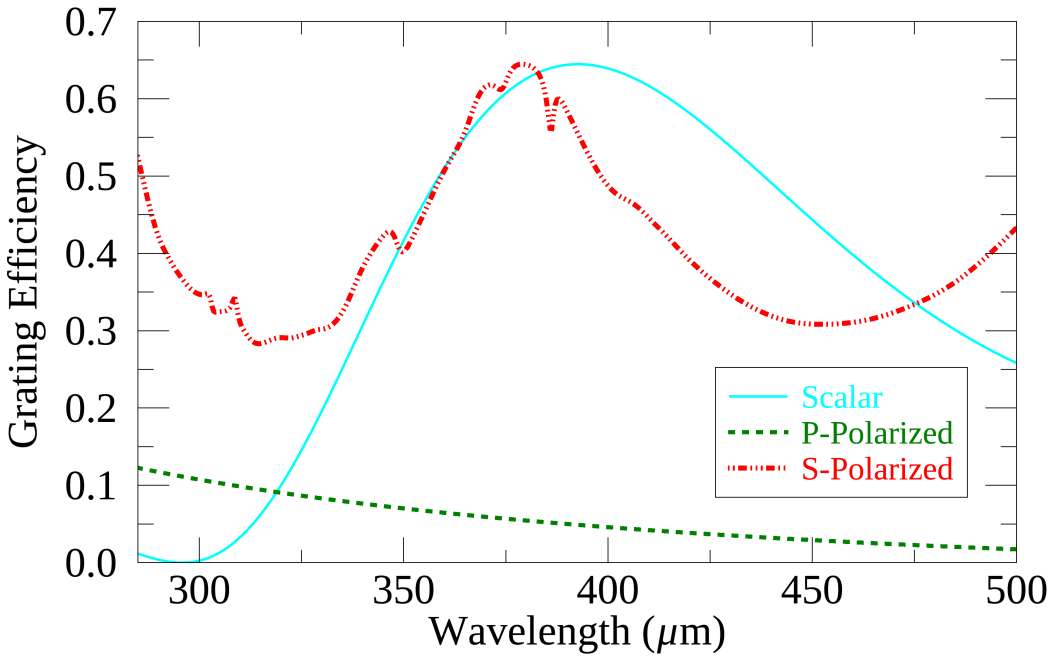

Figure 2.11: Diffraction efficiency for the blazed grating described in this chapter. The scalar curve (blue) was computed using equation 2.67. The p-polarized curve corresponds to light which is linearly polarized parallel to the grating grooves and the s-polarized is linearly polarized perpendicular to the grooves. Both polarization-dependent efficiency curves were computed using pySCATMECH [62].

detail in Chapter 3. The pySCATMECH models also required the optical properties of the grating substrate which was fabricated from aluminum 6061. The optical properties of aluminum at far-infrared wavelengths were taken from [63] who modeled the skin depth of aluminum to be around 100 nm at 500 μm. While equation 2.67 for the scalar intensity distribution does not depend directly on the wavelength, λ, the angles of incidence α and diffraction β are determined from equation 2.39 which does depend on λ. The curves show that there is a much higher efficiency expected for S-polarized light and these models will be compared with experimental results in Chapter 5.

The next chapter uses the theoretical background presented in this chapter to establish the design specifications of the diffraction grating. Additionally, the design of a monolithic module is presented which mounts the grating and its coupling optics within the cryostat. I

will discuss the relevant considerations taken to successfully operate the spectrometer at 4 K. The next chapter will also discuss the optical design of the grating spectrometer.

Chapter 3

Grating Spectrometer Design

> As far as the laws of mathematics refer to reality, they are not certain, and as far as they are certain, they do not refer to reality.
>
> ALBERT EINSTEIN

This chapter will discuss the development of a diffraction grating spectrometer operating at cryogenic temperatures, $\sim$4 K. The discussion will begin with the design of a blazed reflection grating and follow with the design and implementation of a monolithic aluminum enclosure to house the optical components within the cryostat. Cryogenic considerations of the design will be discussed as well as the overall optical setup which required a coupling between room temperature sources and a polarizing Fourier transform spectrometer provided by Blue Sky Spectroscopy Inc. [73] to the cryogenic grating and the bolometer detector [72].

3.1 Diffraction Grating Design

The first component designed and manufactured was the aluminum blazed reflecting diffraction grating. The constraints of this design were to operate over a far-infrared wavelength range which matched the existing test equipment, e.g. detector, sources, high-resolution spectrometer, and was chosen to be from 285 - 500 μm. The next constraint was to achieve a resolving power of $\approx$ 100 at the center of the band (392.5 μm).

The grating equations in the previous section were used to design the diffraction grating proposed for the post-dispersed polarizing Fourier transform spectrometer (PDPFTS).

The grating height, D, was pre-determined to match the beam diameter from the camera mirror which is 50 mm wide. The entrance and exit focal lengths were constrained by the available space within the working volume of the cryostat. The deviation angle was chosen to incorporate a vertical offset from the grating to the detector. The optics were based on a previous system designed by Veenendaal who used a cryogenic diffraction grating spectrometer to order sort the output from a Fabry-Pérot interferometer [64]. The specifications of the grating design that met the above requirements are presented in table 3.1.

The diffraction order, m, was chosen using equation 2.43 where the range of the grating is 285 - 500 µm. This corresponds to a spectral range, $\Delta\lambda_{FSR} = 215$ µm, and $\lambda_L = 285$ µm. The grating must operate in an order less than or equal to the FSR ratio between $\Delta\lambda_{FSR}$ and λ_L to avoid overlapping of spectral orders. Ultimately, it was found that: $m \leq 1.33$, and since m is an integer it was constrained to be 1. The length of the grating is 105 mm so that it can rotate 360° in the enclosure. A trade-off existed between the groove spacing, d, and the width of the entrance slit, w, because from equation 2.50, the resolving power is inversely proportional to both quantities. However, w also restricts the throughput of the system so it could not be too small such that a large fraction of the radiation was lost. Additionally, the groove spacing could not be too small that it resulted in manufacturing difficulties. With these considerations in mind, d, was manufactured to be 312 µm while the width of the entrance slit, w, was chosen to be 5.0 mm. The exit slit width, w'', was chosen to match the image of the entrance slit width, w' at 392.5 µm using equation 2.47 to calculate the image width. The equation returned an image width of 4.02 mm, and due to availability of milling cutters, the as-built exit slit has a width of 4.0 mm.

The theoretical slit-width limited resolving power for this grating was predicted to vary between 69–180 over the wavelength range of 285–500 µm using equation 2.50 as shown in figure 3.1. The full-width half-maximum (FWHM) of the grating profiles is also shown on the figure and was calculated using equation 2.48. The bandpass depends on the maximum width between the image of the entrance slit and the exit slit. The image of the entrance slit

Table 3.1: Specifications of the grating spectrometer designed to operate over 285 - 500 μm.

Parameter	Value
Grating width, W	105 mm
Grating height/Beam diameter, D	50 mm
Order of diffraction, m	1
Slit spacing, d	312 μm
Deviation angle, 2 ϕ	15°
Entrance focal length, r	310 mm
Exit focal length, r′	310 mm
Entrance slit width, w	5.0 mm
Exit slit width, w″	4.0 mm
Blaze angle, θ_B	39.4°

width is greater than the exit slit width until the center of the band (where they were chosen to be equal) after which the exit slit is the dominating width. Consequently, this is seen as a kink in figure 3.1. The experimental data that will be presented in Chapters 4 and 5 will be compared to this theoretical model to assess the performance of the grating.

3.2 Cryogenic Considerations

When designing an instrument to operate at cryogenic temperatures it is important to have an understanding of how it will cool from room temperature to < 4 K. Conductive heat transfer describes the rate in which heat flows from a warm, solid object to a cold object by direct molecular contact [65]. For solid materials, heat energy is transferred via electrons and lattice vibrations. The transfer via electrons dominates for highly conductive solid materials because the same conduction electrons that carry electric current also are responsible for transferred energy. Therefore, metals which are good electrical conductors tend to have higher thermal conductance as well. The rate of conductive heat flow through a solid material can be described by the Fourier heat conduction law [65]:

$$\dot{q} = -k(T)A\frac{\mathrm{d}T}{\mathrm{d}x}, \qquad \text{[W]} \quad (3.1)$$

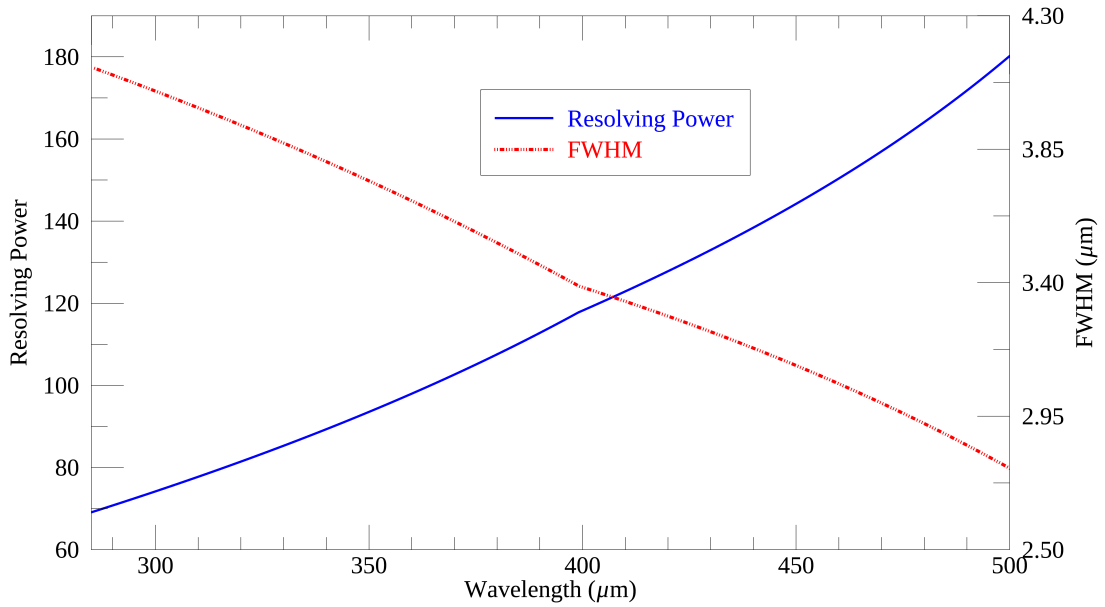

Figure 3.1: The theoretical resolving power (blue; left axis) calculated from equation 2.50 with the slit widths given in table 3.1. The full-width half-maximum (red dashed line; right axis) of the grating profile at each wavelength is superposed. The kink in the middle of the graph corresponds to the point where the grating becomes limited by the width of the exit slit rather than the image of the entrance slit.

where $k(T)$ is the temperature dependent thermal conductivity of the material, A is the cross-sectional contact area, dx describes the thickness of the interface, and dT is the temperature difference between the two objects. The thermal conductivity is a complicated function that depends strongly on the material composition and its purity. In terms of commonly used metals, high-purity, oxygen-free copper has one of the highest thermal conductivities, followed by alloys of aluminum and brass, and stainless steel, respectively. Another important quantity to define is the heat capacity, $C(T)$, of an object which is the amount of heat energy, Q, required to raise the temperature of the object per unit temperature [65]. The specific heat capacity, $c(T)$, expresses the heat capacity per unit mass and, in general, is a temperature dependent quantity. the amount of heat required to change the temperature of an object is thus given by:

$$Q = mc(T)\mathrm{d}T, \qquad [\mathrm{J}] \quad (3.2)$$

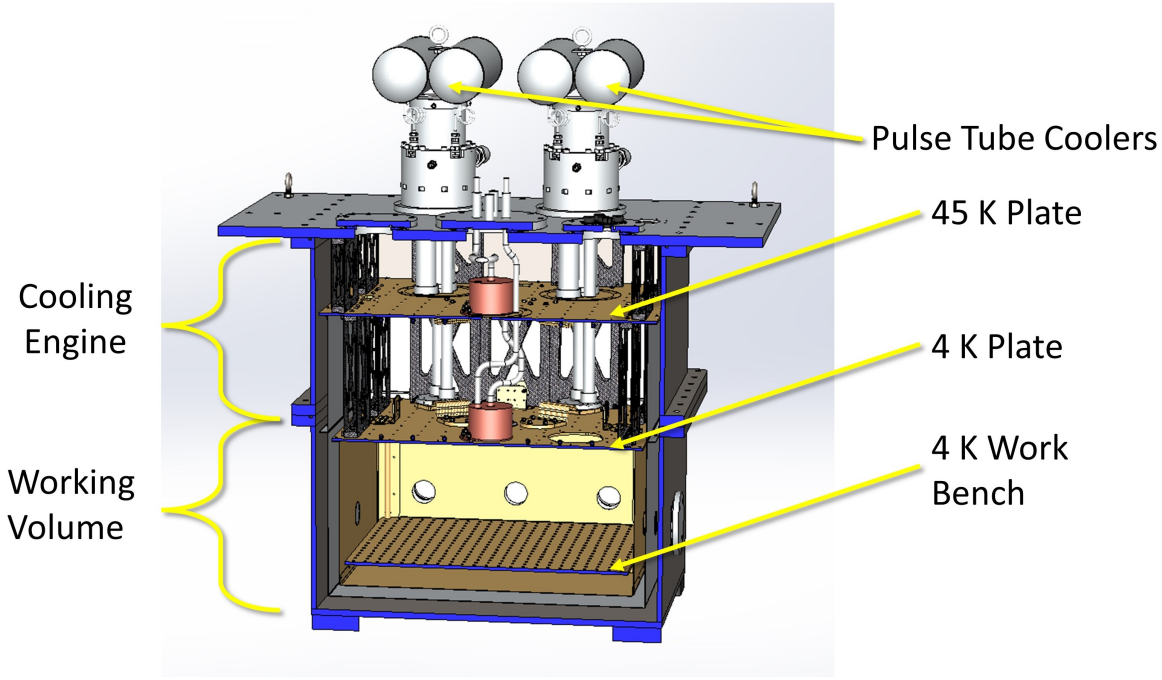

Figure 3.2: CAD rendering of the test facility cryostat (TFC) utilized in this thesis. Image taken from [66].

where m is the mass of the object in kg.

The test facility cryostat (TFC) used in this thesis is shown in figure 3.2 and was designed by Veenendaal in his MSc thesis [66]. Two Cryomech PT415 pulse tube coolers provide a cooling power of 1.5 W each at 4.2 K. The cryostat consists of rectangular cuboid chambers enclosed in a stainless steel outer vacuum chamber (OVC). The first inner chamber is covered with 12 layers of insulating sheets to decrease radiative heat transfer from the OVC. Inside this module, is another rectangular chamber which contains the working volume (580 mm $\times$ 480 mm $\times$ 250 mm) of the cryostat. The working volume achieves a temperature around 4 K [66]. The working surface consists of a flat, square plate (4 K plate) which is composed of oxygen-free high-conductivity copper coated with a thin (5 µm) layer of gold to further increase thermal contact conductance through the surface. Instruments are designed to mount onto the 4 K plate using a rectangular grid of M3 helicoil inserts distributed across the surface.

Although the 4 K plate has been manufactured to optimize heat transfer, the thermal

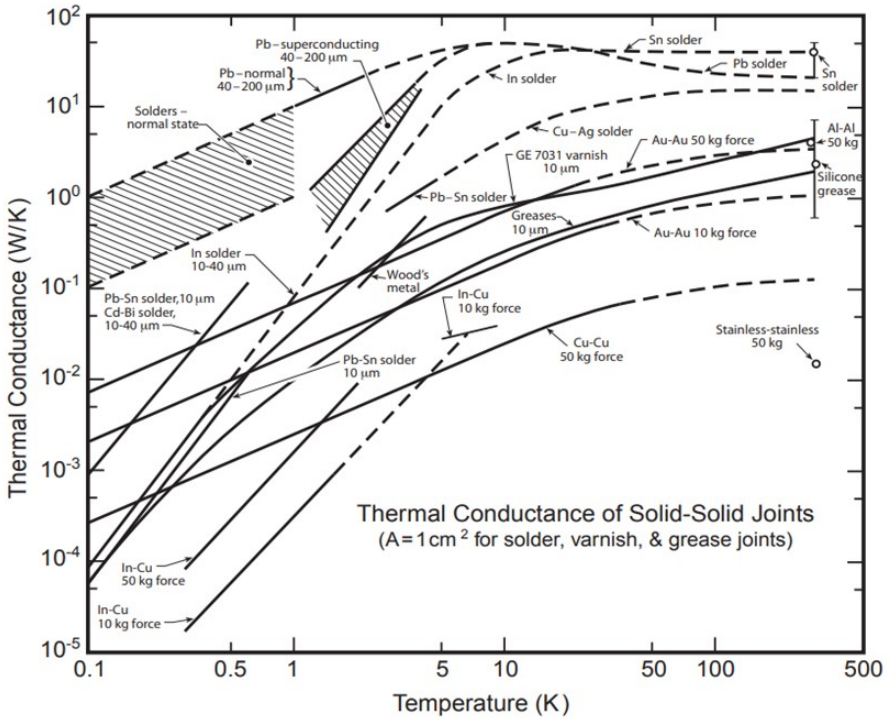

Figure 3.3: Thermal contact conductance as a function of temperature for various materials and joint types. Image taken from [67].

contact conductance depends on how the instrument mounts to the plate. Contact conductance represents the thermal conductivity between a solid-solid interface. This is a complicated function which depends on the composition of the two materials, the method of joining them, the surface properties (cleanliness, roughness, etc.), the temperatures of the two materials, etc. For this reason, theoretical models serve only as a guide to performance experimental results are the main method of characterizing contact conductance. Figure 3.3 shows a collection of thermal conductance measurements for a variety of solid interfaces being attached by solder, varnish and grease, and applied forces. Soldered joints typically produce the highest conductance being followed by varnish and then pressed joints. In terms of mounting an instrument to the 4 K plate, this is done by applying a clamping force to press the instrument into contact with the plate. From figure 3.3, the conductance values that best represent this method of contact are the gold-gold pressed joints with forces of 490 N (50 kg) and 98 N (10 kg) which range from $\sim 0.05\ \mathrm{W\,K^{-1}}$ at 4 K to $\sim 5\ \mathrm{W\,K^{-1}}$ at

room temperature. By comparison, the thermal conductivity of a mass made of aluminum 6061 ranges from 5.4 W K^{-1} at 4 K to 156 W K^{-1} at 300 K.

There has been extensive research to determine an empirical relationship between the force in a pressed joint and the thermal contact conductance as a function of temperature [67–69]. However, with so many variables that influence the contact conductance, it is unlikely for experimental data taken by another group to apply to our system. While numerical estimations carry a high degree of uncertainty, they are nonetheless useful in predicting the thermal performance of a cryogenic system. With bolted joints, it has been found that the conductance is strongly dependent on the tightening torque (clamping force) applied on the bolt and also the number of bolts acting on the joint [68, 69]. Thermal contact conductance is much less dependent on the area of the bolt head because there is only a small area under the bolt which makes a substantial molecular contact to allow the transfer of heat. Stainless steel M3 bolts in helicoil inserts were tested to determine the maximum torque that could be applied before the insert or bolt failed. In these tests, it was determined that the bolts failed at 2.3 N m for insert lengths of 4.5 mm, 6 mm, and 7.5 mm. Based in these values, an operating torque of 1.0 N m was chosen to provide a safety margin. This torque corresponds to a maximum clamping force of 1600 N for a single bolt on the 4 K plate.

There have been a few experiments which are of interest to our application. One of these was a series of tests completed by Schaellig and Seidal [69] where they aimed to determine the contact conductance between a pressed joint of gold-plated copper and aluminum. They completed measurements in a temperature range of 8 - 100 K where they found a relationship between the contact conductance and the temperature and force applied [69]:

$$k(T) = 4.21 \times 10^{-6} T^{1.594} F^{0.893}, \qquad [\mathrm{W\,K^{-1}}] \quad (3.3)$$

where T is the contact temperature and F is the force applied. Schmitt et. al. [70] performed a different experiment measuring the contact conductance between bolted sections of gold plated copper and determined a relationship between conductance and temperature without

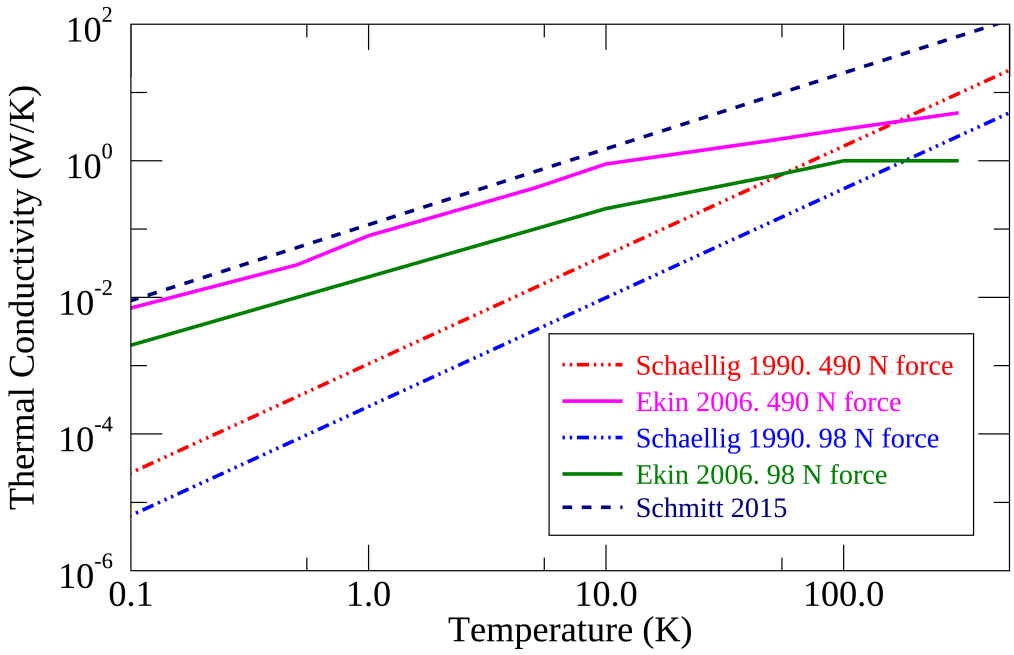

Figure 3.4: Comparison of the thermal contact conductance with varying applied forces. The solid curves are data extrapolated from figure 3.3 for a gold-gold contact [67]. The dashed lines was generated using a formula described in [69] for a gold plated copper - aluminum interface with data collected between 10 K and 100 K. The dashed line is taken from Schmitt [70] for an interface with two sections of gold plated copper bolted together with an unknown force.

knowing the clamping force of the joint [70]:

$$k(T) = 0.1161T^{1.1111}. \qquad [\mathrm{W\,K^{-1}}] \quad (3.4)$$

The empirical relationships in equations 3.3 and 3.4 were compared with data from figure 3.3 from a gold-gold contact with a force of 98 N (10 kg) and 490 N (50 kg). The comparison is shown in figure 3.4 which shows slight agreement between all three sources. However, it should be noted that equation 3.3 was only tested for applied forces between 12 N and 50 N and has been used for forces significantly outside of the known range of validity. It should also be noted that the relationship between thermal conductance and force exists similarly for conductance and contact area. The large area of contact between

two surfaces, the greater the heat flow. This is associated with an increase of force because a larger force helps to increase contact area within a joint and increases the heat transfer rate as per equation 3.1.

With so much uncertainty in the contact conductance values, experimental results are relied on heavily. Figure 3.9, which is presented later in this chapter, shows the temperature curve of the previous grating enclosure (red) and the temperature of the 4 K plate during the same cooldown. As is shown, there is a significant delay ~ 2 hours between the cooldown of the 4 K plate and the grating enclosure. For the new enclosure, the goal was to decrease this lag by a factor of 2. In a crude approximation, assume the grating enclosure starts at a temperature of 50 K and the 4 K plate is at a temperature of 10 K - which are roughly the same values shown in figure 3.9. The heat energy required to remove from the grating to cool it from 50 K to 10 K can be calculated using equation 3.2:

$$\begin{aligned} Q &= mc(T)\mathrm{d}T \\ &= 2.70\mathrm{kg}\int_{10\mathrm{K}}^{50\mathrm{K}} 10^{f(T)}dT \\ &= 7948 \end{aligned} \qquad \text{[J]} \quad (3.5)$$

where $f(T) = a - b\log_{10}(T) + c\log_{10}(T)^2 + d\log_{10}(T)^3 + e\log_{10}(T)^4 + f\log_{10}(T)^5$ $+g\log_{10}(T)^6 + h\log_{10}(T)^7 + i\log_{10}(T)^8$ and the coefficients have been experimentally determined in the NIST Research Library [71]. Therefore, in order to reduce the cooldown time from 2 hours to 1 hour, the heat transfer rate needs to be $\dot{q} = 7948$ J $/3600$ s $= 2.2$ W. From equation 3.1, the rate of heat flow can be determined by solving an integral from $T = 10$ K to $T = 50$ K:

$$\dot{q} = -\frac{A}{d}\int_{10\mathrm{K}}^{50\mathrm{K}} k(T)\mathrm{d}T. \qquad \text{[W]} \quad (3.6)$$

The integral can be numerically computed and will return a different result depending on the model used. Equation 3.6 also depends on the thickness, d, of the interface, which is

not straightforward when considering an instrument with a complicated geometry. For this simple approximation, a thickness of 8 mm was assumed which represents the thickness of the base of the grating module. Aluminum has a high thermal conductivity, it is assumed that the heat transfer within the monolithic enclosure is nearly instantaneous and will be ignored. The integral in equation 3.6 was evaluated for the different contact conductance models shown in figure 3.3 and returned values ranging between 2.44 W m^{-1} for the smallest thermal conductance and $\approx$ 204 W m^{-1} for the largest. Equation 3.6 was rearranged to solve for the contact area required to obtain a heat flow rate of $\dot{q} = 2.2$ W :

$$\begin{aligned} A &= \frac{0.008 \times 2.2}{\int_{10\,\mathrm{K}}^{50\,\mathrm{K}} f(T)\mathrm{d}T} \\ &= 86.3 \times 10^{-5}\mathrm{to}7.23 \times 10^{-3} \end{aligned} \qquad [\mathrm{m}^2] \quad (3.7)$$

Thus, it was determined that the contact area required is estimated to be between 86.3 mm^2 and 7230 mm^2. This range gave a broad baseline target and helped to drive the design of the monolithic enclosure.

3.3 Grating Enclosure Design

The design of the grating spectrometer extends the work of Veenendaal et al. [64] who developed a cryogenic post-dispersed grating to order sort the output from a Fabry-Pérot interferometer. In the new design, the grating is mounted in a monolithic aluminum housing on a pivot driven by a cryogenic stepper motor through worm gear reduction. The incident collimated beam is reflected by a fold mirror onto the grating which disperses the radiation onto a 15° off-axis parabolic mirror, which brings diffracted light to a focus on the exit slit of the spectrometer located on the feedhorn of a 0.3 K composite bolometer detector [72]. A schematic of the monolithic enclosure that houses the grating is shown in figure 3.5. Improvements from the previous design include: a monolithic grating enclosure (teal); a larger diameter filter (50 mm) (brown); a new diffraction grating (yellow) that features a

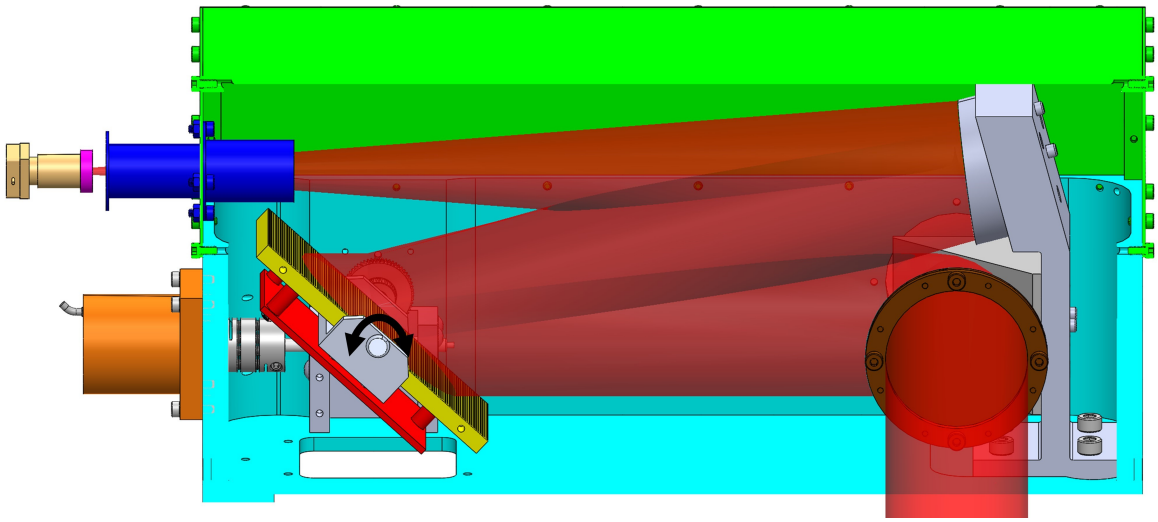

Figure 3.5: Cut-away view of the prototype grating spectrometer CAD model. See text for details.

plane mirror mounted to the rear side (red) free to rotate 360°; and a retractable baffle (blue) that blocks stray light within the grating enclosure from reaching the detector. The new 50 mm windows have customized low-pass optical filters with a cut-off frequency of 58 cm^{-1}. A thermal filter is mounted at the interface between the 4 K and 0.3 K enclosures. The exit slit (pink) is mounted on the feedhorn of a 0.3 K composite bolometer detector (gold). The cryogenic stepper motor (orange) drives the worm and gear system and rotates the grating around the axis indicated by the black arrow. The grating assembly is clamped to the 4 K baseplate of a test-facility cryostat [64].

3.3.1 Grating Rotation

The SPICA far-infrared instrument concept consisted of four diffraction gratings which distribute the signal from a Martin Puplett FTS across different spectral bands of interest. Each grating module was to disperse light onto a 3×294-element array of transition edge sensors [74]. Since I did not have access to a detector array, by necessity my design required that the grating be able to rotate to change the angle of incidence (diffraction) to measure wavelengths across the band using a single detector.

Moving components at cryogenic temperatures are typically avoided because of the

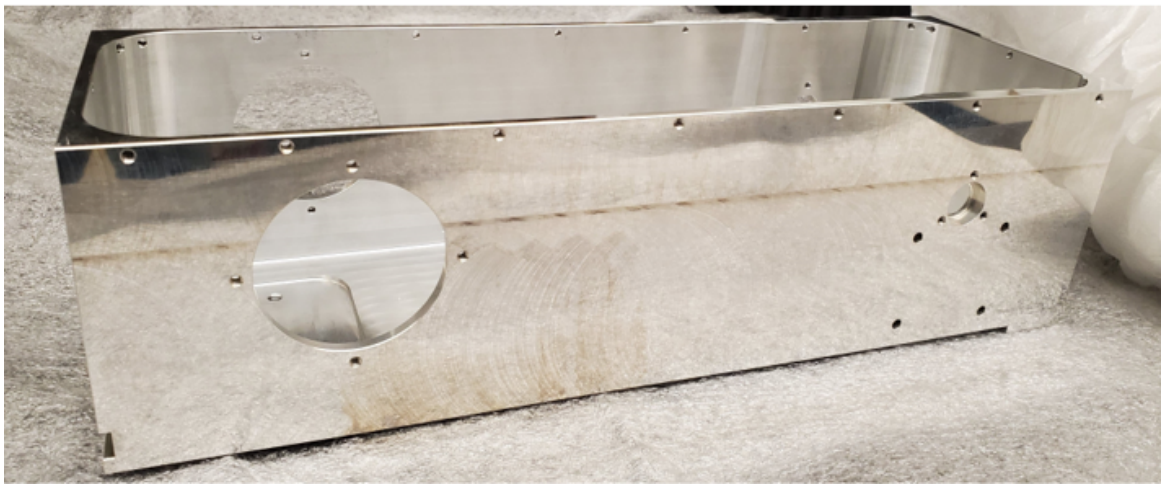

Figure 3.6: Monolithic grating module provided by Blue Sky Spectroscopy Inc. [73]. The enclosure was manufactured by ASDAC C.N.C. Machining LTD.

risks associated with mechanical stress induced by thermal contraction and expansion during cooling and heating cycles, and unwanted thermal dissipation. However, there exist reliable technologies that have been specifically developed for cryogenic applications. The rotation mechanism of the grating is described in [64] and utilizes a Phytron VSS 32.200.1.2 stepper motor [75] to drive a 60:1 worm and gear train. The motor is able to provide a stepping resolution of 0.03° with an additional microstepping mode that produces step sizes of 0.001875° (1/16 of the full step mode). Most of the results presented in the following chapter are collected in 0.06° increments and produced sufficient data points across the wavelength range of the grating.

3.3.2 Cryogenic Considerations

The monolithic grating enclosure was provided by our industrial partner Blue Sky Spectroscopy Inc. Figure 3.6 shows an image of the module when it was first received. The outside of the enclosure is highly reflective to reduce absorption and minimize thermal loading. The inside surfaces were subsequently coated with epoxy and sprinkled with carborundum particles to decrease reflectivity and increase absorptivity of the inner surfaces which serves to reduce stray light from reaching the detector. We adopted the method which was devel-

oped to coat optical components on the Herschel Space Observatory [85]. Care was taken to ensure carborundum particles did not fall into unwanted areas. For example, the square pad where the mirror bracket mounts needs to be flat to ensure sufficient thermal contact and also alignment of the optical axis. This area was taped over as shown in figure 3.7 (top) as were all of the tapped holes within the module. The final product is shown in figure 3.7 (bottom). Another important consideration for the epoxy application was the window into which the incident light enters the module. Epoxy was also applied close to the edge of the entrance window to reduce light being scattered by the aperture. This is the most vulnerable area for introducing stray light.

The monolithic design and choice of material of the enclosure helped to maintain alignment (e.g., gear drive and optics) as the system is cooled to cryogenic temperatures. The retractable baffle (blue) and shield (green) in figure 3.5 are necessary to prevent stray light inside the cryostat from reaching the detector. The baffle mounts to the rear of the shield and radiation travels from the 15 $^\circ$ OAP, through the baffle, and into the detector. As was discussed in section 3.2, required contact area to achieve a heat flow rate of 2.2 W was estimated to be between 86.3 mm^2 and 7230 mm^2, depending on the model used for thermal conductance. The bottom of the monolithic enclosure was designed with three extruded square pads to serve as a three-point contact. Each pad has a surface area of 625 mm^2 for a total of 1875 mm^2 from all three. Slots were designed into the sides of the enclosure for clamps to hook onto and apply a clamping force to increase the contact area of the pads with the 4 K plate. There was a concern that this contact area would not be sufficient to cool the grating enclosure optimally so a copper bracket was designed and mounted onto the outside of the enclosure. The design aimed to optimize the conductance between the bracket by incorporating as many bolts within the space available. 4 M3 bolts are used to attach the bracket to the module and then 2 M3 bolts attach the bracket to the 4 K plate. Figures 3.16 and 3.8 show images of the entire module mounted on the 4 K plate of the TFC.

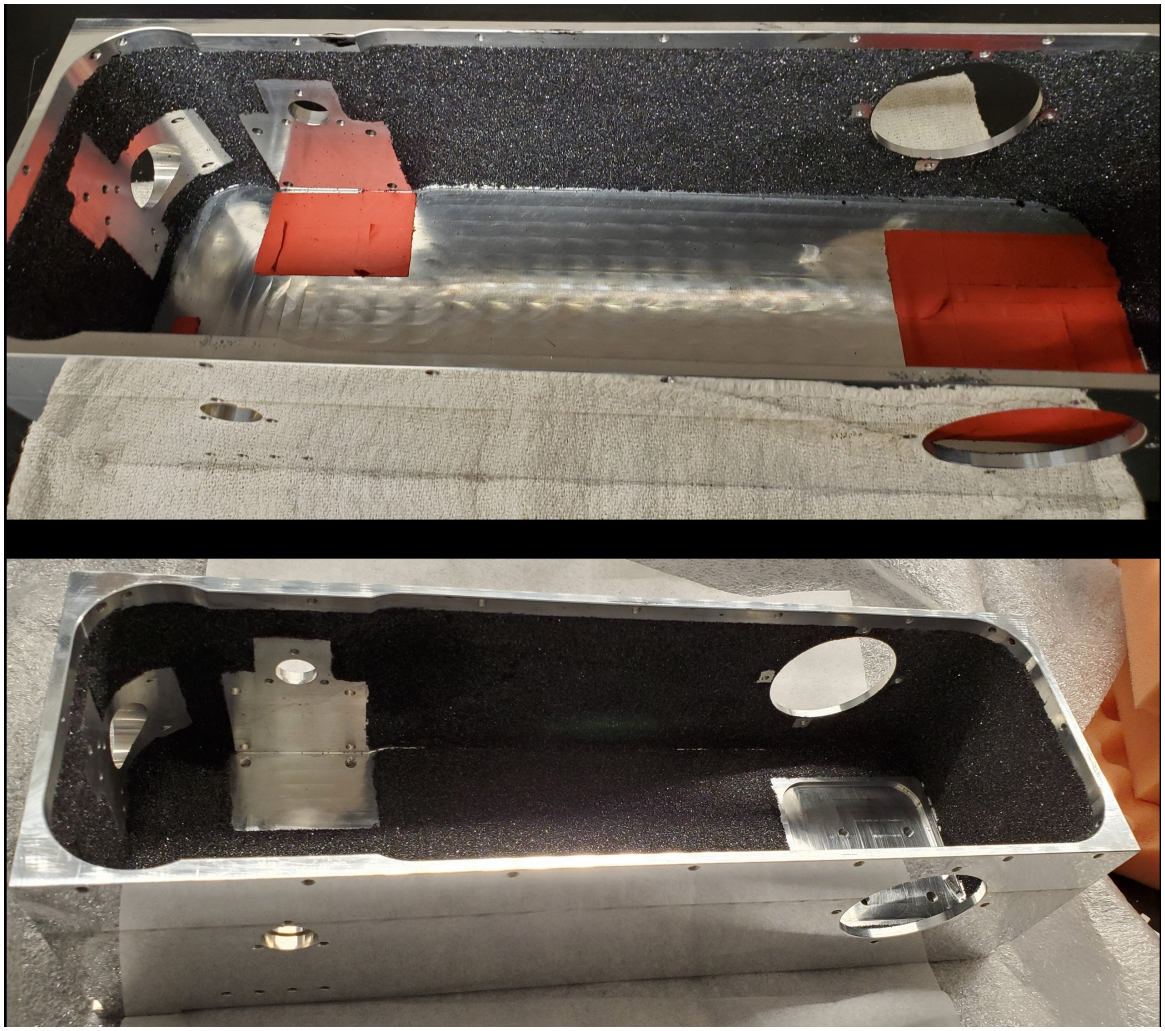

Figure 3.7: Image of the grating enclosure taken during the epoxy-carborundum paste application to the lower surface depicting the tape that was used to ensure the epoxy was applied only to certain areas (top). Overview of the grating enclosure after the coating application was complete (bottom).

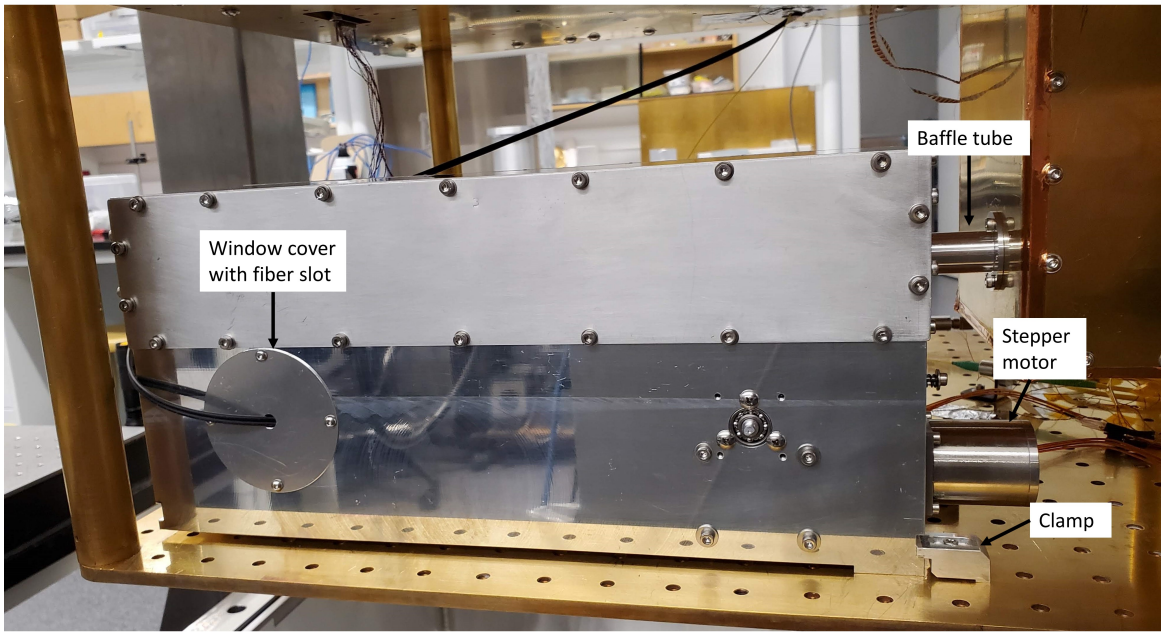

Figure 3.8: Image of the grating module showing the window cover with a slot for the optical fiber encoder, the cryogenic Phytron stepper motor, the baffle tube extending from the grating shields to the detector, and the clamps increasing the contact area between the enclosure and the 4 K plate.

Figure 3.9 shows a comparison between temperature curves measured with the previous grating module (red) and the new monolithic module (green). The temperature delay between the monolithic grating module and the 4 K plate of the TFC is almost negligible indicating there is a strong thermal contanct conductance between the two systems. The design worked much better than expected and has proven that the monolithic grating enclosure will cool to 4 K much faster than the previous design.

Once the module was assembled, it was mounted in the cryostat as shown in figure 3.8. A chopped signal from a blackbody source was fed into the grating without a slit and the grating was rotated 360° to determine if there would be any issues with stray light. The first scan measured with the grating is shown in figure 3.10 (blue). There were some signal peaks identified as reflections from the top of the grating, bottom of the grating, negative and positive first order spectra, zeroth order (grating as a mirror), end of the grating saddle, and the back of the grating. It is critical that the stray light is mitigated when the grating is

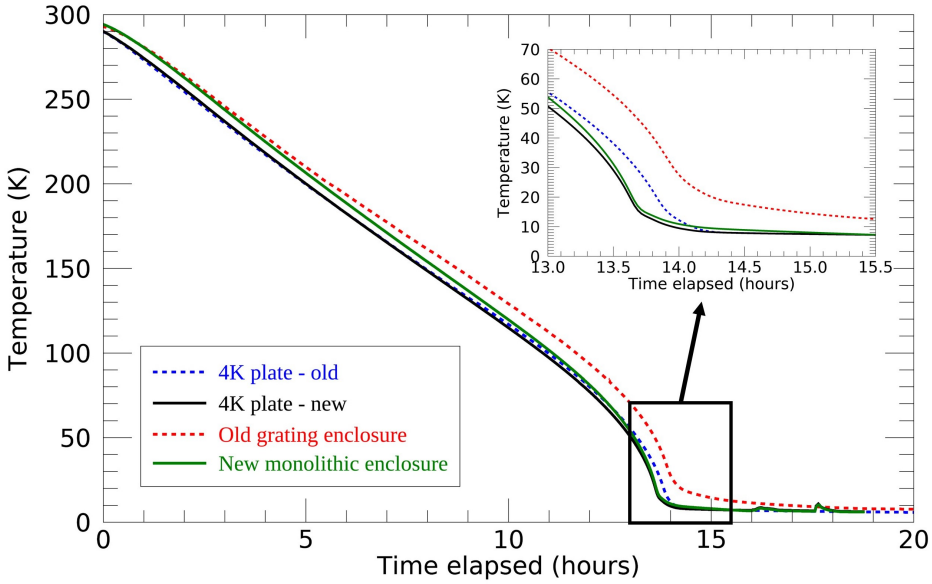

Figure 3.9: Temperature cooldown curves for the previous grating enclosure (red) and the 4 K plate (blue) compared with temperature curves of the new monolithic enclosure (green) and 4 K plate (black) during a recent cooldown.

operating in its useful range ($m = +1$). The zeroth order might reflect stray light within the module that could make its way to the detector, however, this is not something that can be eliminated. The other possible sources of stray light were the bottom and top of the grating and the edges of the saddle. To reduce the reflection off of the top and bottom, aluminum brackets were made and coated with the same epoxy-carborundum mixture as was used in coating the inside of the monolithic enclosure. Another bracket was constructed for the edges of the saddle and attached using varnish. The carborundum coated brackets are shown in figure 3.11. With the brackets added to the grating, the scan was repeated and the result is shown in figure 3.10 (red). Clearly the epoxy-carborundum is effective in reducing reflectivity in the far-infrared and these caps will be useful in mitigating contributions of stray light.

3.3.3 Rear Mounted Mirror

The derivation of the diffraction efficiency for a blazed reflection grating was discussed in Chapter 2. This is a complicated function to model as the polarization-dependent effi-

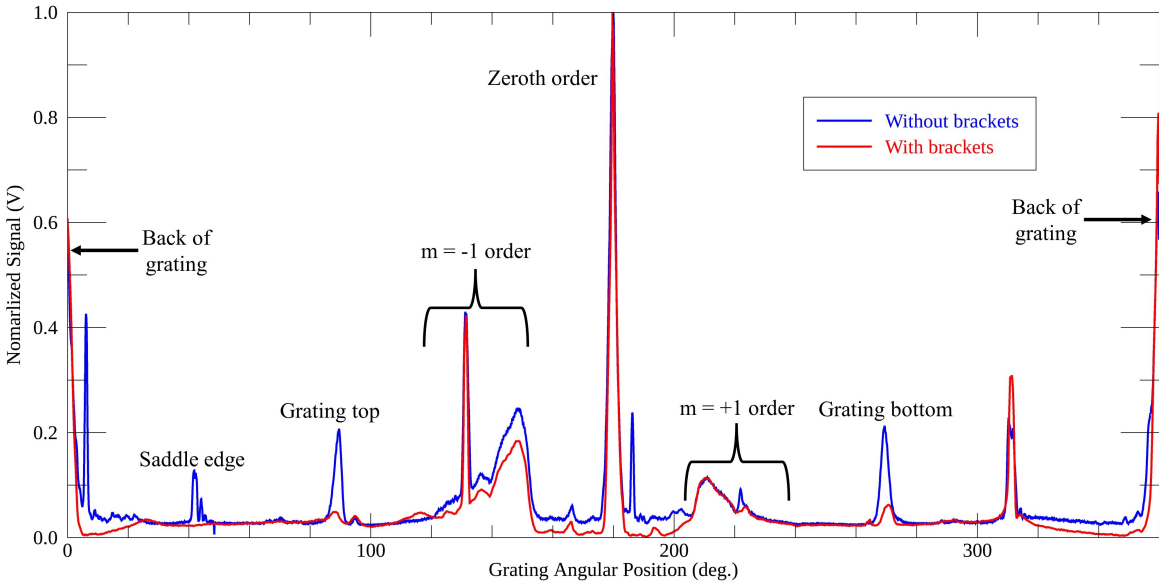

Figure 3.10: Full rotation of the grating mounted in the new enclosure with a blackbody source. The blue curve represents the first measurement taken with the new system and the red curve is the measurement after carborundum-coated brackets were applied to the grating top and bottom and the edges of the saddle.

ciency requires a vector electromagnetic theory of diffraction. While these models provide a means to approximate the efficiency response, they do not account for imperfections in the surface of the grating. While there are groups who publish efficiency measurements with various diffraction grating geometries, the grating used in this study was custom-made and the efficiency could not been characterized prior to receiving it because that would require cryogenic deployment of the grating along with an extensive suite of test kit. We devised a simple method of determining the grating efficiency by mounting a mirror on the rear of the grating saddle as shown in figure 3.12. When the system is coupled to an FTS and the mirror is inserted into the optical path, a single measurement of the entire band is obtained which serves to calibrate the efficiency of the grating as a function of wavelength. The mirror is mounted as close to the plane of the grating as possible, however there is a small offset introduced by the mount of the mirror. This results in the flat mirror having to be oriented at a slightly different angle to direct incident light to the detector as shown in figure 3.13. A ray tracing simulation was completed to determine the optimal angle that the

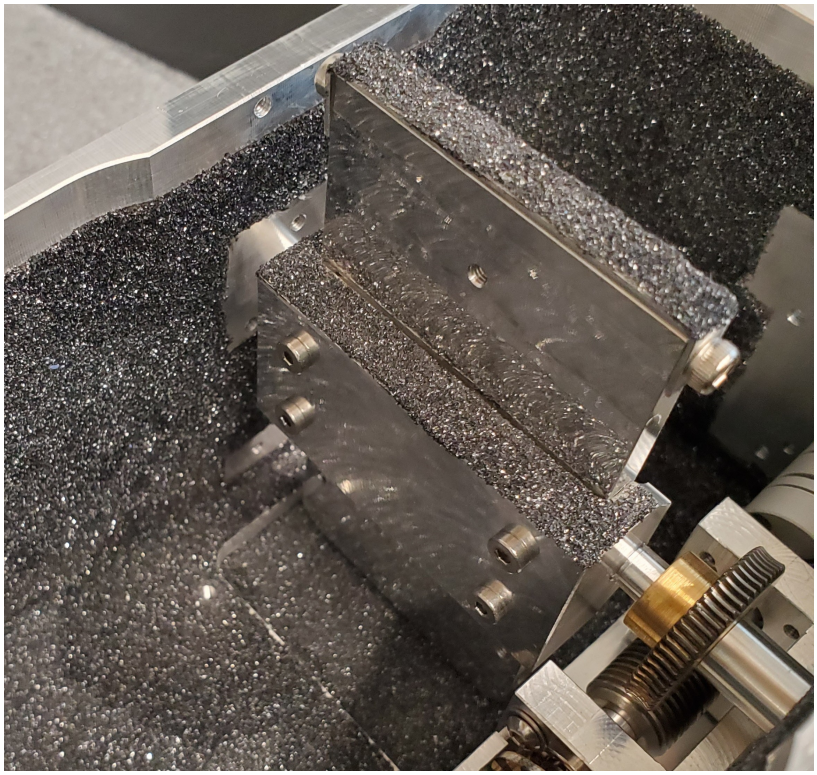

Figure 3.11: Image of the carborundum-coated brackets applied to the ends of the grating and the edges of the saddle.

mirror should be oriented so that the system is most efficient. The optimal angle was found to be at 15.62° from vertical (as opposed to the 15° deviation angle) and the efficiency was 92.6% computed using FRED ray tracing software [76].

The diffraction grating as fabricated was 105 × 50 mm. However, when the mirror was in the position as shown in figure 3.13 (bottom), the grating blocked some of the beam traveling from the OAP to the detector. A decision was made to cut 5 mm off of the 105 mm length of the grating so that the mirror measurements were possible. This only impacted the results at the large incident angle (long wavelength) end of the grating range as the beam did not reach the edges of the grating at shorter incident angles. Using simple geometry, the vertical height of the beam along the grating is equal to the beam diameter, 50 mm, divided by $\cos\alpha$, where α is the angle between the incident light and the grating normal. Therefore, the angle where the beam starts to illuminate past the cut-off edge was found to be: $\frac{50\,\text{mm}}{95\,\text{mm}} = \cos\alpha = 0.526... \therefore \alpha = 58.2°$. An incident angle of 58.2° corresponds to a

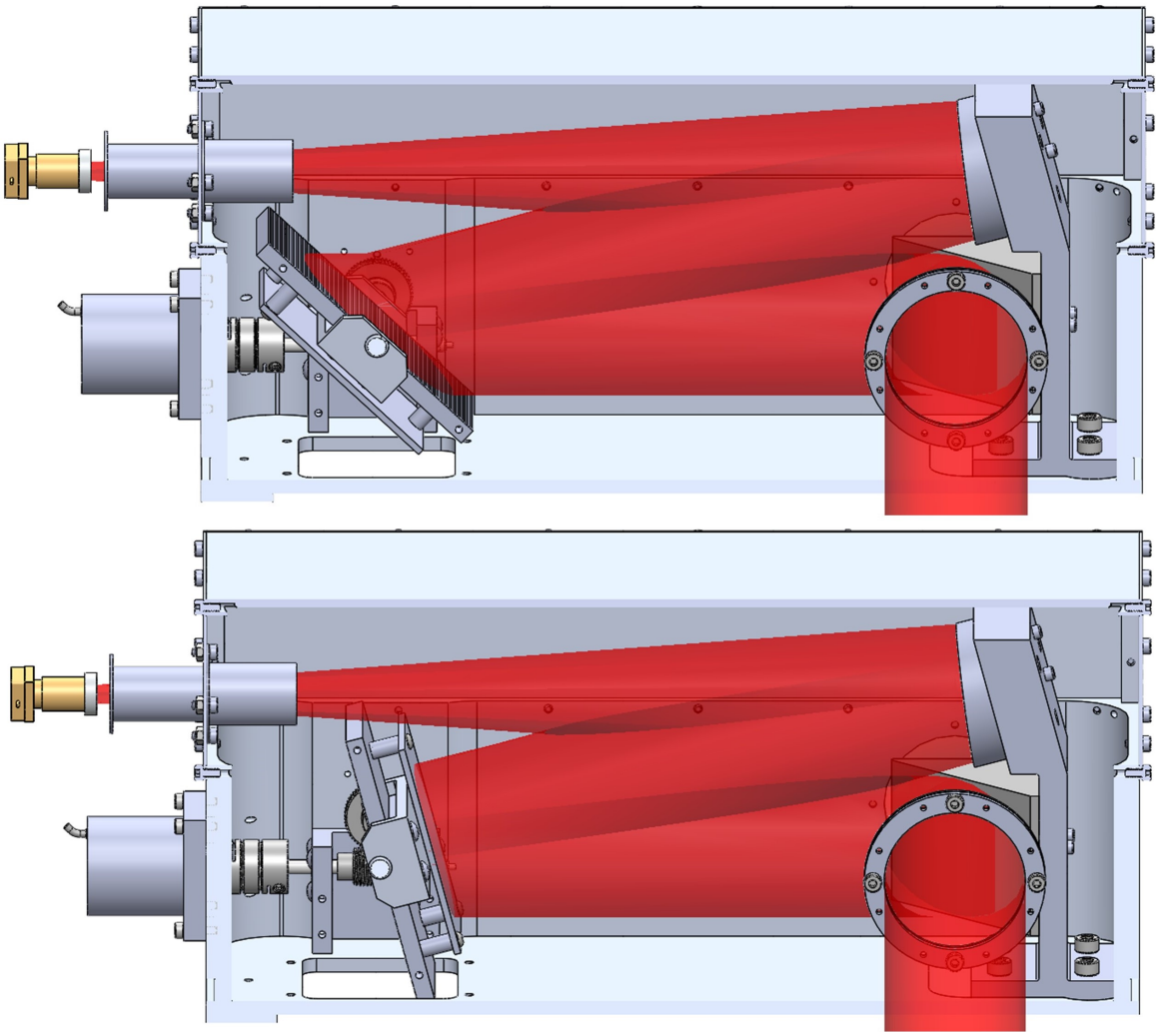

Figure 3.12: CAD rendering of how the mirror will be rotated to calibrate the efficiency of the grating as a function of wavelength.

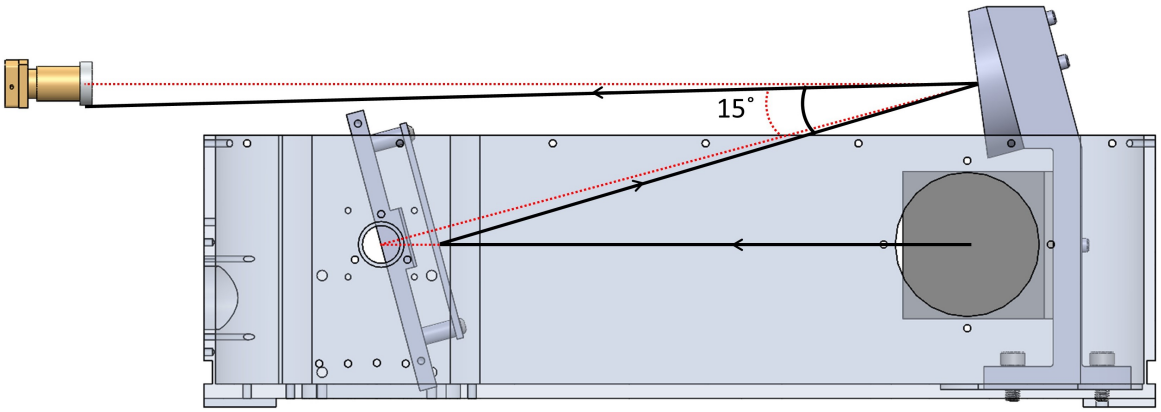

Figure 3.13: CAD model showing the offset of the flat mirror to the axis of the grating and how that will affect the optimal angle of the mirror.

wavelength of 479 μm using the grating equation 2.41. For this reason, in Chapter 4 and 5, the grating performance will be verified over the wavelength range of $285 - 479$ μm to avoid reductions in the resolving power.

3.3.4 Fiber-fed Encoder

When operating instrumentation inside of a cryostat (especially with moving parts) it is important to consider ways of troubleshooting the instrument. For the grating spectrometer, once the system is cooled to 4 K, there is no way to visually determine if the grating is actually rotating when the stepper motor is actuated. The source, detector, and grating modules must all be working properly in order to verify the grating is moving as expected. Using a source that emits radiation which is invisible to the human eye makes this situation even more complicated. Therefore, a method was needed to determine if the grating was rotating without having to rely on the other components. To solve this, an optical fiber encoder was designed to mount on the worm gear bracket inside the monolithic enclosure as shown in figure 3.14. A custom encoder wheel was designed, fabricated and fastened to the end of the worm wheel shaft which rotates as the shaft turns.

Two optical, single-mode fibers are mounted onto a small bracket which is bolted to the worm/gear bracket and is held into place with a set screw. The other end travels up through the 4 K enclosure of the cryostat to a room temperature ($\sim$290 K) section where a photodiode connects to one fiber and a 645 nm LED connects to the other. The red optical light travels through the fiber and is directed towards the encoder wheel where it is reflected by either the polished copper surface or the black painted surface. The contrast in the reflection of the two surfaces creates an oscillatory signal which will change amplitude if the shaft is moving.

Measurements of the encoder signal are shown in figure 3.15 for two full rotations of the worm shaft. Since there is a 60:1 gear reduction value between the worm gear and the grating, this represents an angular movement of 12° for the grating. Each 6° movement of

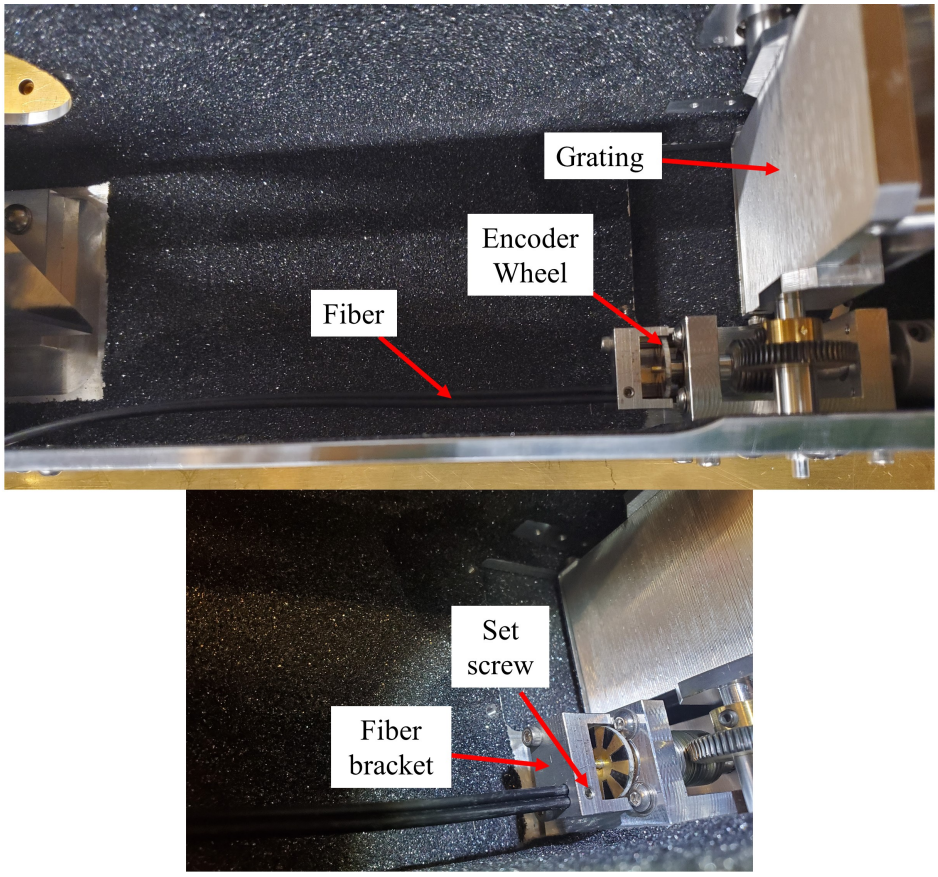

Figure 3.14: Image of the grating enclosure showing how the optical fiber and encoder wheel are mounted. The fiber fits through a slot in an aluminum bracket which has a set screw that holds it in place. The wheel is glued onto the shaft of the worm screw.

the grating corresponds to a total of 16 minima and maxima of the encoder signal which gives an angular resolution of 0.375°. This is sufficient to determine whether the gear shaft is moving, although it does not account for the case of the grating drive shaft slipping on the worm. We found this design to be easily retrofittable and relatively inexpensive. This device worked from its first implementation and has proven to be a useful diagnostic tool.

3.4 Optical Setup

This section describes the optical configuration used to measure the resolving power of the diffraction grating. Three stages of measurements were taken: the first was coupling the room temperature source directly into the grating and passing through the cryogenic

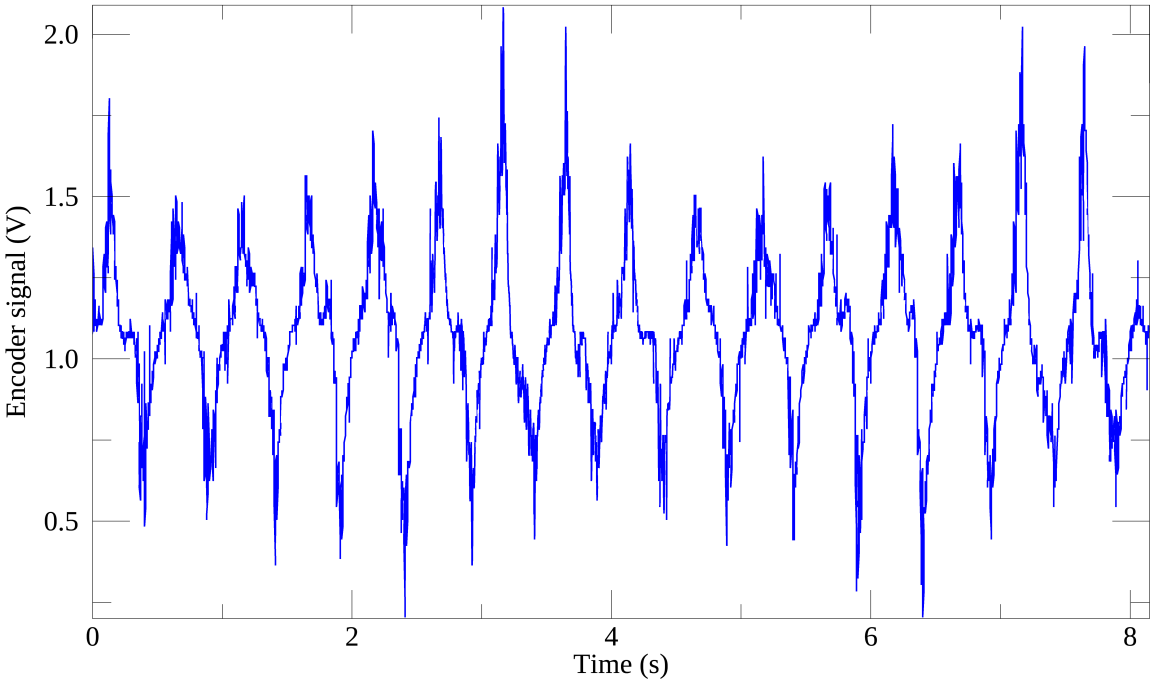

Figure 3.15: Signal from the photodiode measuring the signal reflected off of the encoder wheel. This measurement was taken over two full rotations of the wheel.

entrance slit and the second and third passed the source through a room-temperature polarizing FTS before coupling with the grating. The second configuration produced a collimated beam from the polarizing FTS into the grating spectrometer (4 K). The third and final configuration was realized by changing the exit optic of the polarizing FTS so that it focused through the cryogenic entrance slit and into the grating spectrometer.

The first and third configurations utilizing the cryogenic entrance slit had the cryogenic components mounted as shown in figure 3.16. The CAD rendering in figure 3.17 shows the same components with more visibility and a model of how the radiation passes through the system. A focused beam passes through the entrance slit towards the f/6 15° OAP mounted on the pendulum baseplate. The 15° OAP collimates the light towards a flat mirror which reflects the beam towards the pendulum mirror. The pendulum redirects the light through the 58 cm^{-1} low-pass filter and into the grating spectrometer.

Alignment of this system had to be completed at room-temperature so that components within the cryostat could be adjusted. For the first configuration without the FTS, a bright,

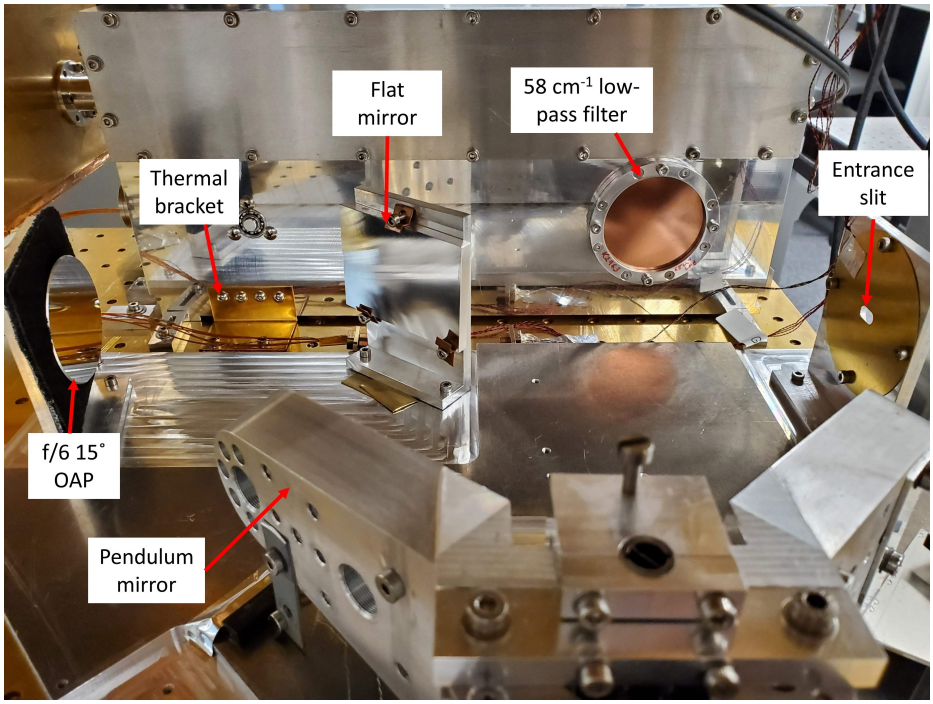

Figure 3.16: Image of the grating module mounted to the 4 K plate of the TFC. This configuration shows the entrance slit followed by the optics which feed a collimated beam through the low-pass filter and into the grating spectrometer.

white LED was placed at the entrance slit and a thin matte window was placed in front of the LED to scatter the light and create a Lambertian source. The light then continues along its path as outlined in the previous paragraph and the flat mirror mounted to the rear of the grating is positioned in the optical path such that the light is reflected to the f/6 15° OAP and imaged onto the exit slit on the detector. Components were then adjusted to ensure the image of the entrance slit was centered on the detector and that the light was not cut-off at any component. This alignment within the cryostat was not expected to change substantially as the system cooled to 4 K because the majority of components are made from aluminum and will contract at the same rate.

The final configuration utilized the polarizing FTS and cryogenic entrance slit. This was the most difficult system to align because the vertical and horizontal position of the FTS was critical in ensuring the beam was not sheared inside the cryostat. The FTS, however, is a massive structure (0.6 m $\times$ 0.7 m) welded from 0.5" thick aluminum and is not easily

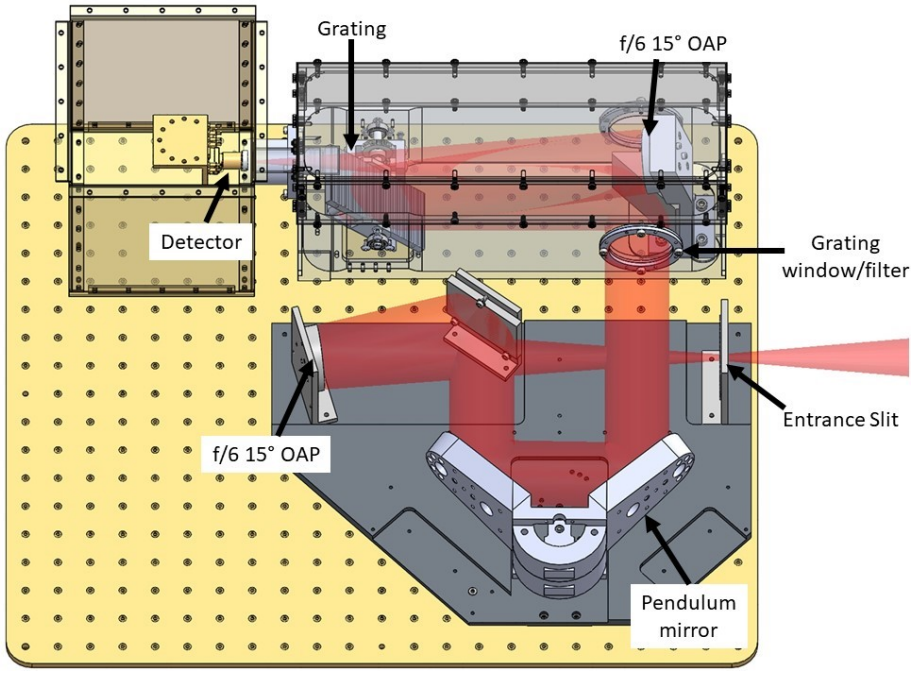

Figure 3.17: CAD model of the optical components within the 4 K chamber of the test facility cryostat. Light is incident into the cryostat window, passes through the entrance slit, and is collimated by an f/6 15° OAP. The collimated beam is reflected by a fold mirror towards a pendulum mirror which feeds the grating spectrometer window. Inside the spectrometer, the beam reflects off of the right angle mirror towards the diffraction grating and is focussed onto the detector via a second f/6 15° OAP. The exit slit is mounted to a filter which sits on the face of the detector.

adjusted. A CAD rendering of the optical components inside the TFC and the FTS mounted beside is shown in figure 3.18. Care was taken to ensure the table that the FTS sits on was level and at a height such that the ports of the FTS were centered vertically on the windows of the TFC which the entrance slit is centered on. A visible laser was then placed at the input of the FTS and approximately cenetered. The path of the laser was traced through the FTS optics and through the entrance slit within the TFC. The light was then imaged onto the exit slit of the detector with the grating rear-mounted mirror in place of the grating. An f/6 90° 100 mm OAP was used as the exit optic of the FTS to feed light through the entrance slit and onto the f/6 15° OAP mounted on the pendulum bracket. The 90° OAP had adjustability in the pitch, yaw and axial translation of the mirror. With the laser at the input of the FTS, the OAP was adjusted to ensure the light passes through the center of all

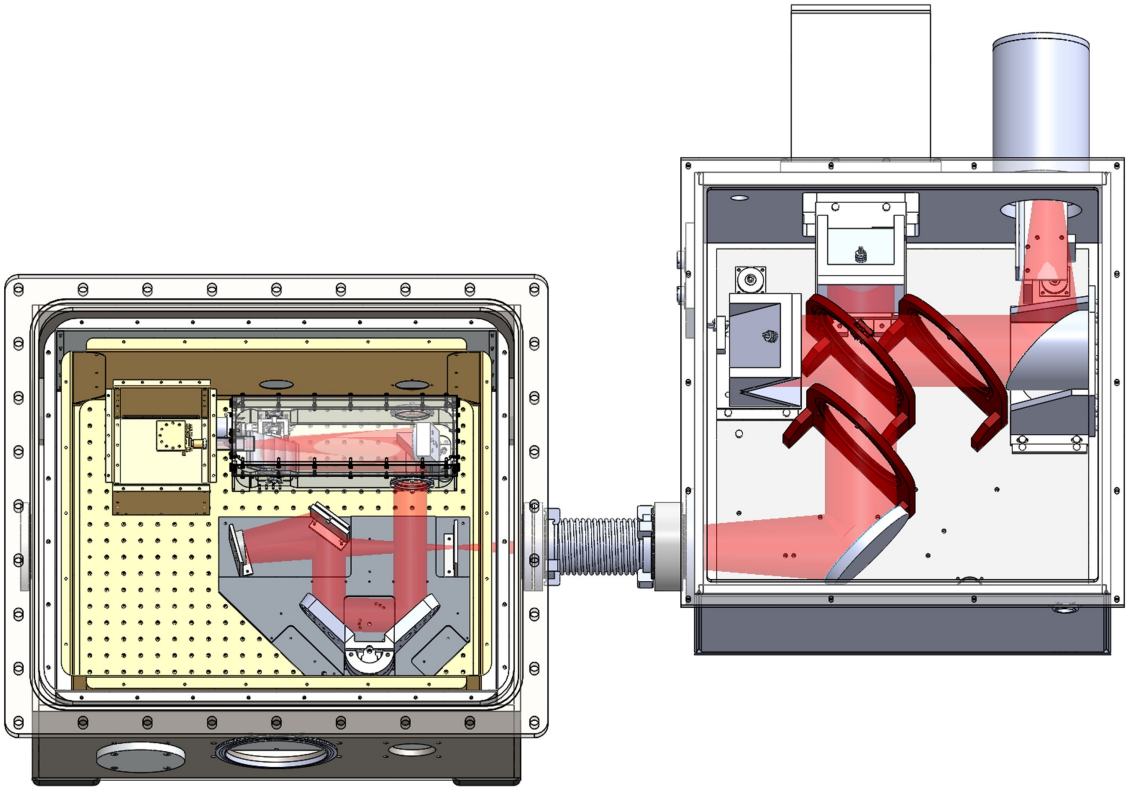

Figure 3.18: CAD model of the optical components within the test facility cryostat coupled to the polarizing FTS provided by Blue Sky Spectroscopy Inc. [73] which operates at room-temperature. The path of the radiation is shown in red.

the optics. The vertical height of the windows and entrance slit within the TFC are expected to shift as the cryostat is cooled to 4 K, however, this should be small enough to account for using the adjustments on the 90° OAP in the FTS. After the system was cooled, the alignment was repeated using a blackbody as the input source and adjusting the 90° OAP to achieve the maximum signal at the detector with the mirror in place of the grating.

Chapter 4 will discuss the experimental equipment used for the grating verification measurements. Results will then be given from the first configuration with the source being directly coupled through the cryogenic entrance slit and into the grating spectrometer. Chapter 5 will detail the integration of the room-temperature polarizing FTS and results will be given from the second configuration where a collimated beam was output from the FTS and the third configuration which incorporated the FTS and cryogenic entrance slit as shown in figure 3.18. Spectral response functions of the grating for different wavelengths of incident

light will be presented as well as a verification of the resolving power across the wavelength band for all three configurations. Chapter 5 will also present results collected with a blackbody source and a diffraction efficiency analysis as a function of both wavelength and polarization.

Chapter 4

Verification of the Grating Spectrometer: First Results

> It doesn't matter how beautiful your theory is, it doesn't matter how smart you are. If it doesn't agree with experiment, it's wrong.
>
> RICHARD P. FEYNMAN

This chapter presents the first steps used to characterize the performance of the diffraction grating spectrometer as an individual instrument. The equations driving the design of the grating were discussed in Chapter 2 and the specifications of the grating as manufactured were detailed in Chapter 3. There were three optical configurations used to test the performance of the grating. The first configuration used a monochromatic source to study the spectral response of the grating individually while the second two configurations incorporated a room-temperature polarizing Fourier transform spectrometer (FTS). The results from the grating used without the FTS will be given in this chapter. A description of the testing apparatus will be outlined including the source module, cryogenic detector, and the signal acquisition and processing equipment. Results will be presented from using a monochromatic source to measure the spectral response of the grating operating in a cryogenic test facility. Chapter 5 will then discuss the integration of the grating spectrometer with the polarizing FTS.

4.1 Test Equipment

The measurements taken with the grating spectrometer required a large suite of additional equipment. This included a tunable monochromatic line source and a heated filament producing continuum emission, a cryogenic, composite bolometer detector operating at ~ 300 mK, and a custom low-noise pre-amplification module which acquired, filtered, and amplified the signal measured by the detector. These components will be described in the following section.

4.1.1 Source Module

As was discussed in Chapter 1, to produce realistic synthetic astronomical spectra the source module should consist of a narrow-band line source (spectral feature) and a broad-band emission (continuum). Generating pseudo-monochromatic radiation at far-infrared wavelengths (terahertz frequencies) is not straightforward. In his Master's thesis, Makiwa reviewed the various methods which can produce narrow-band terahertz radiation and discussed the benefits and drawbacks of each system [77]. The method that was adopted to meet the requirements of the system and proved to be the most cost efficient was the photomixer. A photomixer module was purchased for work done by a previous student, Veenendaal, who used the photomixer as a source of terahertz radiation to validate the performance of a cryogenic post-dispersed Fabry-Pérot interferometer [64]. The photomixer was purchased from Toptica Photonics and operates over a broad frequency range ($\sim 0.1-2$ THz), has a moderate power output (10 μW at 500 GHz), and easily integrates with commercially available photonics equipment [78].

The working principle of a photomixer is fairly straightforward. Two near-infrared lasers, slightly detuned from a central frequency combine to form an optical beat (heterodyne) signal with a frequency equal to the difference frequency between the lasers. Therefore, setting this difference to lie in the THz regime results in the production of THz radiation. This is a relatively new technology, only being realized experimentally in the 1990s

[79]. The actual photomixing module is composed of a p-i-n layered photodiode in which an intrinsic (absorption) layer is sandwiched between p-doped and n-doped regions. The photodiode is composed of indium-galium-arsenide, $In_{0.53}Ga_{0.47}As$, a semiconductor material commonly used in optical fiber communications. The band gap energy of this material is 0.75 eV [80] which corresponds to a photon with a wavelength of 1.65 μm. Any photon with an energy (wavelength) equal or greater (less) than the band gap energy can therefore excite the material and produce electron-hole pairs within the junction. One of the most commonly used frequencies in optical communications is 1.55 μm which occurs within the C-band and happens to be a perfect fit for this device. Working at this frequency helps to drive the cost down as off-the-shelf diode lasers and optical components can be procured which are relatively inexpensive compared to similar products operating in different wavelengths.

The electric field generated by the beat signal from the two combined lasers is given by:

$$\vec{E_{beat}} = \vec{E_1} e^{-i\omega_1 t} + \vec{E_2} e^{i\omega_2 t + \phi} \qquad [\mathrm{V\,m^{-1}}] \quad (4.1)$$

where the first term represents the contribution from the first laser with an angular frequency ω_1 and the second is from the second laser with an angular frequency of ω_2. The intensity of the beat signal is:

$$\begin{aligned} I_{beat} &= \frac{cn\varepsilon_o}{2}\left[|E_1|^2\cos^2(2\omega_1 t) + |E_2|^2\cos^2(2\omega_2 t+\phi) + 2E_1\cdot E_2\cos(\omega_1 t)\cos(\omega_2 t+\phi)\right] \\ &= \frac{cn\varepsilon_o}{2}\left[\frac{E_1^2}{2} + \frac{E_1^2}{2}\cos(\omega_1 t) + \frac{E_2^2}{2} + \frac{E_2^2}{2}\cos(\omega_2 t+\phi)\right. \\ &\left. + E_1\cdot E_2\left(\cos\left[(\omega_1+\omega_2)t+\phi\right] + \cos\left[(\omega_1-\omega_2)t+\phi\right]\right)\right] \\ &= I_1 + I_2 + I_{beat+} + I_{beat-} \end{aligned}$$

$$[\mathrm{W\,m^{-2}}] \quad (4.2)$$

where c is the speed of light, ε_o is the electric permittivity in vacuum and n is the refractive

index of the medium. I_1 and I_2 are the intensities of each laser beam, I_{beat+} is the intensity of the term with frequencies added, $(\omega_1+\omega_2)$, and I_{beat-} is the heterodyne term with frequency $(\omega_1-\omega_2)$. The power can be calculated from the intensity as:

$$\begin{aligned} P_{beat} &= \int (I_1+I_2+I_{beat+}+I_{beat-})\,dA \\ &= P_1+P_2+2\sqrt{mP_1P_2}\,(\cos[(\omega_1+\omega_2)t+\phi]+\cos[(\omega_1-\omega_2)t+\phi]) \end{aligned} \quad \text{[W]} \quad (4.3)$$

where P_1 and P_2 are the powers of each laser and m is a factor called the spatial-mixing efficiency which measures the degree of overlap between the incident beams. When this power is incident on the photomixer, electric current will be generated and modulated at a frequency of $|\omega_1-\omega_2|$. The term with frequency $(\omega_1+\omega_2)$ will have an insignificant effect on modulating this current because the instantaneous power is oscillating at a frequency much greater than can be registered by the photodiode; the carrier recombination time is much slower than the rate at which the amplitude oscillates. Therefore, this term can be ignored and the power registered on the photomixer modules is given as:

$$P_{\text{pm}} = P_1+P_2+2\sqrt{mP_1P_2}\cos[(\omega_1-\omega_2)t+\phi] \quad \text{[W]} \quad (4.4)$$

The actual power output of a photomixer based on the p-i-n diode configuration is a much more complicated function of the material properties and antenna geometry. Chapter 2 in Makiwa's thesis calculates the optical heterodyning efficiency and finds the output power to be equal to [77]:

$$P_{THz} = \frac{\frac{1}{2}(V_B G_0)^2 R_L}{[1+(\omega\tau)^2][1+(\omega R_L C)^2]} \quad \text{[W]} \quad (4.5)$$

This equation is based off of the assumptions that the voltage across the photomixer has a harmonic time dependence and that the device operates in the small signal limit, $G_0 R_A <<$

1. $V_B G_0$ is the bias voltage, V_B multiplied by the DC conductance, G_0 which, when multiplied, is equal to the DC photocurrent. R_L is the photoconductive resistance in the antenna, $\omega = |\omega_1 - \omega_2|$, C is the capacitance of the diode, and τ is the charge carrier lifetime. From this equation it is evident that the output power of the photomixer is proportional to the square of the bias voltage and DC conductance and is inversely proportional to the carrier lifetime. Therefore, it is preferential to bias the circuit with a larger voltage, construct a substrate with a short carrier lifetime (thin material), and increase the DC conductance by having a high carrier mobility within the substrate. Even when optimizing all of these parameters, the conversion efficiency reaches a maximum of about 10^{-5}, resulting in an output power in the order of microwatts. Still, this is an acceptable penalty given the compact nature of the device allowing ease of integration.

Figure 4.1 shows the working principles of the InGaAs photomixer. Two fiber-fed near-infrared lasers are combined with their output creating a beat pattern with an envelope frequency chosen to be in the terahertz regime. The beat signal is incident on the p-i-n junction via a waveguide which couples the radiation into the intrinsic layer through the evanescent component of the electromagnetic waves; a highly efficient method. Electron-holes pairs are created because the energy of each near-infrared photon exceeds that of InGaAs and a bias voltage is applied to the junction to sweep the charge carriers, creating electric current. Unable to respond to the high laser frequency, the current oscillations follow the envelope of the combined wave corresponding to frequencies in the THz regime. When the oscillating current is coupled to an antenna structure, this produces free-space THz electromagnetic waves [79]. The photomixer purchased from Toptica Photonics features a bow-tie antenna which outputs linearly polarized light and can operate over a large frequency range. A hyper hemispherical silicon lens sits adjacent to the photomixing module allowing the focus to be placed 22.3 ± 1.2mm behind the face of the lens which facilitates mounting of the device. The output from the lens is a cone of radiation with a wavelength-dependent 12°-15° opening angle. However, at the wavelengths used in these results, the device always has a

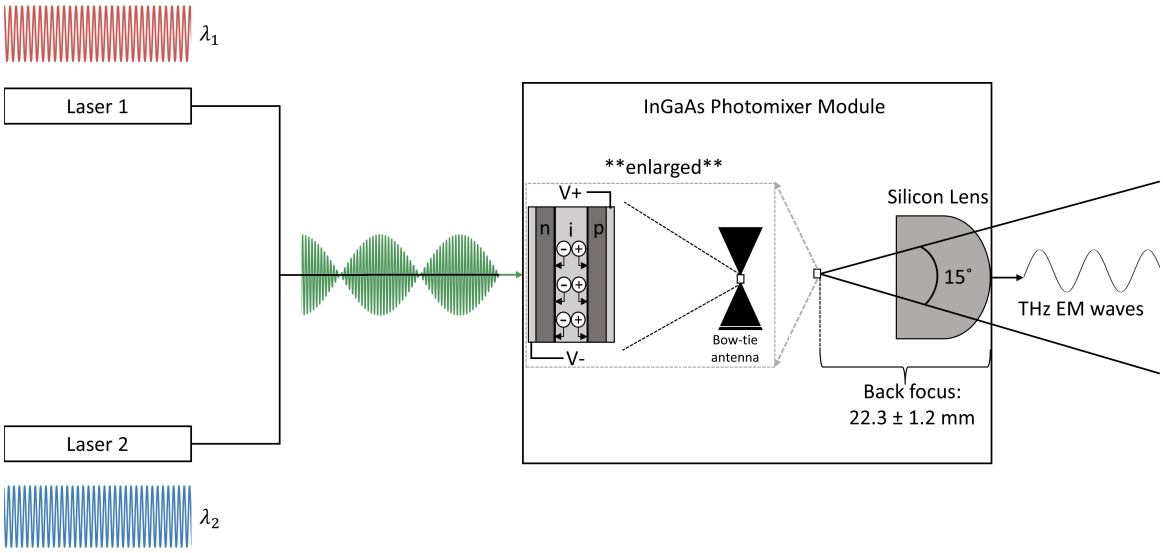

Figure 4.1: Diagram showing the operating principles of the InGaAs photomixer module. The actual size of the bow-tie antenna is 100 μm, much smaller than the 25 mm diameter silicon lens. The photomixing module consisting of the p-i-n junction is even smaller than the antenna and is shown accepting the combined light from lasers 1 and 2 with wavelengths λ_1 and λ_2. Each photon has enough energy to surpass the bandgap of the InGaAs intrinsic layer and produce electron-hole pairs which separate into the n- and p-doped layers. V_+ and V_- correspond to the bias voltage applied across the junction.

15° output angle.

In addition to the line source, a heated element will be used to study the performance of the PDPFTS with a broadband input. The blackbody used in the first FTS configuration was a Scitec IR-12 radiating element consisting of a coiled resistance wire which has a high emissivity at infrared wavelengths[81]. The element is mounted on an aluminum block creating a more uniform temperature ∼1200 K with an input power of 10 W at 5 V. The emissivity of the element is ∼0.8 and the heated area of the source is 3.5 mm x 3.5 mm which produces a sufficiently powerful source when coupled to the FTS. In the second FTS configuration incorporating the cryogenic entrance slit, continuum emission was produced by a commercially available silicon carbide igniter. The ignition element is a rectangular cuboid (5 mm wide x 30 mm long x 2 mm thick) which achieves an emissivity > 0.7 at infrared wavelengths [82] and reaches a temperature around 1500 K. The next section will

describe the composite bolometer detector used in this study.

4.1.2 Bolometer Detector

Thermal infrared bolometer detectors have been used in infrared astronomical spectroscopy for decades [83]. They differ from heterodyne detectors because they measure power and, consequently, do not retain information about the frequency or phase of incident radiation. Therefore, spectral information about the source must be encoded before reaching the detector by passing through some type of interferometer. Bolometric detectors couple well to an FTS which produces an interferogram that can be mathematically transformed into a spectrum [84]. Radiation incident on the bolometer absorbing element causes a temperature change which can be measured via a thermometer. The relationship between the power of the incident radiation and the corresponding temperature change in the detectors absorbing element is dependent on its specific heat capacity, which should be as low as possible to maximize its frequency response [72].

The composite bolometer detector used in this study was developed by Gom [72]. The detector is composed of a nuclear transmutation doped germanium-gallium element mounted on a sapphire disc and figure 4.2(a) shows the working principles of a bolometer detector. Incident radiation is absorbed by the sapphire disc which has a relatively low specific heat capacity (1.356 x 10^{-11} $\mathrm{J\,K^{-1}\,mm^{-3}}$). The incident radiation produces a heat load, Q, in the bolometer element and the bias current, I, adds additional heat to the system represented by $P = I^2 R_{bol}$ where R_{bol} is the resistance of the bolometer. Thus, the total heat flow from the bolometer element to the heat sink is given by $W = P + Q$ [72]. The dynamic thermal conductance, $G_d = \frac{dP}{dT}$, is the rate of heat flow induce by a change in the bolometer temperature with a constant Q. From figure 4.2(b), R_{bol} varies with the temperature of the element, T, and a bias voltage, V_{bias}, is applied across the load resistor, R_L, which produces a bias current, I. The signal of interest induces thermal fluctuations in the bolometer element which is returned to an electrical signal by measuring the voltage drop across the

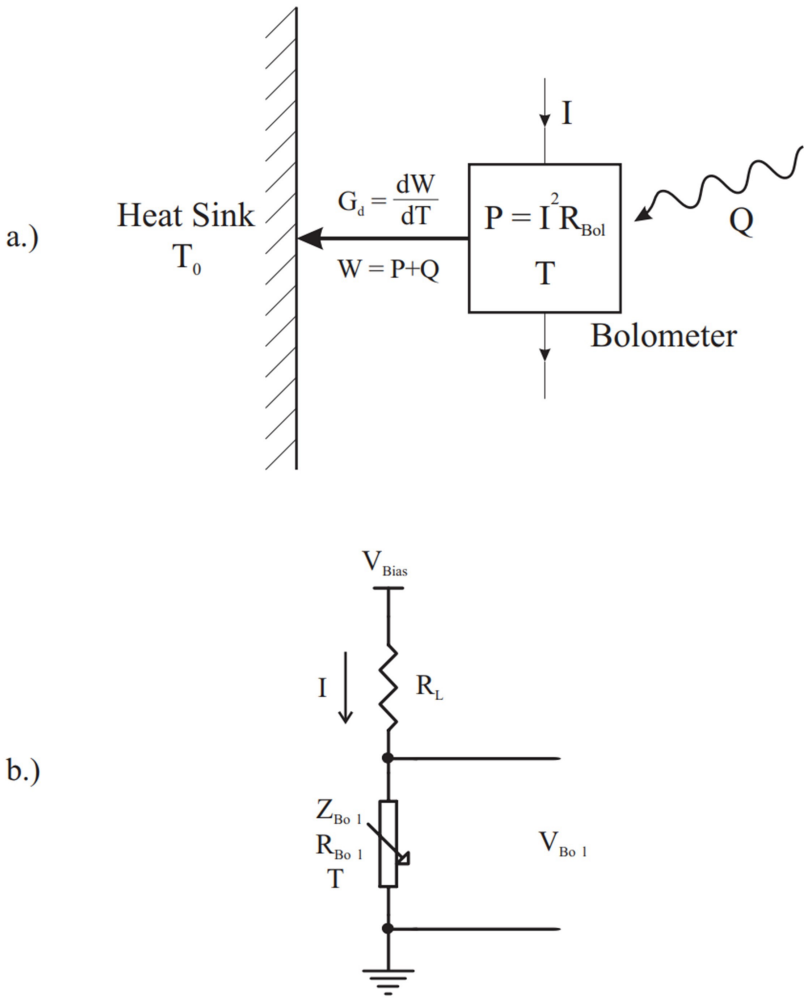

Figure 4.2: Schematic taken from [72] portraying the thermal (a) and electrical (b) working principles of a bolometer detector.

bolometer, V_{bol} [72].

The bolometer element is suspended in an integrating cavity and mounted within an f/3 Winston cone (feedhorn) which couples incident radiation into the cavity. An image of the detector is shown in figure 4.3 where the copper cylinder shown is the exterior of the feedhorn. The detector is mounted to a bracket that is thermally linked to a 0.3 K dual stage ^{4}He:^{3}He:^{3}He closed cycle refrigerator [72]. The exit slit of the grating spectrometer is shown mounted to the face of the bolometer along with a 35 cm^{-1} thermal filter which helps to de-load the detector and restrict the spectral bandpass so that the detector is not measuring multiple spectral orders of radiation from the grating.

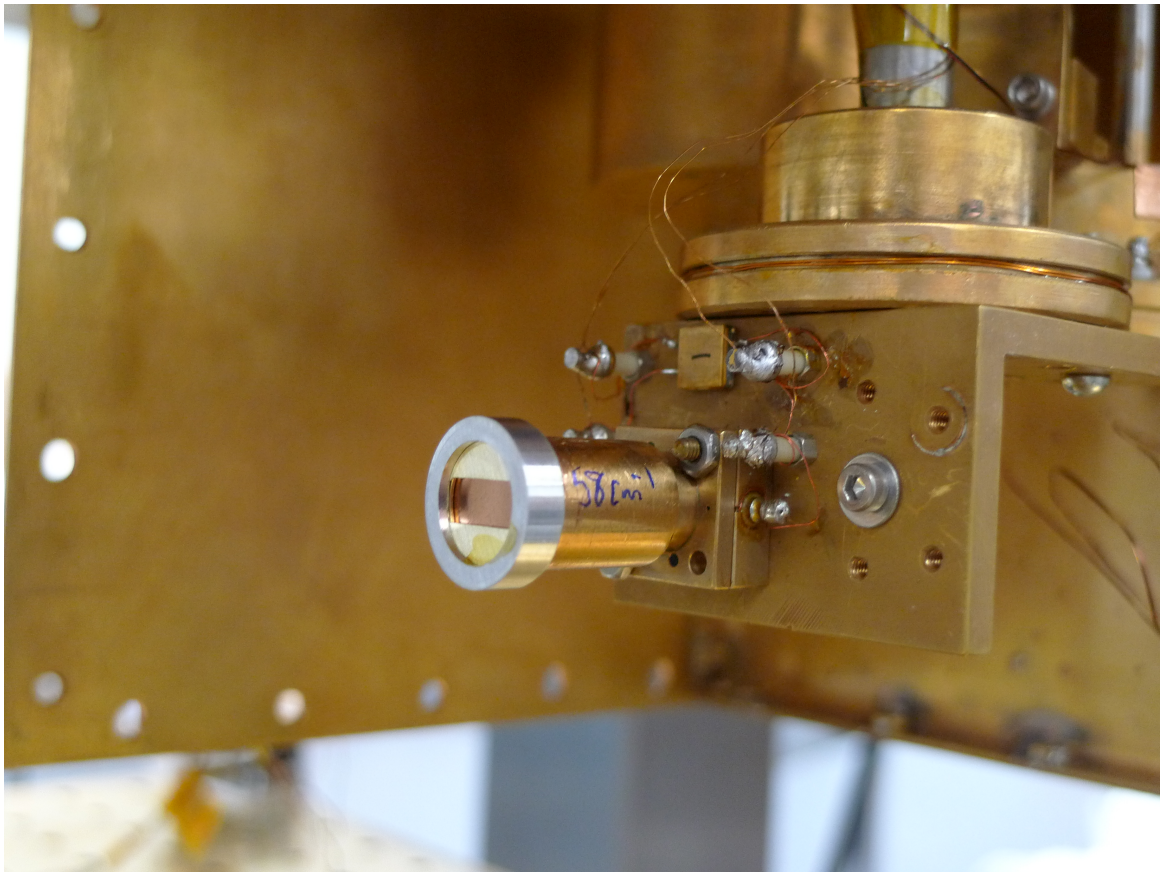

Figure 4.3: Image of the composite bolometer detector within the 0.3 K chamber. The exit slit and thermal filter are shown mounted to the face of the feedhorn. The 58 cm^{-1} filter in the image was replaced by a 35 cm^{-1} filter for the measurements in this thesis.

Since a bolometer is sensitive to radiation of all wavelengths, it is important to reduce the background signal as much as possible while maximizing the efficiency of the source coupling [72]. As was discussed in Chapter 3, the exit optic of the grating spectrometer is an f/6 15° OAP which was chosen due to available space within the cryostat. The detector is a faster optic (more divergent) so its field-of-view will be substantially larger than the f/6 mirror which feeds the signal of interest. To mitigate this, a retractable baffle was constructed to block stray light outside of the signal path from reaching the detector. A shield was also constructed to enclose the spectrometer optics and the interior of these components were coated with epoxy and carborundum to absorb and scatter stray light [85].

4.1.3 Signal Acquisition

Now that the source module and detector have been described, the next module to discuss are the instruments responsible for acquiring and processing the measured signal. A block diagram of the acquisition process is shown in figure 4.4. The photomixer (or blackbody) source is placed at the focus of the external optics which feed the grating spectrometer within the cryostat. An optical chopper driven by a Stanford Research Systems SR540 controller [86] is placed close to the face of the source and serves to modulate the signal at a known frequency. The chopped (modulated) signal is fed into the grating spectrometer and into the bolometer detector. A state-of-the-art low-noise differential pre-amplifier described in [72] measures the signal from opposite sides of the symmetric bolometer element in a fully differential configuration to eliminate common-mode noise. The differential AC signal is measured by a Stanford Research Systems lock-in amplifier (LIA) [87] which uses phase-sensitive detection to single out the component of the input signal which matches the frequency and phase of the reference. In this application, the reference signal is provided by the synchronous output of the SR540 chopper controller so that the LIA is only measuring the frequency component corresponding to the chopped signal. The LIA outputs a DC signal which is proportional to the signal amplitude and is converted to a digital signal using a Measurement Computing USB-1808X analog to digital converter, ADC [88]. The computer receives a digital input from the ADC and the data are able to be analyzed.

The working principle of the LIA is to filter out any unwanted noise components. The benefit of using a phase-sensitive detection loop is that the signal of interest can be singled out within a very narrow bandwidth. The amplified, filtered AC signal is multiplied by the reference signal using a phase-sensitive detection loop which outputs two signals with angular frequencies of $(\omega_r - \omega_l)$ and $(\omega_r + \omega_l)$, where ω_r is the angular frequency of the reference and ω_l is the internal lock-in frequency. The outputs are then passed through a low-pass filter which discards all components other than the DC which corresponds to the case where $\omega_r = \omega_l$. This DC signal then becomes the output of the LIA and represents the

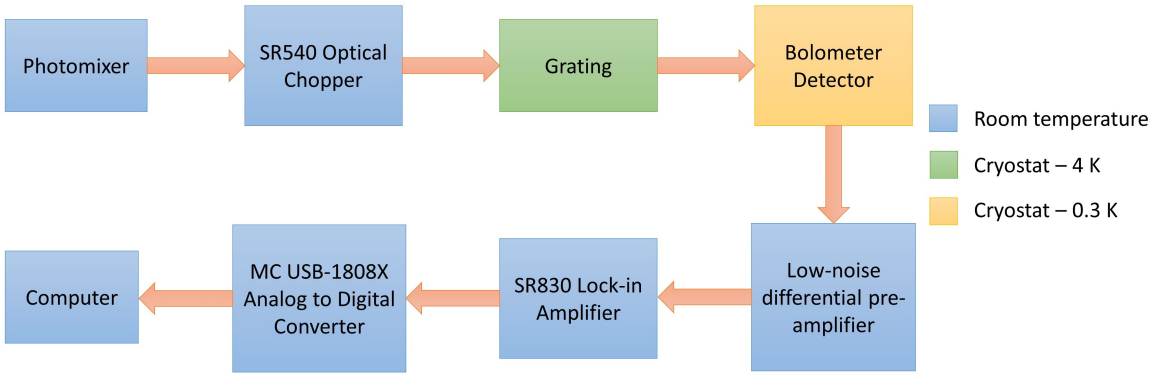

Figure 4.4: Block diagram of the components used to acquire a signal with the grating spectrometer. Radiation produced by the THz photomixer passes through an optical chopper which modulates the signal and directs it towards the grating spectrometer to be measured by the bolometer detector. The electronic signal from the detector is boosted by the low-noise differential pre-amplifier and the resulting AC signal is measured by the lock-in amplifier (LIA). The DC output from the LIA is read by the analog-to-digital converter which feeds the digital output into a PC for analysis.

amplitude of the modulated signal.

As mentioned in Chapter 3, the grating is rotated by a Phytron stepper motor [75]. The motor is driven by a Phidget 1063 bipolar stepper driver which provides a minimum stepping resolution of 0.001875° and a maximum current of 2.5 A per coil [89]. A graphical user interface, GUI, was constructed using Interactive Data Language, IDL, version 8.8 (2020, Harris Geospatial Solutions, Inc.) which allows the user to set the parameters of the phidget driver. The GUI was used to specify and record the angular position of the grating, however, with no method of absolute encoding, it required calibration. Consider the photomixer source which outputs a wavelength (frequency), λ_{pm}, which can be converted to a corresponding angular position, θ_{pm}, of the grating using equation 2.41:

$$\begin{aligned}\theta_{pm} &= \alpha + \frac{\phi}{2} \\ &= \arcsin\left(\frac{\lambda_{pm}}{2d\cos 7.5^\circ}\right) + 7.5^\circ\end{aligned} \qquad [^\circ] \quad (4.6)$$

where α is the angle of incidence, ϕ is the deviation angle, and $d = 312$ µm is the groove spacing. The signal amplitude measured at each uncalibrated angular position can be fitted

with a Gaussian equation:

$$f(\theta) = A_0 \exp\left(\frac{-(\theta - \theta_{\text{fit}})^2}{2\sigma_\theta^2}\right) + \text{offset} \qquad \text{[a.u.]} \quad (4.7)$$

to extract the uncalibrated center angular position, θ_c, which should be calibrated such that $\theta_c = \theta_{\text{pm}}$. With respect to the calibration process, the amplitude, A_0, σ_θ, and offset are unused. Therefore, the calibration requires θ_c to be subtracted from the array of angular positions and θ_{pm} added:

$$\theta = \theta_i - \theta_c + \theta_{\text{pm}} \qquad \text{[rad]} \quad (4.8)$$

where θ represents the array of calibrated angular positions, and θ_i is the i^{th} element in the array of uncalibrated angles.

4.2 Configuration 1: Grating Independent

The results presented here were obtained using the first optical configuration which studied the grating as an individual instrument. Optics are taken from a cryogenic Fabry-Pérot interferometer [64] which included a cryogenic entrance slit which was necessary to control the size and position of the radiation entering the spectrometer. Figure 4.5 shows the optical components and path of the radiation as it travels from the room temperature optics, into the 4 K chamber of the cryostat, and then finally entering the 300 mK section containing the composite bolometer detector. The purpose of the room temperature optics was to take the output from the terahertz photomixer and image it onto the entrance slit mounted on the 4 K plate. An f/2 90° OAP mirror with a 320 mm focal length was used to collimate the light from the photomixer. The collimated beam then traveled towards a custom f/6 90° OAP mirror with a focal length of 600 mm. This OAP was designed to pass light through the entrance slit and feed the f/6 15° OAP at 4 K. The 15° OAP is identical to the OAP inside the grating assembly so this removes any magnification induced by the

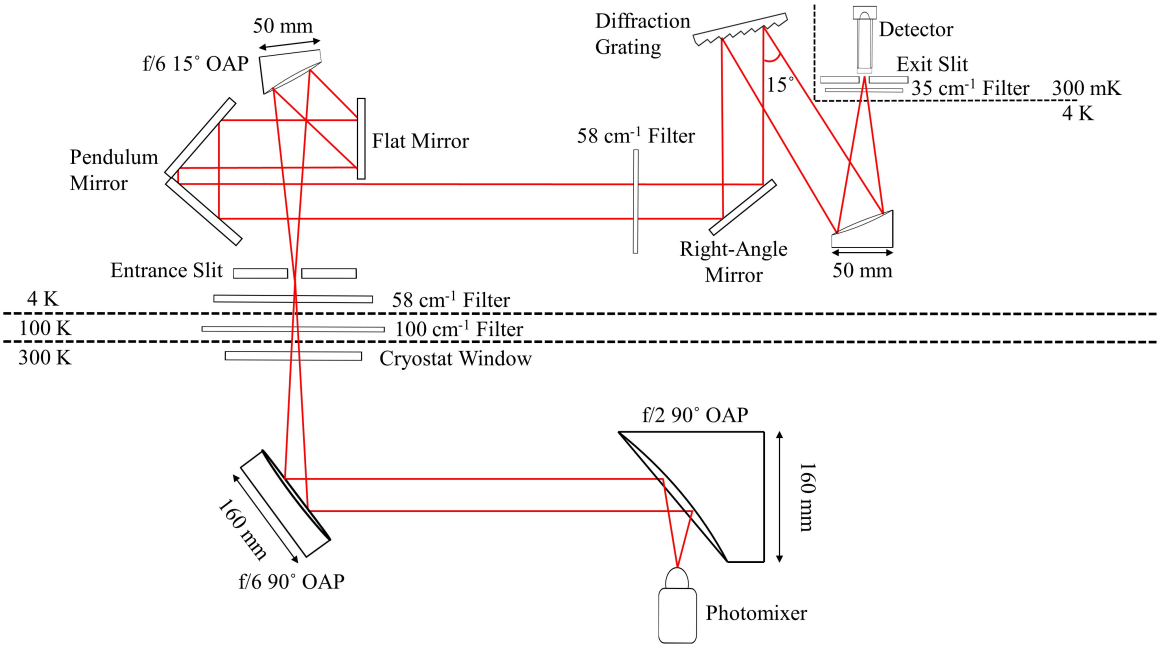

Figure 4.5: Diagram showing the optical setup used to test the performance of the diffraction grating spectrometer. See text for details.

imaging mirrors. The first 15° OAP collimates the light passing through the entrance slit and directs it to a fold mirror which reflects the collimated beam through a pendulum mirror. The collimated beam enters the grating enclosure and is reflected by a right-angle mirror towards the diffraction grating which diffracts the light to the f/6 15° OAP. The final OAP focuses the light through an exit slit mounted on the feedhorn of a bolometer detector and is subsequently measured.

4.2.1 Spectral Response Functions

A method to determine the wavelength of the source is required to measure the spectral response function, SRF, of the grating. When using the photomixer described above in section 4.1, the frequency of the mixed output is equal to the difference between the frequencies of the two lasers, $(\omega_1 - \omega_2)$, from equation 4.4. Therefore, a simple way to measure the output wavelength of the photomixer is to measure the wavelenths of the individual lasers. This was achieved by injecting each fiber laser output into a WA-1500 Wavemeter by EXFO Electro-Optical Engineering Inc. which measures the wavelength of

1550 nm lasers to an accuracy of one part in a million [90]. The difference between the wavelengths of the two lasers is taken to be the photomixer wavelength, λ_{pm}, and is used for calibration of the grating position.

The photomixer frequency was tuned across the grating band (285 - 500 μm) and at each setting of the photomixer the grating was scanned in 0.06° increments (0.58 - 0.40 μm) around the corresponding photomixer wavelength to determine the SRF of the grating. Each scan incorporated around 20-30 data points depending on the width of the profile. At each data point, the grating was moved to the commanded position and after a delay of 1 s, data were collected. The delay was set to be 10 times the time constant of the LIA, 100 ms, to make sure the LIA had sufficient time to respond to the change in signal. At each position, 250 samples of the LIA were recorded using the ADC with a sampling rate of 50 Hz and the grating was moved to the next position and the process was repeated. The commanded angle of the grating is recorded along with the average and standard deviation of the 250 data points taken at each position. Afterwards, the angular position of the grating was calibrated using equation 4.8 where θ_{pm} was calculated from λ_{pm} using equation 4.6. A total of 36 SRFs were measured across the range of the grating and they are all shown in figure 4.6.

It can be seen in figure 4.6 that there are some secondary local maxima within the grating SRFs. This was believed to be stray radiation making its way to the detector from the edges of the saddle which is parallel to the plane of the grating. The width of the input beam in this configuration is 50 mm and the width of the grating is also 50 mm which means the beam is expected to interact with the edges of the saddle which the grating is mounted in. To test if the stray light was caused by the edges of the grating, the input beam was shifted horizontally across the grating to change the direction of the reflection and try to eliminate this contribution of stray light to the detector signal. The result of this test is shown in figure 4.7 where the two plots shown were taken in identical conditions. However, the figure on the right was measured after the beam was shifted horizontally across the grating.

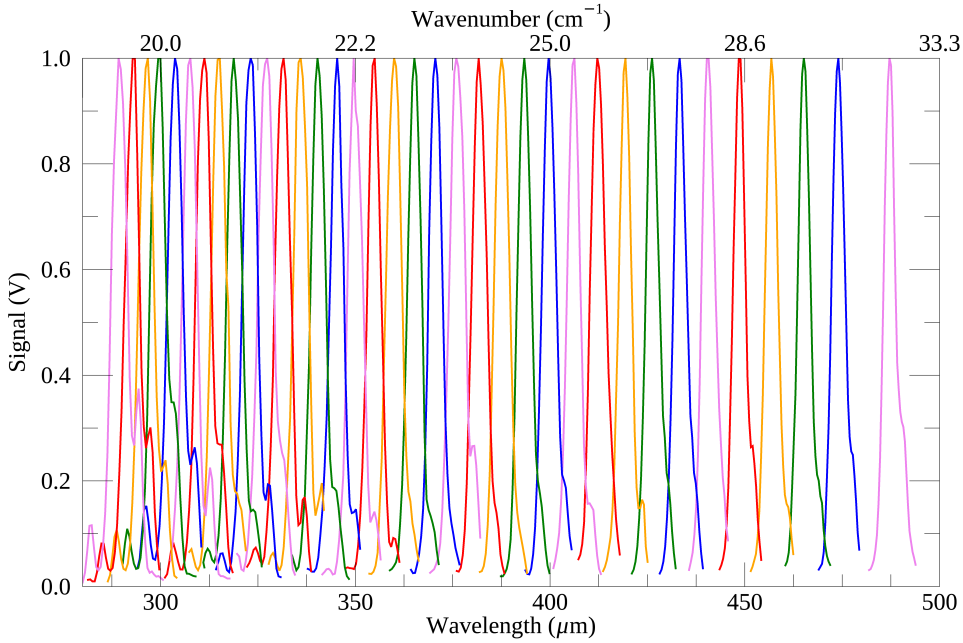

Figure 4.6: All normalized SRFs taken with configuration 2. The profiles show a narrowing in full-width-half-maximum from short to long wavelengths, which was predicted in equation 2.50.

These features were able to be removed by shifting the beam indicating that the features were due to diffraction off of the edges of the saddle. Figure 4.7 included data collected at a wavelength of 289 µm, however, this adjustment did not produce ideal results at longer wavelengths ($\sim$ 500 µm). The resolving power was significantly reduced when this shift was repeated at longer wavelengths and this was probably due to the system being more sensitive to the change in alignment due to the angle of incidence being larger and the beam illuminating a larger portion of the grating. Figure 4.7 verified that the secondary maxima within the grating profile are not a feature of the grating alone. Also, it is shown that the presence of these features affect the accuracy of the Gaussian fit to the data where the chi-squared was found to be $\chi^2 = 423$ for the fit to the original data and $\chi^2 = 0.696$ for the data collected after shifting the beam where both data sets have the same statistical degrees of freedom. Therefore, the data points corresponding to the stray light were excluded from the fitted data to produce a more accurate fit as will be shown in figure 4.8.

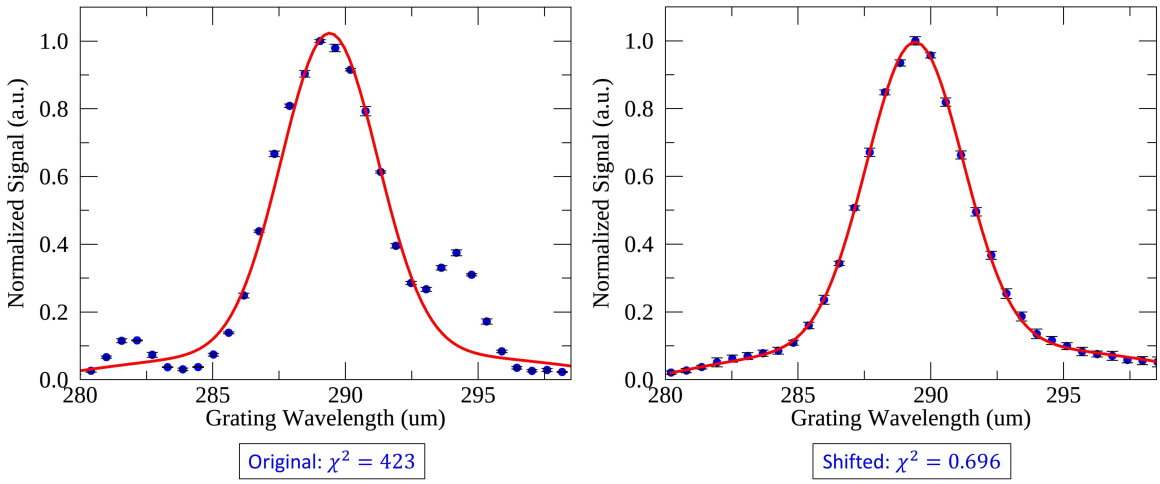

Figure 4.7: The two plots show the measured signal (blue points) and the red curve is the best fit Gaussian profile. Both have the photomixer set to a wavelength of 289 μm. The figure on the left was taken with the original alignment and the fit returned a χ^2 of 423. The right was taken after the alignment was shifted to reduce the impact of stray reflections and returned a χ^2 of 0.696.

The wavelength-dependent grating SRF is then fit with a Gaussian equation:

$$f(\lambda) = A_0 \exp\left(\frac{-(\lambda-\lambda_c)^2}{2\sigma_\lambda^2}\right) + A_1 + A_2\lambda + A_3\lambda^2, \qquad \text{[a.u.]} \quad (4.9)$$

to determine the center wavelength, λ_c, and σ_λ. The SRFs were normalized because the signal amplitudes did not provide any meaningful information so A_0 was kept at unity. A quadratic function, $A_1 + A_2\lambda + A_3\lambda^2$, was added to the baseline of the Gaussian to account for asymmetries in the profile. Grating SRFs are shown in figure 4.8. The top of the figure shows two profiles at the short wavelength end (290 and 355 μm), the middle two were taken near the center of the band (393 and 419 μm), and the bottom two were taken at the long wavelength end (465 and 487 μm).

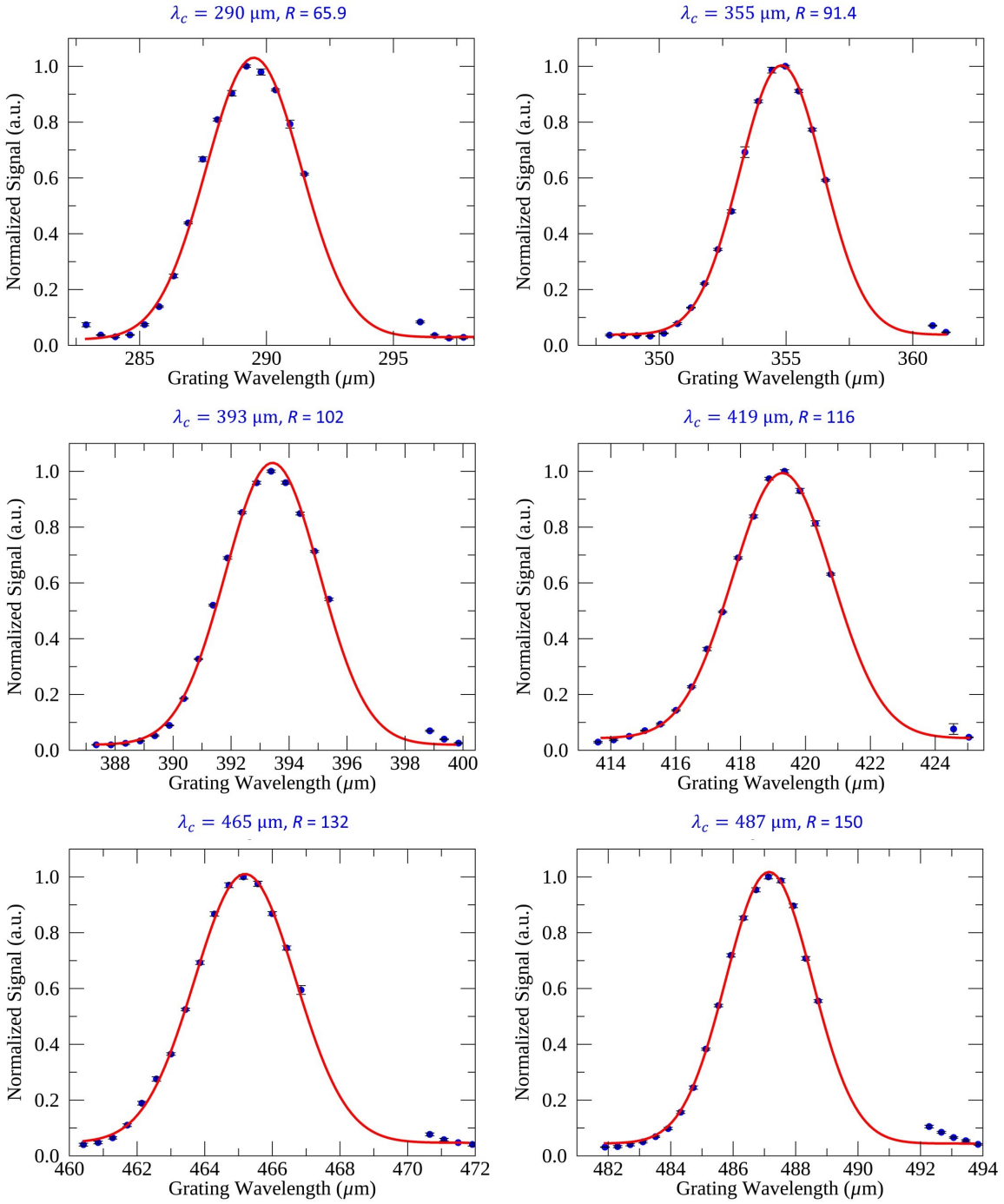

Figure 4.8: Normalized signal (blue points) and the best fit Gaussian profile (red curve). Vertical error bars (black) are calculated as the standard deviation of 250 measurements taken at each data point. Horizontal error bars (black) are too small to be seen as they represent the error in the determination of the photomixer wavelength. Measurements of the wavelength of the individual photomixer lasers yielded a typical uncertainty of $\pm$ 0.03 µm. The photomixer wavelength and measured resolving power are labeled above each plot.

4.2.2 Resolving Power

The σ_λ term extracted from fitting a Gaussian function to the grating SRF was used to determine the full-width-half-maximum, $\Delta\lambda$, of the grating profile:

$$\Delta\lambda = 2\sqrt{2\ln 2}\sigma_\lambda. \qquad [\mu m] \quad (4.10)$$

The resolving power, R, is then found by equation 2.46:

$$R = \frac{\lambda_c}{\Delta\lambda}. \qquad [1] \quad (4.11)$$

Figure 4.9 shows the resolving power measured by all grating SRFs across the wavelength range. The data were fitted with equation 4.11 to extract a multiplication factor between the theoretical curve and the data. The fit returned a factor of 0.88 which means the measured resolving power was 0.88 times the expected value. This lowered resolving power is likely due to several factors, one being the impact of stray light within the profiles which was discussed in the previous results. Additionally, the alignment was difficult to optimize and may have led to a reduced beam diameter incident on the grating. Stray light also had a clear impact on these results and may have led to a broadening of the profiles.

While this setup had significant advantages by incorporating a cryogenic slit, it was still not the most optimal configuration. The photomixer frequency could be measured with knowledge of the frequency of the two combining lasers, however, with these optics at room temperature there is contribution from thermal emission as well. Additionally, the blackbody source could not be used to characterize the spectral response of the grating which is necessary to verify the instrumental performance. Therefore, the optimal configuration includes a method to accurately measure the spectrum of incident radiation; something which an FTS is designed for. In preparation for the final measurements taken with the integrated post-dispersed room-temperature FTS and cryogenic entrance slit, the saddle supporting the grating was coated with the same epoxy-carborundum mixture as was used to coat the

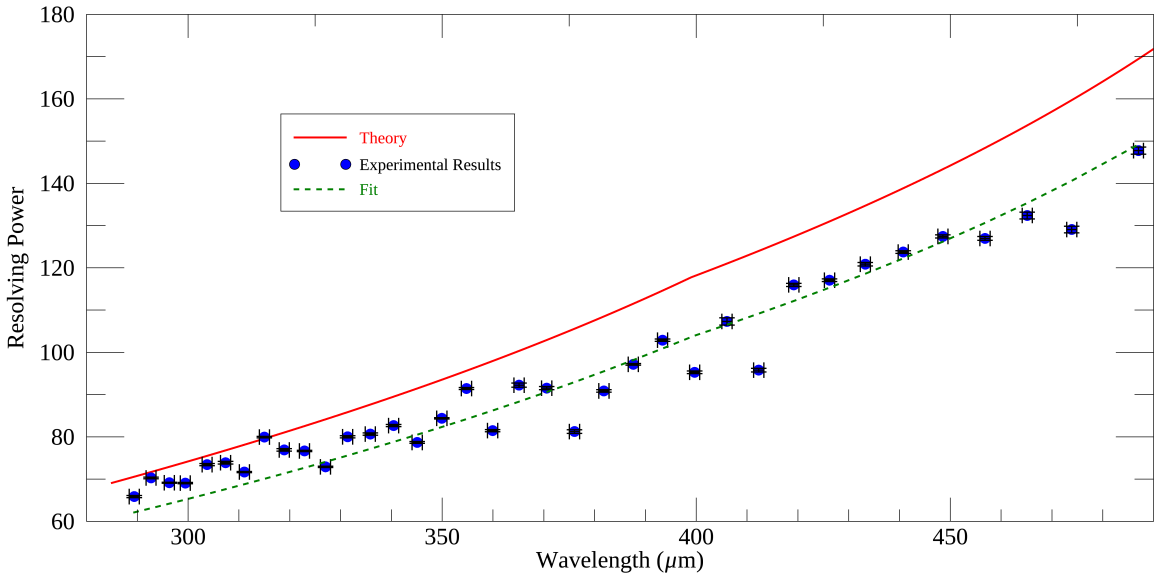

Figure 4.9: Experimental resolving power (blue) calculated from grating spectral response profiles. Error bars in the data are calculated from the errors in the standard deviation and center wavelength extracted from the Gaussian fit. The theoretical resolving power (red) is described by equation 2.50 and the data was fit (green) with the same equation to extract a multiplication factor. The fit returned a factor of 0.88 compared to theory.

inside of the grating enclosure [85]. The result is shown in figure 4.10. Care was taken to get as close to the edges of the saddle without having the carborundum mixture coated over the edge as to impinge on the incident beam. The epoxy-carborundum mixture has proven to effectively mitigate stray light and will make sure any reflections are less likely to reach the detector. Chapter 5 will detail the results of the grating spectrometer coupled to a room-temperature polarizing FTS in two configurations: a collimated output from the FTS sent directly into the grating spectrometer, and a focused output passing through a cryogenic entrance slit. Spectral response functions of the grating will be given in both configurations as well as a verification of the resolving power across the wavelength range of the grating and for different polarization of incident light. These measurements with be repeated with the blackbody source. In the final configuration incorporating the cryogenic entrance slit, I will present an efficiency analysis with the diffraction grating as a function of the wavelength and polarization of incident light.

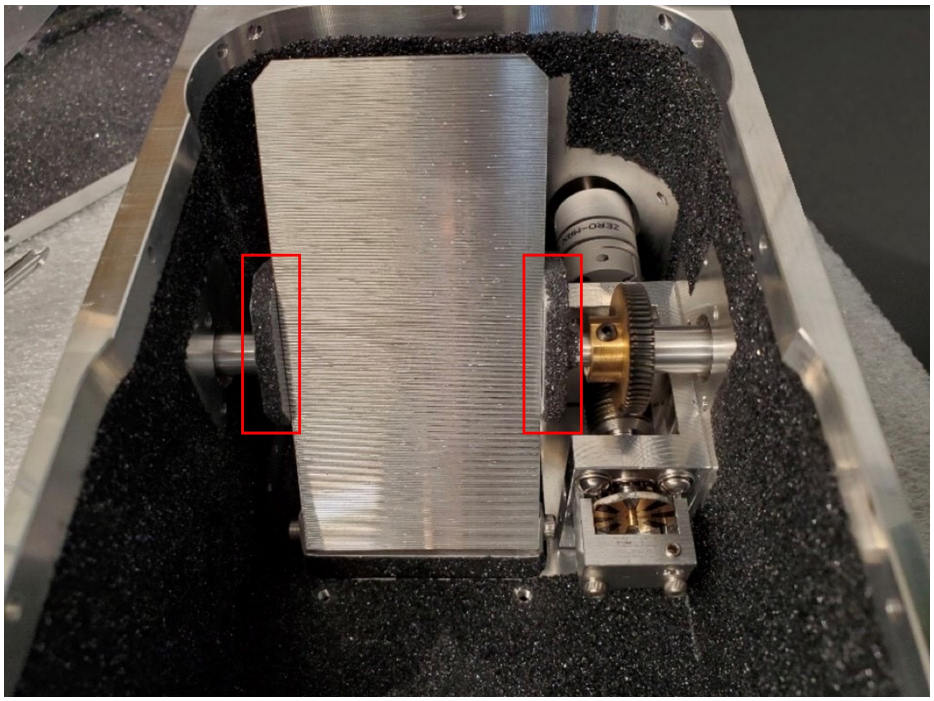

Figure 4.10: Image of the grating mounted in the enclosure after an epoxy-carborundum mixture was applied to the edges of the saddle (red boxes). This will help to reduce stray light reaching the detector.

Chapter 5

Post-dispersed Fourier Transform Spectrometer Results

> The good thing about science is that it's true whether or not you believe in it.
>
> NEIL DEGRASSE TYSON

There were three experimental configurations employed to measure the spectral response function of the grating spectrometer. The first configuration was described in Chapter 4 which was used to measure the response of the grating as an independent instrument. The results from the second and third optical configurations are presented in this chapter. Both of these setups incorporate the room-temperature polarizing Fourier transform spectrometer, FTS. The second configuration will be described first and was distinguished by outputting a collimated beam from the room-temperature FTS into the cryogenic grating spectrometer to simplify the alignment process. The third configuration replaced the exit optic of the FTS with a 90° off-axis parabolic mirror to input a focused beam through an entrance slit within the cryostat. The purpose of the slit is to define the throughput and resolution of the system and is, therefore, a key element in optimizing the performance of the grating. The grating spectral response was studied using a line source produced by a terahertz photomixer described in section 4.1 and a broadband continuum source produced by a heated filament. The final configuration allowed measurements of the diffraction efficiency of the grating as a function of wavelength and polarization which will be presented later in this chapter. Since the standard spectral unit of measurement for a diffraction grating is

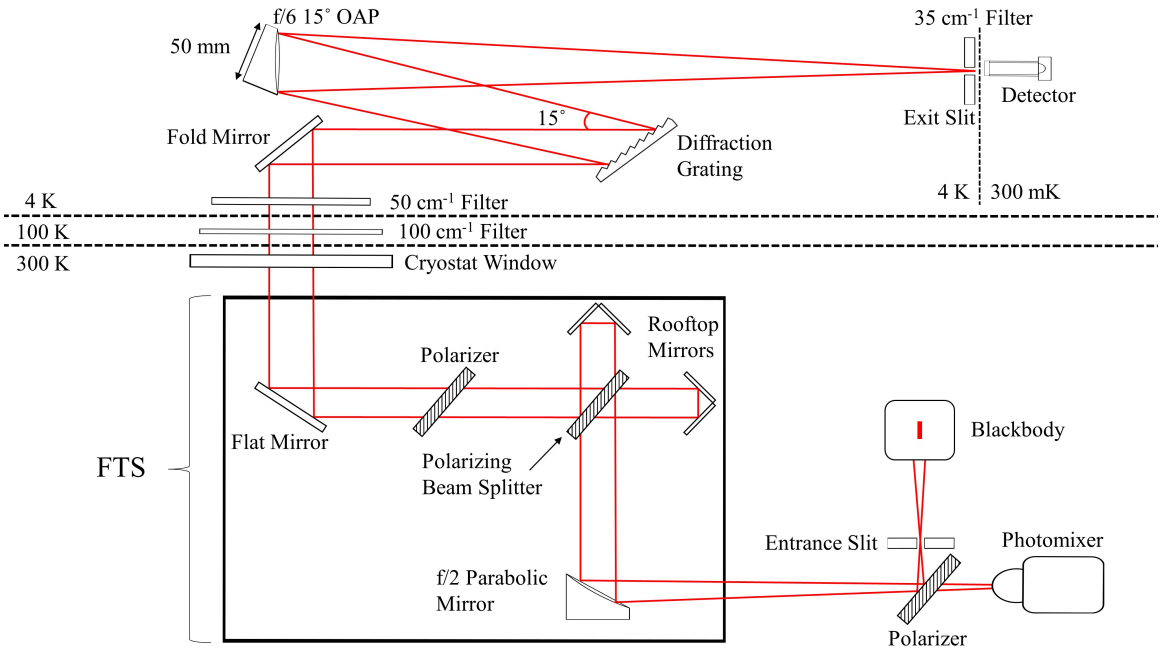

Figure 5.1: Diagram of configuration 2 showing the source module (photomixer line source and black body continuum source) coupled to the polarizing FTS which outputted a collimated beam into the grating spectrometer. The dashed lined barriers indicate the separation between room temperature (300 K) components, the cryogenic (4 K) grating assembly, and the 300 mK composite bolometer detector. Thermal filters are mounted to the 100 K, 4 K, grating, and detector shields with the purpose of defining the bandwidth of radiation seen by the detector.

wavelength (μm) while for the FTS it is wavenumber (cm^{-1}). To allow the reader to readily switch back and forth between the two spectral domains, the figures in this chapter will be presented in terms of both wavelength and wavenumber.

5.1 Configuration 2: PDPFTS Collimated Output

The second configuration used to measure the grating resolving power is detailed in figure 5.1. The FTS used in these measurements was a calibration FTS (cFTS) provided by Blue Sky Spectroscopy [73]. The specifications of the cFTS are described in Appendix C. The optical configuration of the instrument is a polarizing Martin Puplett interferometer shown schematically in figure C.2 with a maximum resolution of 0.032 cm^{-1}. The maximum circular beam diameter produced by the cFTS is 110 mm. In this configuration,

the grating receives the collimated beam directly from the cFTS without passing through a cryogenic entrance slit. The decision to omit the entrance slit was made to simplify the alignment process. An oversized collimated beam (110 mm beam into a 40 mm grating entrance aperture) is much less sensitive to misalignment than a beam focused onto a 5 mm wide slit. As discussed in Chapter 2, the spectrometer is designed to image light incident on the entrance slit onto the exit slit. From equation 2.50, the slit-width limited resolving power is proportional to the larger of the width of the entrance slit image, w', and the exit slit, w''. As described in section 4.1, the photomixer couples electromagnetic radiation into free space via a 100 μm strip-line bow-tie antenna. Taking the antenna to be the entrance slit and ignoring self-emission by the room temperature source, the system was assumed to be limited only by the width of the exit slit ($w' = 4.0$ mm $\gg$ 100 μm). This assumption did not account for the thermal emission from the hyper-hemispherical silicon lens of the photomixer and other auxiliary room temperature components, or contributions from atmospheric emission. However, the photomixer signal was found to dominate these contributions and they were deemed to be negligible.

The data collected with the FTS did not require the mechanical chopper or the SR830 lock-in-amplifier as in Chapter 4 because the translating rooftop mirror modulates the signal and this modulation encodes spectral information about the signal. The modulated signal, or interferogram, is measured by the detector and the resulting signal passes through a Stanford Research Systems SR560 — Low-noise voltage preamplifier [91]. The preamplifier filters the detector signal with a bandpass of $3 - 100$ Hz to reject $1/f$ noise. The gain factors at each stage are recorded so that the measured voltage can be compared with the actual signal incident on the detector. The DC output from the preamplifier is recorded using the same ADC [88] from the results in Chapter 4.

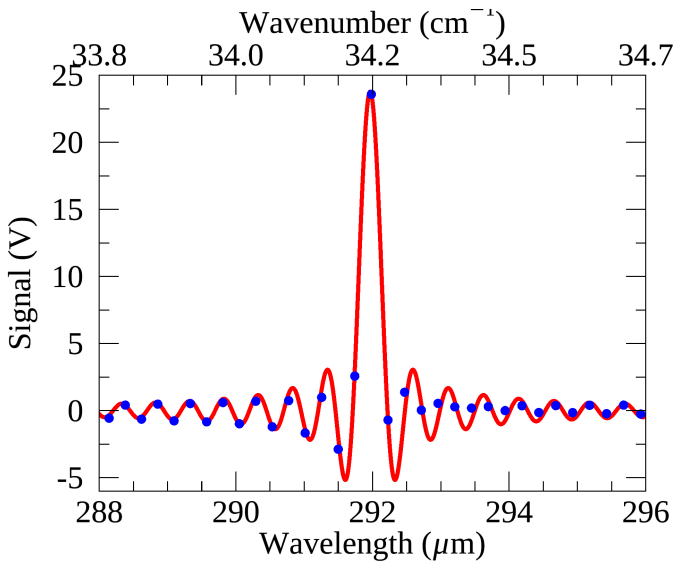

Figure 5.2: Spectrum measured with the FTS (blue points) and a sinc fit to the data (red curve). The photomixer was set to a wavelength of 292 µm (34.2 cm^{-1}). The sinc fit returned a value of 0.030 ± 0.0002 cm^{-1} for the full-width-half-maximum of the profile.

5.1.1 Photomixer Results

Spectral Response Functions

The results presented in this section were obtained using the second optical configuration; a collimated beam from the cFTS input directly into the grating spectrometer. The diffraction grating described in section 3.1 was mounted in a spectrometer enclosure designed by Veenendaal [64] because the monolithic grating enclosure was not yet complete. The grating spectrometer was operated at 4 K and was coupled to the evacuated ($<$ 10 mTorr) room temperature cFTS. The photomixer frequency (wavelength) was tuned across the grating band (285 - 500 µm; 35.1 - 20 cm^{-1}), by changing the difference frequency between the two direct feedback continuous-wave 1550 nm lasers illuminating the photomixer element 4.4. Similar to the results presented in section 4.2, the grating was scanned in 0.06° increments ($\sim$ 0.58 - $\sim$ 0.40 µm) around the corresponding photomixer wavelength to determine the spectral response function, SRF, of the grating. At each grating angular position, the FTS was scanned to produce a high resolution interferogram. Following the steps outlined in Appendix C, the interferogram data were processed and Fourier trans-

formed to return the measured spectrum. The spectrum was then fitted with a sinc function (the instrumental line shape of a FTS) to extract the photomixer wavelength and amplitude of the signal at each angular position. An example of the sinc fit and a measured spectrum is shown in figure 5.2. There was a strong agreement between the sinc fits and the data measured with the FTS which corresponded to a small uncertainty in the amplitude at each grating position. The wavelength of the photomixer, λ_{pm}, measured by the cFTS was used to calibrate the grating position as described in equation 4.8.

The calibrated angular position of the grating was converted to grating wavelength via the grating equation 2.41:

$$\begin{aligned} m\lambda &= 2d\cos(\phi/2)\sin(\theta-\phi/2) \\ \lambda &= 624\ \mu\text{m} \times \cos 7.5^\circ \sin(\theta - 7.5^\circ) \end{aligned} \qquad [\mu\text{m}] \quad (5.1)$$

This conversion is useful because it describes the SRF in terms of wavelength rather than the angular orientation of the grating. The wavelength-dependent grating SRF was fitted with the Gaussian function described in equation 4.9 to determine the center wavelength, λ_c, and the standard deviation, σ_λ, with a quadratic function added to account for asymmetries in the baseline. Since the signal amplitudes are arbitrary, the SRFs were normalized for ease of comparison. Some measured grating SRFs are shown in figure 5.3. The top two plots show profiles at the short wavelength end (285 and 349 μm; 35.1 and 28.7 cm^{-1}), the middle two were taken near the center of the band (393 and 426 μm; 25.4 and 23.5 cm^{-1}), and the bottom two were taken at the long wavelength end (449 and 502 μm; 22.3 and 19.9 cm^{-1}). A total of 14 SRFs were measured using this configuration and figure 5.4 shows all of them.

Resolving Power

The standard deviation, σ_λ, extracted from the grating SRF was used to determine the full-width-half-maximum, $\Delta\lambda$, of the grating profile. The resolving power, R, is then found

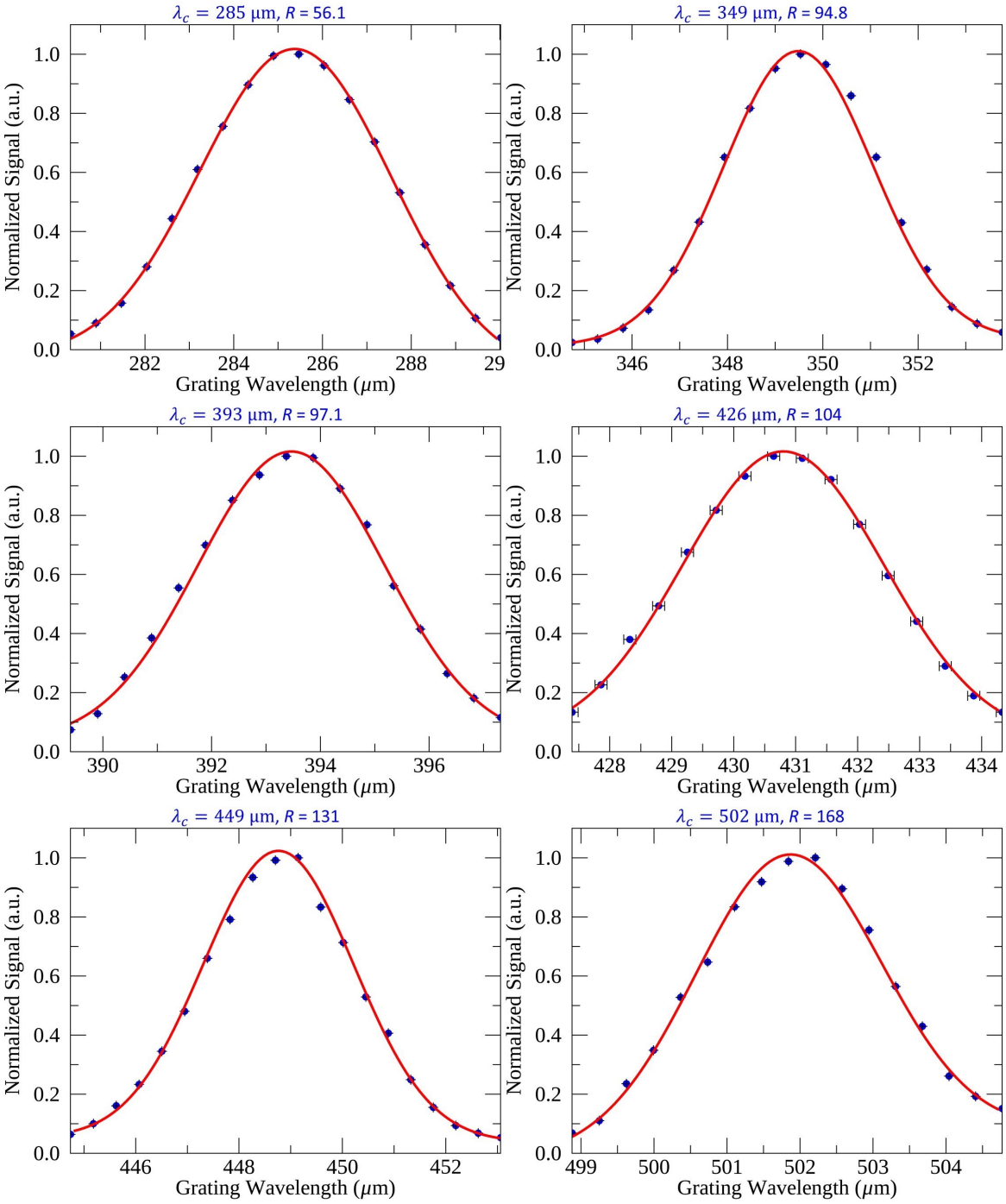

Figure 5.3: Normalized signal (blue points) and the best fit Gaussian profile (red curve). Vertical and horizontal error bars were determined from the error in the sinc fit to the FTS measured spectra. The photomixer wavelength and measured resolving power are labeled above each plot.

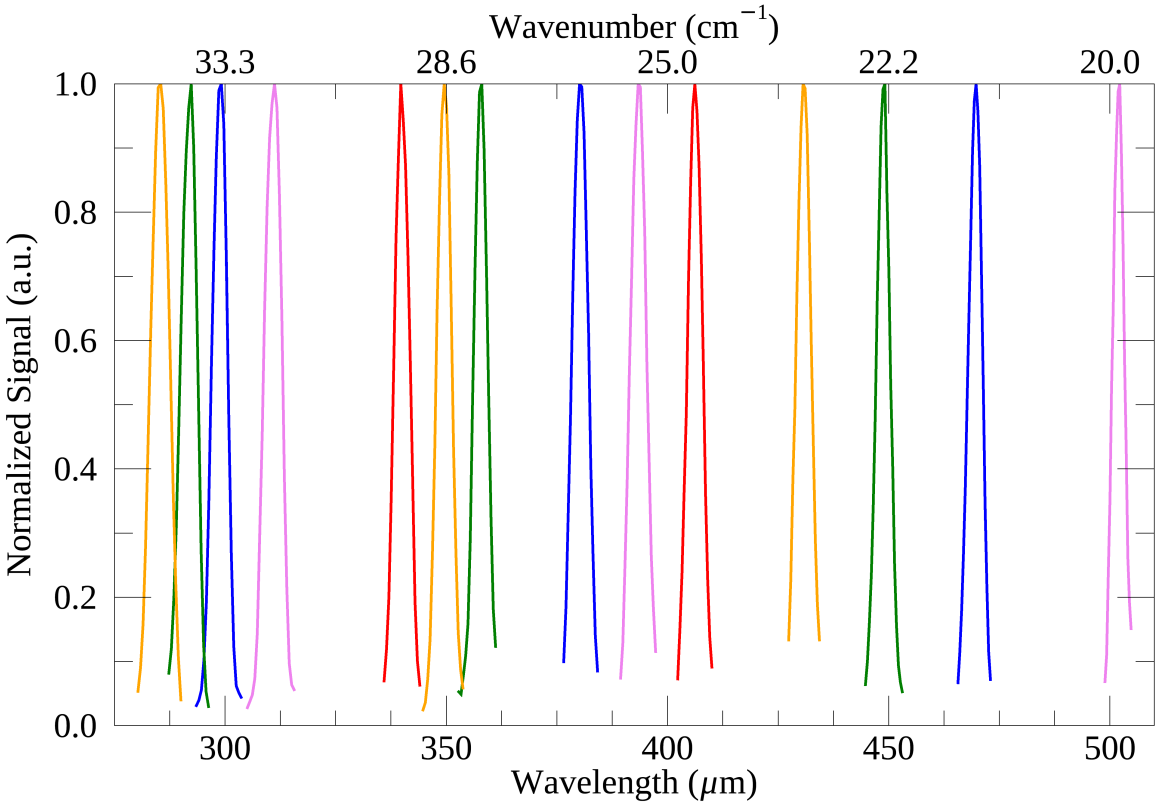

Figure 5.4: All normalized SRFs taken with configuration 1. The profiles show a clear narrowing from short to long wavelengths, which is expected.

by equation 4.11. Figure 5.5 shows the resolving power measured by all grating SRFs across the wavelength range. The theoretical curve shown in red is calculated using the slit-limited resolving power outlined in equation 2.50. The system is assumed to be completely dominated by the width of the exit slit, w', because the exit slit was much larger than the small emitting region of the THz antenna which acted as an entrance slit. The data were fitted with equation 2.50 to extract a multiplication factor between the theoretical curve and the measured data. The fit returned a factor of 0.88 which means the measured resolving power was 0.88 times the expected value. This lowered resolving power is likely due to several factors, one being the module which housed the diffraction grating had 40 mm windows as opposed to the 50 mm aperture designed in the new monolithic enclosure. The resolving power is inversely proportional to the groove spacing (proportional to the number of grooves) as shown in equation 2.50, so the decrease in beam size is expected

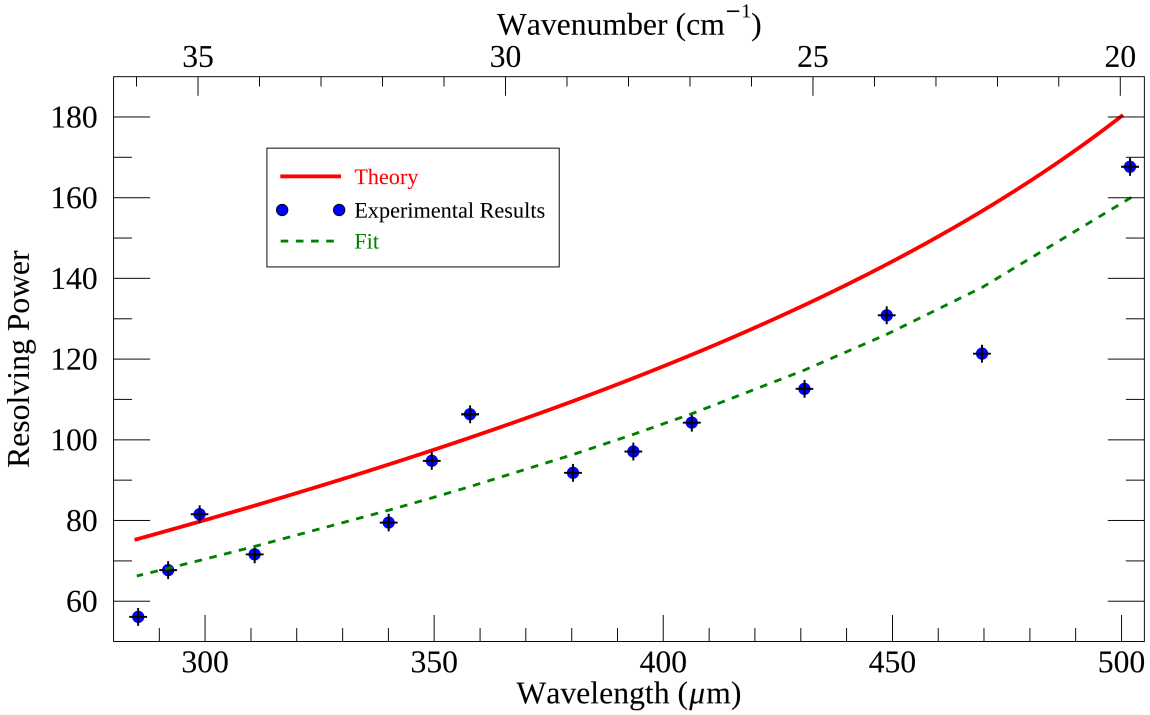

Figure 5.5: Experimental resolving power (blue) calculated from grating SRFs. Vertical and horizontal error bars are a combination of error in the the sinc fits to the FTS spectra and the Gaussian fit to the grating SRF. The theoretical resolving power (red) is described by equation 2.50 for the case of $w' > w''$ and the data were fitted with the same equation to extract a multiplication factor (green). The fit returned a factor of 0.88 compared to theory.

to lead to a decrease in resolving power. Additionally, this system did not incorporate a well-defined (cryogenic) entrance slit. Therefore, any thermal emission from the room-temperature optics is likely to contribute to the SRF and would be expected to broaden the profile. This was further confirmed in the blackbody results outlined below.

5.1.2 Blackbody Results

The results in this section were taken with the second optical configuration incorporating a heated filament source of the photomixer to measure the response of the grating with a broadband source. The blackbody used in these results is a Scitec IR-12 radiating element consisting of a coiled resistance wire which has a high emissivity at infrared wavelengths[81]. The element is mounted on an aluminum block creating a more uniform temperature which around $\sim$1200 K with an input power of 10 W at 5 V. The emissivity of

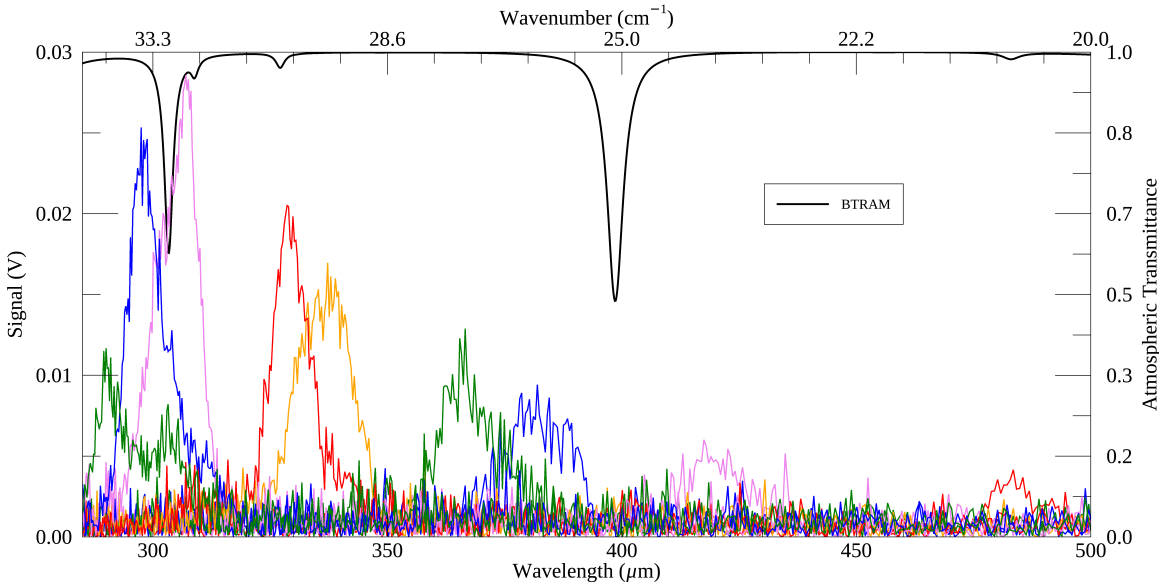

Figure 5.6: The grating scans (colored lines) correspond to an average of 5 FTS scans at different angular positions of the grating. An atmospheric model was generated using BTRAM v3 [73] and is superposed on the figure to show the location of absorption lines. It is immediately obvious that the grating profiles measured with the blackbody source are significantly broader than in figure 5.4 measured with the photomixer source.

the element is ∼0.8 and the heated area of the source is 3.5 mm x 3.5 mm which produces a sufficiently powerful source when coupled to the FTS. For these measurements, the grating was left stationary at an angular position and the cFTS was scanned 5 times. The scans were averaged to improve the signal to noise ratio. The averaged interferogram was analyzed using the methods outlined in Appendix C and a spectrum was returned. The angular position of the grating was then adjusted to view the grating spectral response at a different wavelength and the FTS measurement was repeated. The collection of measurements across the wavelength range of the grating are shown in figure 5.6. A transmission model was generated using the Blue Sky Spectroscopy Transmission and Radiance Atmospheric Model, BTRAM [73]. The parameters used in the model include an atmospheric path of 0.1 m which is the length of travel between the blackbody and the evacuated cFTS, a relative humidity of 25%, temperature of 21.8°C, and an atmospheric pressure of 1015 mBar. Within the spectral range of the grating, 285 - 500 µm (35.1 - 20.0 cm^{-1}), and with these atmospheric conditions, the only visible features are water vapour absorption lines.

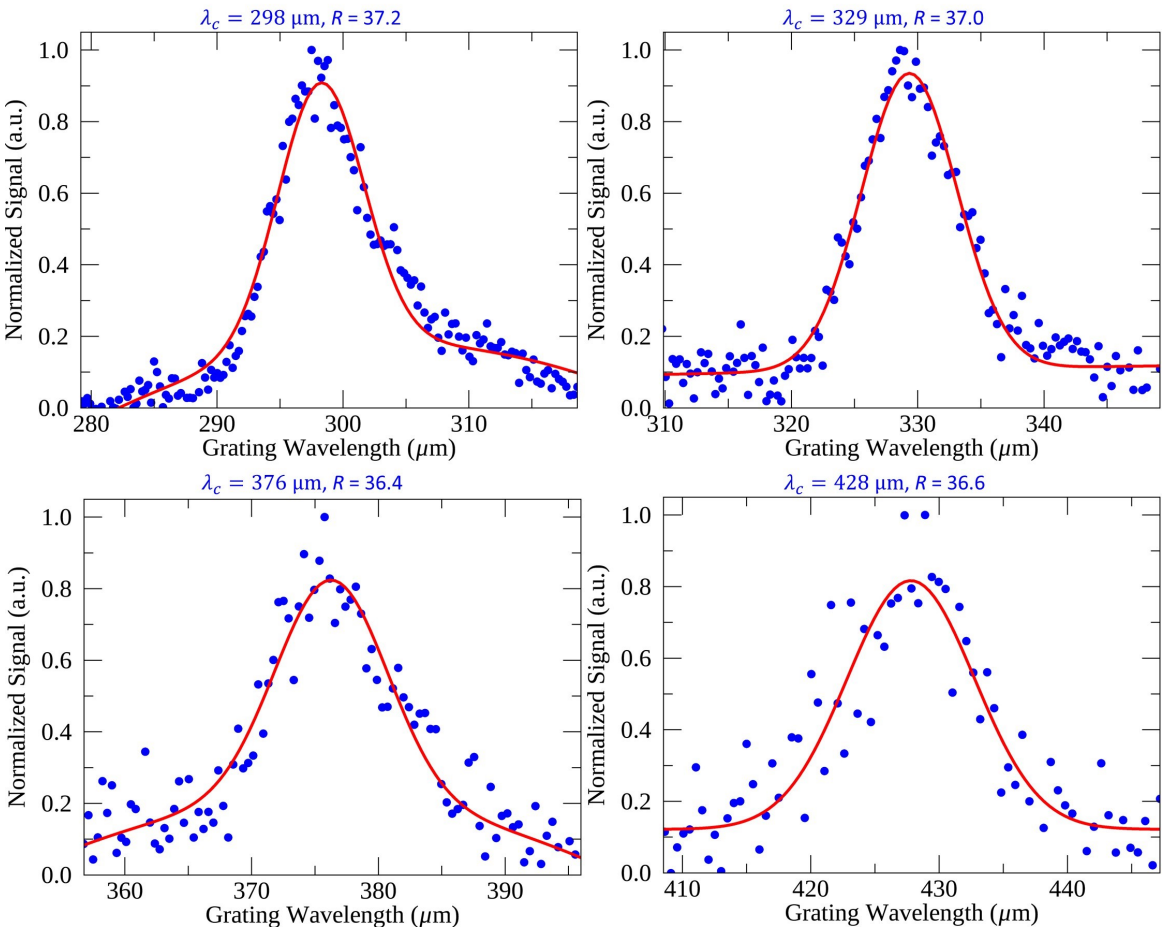

Figure 5.7: FTS measured data (blue points) and the best-fit Gaussian profile (red curve). The photomixer wavelength and measured resolving power are labeled above each plot.

The spectral response of the grating can be analyzed from the profiles shown in figure 5.6. Four of these scans are shown in figure 5.7 where the data are shown along with the best-fit Gaussian from equation 4.9. The top plots show the grating at a wavelength position centered at 298 µm (33.6 cm^{-1}) and 329 µm (30.4 cm^{-1}). The bottom two plots show the grating at a wavelength position centered at 376 µm (26.6 cm^{-1}) and 428 µm (23.4 cm^{-1}). The resolving power of each grating SRF measured with the blackbody source was calculated using equation 4.11. The calculated resolving power ranged from 23 - 44 across the band, significantly lower than the 69 - 180 expected from the slit-limited theoretical model. These values were also much less than what was measured using the photomixer source from figure 5.5. The disagreement between the data measured with the photomixer and that

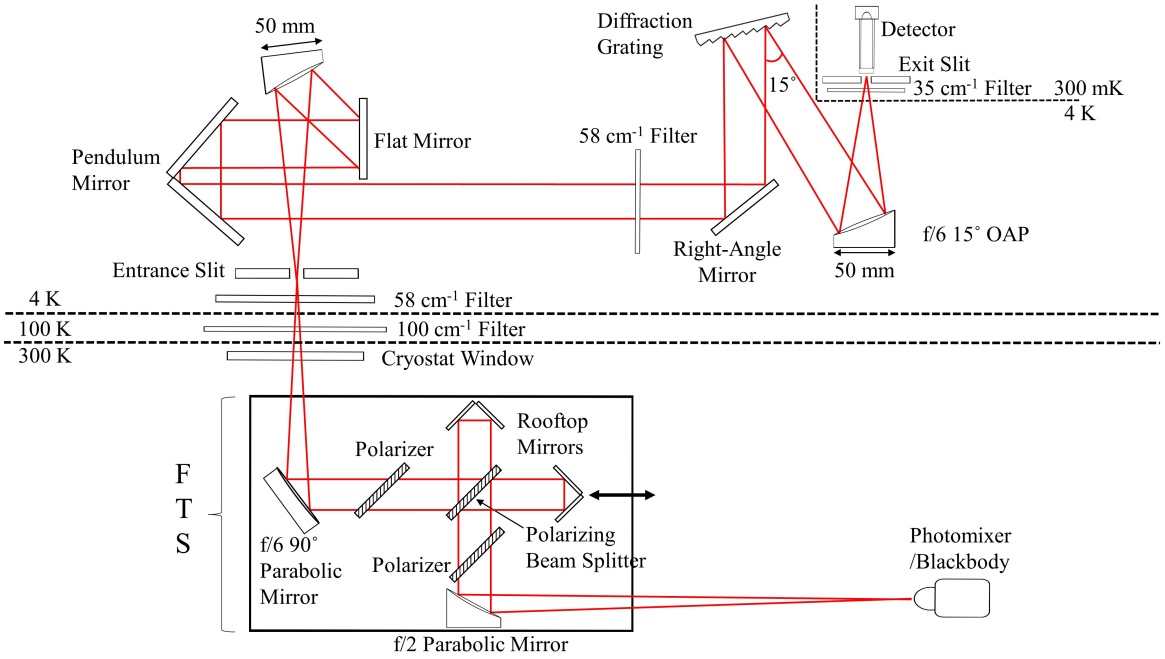

Figure 5.8: Diagram showing the third and final optical configuration used to accurately measure the slit-limited resolving power of the diffraction grating spectrometer as a post-dispersion module for the room temperature FTS. The output of the FTS was focused through the cryogenic entrance slit using a custom f/6 90° OAP. After passing through the slit, the divergent beam was collimated by a f/6 15° OAP, reflected by a flat mirror towards a pendulum mirror, and passed into the grating spectrometer.

measured with the blackbody indicates the system is limited by the room-temperature entrance slit. The blackbody is expected to be impacted more than the photomixer because the size of the emitter is larger: 3.5 mm x 3.5 mm vs. the 100 µm strip-line antenna. These results clearly indicate that the omission of a cryogenic entrance slit significantly reduces the resolving power of the grating. In the final design, a cryogenic entrance slit was employed to properly measure the spectral response of the grating. Additionally, the new monolithic module was employed and a high-resolution modification was made to the cFTS.

5.2 Configuration 3: PDPFTS Cryogenic Slit

A diagram of the third and final optical configuration is shown in figure 5.8. The cryogenic components are the same as shown in figure 3.17, however, this configuration passes light from the cFTS into the cryogenic slit to attain the most optimal experiment. The cFTS

was upgraded between the measurements with the collimated FTS output to the measurements discussed in this section. The length of the linear translation stage was increased by a factor of 2 from 62.5 cm to 125 cm. The new stage provides the cFTS with a maximum resolution of 0.016 cm^{-1}. However, due to memory limitations in the data acquisiton software, the travel of the stage was limited to 100 cm corresponding to a maximum resolution of 0.020 cm^{-1}. The final configuration was also the first to incorporate the flat mirror mounted to the back of the grating to enable efficiency measurements. When the mirror is inserted into the optical path, a scan of the cFTS measures the spectrum of the entire band and can be used to calibrate the efficiency of the grating as a function of wavelength. As mentioned in section 2.5, this is a complicated function to model. Experimental results will be presented and compared with models that were available to me.

5.2.1 Photomixer Results

Grating SRFs were measured with the photomixer source repeating the same procedure as the results above. However, these measurements incorporated the new diffraction grating module, the cryogenic entrance slit, and the high-resolution addition to the cFTS. As discussed in section 5.1, grating SRFs were measured by scanning the grating in 0.06° increments around the corresponding photomixer wavelength. At each increment of the grating, the cFTS was scanned to obtain an interferogram which was processed to return the transformed spectrum. A sinc function was fitted to the FTS measured spectrum as shown in figure 5.9 to extract the center wavelength and amplitude of the signal at each grating position. The center wavelength measured by the cFTS was used to calibrate the grating position as described in equation 4.8. Compared to figure 5.2, the profile of this sinc is clearly more narrow, 0.017 ± 0.00006 cm^{-1} with the new FTS data vs. 0.030 ± 0.0002 cm^{-1} with the previous data as expected. Higher resolution in the FTS measurements gives more spectral information in each scan which will help to determine the spectral response of the grating with more accuracy. SRFs were measured across the wavelength range of

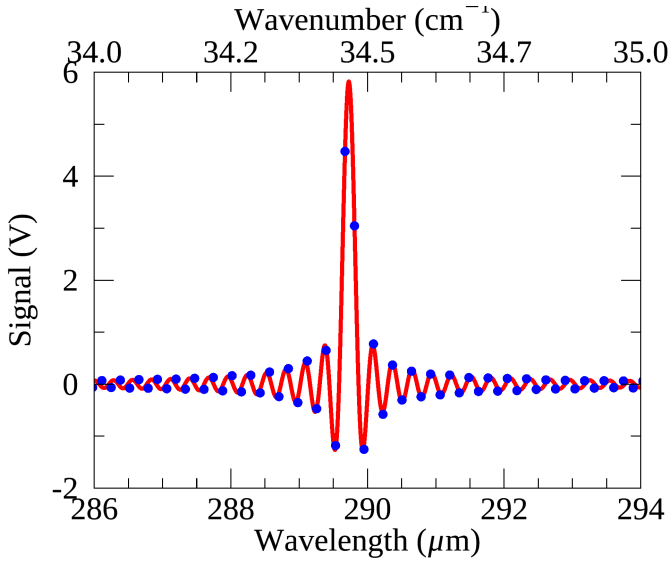

Figure 5.9: Spectrum measured with the cFTS (blue points) and a sinc fit to the data (red curve). The photomixer was set to a wavelength of 290 µm (34.5 cm^{-1}). The sinc fit returned a value of 0.017 ± 0.00006 cm^{-1} for the full-width-half-maximum of the profile.

the grating and the measurements were repeated with the output polarization of the cFTS oriented perpendicular (s-polarized) and parallel (p-polarized) to the grooves of the grating.

P-Polarization

The results presented here were obtained with the output polarization of the cFTS oriented parallel to the grooves of the diffraction grating. As was discussed in Chapter 2, the parallel polarization, or p-polarization state, is expected to be less efficient than the perpendicular, s-polarization. However, the SRFs are not expected to be impacted by the polarization state, except for a possible change in diffracted amplitude. Grating SRFs were measured across the wavelength range as shown in figure 5.10. The top two profiles show data collected with the photomixer set to a wavelength of 290 µm (34.5 cm^{-1}) and 308 µm (32.5 cm^{-1}), the middle two were taken at 341 µm (29.3 cm^{-1}) and 388 µm (25.8 cm^{-1}), and the bottom two were taken at 449 µm (22.3 cm^{-1}) and 483 µm (20.7 cm^{-1}). The resolving power for each SRF was calculated using equation 4.11 and the measured value for each profile is shown above in figure 5.10. There were a total of 19 grating SRFs taken across the wavelength range of the grating and they are all shown in figure 5.11. As was discussed in

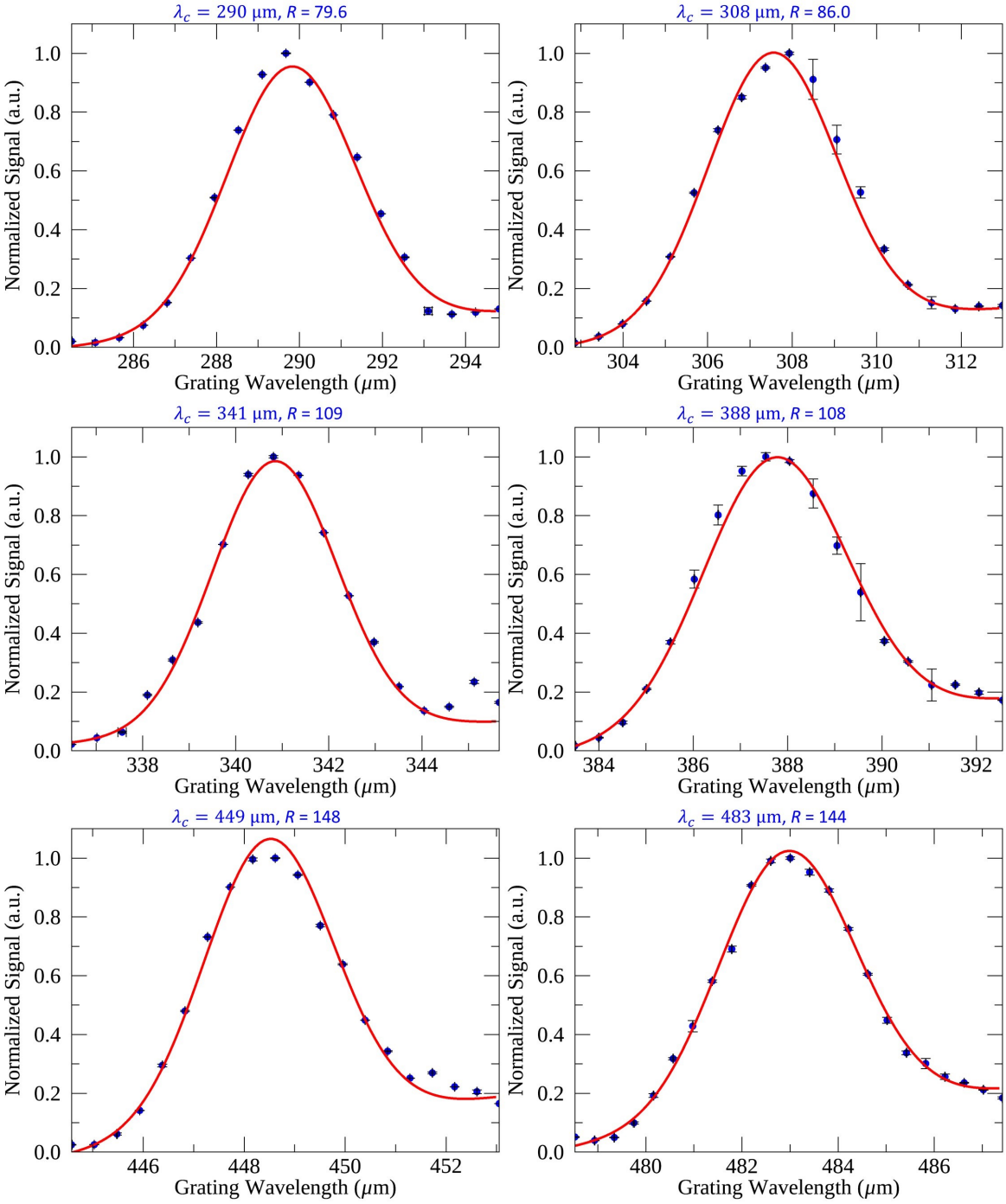

Figure 5.10: Normalized signal (blue points) and the best fit Gaussian profile (red curve). Vertical and horizontal error bars were determined from the error in the sinc fit to the FTS measured spectra. The data were measured with the output polarization of the FTS configured parallel to the grating grooves (p-polarized) and the photomixer wavelength and measured resolving power are labeled above each plot.

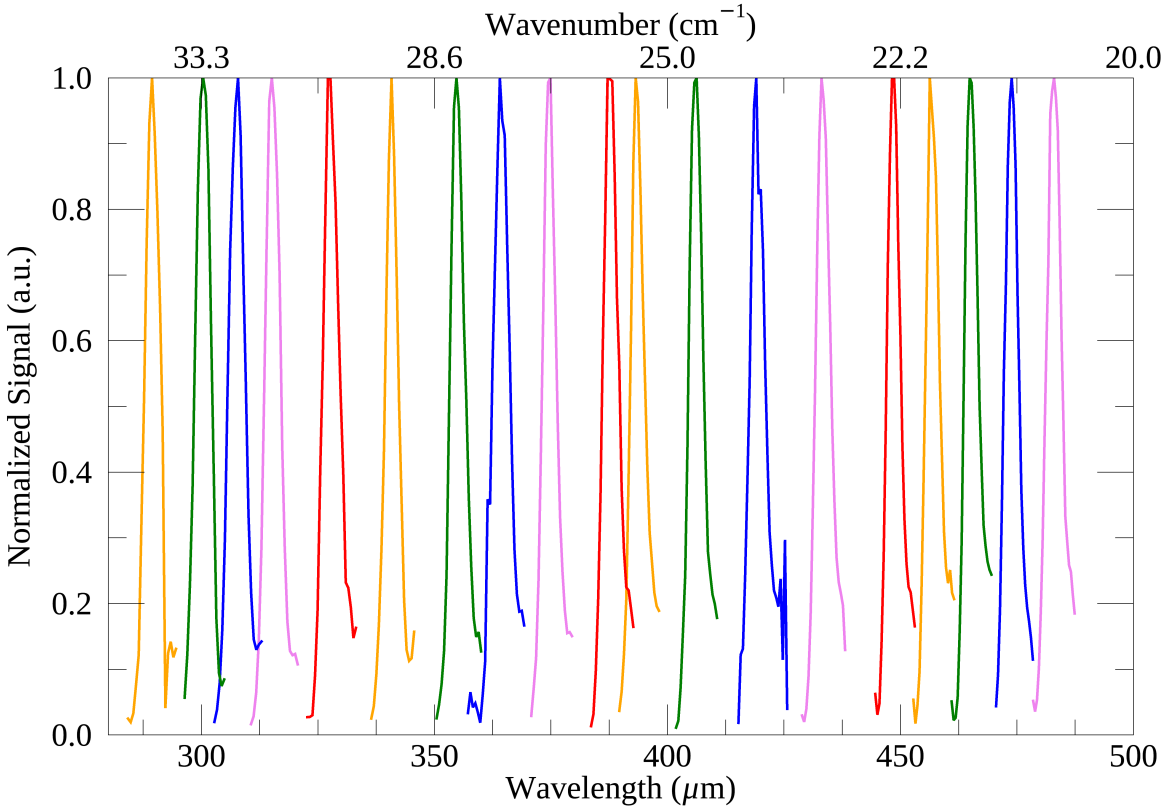

Figure 5.11: All normalized grating SRFs taken with the photomixer source. The data were measured with the output polarization of the FTS configured parallel to the grating grooves (p-polarized). The profiles show a slight narrowing with increase in wavelength which is expected.

the results of Chapter 4, there were some issues with stray light appearing as a bump on the side of the grating profiles. It can be seen in figure 5.11 that these effects are still present, although the amount of stray light has been decreased. The epoxy-carborundum mixture applied to the edges of the saddle was impactful in reducing the stray light, however, was not abe to completely eliminate it. Therefore, a method to restrict the width of the beam is necessary to further reduce the stray reflections.

S-Polarization

The grating SRF measurements were repeated with the cFTS polarization oriented perpendicular (s-polarized) to the grooves of the grating. The s-polarization state is expected to produce a higher diffraction efficiency than with p-polarized light, however the grating

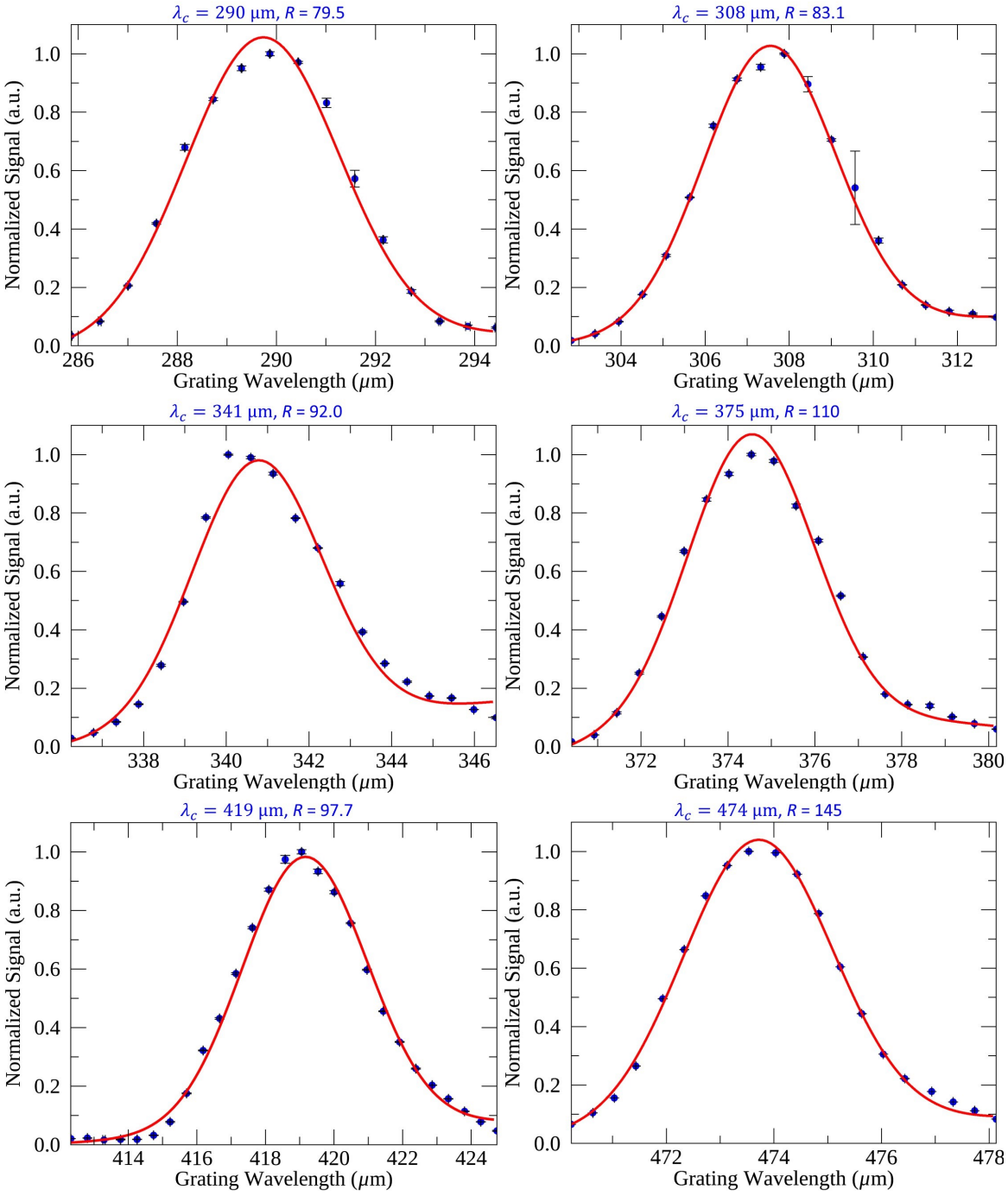

Figure 5.12: Normalized signal (blue points) and the best fit Gaussian profile (red curve). Vertical and horizontal error bars were determined from the error in the sinc fit to the FTS measured spectra. The data were measured with the output polarization of the FTS configured perpendicular to the grating grooves (s-polarized) and the photomixer wavelength and measured resolving power are labeled above each plot.

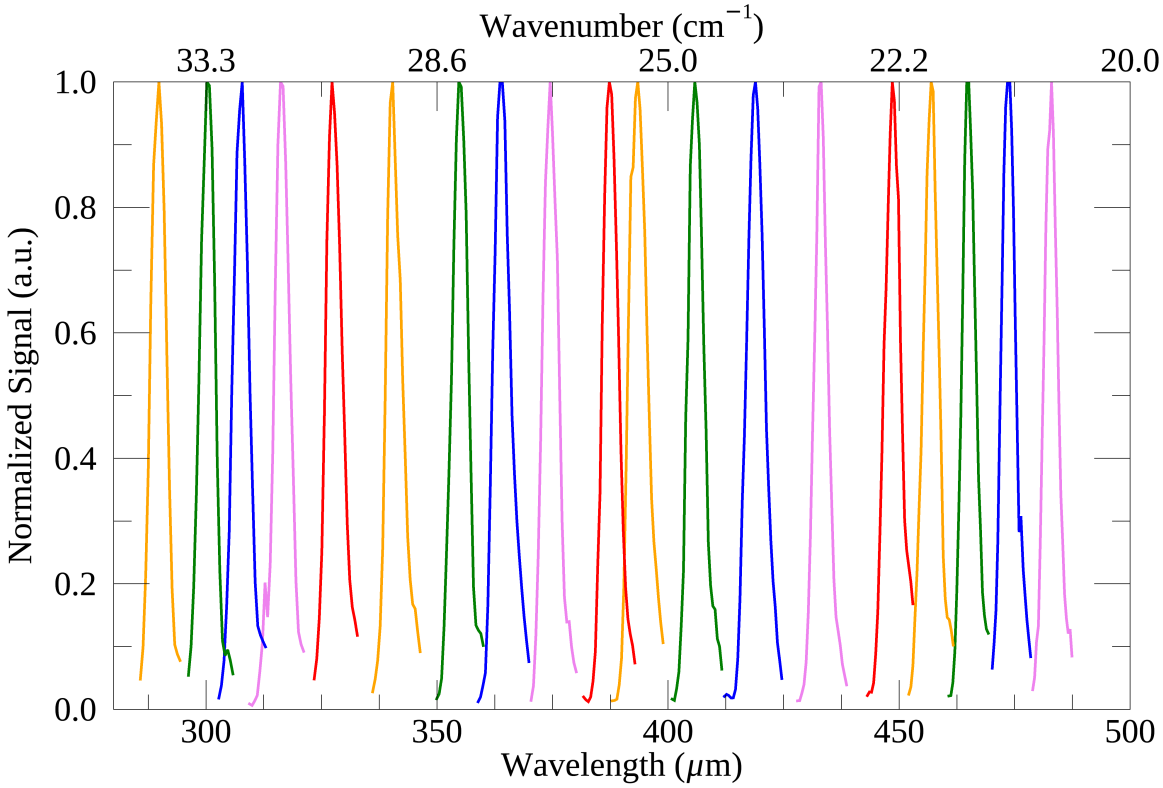

Figure 5.13: All normalized grating SRFs taken with the photomixer source. The data were measured with the output polarization of the FTS configured perpendicular to the grating grooves (s-polarized).

SRF is not expected to change. The SRFs measured across the wavelength range are shown in figure 5.12. The top two profiles show data collected with the photomixer set to a wavelength of 290 µm (34.5 cm^{-1}) and 308 µm (32.5 cm^{-1}), the middle two were taken at 341 µm (29.3 cm^{-1}) and 375 µm (26.7 cm^{-1}), and the bottom two were taken at 419 µm (23.9 cm^{-1}) and 474 µm (21.1 cm^{-1}). The measured resolving power calculated from equation 4.11 is shown above each profile. Grating SRFs were taken with the same photomixer settings as in the p-polarized results and the 19 measured profiles are shown in figure 5.13. Bumps on the side of the grating profiles indicated stray light was also present in these results. The resolving power was measured for each grating SRF and will be discussed after the next section presenting the measurements with the broadband input.

5.2.2 Blackbody Results: FTS in Atmosphere

A significant advantage to the final optical configuration is the incorporation of the cryogenic entrance slit with the high-resolution FTS. As was shown in the previous results, using broadband input without the entrance slit resulted in broad grating spectral profiles. Now that the input radiation is constrained by the entrance slit, a broadband source should produce much more narrow grating profiles with a slit-limited resolving power predicted by equation 2.50. Continuum emission was produced by a commercially available silicon carbide, SiC, igniter with a rectangular element which achieves an emissivity > 0.7 at infrared wavelengths [82]. For the blackbody measurements, the SiC igniter was placed at the input to the cFTS and was operated at a temperature of $\sim$1500 K. When the mirror on the back of the grating is in line with the incident beam, a scan of the cFTS is used to obtain a measurement of the entire spectrum. Figure 5.14 shows three separate cFTS scans with the mirror in the optical path and the output of the cFTS p-polarized. Each scan was taken a few hours apart and the system response did not vary much, therefore, a single scan could be used to calibrate the efficiency of the grating. An atmospheric model was generated using BTRAM v3[73] and is added to the figure to show the location of absorption features. The atmospheric path length was estimated to be around 2 m because the cFTS was not evacuated for these measurements. Later in this chapter, some blackbody measurements were repeated with the FTS evacuated. As was discussed in Chapter 1, blackbody emission follows Planck's Law as outlined in equation 1.1. However, at long wavelengths, the emission follows the Rayleigh-Jeans law:

$$B_\nu(T) = \frac{2\nu^2 k_B T}{c^2}, \qquad [\mathrm{W\,m^{-2}\,Hz^{-1}\,sr^{-1}}] \quad (5.2)$$

where ν is the freqeuncy of radiation, k_B is the Boltzmann constant, T is the temperature of the blackbody, and c is the speed of light. Thus, the atmospheric model is multiplied by ν^2 and normalized to better represent the data in figure 5.14. The sharp drop in signal

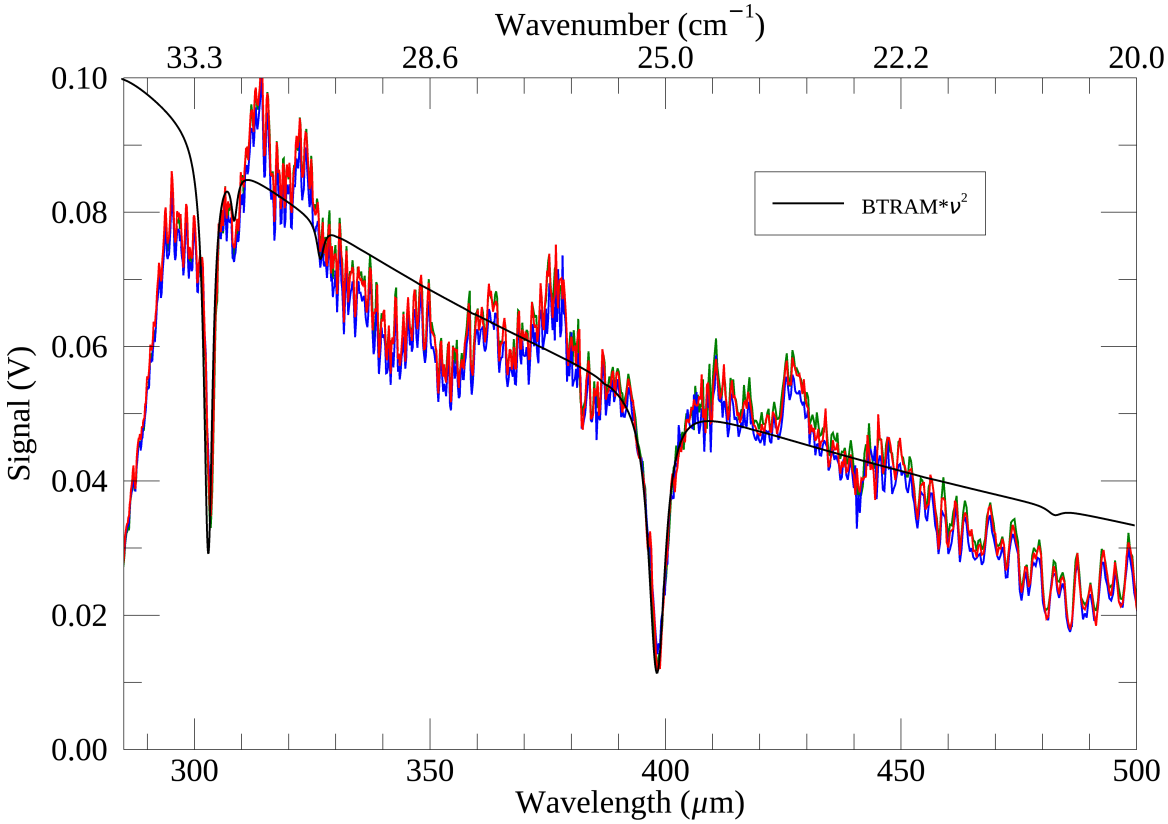

Figure 5.14: cFTS scans with the grating flat mirror in line with the optical path showing the entire spectrum of radiation. An atmospheric model was generated using BTRAM v3 [73] and was multiplied by ν^2 to incorporate the blackbody emission relationship given in equation 5.2.

around 300 µm (33.3 cm^{-1}) corresponds to the 285 µm (35 cm^{-1}) cutoff frequency of the filter mounted on the face of the detector which is necessary to order sort the grating and deload the detector.

With the output of the cFTS oriented p-polarized, the grating was rotated into the optical path and several scans were taken around the absorption feature at 398 µm (25.1 cm^{-1}) as shown in figure 5.15. To measure each profile, the grating was rotated into a position around the feature and then remained stationary. The cFTS was scanned 10 times and the interferograms were averaged. The interferograms were averaged and transformed into a spectrum and compared with the atmospheric model in figure 5.15. The atmosphere clearly has an impact on the grating profiles which shows that the spectrometer is encoding accurate spectral information. The next sections will present the blackbody measurements

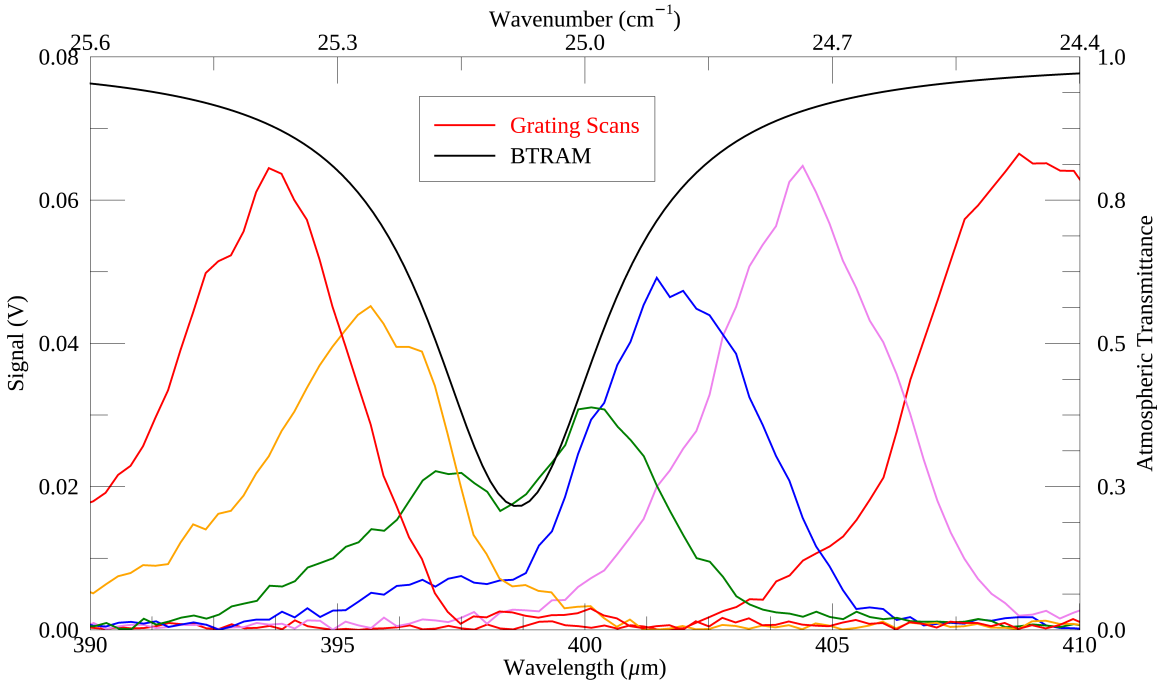

Figure 5.15: cFTS scans with the grating positioned around the atmospheric absorption feature at 398 µm (25.1 cm^{-1})

taken across the entire range of the grating for s-polarized and p-polarized light.

P-Polarization

The results continue with the output polarization of the cFTS oriented p-polarized. The grating was rotated in angular positions across the wavelength range and at each position the cFTS was scanned 10 times. The 10 interferograms at each point were averaged and the Fourier transform was taken to return the spectrum at each point. The power spectra corresponding to the grating SRFs along the band are shown in figure 5.16. Closer inspection of the profiles show some asymmetries which could originate from phase errors in the interferogram induced by instrumental imperfections in the cFTS. Normally, the phase of an interferogram is corrected to produce a real signal in the transformed spectrum [84]. However, the grating profiles were extremely narrow and there were not enough data points in the grating spectral band to extract phase information. In principal, it is possible to combine phase information from adjacent spectral bands of the grating to establish a more

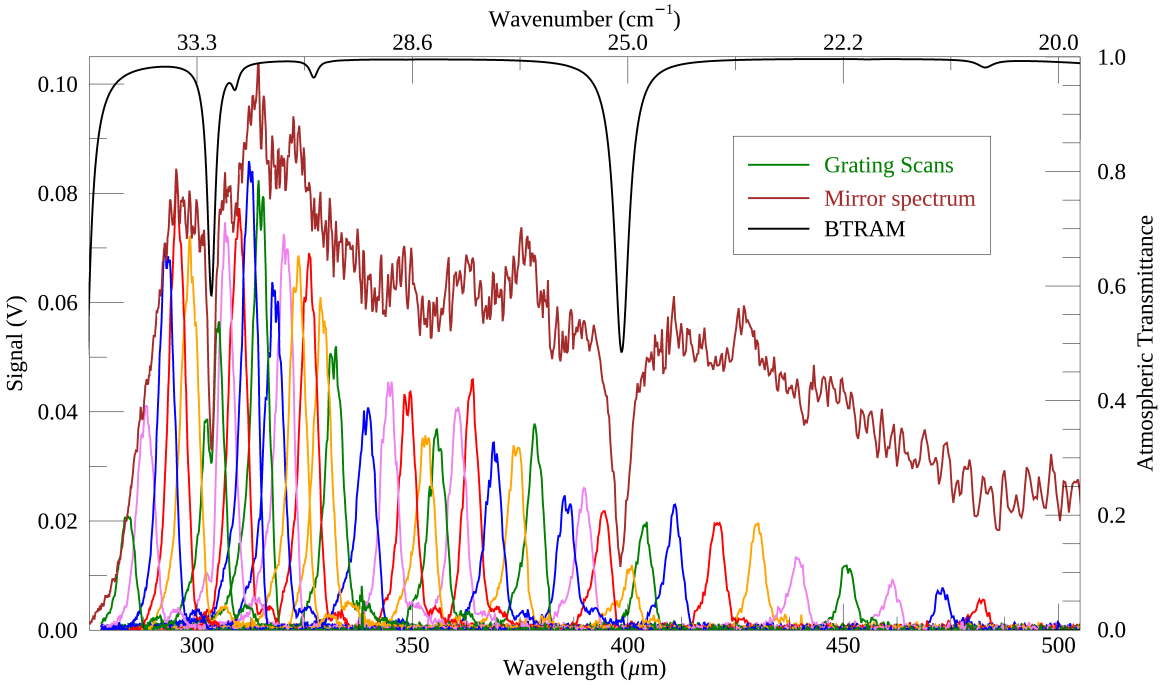

Figure 5.16: The grating scans (colored lines) correspond to all FTS scans measured with the blackbody source at different angular positions of the grating. An FTS measurement of the entire band (black) was taken with the flat mirror in place of the grating. The data were measured with the output polarization of the FTS configured parallel to the grating grooves (p-polarized).

robust phase correction since the phase of the FTS is independent of the grating. However, the processing code required to do this was not fully developed. Without phase correction, the overall line shape of the grating profiles as measured by the cFTS should not be over-interpreted until they are properly processed in future work. It is still useful to measure the resolving power of the SRFs measured with the blackbody to assess the grating performance with the first results.

A closer view of six grating SRFs measured with the blackbody source are shown in figure 5.17. The top two profiles show data collected with the photomixer set to a wavelength of 293 µm (34.1 cm^{-1}) and 326 µm (30.7 cm^{-1}), the middle two were taken at 364 µm (27.5cm^{-1}) and 404 µm (24.8 cm^{-1}), and the bottom two were taken at 431 µm (23.2 cm^{-1}) and 485 µm (20.6 cm^{-1}). The measured resolving power calculated from equation 4.11 is shown above each profile. Unlike with the blackbody results from configuration

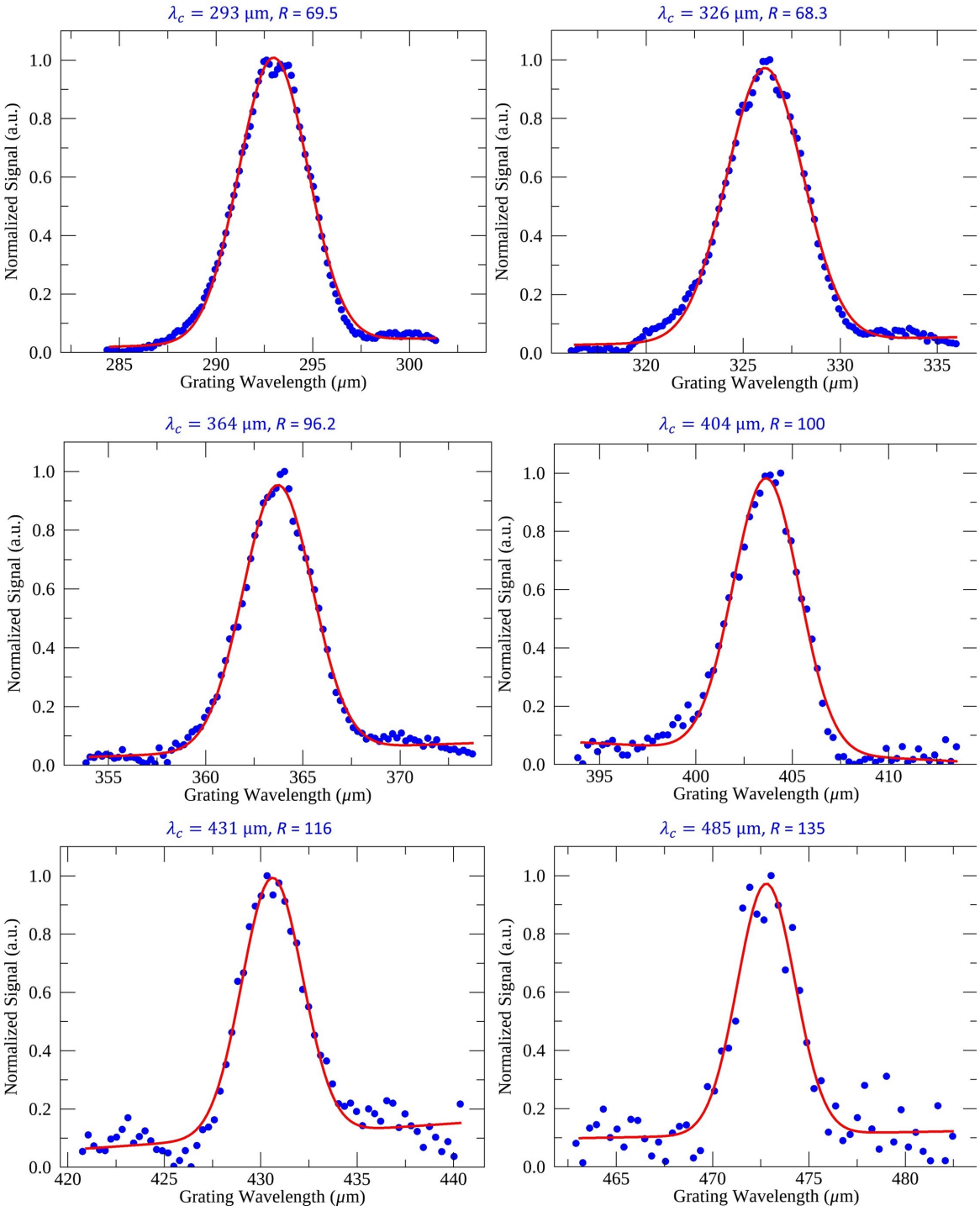

Figure 5.17: FTS measured data (blue points) and the best-fit Gaussian profile (red curve). The data were measured with the output polarization of the FTS configured parallel to the grating grooves (p-polarized and the photomixer wavelength and measured resolving power are labeled above each plot.

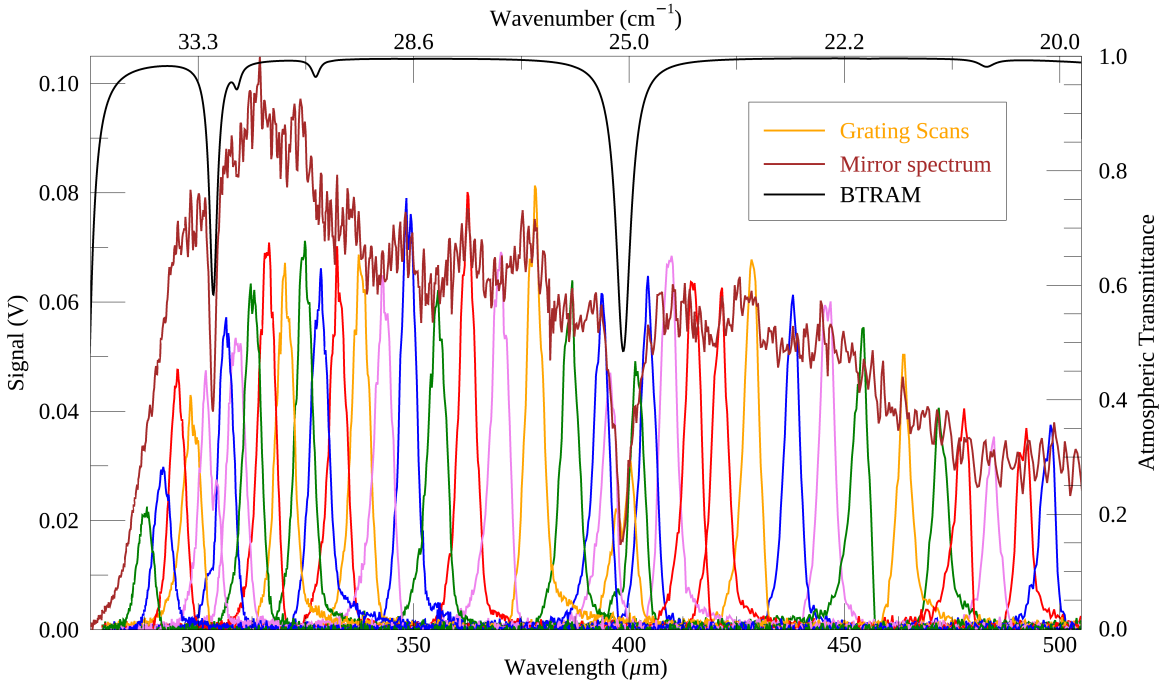

Figure 5.18: The grating scans (colored lines) correspond to all FTS scans measured with the blackbody source at different angular positions of the grating. An FTS measurement of the entire band (black) was taken with the flat mirror in place of the grating. The data were measured with the output polarization of the FTS configured perpendicular to the grating grooves (s-polarized).

2 which returned resolving powers around 20 - 40, these profiles are much more narrow and achieves the target resolving power of $R = 100$ near 392.5 µm. It is evident that the cryogenic entrance slit is restricting the path of the radiation and the results have shown a significant improvement over the previous configuration. The next section will present the grating SRFs measured with the blackbody source with s-polarized light.

S-Polarization

The blackbody measurements were repeated with the cFTS output s-polarized. The power spectra measured by the FTS at all grating positions across the band are shown in figure 5.18 along with the spectrum measured with the flat mirror. It can be seen in these measurements that the signal measured by the grating exceeds the signal measured with the mirror. As was mentioned in Chapter 3, there is an expected signal drop of $\sim 93\%$ due to the mirror being offset from the plane of the grating. The main factor impacting the data

is expected to come from the nonlinear response of the detector. When the flat mirror is in the optical path, radiation from across the entire spectral band is incident on the detector and produces a significant heat load within the bolometer element. Contrastingly, when the grating is in the path, the signal is only a narrow band of the entire spectrum. Like all bolometer detectors, the response is a function of radiant loading and will be different when viewing the entire spectral band compared with viewing a filtered section of the band [72]. In some cases, a gain factor of 2 has been seen in the responsivity between the narrowband and broadband input. Therefore, this non-linearity is impacting the absolute determination of the signal amplitude with the mirror in path compared with the grating in path. The exact change in responsivity can be measured by changing the power emitted by the blackbody source by a known amount, e.g. changing the temperature of the heated element, and recording the change in signal amplitude with the grating in the path compared to with the mirror in path. However, due to time constraints, this test was not completed so the grating and mirror signal amplitudes should be considered as relative measurements with an unknown gain factor. It is expected that the small change in amplitude between successive grating profiles is insufficient to produce non-linear effects in the detector. Thus, the responsivity of the detector is expected to be constant between grating measurements so that the overall trend in efficiency is representative of the true data by a multiplicative factor.

Grating SRFs with s-polarized light are detailed in figure 5.19. The top two profiles show data collected with the photomixer set to a wavelength of 292 μm (34.1 cm^{-1}) and 316 μm (31.6 cm^{-1}), the middle two were taken at 343 μm (29.2 cm^{-1}) and 366 μm (27.3 cm^{-1}), and the bottom two were taken at 438 μm (22.8 cm^{-1}) and 485 μm (20.6 cm^{-1}). The measured resolving power calculated from equation 4.11 is shown above each profile. The signal to noise ratio on the measurements at longer wavelengths were seen to be greater than the p-polarized data because the diffraction efficiency was much higher. The next section will compare the measured resolving power from the photomixer data to the blackbody data

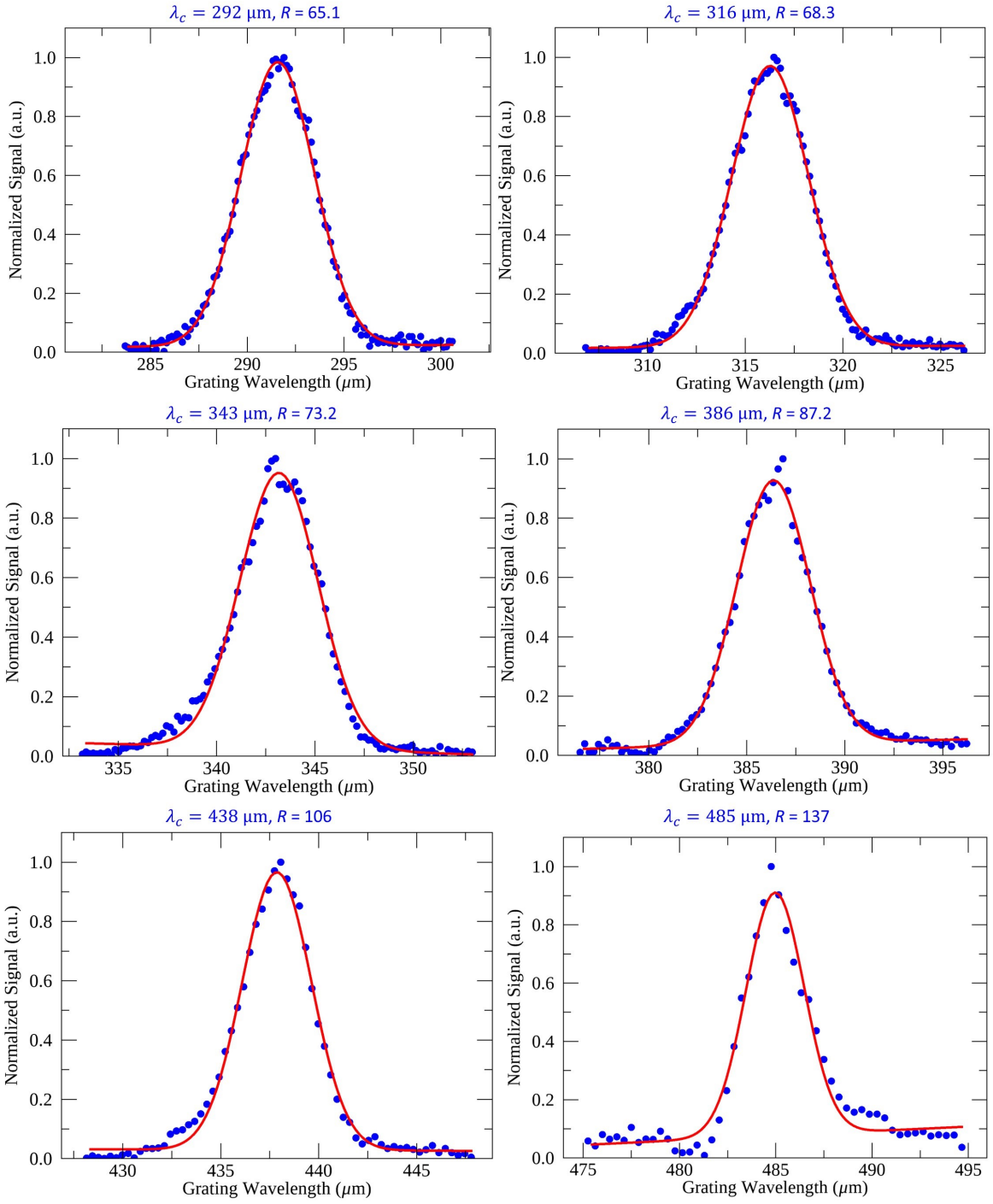

Figure 5.19: FTS measured data (blue points) and the best-fit Gaussian profile (red curve). The data were measured with the output polarization of the FTS configured perpendicular to the grating grooves (s-polarized) and the photomixer wavelength and measured resolving power are labeled above each plot.

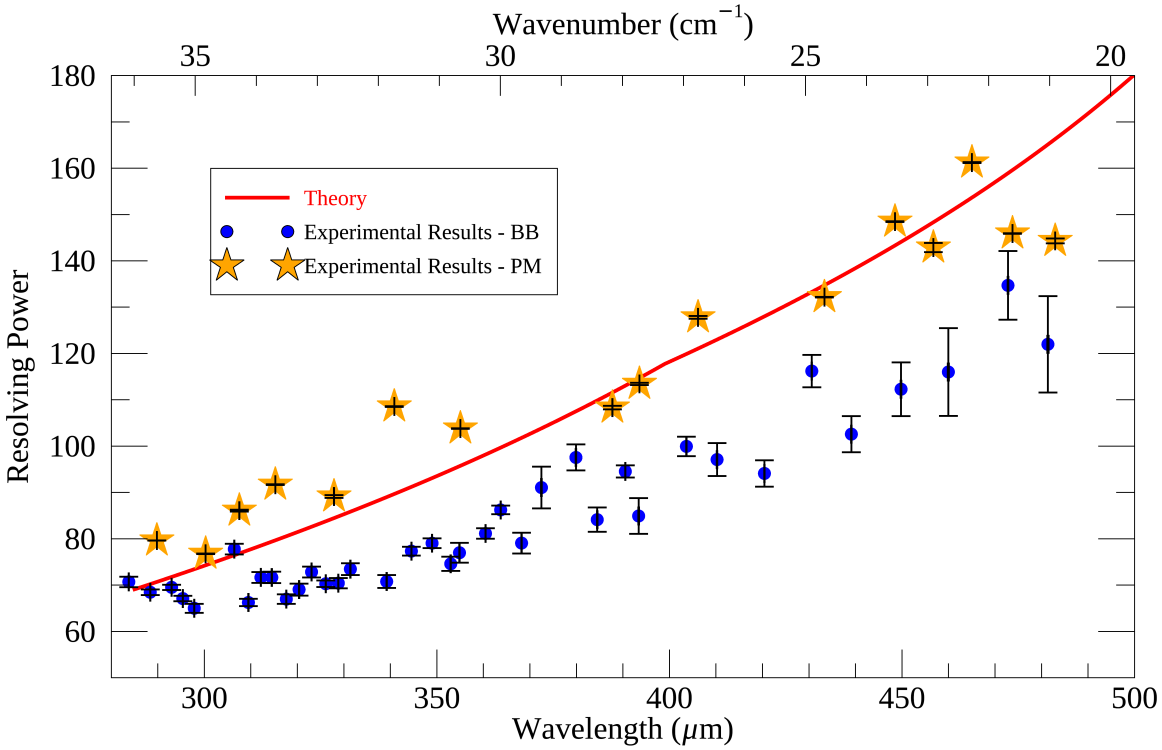

Figure 5.20: Experimental resolving power (blue circles) calculated from grating spectral response profiles with the blackbody source compared with measurements with the photomixer source (yellow stars). Both experimental data were collected with the output polarization of the FTS configured parallel to the grating grooves (p-polarized). The error bars are calculated from errors in the Gaussian fits to the measured data. The theoretical resolving power (red) is described by equation 2.50.

in both polarization states.

5.2.3 Resolving Power

The grating SRFs presented in the previous section were fitted with the Gaussian equation 4.9 to extract the standard deviation, σ_λ, which is used to calculate the resolving power with equation 4.11. For the grating measurements taken with the cFTS output p-polarized, the measured resolving power is shown in figure 5.20 comparing SRFS taken with the blackbody source (blue points) and the photomixer source (yellow stars). The resolving power measured from the photomixer profiles show good agreement with the slit-limited theoretical curve from equation 2.50. The grating SRFs obtained with the blackbody source required the measured interferogram to be transformed to the spectral domain. Any phase

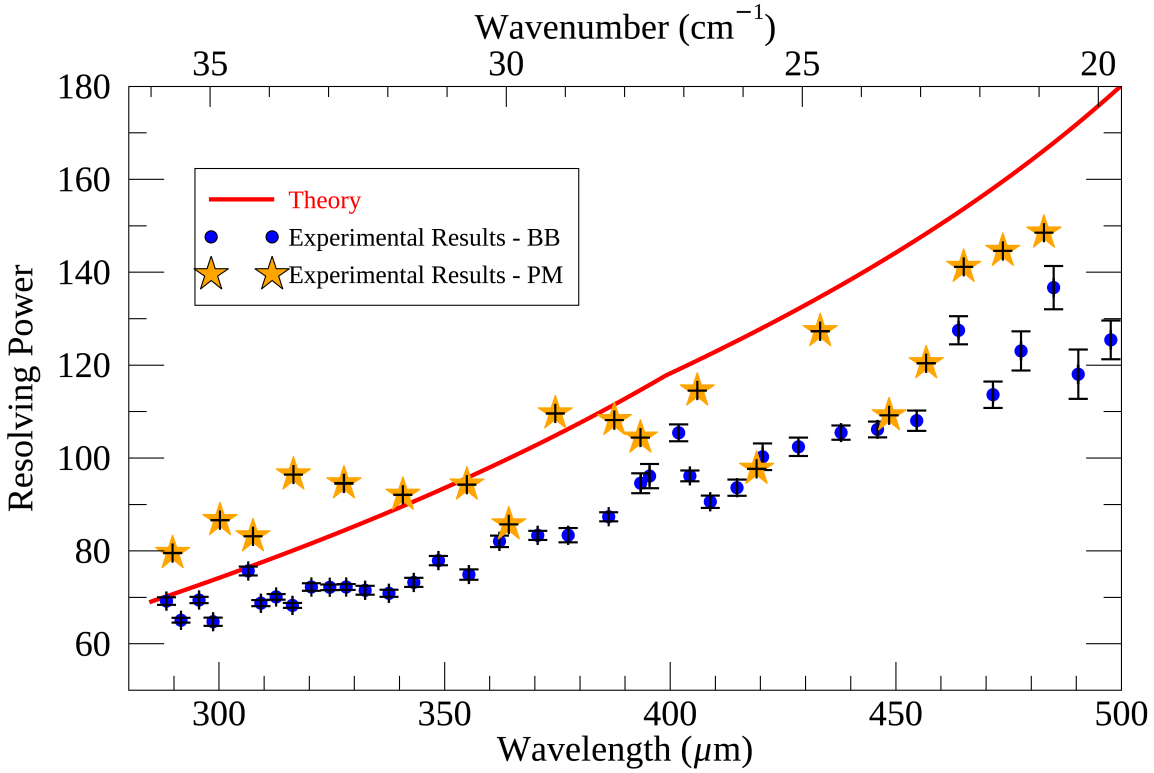

Figure 5.21: Experimental resolving power (blue circles) calculated from grating spectral response profiles with the blackbody source compared with measurements with the photomixer source (yellow stars). Both experimental data were collected with the output polarization of the FTS configured perpendicular to the grating grooves (s-polarized). The error bars are calculated from errors in the Gaussian fits to the measured data. The theoretical resolving power (red) is described by equation 2.50.

error in the interferogram will contribute to uncertainty in determining the true profile of the grating. Therefore, a proper phase correcting routine is required. From figure 5.20, the grating achieves a resolving power of $R = 100$ at 404 μm which is similar to the target of $R = 100$ at 392.5 μm.

Resolving power measurements were repeated with the data collected for the s-polarized FTS output as shown in figure 5.21. Interestingly, these results show a slightly lower overall resolving power compared with figure 5.20, contrasting what would be expected with the higher signal to noise ratio of the data collected in the s-polarization. The data follow the general trend of the slit-limited resolving power curve and measured a resolving power of $R = 105$ at 402 μm, near the band center. Overall, these data show significant improvement

over the measurements taken in the first two optical configurations. Even with a slightly lower resolving power, the blackbody measurements still verify that the grating succeeds as a post-dispersing module by heavily restricting the spectral band of radiation viewed with the detector. The next area to investigate is the diffraction efficiency achieved in both polarization states.

5.3 Efficiency Analysis

Chapter 2 discussed some existing theoretical frameworks to model the diffraction efficiency of a blazed grating with a user-defined groove geometry. Among the available models, a derivation using scalar electromagnetic equations was given with the result outlined in equation 2.67. The scalar model is intended to be useful for unpolarized light, however, measurements were taken with linearly s-polarized and p-polarized light. Therefore, a model incorporating vectorial electromagnetic calculations was formed by applying the rigorous coupled wave, RCW, analysis within the pySCATMECH library [62]. The scalar model and polarization sensitive vector models are shown in figure 5.22. The experimental efficiency measurements were calculated by dividing the peak of the grating SRF by the signal measured with the mirror at the same wavelength as the center of the grating profile. As was mentioned in the blackbody results, there were some issues in determining the absolute efficiency of the system due to the nonlinear response of the detector. Measurements of the DC bias voltage were taken with the mirror in path and with the grating in path and these were compared with response curves for the bolometer detector [72]. It was found that a factor of ~ 2 is expected for the change in responsivity so the experimental data were subsequently divided by 2 for a more accurate comparison.

The s-polarization diffraction efficiency is shown to be greater than the p-polarization efficiency except for shorter wavelengths. The crossover point where the experimental s-polarization efficiency surpasses the p-polarization efficiency happens around 325 μm (30.8 cm^{-1}). Recall the groove spacing of the diffraction grating is $d = 312$ μm. The diffraction

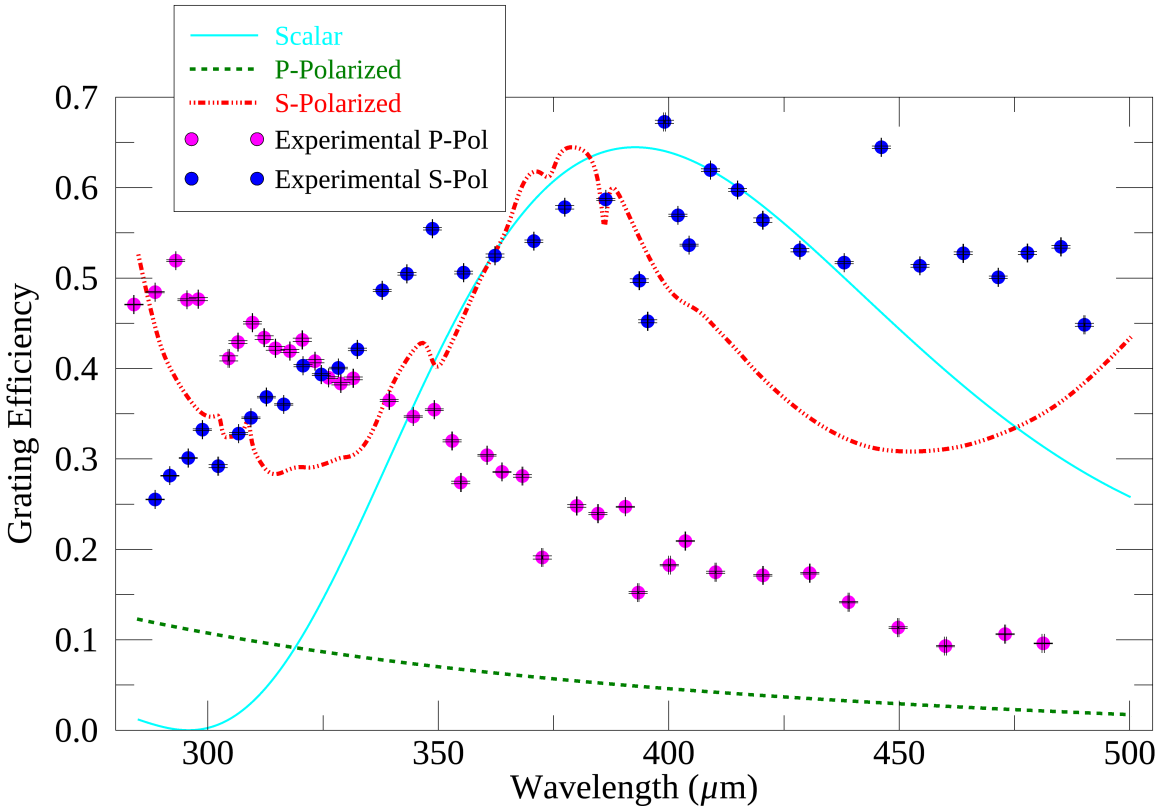

Figure 5.22: Scalar diffraction efficiency model (cyan curve) compared to vectorial polarization sensitive models calculated using pySCATMECH for p-polarized light (green dashed curve) and s-polarized light (red dashed curve). Efficiency measurements were taken with the blackbody source for p-polarized light (pink circles) and s-polarized light (blue circles). Vertical and horizontal error bars are calculated from the uncertainty in determining the amplitude and center of each grating SRF.

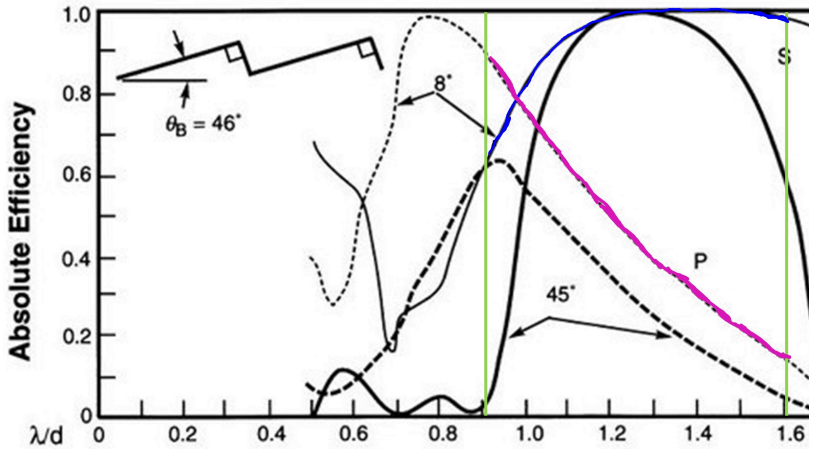

Figure 5.23: Efficiency curves for a diffraction grating blazed at an angle of 46° with an 8° and 45° deviation angle between the incident and diffracted beams. The efficiency of s-polarized light (blue curve) and p-polarized light (pink curve) are computed with the 46° blazed grating having an 8° deviation angle. The vertical green lines represent the operating range of the grating in this thesis, $\lambda/d = 0.91 - 1.60$.

grating handbook [55] discusses the efficiency properties of gratings with large blaze angles, $> 38°$, where the grating in this thesis was designed with a blaze angle of 39.4°. For large blaze angles, there is a high efficiency expected for p-polarized light at wavelengths $\lambda/d < 1$. Figure 5.23 shows a plot taken from [55] for a blazed diffraction grating with a blaze angle of 46° and deviation angles of 8° and 45°. Recall the deviation of the grating spectrometer in this thesis was 15°, therefore, the data will be compared with the theoretical curve for the 8° deviation. In figure 5.23, the blue outline corresponds to s-polarized light and the pink outline is the p-polarized efficiency curve. The experimental data in figure 5.22 resembles the theoretical curves in figure 5.23 much better than the models derived using pySCATMECH. The discrepancy between the theoretical models is likely due to the RCW analysis being incomplete. The available libraries from pySCATMECH do not allow the user to specify the mounting configuration, specifically, the deviation angle between the incident and diffracted waves. As was shown in figure 5.23, there is a significant dependence on the deviation angle which is illustrated between the efficiency curves for an 8° and 45° deviation angle. Therefore, the s-polarized and p-polarized curves in figure 5.22 should not be over-interpreted until a more complete theoretical model is obtained.

The experimental efficiency measurements were then compared individually to the p-polarized and s-polarized RCW models. Figure 5.24 shows the s-polarized data (blue circles) compared with the RCW model (red dashed curve) which doesn't show a great agreement. However, the expected maximum efficiency at the blaze wavelength, 392.5 μm, is seen in the data. Figure 5.25 shows the experimental data (pink circles) compared with the RCW model (green dashed line) which has been multiplied by a factor to account for the nonlinearity of the detector. From figure 5.22, the p-polarized experimental data had a much greater amplitude than the theoretical curve, however, it is interesting to see how well the shape of the curve matches the data. There is much better agreement than with the s-polarized data which indicates that the RCW model might still be useful for our application. It was seen in figure 5.24 that at longer wavelengths, the grating has a high efficiency for s-polarized light compared to p-polarized. When using the blackbody source as illustrated in figure 5.14, the signal is strongest at short wavelengths and then drops off rapidly at longer wavelengths. Therefore, when the blackbody source is used, the grating is optimally efficient when the output polarization of the FTS is oriented to be s-polarized as was expected. The efficiency measurements are made possible because the FTS is polarizing which eliminates the need for an expensive polarizing source. In this section, I have presented a method for probing the polarization and wavelength dependent diffraction efficiency of a blazed reflection grating operating over far-infrared (285 - 500 μm) wavelengths at a temperature of 4 K.

5.3.1 Blackbody Results: Evacuated FTS

Blackbody measurements were repeated for s-polarized light with the cFTS under vacuum $<$ 10 mTorr. This reduced the atmospheric path from 2 m to 0.1 m, significantly reducing the amount of absorption as seen in figure 5.26. The grating SRF power spectra are shown along with the mirror scan for 10 cFTS scans averaged at each position. As was discussed in Chapter 3, the diffraction grating was blazed to achieve a maximum ef-

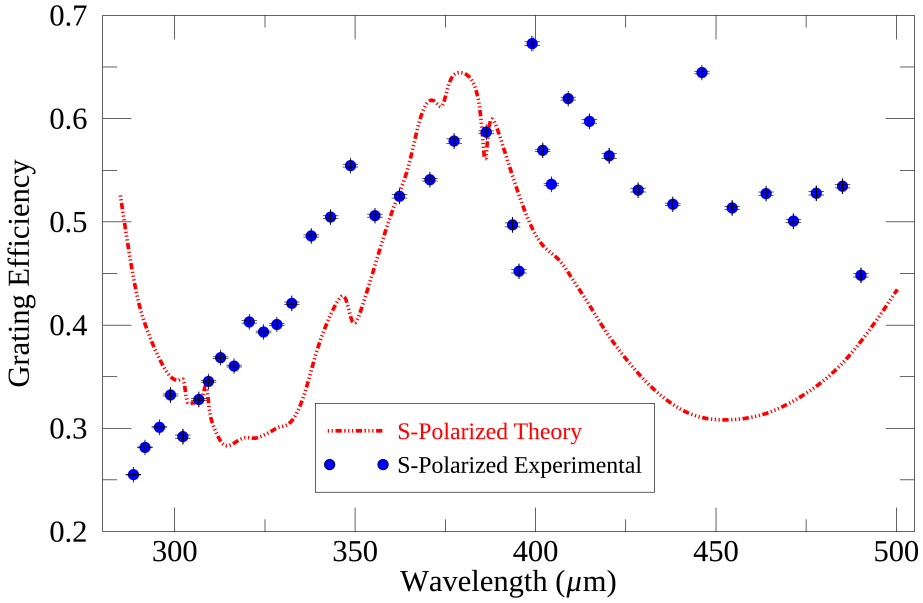

Figure 5.24: Diffraction efficiency calculated using pySCATMECH for s-polarized light (red dashed curve) compare with efficiency measurements taken with the blackbody source s-polarized light (blue circles). Vertical and horizontal error bars are calculated from the uncertainty in determining the amplitude and center of each grating SRF.

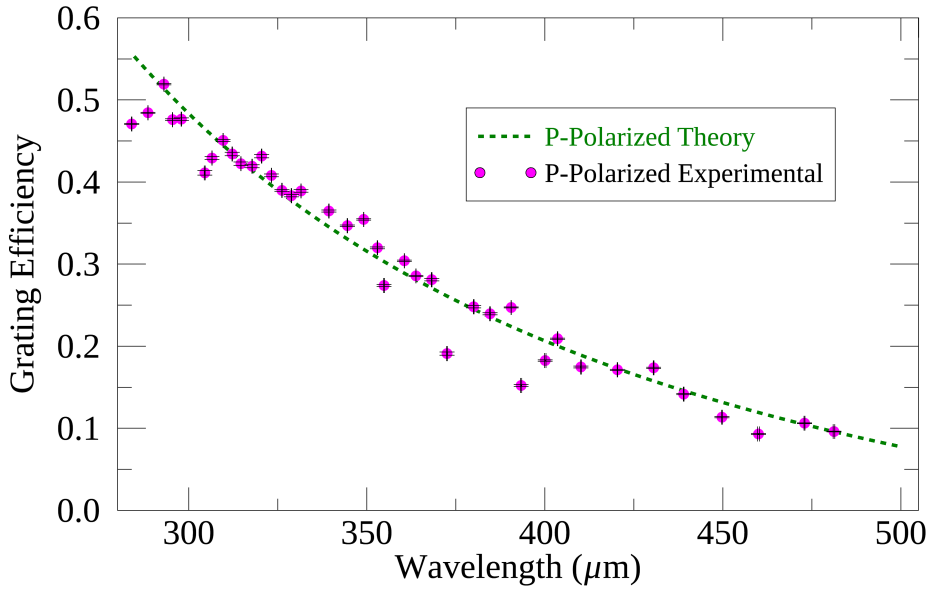

Figure 5.25: Diffraction efficiency calculated using pySCATMECH for p-polarized light (green dashed curve) compare with efficiency measurements taken with the blackbody source p-polarized light (pink circles). Vertical and horizontal error bars are calculated from the uncertainty in determining the amplitude and center of each grating SRF.

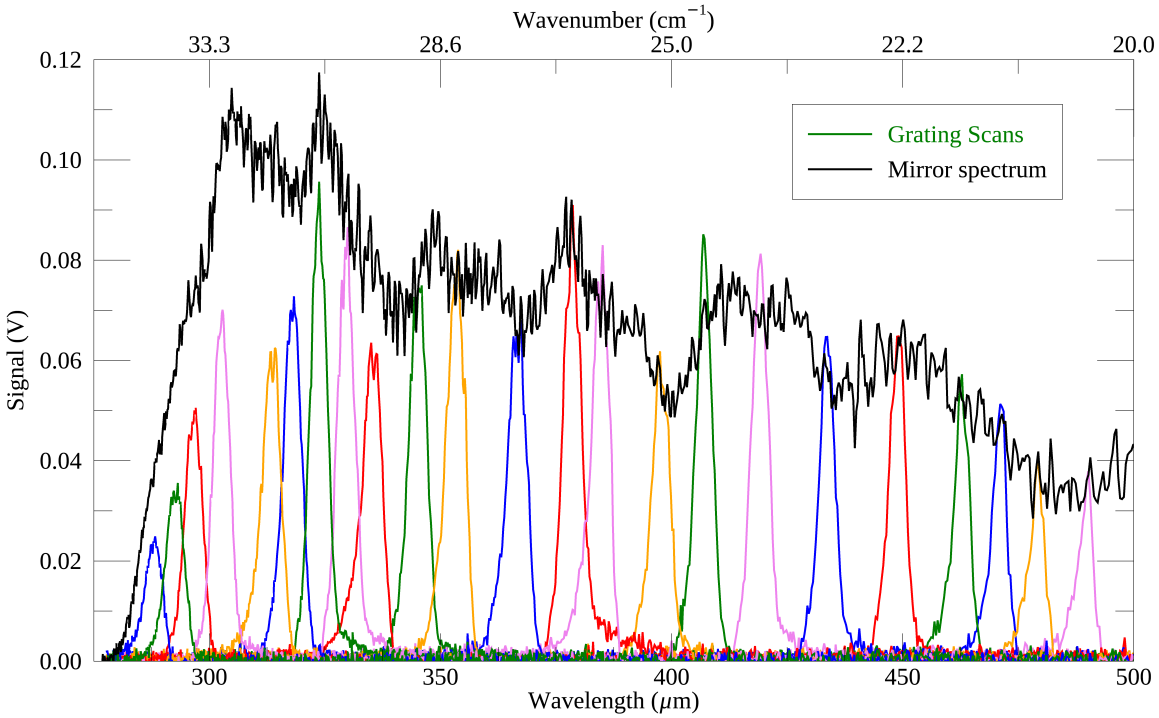

Figure 5.26: The grating scans (colored lines) correspond to all FTS scans measured with the blackbody source at different angular positions of the grating. An FTS measurement of the entire band (black) was taken with the flat mirror in place of the grating. The data were measured with the output polarization of the FTS configured perpendicular to the grating grooves (s-polarized).

ficiency at 392.5 μm (25.5 cm^{-1}). There is an absorption feature at 398 μm (25.1 cm^{-1}) which is expected to add uncertainty to the efficiency measurements near the feature. Thus, the evacuated FTS measurements are particularly important to probe the region of expected maximum efficiency which lies in the range of an absorption feature. Besides the reduced atmospheric absorption, the overall shape of the measured spectrum in figure 5.26 is the same as figures 5.14, 5.16 and 5.18. The efficiency of the evacuated data were calculated by fitting the grating power spectra with the Gaussian function in equation 4.9 to extract the amplitude and center wavelength. The amplitude of the grating signal is compared at the signal measured with the mirror at the same wavelength and the efficiency measurements are shown in figure 5.27. These data were also divided by 2 to account for the non-linearity in the absolute signal amplitude as measured with the grating compared with the mirror. The yellow circles represent the efficiency measurements with the evacuated cFTS

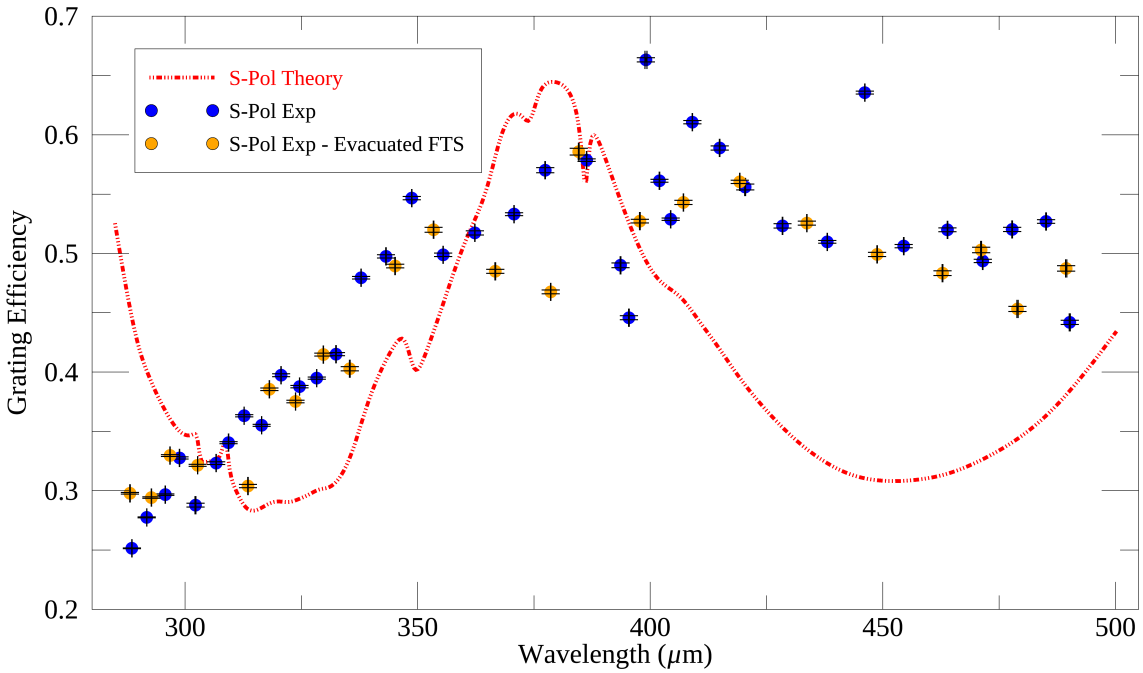

Figure 5.27: Polarization sensitive model calculated using pySCATMECH for s-polarized light (red dashed curve) and efficiency measurements with the cFTS in atmosphere (blue circles) and with the cFTS evacuated (yellow circles). Vertical and horizontal error bars are calculated from the uncertainty in determining the amplitude and center of each grating SRF.

compared with the blue circles which represent the measurements with the cFTS in atmosphere. Both sets of experimental data follow the same overall efficiency trend and have returned approximately the same amplitude indicating that the efficiency measurements are repeatable and not significantly sensitive to the experimental setup.

The results in this chapter have indicated a significant improvement to the experimental configuration by incorporating the cryogenic entrance slit with the high-resolution polarizing FTS. The spectral response of the grating has been characterized as a function of wavelength and polarization and the measurements of resolving power agree with the slit-limited theory. The results have also shown a reliable method to measure the diffraction efficiency of the grating as a function of wavelength and polarization using a broadband input produced by a commercially available heated filament source. The next chapter will discuss the conclusions and future work to be completed with the grating spectrometer.

Chapter 6

Conclusions and Future Work

> You only grow by coming to the end of something and by beginning something else.
>
> *The World According to Garp*
> JOHN IRVING

Through my MSc thesis, I have been fortunate enough to take part in the design, assembly and performance verification of a cryogenic instrument architecture that is widely considered to be the leading candidate for the next generation far-infrared space based observatory. I have developed knowledge in cryogenic instrumentation techniques, optical design, and familiarity with methods in low and high-resolution spectroscopy. During my MSc degree, I have co-authored 6 papers being the first author on 2 of these which were both accepted for oral presentations at international conferences. I have been supported throughout my studies by my industrial partner Blue Sky Spectroscopy Inc. where I learned techniques for vacuum and cryogenic systems, optical design, and infrared spectroscopy. This final chapter serves to summarize the work completed in my thesis and highlight future work to be implemented and the path to a fully cryogenic post-dispersed Fourier transform spectrometer (PDPFTS).

6.1 Summary of Results

As was discussed in Chapter 1, observations in the far-infrared are critical for understanding the formation and early evolution of stars and planetary systems, and to probe the high-redshift universe. It has been established that approximately one half of radiation

emitted in the universe is detected at far-infrared wavelengths (30 - 1000 μm) [92]. This is due to two main factors: the first is that the youngest systems in the universe including galactic protostars and ultra-luminous galaxies in the local universe are often shrouded in dust and gas [93]. Radiation traveling from within these enshrouded systems suffers from extinction which, due to the typical size of dust grains ($\sim$1 μm), favours the absorption and scattering of radiation at shorter (visible) wavelengths. Far-infrared radiation experiences less extinction and can probe into these obscured regions more efficiently. Additionally, the dust particles in dense star forming regions typically have a temperature around 20 - 40 K which means they produce continuum emission that peaks in the far-infrared. The second reason is that distant galaxies will have their emission shifted into longer wavelengths due to cosmological expansion of the universe [5]. Because of their ability to probe both obscured regions in the nearby universe and distant galaxies, far-infrared spectroscopic observations provide a unique means of addressing some of the leading questions in modern astrophysics from the formation of stars and planets in our own galaxy to the evolution of galaxies over cosmic time [93].

The next generation of far-infrared astronomical observatories will employ a high-resolution spectrometer coupled with ultra-sensitive superconducting bolometer detectors achieving noise equivalent power (NEP) measurements on the order of $10^{-19}\mathrm{W}/\sqrt{\mathrm{Hz}}$ [46]. With a sensitivity more than two orders of magnitude better than any previous far-infrared space mission, the detector becomes limited by photon noise unless the spectral bandwidth of radiation falling on the detector is restricted. The leading approach is to use a reflection diffraction grating to post-disperse the output from the high-resolution spectrometer. This thesis has described the design, development, and verification of a diffraction grating spectrometer which was developed to study the instrument concept of a cryogenic post-dispersed Fourier transform spectrometer (PDPFTS).

Chapter 2 introduced the key equations that describe interference and diffraction which were used to design the diffraction grating spectrometer. The specifications of the grating

were outlined in Chapter 3 which detailed the design of the blazed diffraction grating as well as the monolithic enclosure that was mounted within the test facility cryostat. Chapter 3 also discussed the cryogenic considerations taken to ensure the grating module would reach a base temperature of $\sim$4 K within 2 hours of the cryostat mounting plate. Temperature measurements confirmed that the thermal contact conductance between the grating spectrometer and the baseplate was sufficient to produce a negligible temperature delay, well within the 2 hour target.

Chapters 4 and 5 presented the steps taken to validate the performance of the grating spectrometer as an individual instrument and as a post-dispersing module to a polarizing FTS. Three measurement configurations were explored to study the performance of the diffraction grating spectrometer. The first configuration outlined in Chapter 4 produced measurements of the grating used alone, i.e without the polarizing FTS. A THz photomixer source was used to determine the spectral response of the grating and measurements of the resolving power were presented to quantify the agreement between the data and theory. While the first configuration included a cryogenic entrance slit to define the bandpass of the system, it lacked a determination of the spectral content of the source which would have included thermal emission from the room-temperature photomixer. Therefore, measurements with the polarizing FTS were required to characterize the incident radiation.

In Chapter 5, the second configuration involved coupling the room-temperature source and FTS to the cryogenic grating spectrometer by passing a collimated beam through the cryostat window. This configuration was found to be sub-optimal because it did not include a cryogenic entrance slit. Therefore, measurements obtained with the continuum source had no means to control the spectral throughput/direction of radiation viewed by the grating and the bandpass of the grating profiles was much wider than measurements taken with the photomixer line source whose emitting region acted as a slit.

The third and final configuration was presented in Chapter 5 and included the room-temperature source and FTS which coupled a focused beam onto a cryogenic entrance slit

before passing onto the grating spectrometer. Measurements with the final configuration produced spectral response profiles which were nearly identical for the continuum source and the line source. The results verified that the grating spectrometer could be operated at 4 K and was able to post-disperse the signal from a polarizing FTS such that the bandpass of radiation viewed by the detector was roughly 1% ($R \sim 100$).

The final configuration of the grating spectrometer also incorporated a flat mirror mounted to the rear of the grating which allowed the determination of the grating efficiency. There are few experimental measurements exploring the diffraction efficiency of a blazed grating as a function of polarization and, to our knowledge, none at cryogenic temperatures and at far-infrared wavelengths. The diffraction grating grooves were blazed to achieve a maximum efficiency at the band center (392.5 μm). The results in Chapter 5 confirm the analysis presented in Chapter 2 that the efficiency was strongly dependent on the polarization state of incident light. When the output from the polarizing FTS was oriented perpendicular to the grating grooves (s-polarized), the measured efficiency did peak at the center of the band as expected. However, when the output was parallel to the grooves (p-polarized), the efficiency peaked at the short wavelength end of the band (285 μm) and was significantly lower at long wavelengths. Overall, figure 5.22 showed that the measured efficiency was greater with p-polarized light from 285 - 320 μm and from 320 - 500 μm the efficiency was greater for the s-polarized state. The next section will discuss the improvements that are underway with the final configuration of the hybrid room-temperature/cryogenic PDPFTS. The final section will discuss the current development status of the fully cryogenic PDPFTS.

6.2 Next Steps

The results presented in the final configuration from Chapter 5 indicated a few areas of improvement which will be implemented for the next series of measurements. FTS scans with the continuum source returned grating profiles that had slight asymmetries due to phase errors in the measured interferograms. An FTS data processing pipeline which

was developed by a previous student [94] is being modified to perform phase correction iteratively by combining interferograms measured at adjacent grating angular (wavelength) positions. By combining the phase information within the spectral band of the grating at multiple positions it is possible to acquire additional information to phase correct the data [95]. The corrected data will yield a more accurate representation of the true spectrum and eliminate the need to study the power spectrum of the signal which has the adverse effect of making the noise positive definite [84]. Once the improved phase correction algorithm is completed, the data can be reanalyzed to reduce the uncertainty in the line profile.

Another minor issue that was identified from the grating independent results in the first configuration presented in Chapter 4, as well as the data in the final configuration in Chapter 5, was the issue of stray/scattered light appearing in the grating spectral response profiles measured with the photomixer source. Steps were taken before the final measurements in Chapter 5 to coat the reflective components around the grating with an epoxy-carborundum mixture, however, this did not completely eliminate stray reflections. An additional cryogenic aperture will be placed at the entrance of the diffraction grating to stop down the width of the beam so it does not interact with the edges of the grating and the saddle. The horizontal width of the beam is not critical to achieving the desired spectral response of the grating since the entrance and exit slits are oriented horizontally, i.e. diffraction is occurring in the vertical direction. Thus, as long as the beam incident on the grating is 50 mm in the vertical direction, the horizontal width of the beam can be decreased without impacting the spectral profile at the cost of a slight reduction in signal to noise.

The final issue which will be addressed in the next set of measurements is the uncertainty in the absolute diffraction efficiency. As was discussed in Chapter 5, when the power incident on the detector changes by more than two orders of magnitude as was seen between measurements with the grating in the optical path and with the flat mirror in the path, detector nonlinearity is a problem. Due to the change in responsivity of the detector, there is a gain factor applied to the data which is different for the grating measurements compared

to the mirror measurements. In order to correct for the non-linearity, a simple measurement can be made using a variable blackbody in which the temperature (signal power) is changed by a known amount. By recording the change in signal amplitude measured by the detector due to a known change in power, the responsivity can be measured with the grating in the path and compared to the responsivity with the mirror in path. The data can be corrected for nonlinearity to provide a more accurate determination of the absolute efficiency. However, regardless of the amplitude uncertainties, the detector behaves linearly throughout the grating range and, therefore, the relative efficiency measurements are robust. The final steps in the PDPFTS project are to incorporate a cryogenic FTS module which is discussed in the following section.

6.3 Future Work

While the hybrid room-temperature/cryogenic PDPFTS has been extremely useful in verifying the performance of the grating spectrometer and in developing data processing routines, the final PDPFTS configuration will employ a fully cryogenic source and polarizing FTS to couple with the cryogenic grating and bolometer. Figure 6.1 shows a schematic of the cryogenic PDPFTS layout. This thesis has discussed the overall development and integration of the cryogenic diffraction grating spectrometer with the 0.3 K bolometer detector. The next step will incorporate a cryogenic source module as an intermediate step before the cryogenic FTS is installed. A cryogenic PB1319 fiber-fed photomixer module has been procured from Bakman Technologies which has a proven reliability at temperatures as low as 4.5 K [96]. The cryogenic photomixer element is composed of low-temperature grown gallium arsenide which has an operating optical wavelength between 760 - 785 nm. Laser diodes and photonics components manufactured to operate within this wavelength range are less readily available and more expensive compared to the 1550 nm equipment required for the room-temperature photomixer module. However, for a line-source which is able to provide terahertz radiation at cryogenic temperatures the extra cost is justifiable.

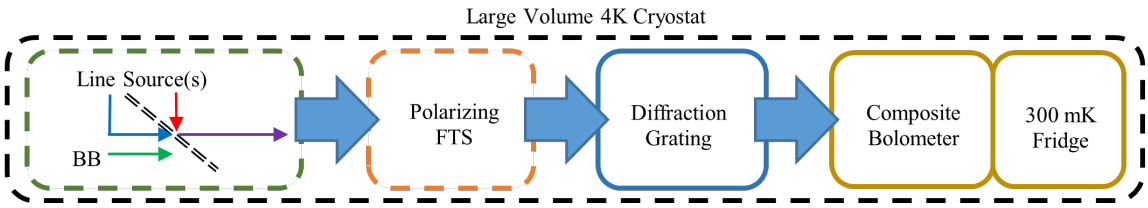

Figure 6.1: An overview of the cryogenic PDPFTS configuration taken from [100]. The system is characterized by four modules: the source, a polarizing FTS, a reflection diffraction grating, and a bolometric detector. The source module consists of a cryogenic photomixer (PM) and blackbody (BB). The source, FTS and diffraction grating all operate at 4 K within a large volume cryostat. The composite bolometer detector [72] operates at 0.3 K within a ^{4}He:^{3}He:^{3}He closed cycle refrigerator mounted in the cryostat.

Two tunable Photodigm PH789DBR040BF 780 nm diode lasers [97] have been purchased to integrate with the photomixer. The incorporation of the newly acquired photomixer will allow the complete validation of the grating spectrometer at cryogenic temperatures. The fully cryogenic configuration will be completely sealed in a 4 K environment with no room temperature radiation able to reach the detector. Additionally, our group has been provided the flight-spare spectrometer calibration (SCAL) source developed for the Herschel SPIRE instrument [98, 99]. SCAL provides thermal emission at cryogenic temperatures ($\sim$4 K) and is able to reach temperature of 160 K with an input power of 10 mW [99]. The diffraction grating spectrometer can be used to validate the performance of the cryogenic continuum source before integration with the cryogenic FTS. Combining SCAL with the cryogenic line source will allow the generation of accurate, synthetic astronomical spectra at 4 K.

As mentioned in figure 6.1, the cryogenic PDPFTS is located within a large volume cryogenic facility. Our group is currently developing a large facility cryostat (LFC) which encompasses many of the design aspects used in the test facility cryostat (TFC) [66]. The TFC was described briefly in section 3.2 and was used in the results presented in this thesis. The LFC incorporates a 4 K working volume of 650 mm $\times$ 650 mm $\times$ 250 mm and utilizes two Cryomech PT-415 pulse tube cryocoolers; the same cooling system as the TFC. The LFC has a large enough working volume to contain the source module, FTS module, grat-

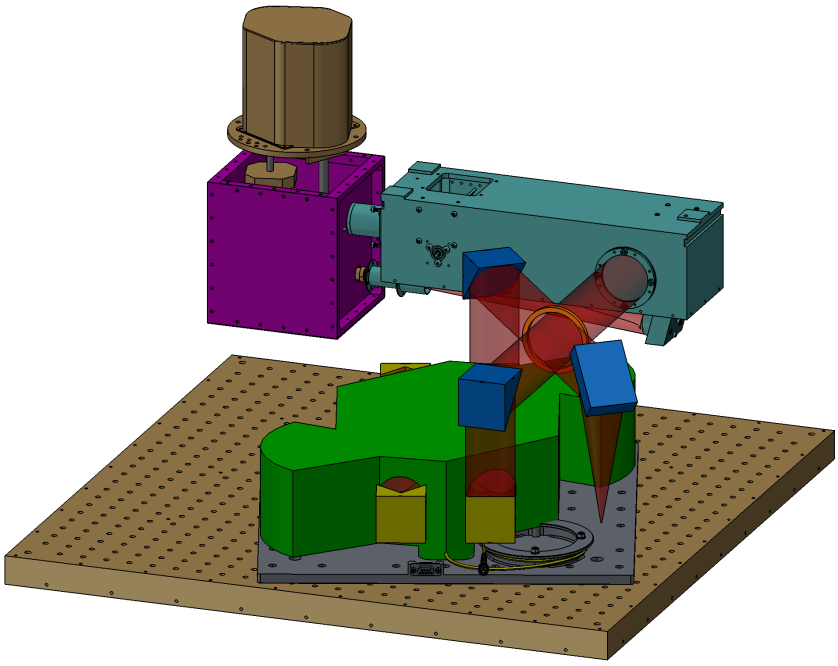

Figure 6.2: CAD rendering of the cryogenic PDPFTS within the 4 K volume of the LFC. The scanning mechanism (green) is provided by ABB Inc.[101]. Auxiliary optics (yellow and blue) couple light from the FTS mechanism into the grating spectrometer (teal) and the signal from the grating is measured by the bolometer detector (purple). Image credit to Matthew Buchan (Blue Sky Spectroscopy Inc.) [73].

ing spectrometer, and the bolometer detector assembly. The final component required to complete the cryogenic PDPFTS is the polarizing FTS which is currently being developed by ABB Inc. [101]. The optical configuration of the FTS mechanism (FTSM) is a Martin Puplett interferometer with dual scanning rooftop mirrors which share a common apex [101]. The novel FTSM scanning mechanism features ultra-low thermal dissipation (< 1.5 mW), mirror position accuracy of < 10 nm RMS and low vibration levels (30 $\mu g/\sqrt{Hz}$), all while operating at cryogenic temperatures ($\sim$4 K) [101]. A CAD rendering of the FTSM mounted within the LFC is shown in figure 6.2. The space constraints within the LFC requires the grating spectrometer to be mounted upside down on the top of the 4 K volume. A

considerable amount of work has already been completed in the development of the FTSM and the LFC. The culmination of the PDPFTS instrument concept study will be achieved upon the successful integration of the fully cryogenic PDPFTS within the LFC.

Bibliography

[1] H. C. King, *The history of the telescope*. Cambridge, Mass: Sky Publishing Co, 1955.

[2] W. Herschel and J. L. E. Dreyer, "The Scientific Papers of Sir William Herschel," *Astrophysical Journal*, vol. 35, p. 296, May 1912.

[3] "Herschel discovers infrared light," https://web.archive.org/web/20120225094516/http://coolcosmos.ipac.caltech.edu/cosmic_classroom/classroom_activities/herschel_bio.html, 2012.

[4] J. C. D. Brand, "Lines of Light: The Sources of Dispersive Spectroscopy, 1800–1930," *Gordon and Breach Publishers*, pp. 37–42, 1995.

[5] A. R. Choudhuri, *Astrophysics for physicists*. Cambridge, UK;New York;: Cambridge University Press, 2010.

[6] M. Planck, *Über eine Verbesserung der Wienschen Spektralgleichung*. Wiesbaden: Vieweg+Teubner Verlag, 1978, pp. 175–178. [Online]. Available: https://doi.org/10.1007/978-3-663-13885-3_15

[7] I. M. Chapman, "The atmosphere above Mauna Kea at mid-infrared wavelengths," Master's thesis, University of Lethbridge, 2002.

[8] G. Kirchhoff, "Ueber das verhältniss zwischen dem emissionsvermögen und dem absorptionsvermögen der körper für wärme und licht," *Annalen der Physik*, vol. 185, no. 2, pp. 275–301, 1860.

[9] C. Turon, "Esa space science programme, cosmic vision 2015-2025, for astrophysics," *Proceedings of the International Astronomical Union*, vol. 2, no. 14, p. 530–531, 2006.

[10] P. R. Roelfsema, H. Shibai, L. Armus, D. Arrazola, M. Audard, M. D. Audley, C. M. Bradford *et al.*, "SPICA—A Large Cryogenic Infrared Space Telescope: Unveiling the Obscured Universe," *Publications of the Astronomical Society of Australia*, vol. 35, p. e030, 2018.

[11] H. Kaneda, D. Ishihara, S. Oyabu, M. Yamagishi, T. Wada, L. Armus, M. Baes *et al.*, "Unbiased large spectroscopic surveys of galaxies selected by SPICA using dust bands," *Publications of the Astronomical Society of Australia*, vol. 34, p. e059, 2017.

[12] F. F. S. van der Tak, S. C. Madden, P. Roelfsema, L. Armus, M. Baes, J. Bernard-Salas, A. Bolatto *et al.*, "Probing the baryon cycle of galaxies with SPICA mid- and far-infrared observations," *Publications of the Astronomical Society of Australia*, vol. 35, p. e002, 2018.

[13] L. Spinoglio, A. Alonso-Herrero, L. Armus, M. Baes, J. Bernard-Salas, S. Bianchi, M. Bocchio *et al.*, "Galaxy Evolution Studies with the SPace IR Telescope for Cosmology and Astrophysics (SPICA): The Power of IR Spectroscopy," *Publications of the Astronomical Society of Australia*, vol. 34, p. e057, 2017.

[14] E. Egami, S. Gallerani, R. Schneider, A. Pallottini, L. Vallini, E. Sobacchi, A. Ferrara *et al.*, "Probing the high-redshift universe with SPICA: Toward the epoch of reionisation and beyond," *Publications of the Astronomical Society of Australia*, vol. 35, p. e048, 2018.

[15] C. Gruppioni, L. Ciesla, E. Hatziminaoglou, F. Pozzi, G. Rodighiero, P. Santini, L. Armus *et al.*, "Tracing the evolution of dust obscured star formation and accretion back to the reionisation epoch with SPICA," *Publications of the Astronomical Society of Australia*, vol. 34, p. e055, 2017.

[16] E. González-Alfonso, L. Armus, F. J. Carrera, V. Charmandaris, A. Efstathiou, E. Egami, J. A. Fernández-Ontiveros *et al.*, "Feedback and feeding in the context of galaxy evolution with SPICA: Direct characterisation of molecular outflows and inflows," *Publications of the Astronomical Society of Australia*, vol. 34, p. e054, 2017.

[17] J. A. Fernández-Ontiveros, L. Armus, M. Baes, J. Bernard-Salas, A. D. Bolatto, J. Braine, L. Ciesla *et al.*, "SPICA and the chemical evolution of galaxies: The rise of metals and dust," *Publications of the Astronomical Society of Australia*, vol. 34, p. e053, 2017.

[18] R. B. Larson, "The physics of star formation," *Reports on Progress in Physics*, vol. 66, no. 10, pp. 1651–1697, Oct. 2003.

[19] R. L. Bowers and T. Deeming, *Astrophysics*. Boston: Jones and Bartlett Publishers, 1984.

[20] E. Chaisson and S. McMillan, *Astronomy Today*. Boston: Addison-Wesley, 2011.

[21] "Comparing Stars." [Online]. Available: https://www.open.edu/openlearn/science-maths-technology/comparing-stars/content-section-0?active-tab=description-tab

[22] G. Tinetti, P. Drossart, P. Eccleston, P. Hartogh, A. Heske, J. Leconte, G. Micela *et al.*, "The science of ARIEL (Atmospheric Remote-sensing Infrared Exoplanet Large-survey)," in *Space Telescopes and Instrumentation 2016: Optical, Infrared, and Millimeter Wave*, H. A. MacEwen, G. G. Fazio, M. Lystrup, N. Batalha, N. Siegler, and E. C. Tong, Eds., vol. 9904, International Society

for Optics and Photonics. SPIE, 2016, pp. 658 – 667. [Online]. Available: https://doi.org/10.1117/12.2232370

[23] I. Kamp, M. Honda, H. Nomura, M. Audard, D. Fedele, L. B. F. M. Waters, Y. Aikawa *et al.*, "The formation of planetary systems with SPICA," *Publications of the Astronomical Society of Australia*, vol. 38, p. e055, 2021.

[24] C. Simoes, "Frost line or snow line or ice line in the solar system," www.astronoo.com/en/articles/frost-line.html.

[25] "Biography of Edwin Powell Hubble (1889 - 1953)," https://asd.gsfc.nasa.gov/archive/hubble/overview/hubble$_$bio.html.

[26] C.-A. Faucher-Giguère, A. Lidz, and L. Hernquist, "Numerical simulations unravel the cosmic web," *Science*, vol. 319, no. 5859, p. 52–55, Jan 2008. [Online]. Available: http://dx.doi.org/10.1126/science.1151476

[27] "James Clerk Maxwell Telescope Science," https://www.eaobservatory.org/jcmt/science/.

[28] "IR Atmospheric Windows," http://coolcosmos.ipac.caltech.edu/cosmic$_$classroom/ir$_$tutorial/irwindows.html.

[29] A. Wootten and A. R. Thompson, "The Atacama large millimeter/submillimeter array," *Proceedings of the IEEE*, vol. 97, no. 8, pp. 1463–1471, 2009.

[30] S. C. Parshley, J. Kronshage, J. Blair, T. Herter, M. Nolta, G. J. Stacey, A. Bazarko *et al.*, "CCAT-prime: a novel telescope for sub-millimeter astronomy," in *Ground-based and Airborne Telescopes VII*, H. K. Marshall and J. Spyromilio, Eds., vol. 10700, International Society for Optics and Photonics. SPIE, 2018, pp. 1744 – 1758. [Online]. Available: https://doi.org/10.1117/12.2314046

[31] S. P. Denny, J. Y. Suen, and P. M. Lubin, "Fundamental limits of detection in the far infrared," *New Astronomy*, vol. 25, p. 114–129, Dec 2013. [Online]. Available: http://dx.doi.org/10.1016/j.newast.2013.04.008

[32] R. M. Cameron, "NASA's 91-cm Airborne Telescope," *Sky and Telescope*, vol. 52, p. 327, Nov. 1976.

[33] A. Krabbe, D. Mehlert, H.-P. R oser, and C. Scorza, "SOFIA, an airborne observatory for infrared astronomy," *European journal of physics*, vol. 34, no. 6, pp. S161–S177, 2013.

[34] G. Neugebauer, H. J. Habing, R. van Duinen, H. H. Aumann, B. Baud, C. A. Beichman, D. A. Beintema *et al.*, "The Infrared Astronomical Satellite (IRAS) mission." *Astrophysical Journal*, vol. 278, pp. L1–L6, Mar. 1984.

[35] M. F. Kessler, "The Infrared Space Observatory (ISO) mission," *Advances in Space Research*, vol. 30, no. 9, pp. 1957 – 1965, 2002.

[36] M. W. Werner *et al.*, "The Spitzer Space Telescope Mission," *The Astrophysical Journal Supplement Series*, vol. 154, no. 1, pp. 1–9, 2004.

[37] H. Murakami, H. Baba, P. Barthel, D. L. Clements, M. Cohen, Y. Doi, K. Enya *et al.*, "The Infrared Astronomical Mission AKARI*," *Publications of the Astronomical Society of Japan*, vol. 59, no. sp2, pp. S369–S376, 10 2007. [Online]. Available: https://doi.org/10.1093/pasj/59.sp2.S369

[38] L. Spencer, D. A. Naylor, and B. Swinyard, "Performance Evaluation of the Herschel/SPIRE Imaging Fourier Transform Spectrometer through ground-based measurements," *Measurement Science and Technology*, vol. 21, no. 6, p. 065601, 2010.

[39] Z. Zhang, "Far-Infrared Herschel SPIRE Spectroscopy of Lensed Starbursts Reveals Physical Conditions of Ionized Gas," *Monthly Notices of the Royal Astronomical Society*, vol. 481, no. 1, pp. 59–97, 2018.

[40] M. Harwit, "The Herschel Mission," *Advances in Space Research*, vol. 34, no. 3, pp. 568–572, 2004.

[41] J. P. Gardner, J. C. Mather, M. Clampin, R. Doyon, M. A. Greenhouse, H. B. Hammel, J. Hutchings *et al.*, "The James Webb Space Telescope," *Space Science Reviews*, vol. 123, no. 4, pp. 485–606, 2006.

[42] G. S. e. a. Wright, "The Mid-Infrared Instrument for JWST, II: Design and Build," 2015.

[43] Griffin, M. J., Abergel, A., Abreu, A., Ade, P. A. R., André, P., Augueres, J.-L., Babbedge, T. *et al.*, "The Herschel-SPIRE instrument and its in-flight performance," *Astronomy & Astrophysics*, vol. 518, p. L3, 2010. [Online]. Available: https://doi.org/10.1051/0004-6361/201014519

[44] B. Swinyard, T. Nakagawa, P. Merken, P. Royer, T. Souverijns, B. Vandenbussche, C. Waelkens *et al.*, "The space infrared telescope for cosmology and astrophysics: SPICA A joint mission between JAXA and ESA," *Experimental Astronomy*, vol. 23, no. 1, pp. 193–219, Mar. 2009.

[45] D. Naylor, B. Gom, I. Veenendaal, D. van Loon Willem Jellema, P. Roelfsema, K. Wafelbakker, A. Cournoyer, and F. Grandmont, "The SPICA SAFARI Fourier Transform Spectrometer," *The Optical Society of America*, 2018.

[46] M. Ridder, P. Khosropanah, R. Hijmering, T. Suzuki, M. Bruijn, H. Hoevers, J. Gao, and M. Zuiddam, "Fabrication of Low-Noise TES Arrays for the SAFARI Instrument on SPICA," *Journal of Low Temperature Physics*, vol. 184, 07 2016.

[47] J. Mather, "Bolometer noise: nonequilibrium theory," *Applied optics*, vol. 21, pp. 1125–9, 03 1982.

[48] D. A. Jellema, W. Naylor and P. Roelfsema, "Post-dispersed FTS Spectroscopy on SPICA-SAFARI," *The Optical Society of America*, 2016.

[49] E. National Academies of Sciences and Medicine, *Pathways to Discovery in Astronomy and Astrophysics for the 2020s*. Washington, DC: The National Academies Press, 2021. [Online]. Available: https://www.nap.edu/catalog/26141/pathways-to-discovery-in-astronomy-and-astrophysics-for-the-2020s

[50] M. Born and E. Wolf, *Principles of optics: electromagnetic theory of propagation, interference and diffraction of light*, 6th ed. Cambridge, UK: Cambridge University Press, 1997.

[51] B. E. A. Saleh and M. C. Teich, *Wave Optics*. John Wiley & Sons, Ltd, 1991, ch. 2, pp. 41–79. [Online]. Available: https://onlinelibrary.wiley.com/doi/abs/10.1002/0471213748.ch2

[52] R. P. Feynman, R. B. Leighton, and M. Sands, "The Feynman Lectures on Physics; Vol. I," *American Journal of Physics*, vol. 33, no. 9, pp. 750–752, 1965. [Online]. Available: https://doi.org/10.1119/1.1972241

[53] J. D. Jackson, *Classical electrodynamics*, 3rd ed. New York, NY: Wiley, 1999. [Online]. Available: http://cdsweb.cern.ch/record/490457

[54] A. Sommerfeld, "Chapter V - eigenfunctions and eigen values," in *Partial Differential Equations in Physics*. Academic Press, 1949, pp. 166–235. [Online]. Available: https://www.sciencedirect.com/science/article/pii/B9780126546583500094

[55] C. Palmer, *Diffraction Grating Handbook (7th edition)*. Newport, 01 2014.

[56] M. Czerny and A. F. Turner, "Ãber den Astigmatismus bei Spiegelspektrometern," *Zeitschrift fãr Physik*, vol. 61, no. 11-12, p. 792–797, 1930.

[57] J. M. Lerner and A. Thevenon, "Optics of Spectroscopy - A Tutorial," *HORIBA Scientific*, 2013.

[58] E. Hecht, *Optics*. Addison-Wesley, 2002.

[59] R. Casini and P. Nelson, "On the intensity distribution function of blazed reflective diffraction gratings," *Journal of the Optical Society of America A*, 10 2013.

[60] D. F. Gray, *The Observation and Analysis of Stellar Photospheres*, 3rd ed. Cambridge University Press, 2005.

[61] G. Van Rossum and F. L. Drake, *Python 3 Reference Manual*. Scotts Valley, CA: CreateSpace, 2009.

[62] T. A. Germer, "pySCATMECH: a Python interface to the SCATMECH library of scattering codes," in *Reflection, Scattering, and Diffraction from Surfaces VII*, L. M. Hanssen, Ed., vol. 11485, International Society for Optics and Photonics. SPIE, 2020, pp. 43 – 54. [Online]. Available: https://doi.org/10.1117/12.2568578

[63] T. Heggie, "Subwavelength imaging using plasmonic lenses at terahertz frequencies," Master's thesis, University of Lethbridge, 2014.

[64] I. Veenendaal, "A novel cryogenic Fabry-Pérot interferometer for far-infrared astronomy," Ph.D. dissertation, University of Lethbridge, 2019.

[65] D. V. Schroeder, *An introduction to thermal physics*. San Francisco, CA: Addison Wesley, 2000.

[66] I. Veenendaal, "A cryogenic test facility," Master's thesis, University of Lethbridge, 2016.

[67] J. W. Ekin, *Experimental techniques for low-temperature measurements: cryostat design, material properties, and superconductor critical-current testing*. Oxford;Toronto;: Oxford University Press, 2006.

[68] A. K. Hasselström and U. Nilsson, "Thermal contact conductance in bolted joints," in *Engineering, Physics*, 2012.

[69] R. Schaellig and A. Seidel, "Very low force cooling contacts for the ISO cryostat cover," *Cryogenics (Guildford)*, vol. 30, no. 3, pp. 173–177, 1990.

[70] R. L. Schmitt, G. Tatkowski, M. Ruschman, S. Golwala, N. Kellaris, M. Daal, J. Hall, and E. W. Hoppe, "Thermal conductance measurements of bolted copper joints for SuperCDMS," *Cryogenics (Guildford)*, vol. 70, pp. 41–46, 2015.

[71] G. Hardin, "Aluminum 6061-T6 (UNS AA96061)," https://www.nist.gov/mml/acmd/aluminum-6061-t6-uns-aa96061, Nov 2019.

[72] B. G. Gom, "A cryogenic detector for submillimetre astronomy," Master's thesis, University of Lethbridge, 1999.

[73] "Blue Sky Spectroscopy Inc." https://blueskyspectroscopy.com/?page_id=21.

[74] M. D. Audley, G. de Lange, J.-R. Gao, B. D. Jackson, R. A. Hijmering, M. L. Ridder, M. P. Bruijn *et al.*, "The SAFARI detector system," in *Millimeter, Submillimeter, and Far-Infrared Detectors and Instrumentation for Astronomy IX*, J. Zmuidzinas and J.-R. Gao, Eds., vol. 10708, International Society for Optics and Photonics. SPIE, 2018, pp. 45 – 51. [Online]. Available: https://doi.org/10.1117/12.2313361

[75] "VSS / VSH Stepper Motor," https://www.phytron.eu/fileadmin/user_upload/produkte/motoren_aktuatoren/pdf/ds-vacuum-en.pdf, 2018.

[76] L. W. Fredrick and R. H. Baker, *Astronomy*. New York: D. Van Nostrand Co, 1976.

[77] G. Makiwa, "Performance characterization of a millimeter-wave photomixer," Ph.D. dissertation, University of Lethbridge, Dept. of Physics and Astronomy, 2011.

[78] *Terahertz Technologies Systems and Accessories*, Toptica Photonics. [Online]. Available: https://www.toptica.com/fileadmin/Editors_English/11_brochures_datasheets/01_brochures/toptica_BR_Terahertz_Technologies.pdf

[79] A. Deninger, "Chapter 11 - State-of-the-art in terahertz continuous-wave photomixer systems," in *Handbook of Terahertz Technology for Imaging, Sensing and Communications*, ser. Woodhead Publishing Series in Electronic and Optical Materials, D. Saeedkia, Ed. Woodhead Publishing, 2013, pp. 327–373. [Online]. Available: https://www.sciencedirect.com/science/article/pii/B9780857092359500112

[80] Y. Takeda, A. Sasaki, Y. Imamura, and T. Takagi, "Electron mobility and energy gap of $In_{0.53}Ga_{0.47}As$ on InP substrate," *Journal of Applied Physics*, vol. 47, no. 12, pp. 5405–5408, 1976. [Online]. Available: https://doi.org/10.1063/1.322570

[81] *Scitec Instruments: Infrared Source Series 12 Manual*. [Online]. Available: https://scitec.uk.com//irsources/pdf/ir12v2.pdf

[82] C. Cagran, L. Hanssen, M. Noorma, A. Gura, and S. Mekhontsev, "Temperature-Resolved Infrared Spectral Emissivity of SiC and Pt–10Rh for Temperatures up to 900°C," *International Journal of Thermophysics*, vol. 28, pp. 581–597, 06 2007.

[83] F. J. Low, "Low-Temperature Germanium Bolometer," *J. Opt. Soc. Am.*, vol. 51, no. 11, pp. 1300–1304, Nov 1961. [Online]. Available: http://opg.optica.org/abstract.cfm?URI=josa-51-11-1300

[84] S. P. Davis, M. C. Abrams, and J. W. Brault, *Fourier transform spectrometry*. San Diego: Academic Press, 2001.

[85] P. Hargrave, Private communications.

[86] *Stanford Research Systems: Model SR540 Optical Chopper*, 2009.

[87] "Model sr830 dsp lock-in amplifier," https://www.thinksrs.com/downloads/pdfs/manuals/SR830m.pdf, 1993.

[88] *Measurement Computing: USB-1808X User Guide*, 2019. [Online]. Available: https://www.mccdaq.com/data-acquisition-and-control/simultaneous-daq/USB-1808-Series.aspx

[89] *1063 - PhidgetStepper Bipolar 1-Motor*, Phidgets Inc. [Online]. Available: https://www.phidgets.com/?&prodid=60

[90] *WA-1000/WA-1500 Wavemeter - Laser Wavelength Meters*, © EXFO Electro-Optical Engineering Inc., 2004.

[91] *SR560 - Low-noise voltage preamplifier*, Stanford Research Systems. [Online]. Available: https://www.thinksrs.com/products/sr560.htm

[92] M. G. Hauser and E. Dwek, "The Cosmic Infrared Background: Measurements and Implications," *Annual Review of Astronomy and Astrophysics*, vol. 39, no. 1, pp. 249–307, 2001. [Online]. Available: https://doi.org/10.1146/annurev.astro.39.1.249

[93] D. Naylor, B. Gom, A. Huber, A. Anderson, A. Christiansen, W. Jellema, B. Lap *et al.*, "Development of a cryogenic far-infrared post-dispersed polarizing Fourier transform spectrometer: a demonstrator for the SPICA SAFARI instrument," in *Millimeter, Submillimeter, and Far-Infrared Detectors and Instrumentation for Astronomy X*, J. Zmuidzinas and J.-R. Gao, Eds., vol. 11453, International Society for Optics and Photonics. SPIE, 2020, pp. 117 – 127. [Online]. Available: https://doi.org/10.1117/12.2561100

[94] A. I. Huber, "Exploring the challenges of a far-infrared post-dispersed polarising Fourier transform spectrometer," Master's thesis, University of Lethbridge, 2021.

[95] T. Fulton, D. Naylor, A. Huber, and S. Gunuganti, "Overcoming processing challenges for a post-dispersed Fourier transform spectrometer," in *OSA Optical Sensors and Sensing Congress 2021 (AIS, FTS, HISE, SENSORS, ES)*. Optica Publishing Group, 2021, p. JTu5A.5. [Online]. Available: http://opg.optica.org/abstract.cfm?URI=ES-2021-JTu5A.5

[96] *PB1319 Fiber Coupled Terahertz Photomixers*, Bakman Technologies. [Online]. Available: https://www.bakmantechnologies.com/documents/PB1319-Photomixer.pdf

[97] *PH780DBR Series High-Power Single-Frequency Laser Diode*. [Online]. Available: https://www.photodigm.com/products/780-nm-laser-diode

[98] P. C. Hargrave, J. W. Beeman, P. A. Collins, I. Didschuns, M. J. Griffin, B. Kiernan, and G. Pisano, "In-flight calibration sources for Herschel-SPIRE," in *IR Space Telescopes and Instruments*, ser. Society of Photo-Optical Instrumentation Engineers (SPIE) Conference Series, J. C. Mather, Ed., vol. 4850, Mar. 2003, pp. 638–649.

[99] P. Hargrave, T. Waskett, T. Lim, and B. Swinyard, "Performance of flight-model on-board calibration sources on Herschel-SPIRE," *Proceedings of SPIE - The International Society for Optical Engineering*, vol. 6275, 07 2006.

[100] D. Naylor, B. Gom, A. Huber, A. Andersona, A. Christiansen, W. Jellema, B. Lap *et al.*, "Development of a cryogenic far-infrared post-dispersed polarizing fourier transform spectrometer," in *OSA Optical Sensors and Sensing Congress 2021 (AIS, FTS, HISE, SENSORS, ES)*. Optica Publishing Group, 2021, p. FM5C.3. [Online]. Available: http://opg.optica.org/abstract.cfm?URI=FTS-2021-FM5C.3

[101] A. Cournoyer, Éric Carbonneau, P. Gilbert, L.-P. Bibeau, S. Houle, H. Bourque, I. Silversides *et al.*, "Design of a novel cryogenic stiffness-compensated reactionless scan mechanism for the Fourier transform spectrometer of SPICA SAFARI instrument," in *Millimeter, Submillimeter, and Far-Infrared Detectors and Instrumentation for Astronomy X*, J. Zmuidzinas and J.-R. Gao, Eds., vol. 11453, International Society for Optics and Photonics. SPIE, 2020, pp. 526 – 545. [Online]. Available: https://doi.org/10.1117/12.2560530

[102] "WiDy SenS 640," https://new-imaging-technologies.com/product/widy-sens-640/.

[103] A. A. Michelson and E. W. Morley, "On the relative motion of the Earth and the luminiferous ether," *American journal of science (1880)*, vol. s3-34, no. 203, pp. 333–345, 1887.

[104] D. A. Naylor, B. G. Gom, M. H. D. van der Wiel, and G. Makiwa, "Astronomical imaging Fourier spectroscopy at far-infrared wavelengths," *Canadian Journal of Physics*, vol. 91, no. 11, pp. 870–878, 2013. [Online]. Available: https://doi.org/10.1139/cjp-2012-0571

[105] J. W. Cooley and J. W. Tukey, "An algorithm for the machine calculation of complex Fourier series," *Mathematics of Computation*, vol. 19, pp. 297–301, 1965.

[106] "Interactive data language," https://www.l3harrisgeospatial.com/Software-Technology/IDL#language.

[107] "Aerotech Inc." https://www.aerotech.com/.

[108] T. Fulton, D. A. Naylor, E. T. Polehampton, I. Valtchanov, R. Hopwood, N. Lu, J.-P. Baluteau *et al.*, "The data processing pipeline for the Herschel SPIRE Fourier Transform Spectrometer," *Monthly Notices of the Royal Astronomical Society*, vol. 458, no. 2, pp. 1977–1989, 02 2016. [Online]. Available: https://doi.org/10.1093/mnras/stw343

[109] D. H. Martin and E. Puplett, "Polarised interferometric spectrometry for the millimetre and submillimetre spectrum," *Infrared Physics*, vol. 10, no. 2, pp. 105–109, 1970. [Online]. Available: https://www.sciencedirect.com/science/article/pii/0020089170900060

Appendix A

Diffraction Through Apertures

This appendix will explore the phenomena of diffraction from theoretical descriptions outlined in classical electromagnetic wave theory. Measurements are taken with near-infrared monochromatic light passing through apertures of different sizes and shapes. The data will be compared with equations formulated by Fraunhofer in the far-field (distance to observing screen $>>$ wavelength of light) diffraction limit.

As was discussed in Chapter 2, section 2.3, the Fraunhofer diffraction integral is given by:

$$\psi(P) = C\int_{S_1} e^{-ik(p\xi+q\eta)}\mathrm{d}\xi\mathrm{d}\eta \qquad [\sqrt{W}\ /\mathrm{m}] \quad \text{(A.1)}$$

which describes diffraction of light through an aperture with geometry specified by S_1 in a plane screen as was shown in figure 2.3. The coordinates, $p = l - l_o$ and $q = m - m_o$ describe the relative direction between the source position at (x_o, y_o, z_o) and the observation point at (x, y, z). The aperture geometries of interest in this investigation are the narrow slit and circular aperture. The intensity of the Fraunhofer diffraction integral is found by taking $|\psi(P)|^2$ over the surface S_1 which includes the relevant aperture dimensions. The intensity distribution for light diffracted through a narrow slit is given by [50]:

$$I(p) = |\psi(p)|^2 = I_o\left(\frac{\sin(kpa)}{kpa}\right)^2 \qquad [\mathrm{W\,m^{-2}}] \quad \text{(A.2)}$$

where $k = \frac{2\pi}{\lambda}$ is the wavenumber, I_o is the amplitude of the intensity, $p = l - l_o$, and a is the width of the slit. The second geometry investigated was a circular aperture where the diffracted intensity is give by [50]:

$$I(p) = I_o\left(\frac{2J_1(kaw)}{kaw}\right)^2 \qquad [\mathrm{W\,m^{-2}}] \quad \text{(A.3)}$$

where w is the positional vector in terms of polar coordinates, a is the radius of the aperture, and J_1 is the first-order Bessel function. The result is known as the Airy disk, named after the astronomer who first derived it. The radius of the Airy disk is the distance from the center of the profile to the 1st dark ring, q_1, which is given by:

$$q_1 = 1.22\frac{S\lambda}{2a} \qquad [\mathrm{m}] \quad \text{(A.4)}$$

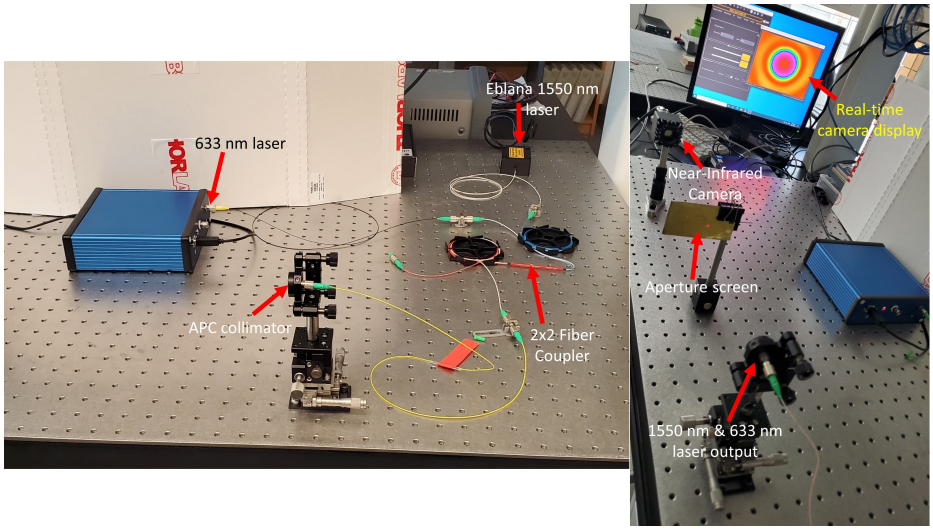

Figure A.1: Experimental configuration to measure diffraction through apertures of different shapes and sizes with a near-infrared (0.9 - 1.7 µm) camera. A 633 nm laser is mounted within the blue enclosure and a 1550 nm laser is mounted in an Eblana DX Laser Driver. The fiber output from both lasers are input into a single-mode fiber which connects with a 2x2 fiber coupler. The coupled signal passes through a ∼30 dB attenuator and into a Thorlabs F220APC-1550 collimator. The 633 nm laser was used to align the system as is seen with the red dot on the aperture screen (right image). The 1550 nm light then diffracted through a hole in the screen and was imaged by the camera placed 10 cm away from the screen. The computer shows the airy disk pattern arising from diffraction through a circular aperture.

where $S = |s'|$ from figure 2.3.

Figure A.1 shows the experimental setup used to measure the Fraunhofer diffraction pattern from a various apertures, including a slit and a circular aperture. A 1550 nm laser is used as the source in all of these results, however, a visible, 633 nm laser was fed into the same optical fiber to assist with alignment. A WiDy SenS 640 near-infrared, NIR (0.9 - 1.7 µm), indium galium arsenide, InGaAs, camera [102] was used to image the diffracted intensity. The camera is comprised of 512 x 640 15 µm pixels which produce a high-resolution image in the near-infrared. The first aperture screen used was a 1.0 ± 0.1 mm slit which was expected to return an intensity distribution described by equation A.2. Figure A.2 shows the measured diffracted intensity for the camera placed a distance of 33.5 cm from the slit (left) and then the camera moved closer to a distance of 17.5 cm from the slit. The data shows the characteristic $\text{sinc}^2(x)$ function and that the location of the first minima is closer to the first maxima with a shorter observation distance. This is expected because the coordinate, p, in equation A.2 increases with an increased observation distance leading to a more narrow sinc profile.

The next results were taken with the aperture screen shown in figure A.3. Using the ruler as calibration, the diameters of the holes were measured to be: 372 ± 20 µm, 313 ± 20 µm, 197 ± 10 µm, and 102 ± 10 µm from left to right (1-4). The measured results are shown in figure A.4. The data were fit with the Airy disk function as per equation A.3 to extract the

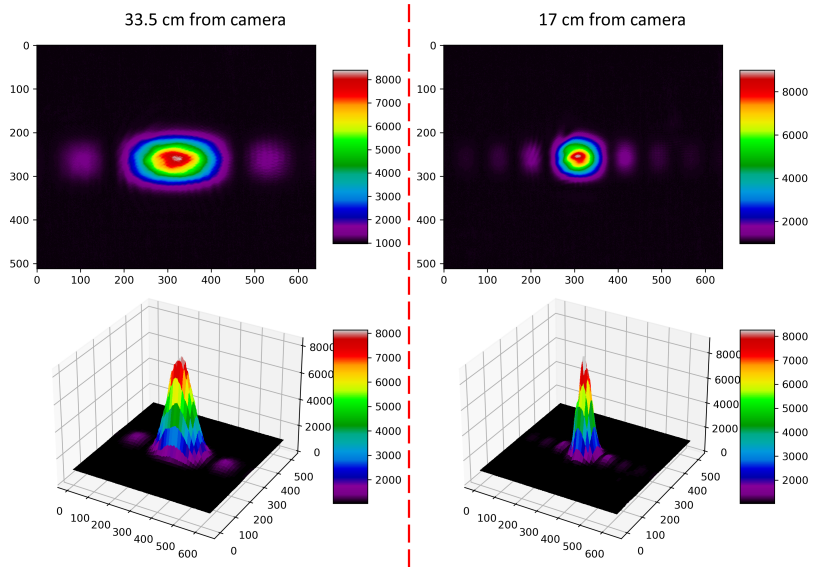

Figure A.2: Fraunhofer diffraction of 1550 nm monochromatic light through a slit as measured by a NIR InGaAs camera. The data on the left show the camera placed 33.5 cm from the slit and the image on the right is with the camera placed 17 cm from the slit. The x and y axes are labeled in terms of pixels where one pixel is equal to 15 µm. The scale shows the relative intensity measured by the camera in arbitrary units.

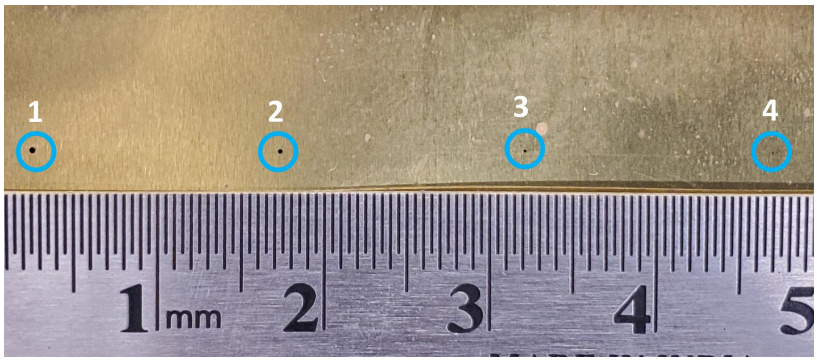

Figure A.3: Thin, metal screen with circular holes of varying diameter used to measure Airy disk patterns.

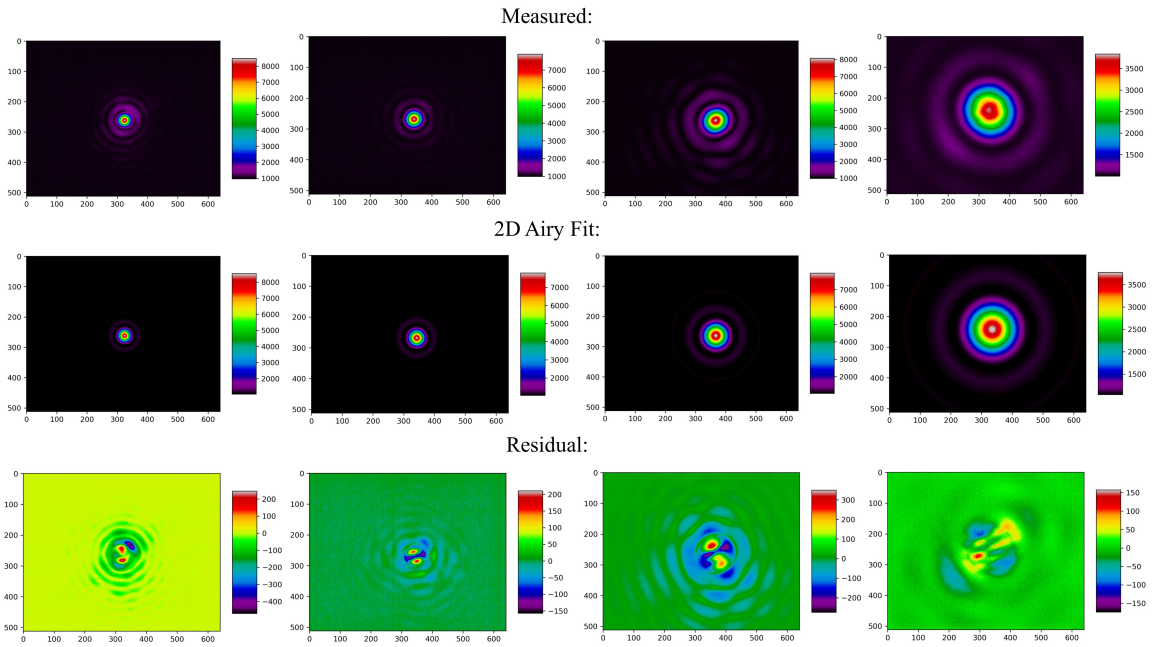

Figure A.4: Fraunhofer diffraction of 1550 nm monochromatic light through 4 circular apertures of different diameters. The data were fit with a 2D Airy equation to extract the radius of the first fringe. From left to right, the fit returned radii of: 510 µm, 639 µm, 984 µm, and 1936 µm. The residual between the measured data and the fit are shown in the bottom row.

radius of the first dark fringe, q_1. From left-to-right the fit returned radii of: 510 µm, 639 µm, 984 µm, and 1936 µm. The setup had the distance from the aperture to the camera set at $S = 10$ cm, and $\lambda = 1550$ nm. Rearranging equation A.4 to solve for a returned diameters of: 371 ± 47 µm, 314 ± 56 µm, 192 ± 15 µm, and 98 ± 15 µm. The fitted values agree within error with all of the measured values.

The last measurements utilized complicated geometries as shown in figure A.5. The results measured with the NIR camera are shown in figure A.6. Clearly, there are some symmetries present from the shapes of the apertures, however, it is more complicated to theoretically model.

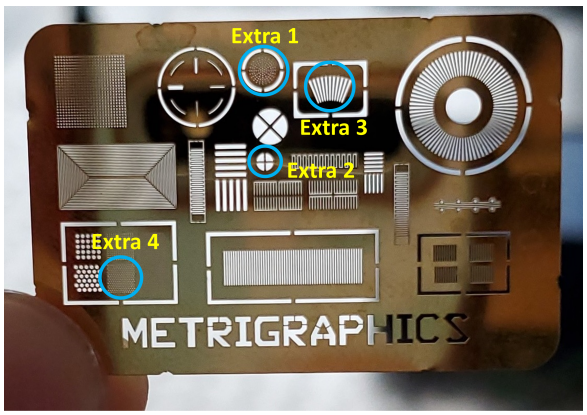

Figure A.5: Metrigraphics aperture screen with various aperture shapes that were used to measure complicated diffraction patterns.

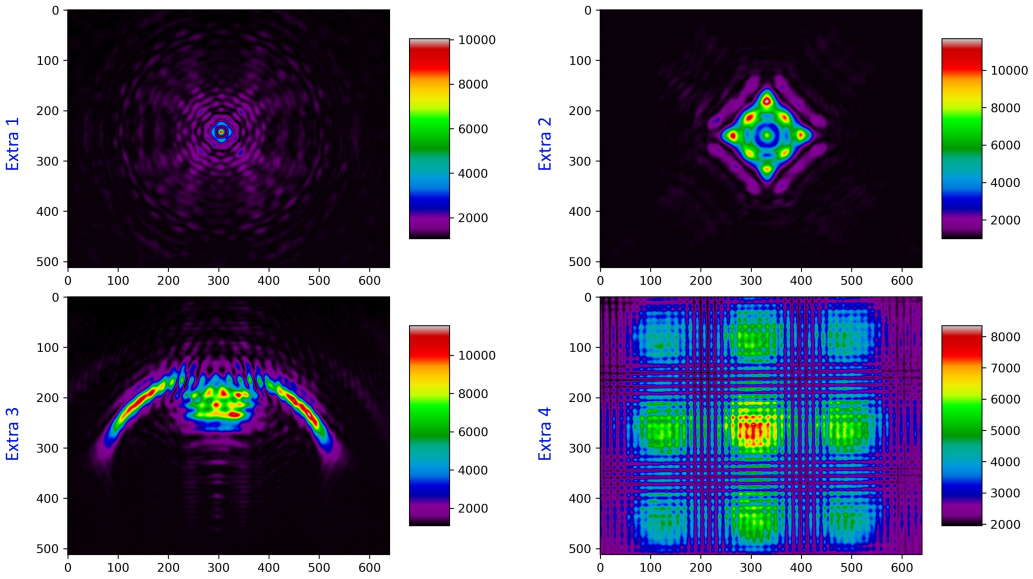

Figure A.6: Diffraction of 1550 nm monochromatic light through apertures with complicated geometries.

Appendix B

Fraunhofer Diffraction as a Fourier Transform

The derivation of diffraction through a transmission grating begins by considering the Fraunhofer diffraction integral as a Fourier transform. This section will employ similar methods to those outlined in Chapter 3 of Observation and Analysis of Stellar Photospheres by Gray [60].

Consider a wavefront incident on the plane of a transmission grating at an angle α with the plane normal that gets diffracted at an angle β as was shown in figure 2.4 (b). The incident wave with wavelength λ can be expressed as [60]:

$$\psi(\xi,t) = \psi_o e^{2\pi i(\xi \sin\alpha)/\lambda} \qquad [\sqrt{W}\ /\mathrm{m}] \quad \text{(B.1)}$$

where ψ_o is a constant and ξ is the linear coordinate along the grating. The grating will pass through the grating whenever ξ is within the dimensions of the slit and is assumed to be completely blocked anywhere else. Therefore, the transmission function is given by:

$$G(\xi) = \begin{cases} 1 & \text{for } \xi \text{ along the slits} \\ 0 & \text{for } \xi \text{ elsewhere} \end{cases} \qquad [1] \quad \text{(B.2)}$$

The diffracted wave is the sum of all contributions from incident line along the grating in the direction of ξ which is found by integrating the transmission function with the incident wave:

$$\psi(\beta) = \int_{-\infty}^{\infty} \psi_o G(\xi) e^{2\pi i(\xi \sin\alpha + \xi \sin\beta)/\lambda} \mathrm{d}\xi \qquad [\sqrt{W}\ /\mathrm{m}] \quad \text{(B.3)}$$

The phase difference from the diffracted wave, $2\pi(\xi \sin\beta)/\lambda$ is taken into account inside the integral. $\sin\alpha + \sin\beta$ can be substituted with θ which represents the overall phase shift between the incident and diffracted waves. Taking ξ to be measured in multiples of the wavelength this gives:

$$\psi(\theta) = \psi_o \int_{-\infty}^{\infty} G(\xi) e^{2\pi i \theta \xi} \mathrm{d}\xi \qquad [\sqrt{W}\ /\mathrm{m}] \quad \text{(B.4)}$$

One can recognize this as the Fourier transform of the transmission function, $G(\xi)$, which describes the diffracted wavefront [60]. Gray continues this derivation to show that the

transmission function for a simple line gating is given by:

$$G(\xi) = B_1(\xi) * III(\xi) B_2(\xi), \qquad [1] \quad \text{(B.5)}$$

$B_1(\xi)$ is a box function that defines the width of each slit and $B_2(\xi)$ defines the extent of the grating. The Shah function (or Dirac comb) is a series of delta functions representing the spacing of each slit, d: $III(\xi) = \sum \delta(\theta - n/d)$. $B_1(\xi)$ is convolved with the Shah function to represent the slits of width s spaced equidistant of d apart and then the entire grating is confined to the width given by $B_2(\xi)$. Substituting this into equation B.4, the result is:

$$\psi(\theta) = \sum_n \frac{W \sin \pi(\theta - n/d) W}{\pi(\theta - n/d) W} \frac{s \sin \pi\theta s}{\pi\theta s} \qquad [\sqrt{W}\ /\mathrm{m}] \quad \text{(B.6)}$$

where $W = N \times d$ is the total length of the grating. The intensity is found by computing $I(\theta) = |\psi(\theta)|^2$ and it is clearly shown that the result will be two sinc^2 functions; identical to equation 2.36. Equation B.6 corresponds to the diffracted intensity distribution for a transmission diffraction grating.

Appendix C

Fourier Transform Spectroscopy

This appendix provides a brief introduction to Fourier analysis with respect to how it was applied to process data measured by a Fourier transform spectrometer, FTS, provided by Blue Sky Spectroscopy Inc. [73]. Fourier decomposition of light into its constituent components can be achieved using several devices including a diffraction grating spectrometer, Fabry-Pérot, FTS, etc. However, with respect to providing high-resolution spectroscopy of astronomical sources in the far-infrared, the FTS is ideally suited with its broad spectral coverage, high throughout, and well-known instrumental line shape [93]. A simple example showing a FTS with a Michelson interferometer optical configuration [103] is shown in figure C.1. Light from a monochromatic source at the object plane is divided into two equal beams by a beam splitter which passes one beam towards a stationary mirror and the other towards a movable mirror. The two beams are then reflected by their respective mirrors and are recombined at the beam splitter. The recombined beams produce an interference signal, known as the interferogram which is measured by the detector. As the mirror moves, the path length traveled by one beam changes relative to the other which changes the phase between the two interfering beams. As was discussed in Chapter 2, constructive interference occurs when the phase between the two monochromatic beams, δ, is equal to even multiples of π, $\delta = 2n\pi$, and destructive interference occurs when $\delta = (2n+1)\pi$. Thus, as the mirror moves and δ is varied, the detector plane will view bright (constructive interference) and dark (destructive interference) fringes coinciding with the mirror position [84]. This modulated signal, or interferogram, can be transformed to recover the frequency-dependent spectrum which will be discussed in the next section [84, 104].

As was mentioned in Chapter 1, the spectrum from an astrophysical source is comprised of continuum and line emission and absorption. The spectral lines or features occur from emitted or absorbed energy by atoms and molecules undergoing quantum transitions. The types of transitions present in a spectrum give insight into the chemical composition, structure, and physical environments of the source. The following section will describe the analysis methods used to transform the FTS measured interferogram into a spectrum.

C.1 Fourier Transform Analysis

Consider the Michelson interferometer FTS as shown in figure C.1. For an input source of purely monochromatic light with a frequency, σ_o, and intensity, $B(\sigma_o)$, the intensity of the interferogram as a function of the OPD, x, is given by [84]:

$$I_o(x) = B(\sigma_o)\left[1 + \cos(2\pi\sigma_o x)\right]. \qquad \text{[W]} \quad \text{(C.1)}$$

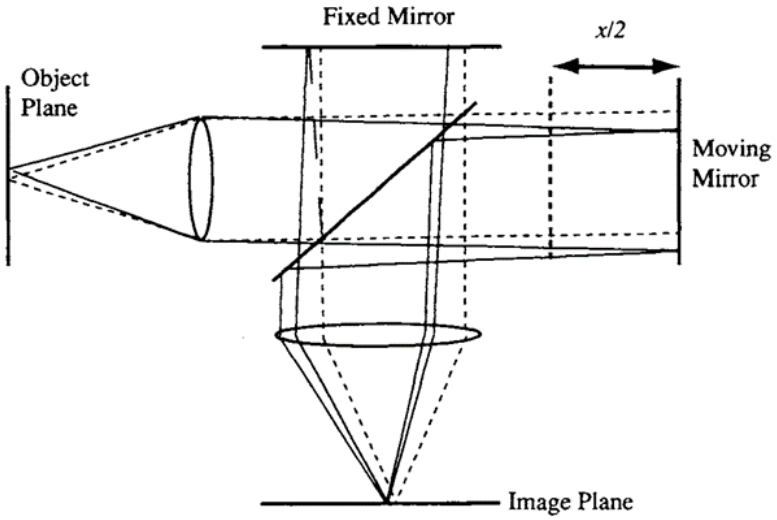

Figure C.1: Diagram taken from [84] showing the configuration of the Michelson interferometer. Light is incident from the object plane, gets collimated, passes through a 50:50 beam splitter and is either reflected towards a stationary mirror or passes through towards a movable mirror. After the light reflects off of the mirrors it gets recombined at the beam splitter and the combined signal is focused and then measured at the image plane.

For an input source composed of many frequencies the interferogram intensity is given by:

$$I_o(x) = \int_0^\infty B(\sigma)\,[1+\cos(2\pi\sigma x)]\,d\sigma, \qquad \text{[W]} \quad \text{(C.2)}$$

where the source is now described by a superposition of cosines. Subtracting the mean value of the interferogram, $\bar{I}_o(x)$, from $I_o(x)$ the result is:

$$I(x) = I_o(x) - \bar{I}_o(x) = \int_0^\infty B(\sigma)\cos(2\pi\sigma x)d\sigma. \qquad \text{[W]} \quad \text{(C.3)}$$

Equation C.3 is referred to as Fourier synthesis because it describes a function $I(x)$ which is composed of sinusoids. There is also a reverse process known as Fourier decomposition which describes how one can deconstruct a function, $I(x)$, to retrieve the constituent sinusoids, $B(\sigma)$. The Fourier theorem states that an periodic, continuous function, $f(x)$ can be decomposed into a series of constituent sinusoids and cosines [84]:

$$f(x) = \int_{-\infty}^\infty F(\sigma)e^{i2\pi\sigma x}d\sigma \equiv \tilde{F}(\sigma), \qquad \text{[a.u.]} \quad \text{(C.4)}$$

and $F(\sigma)$ is denoted as the Fourier transform (FT) of $f(x)$. The reverse FT is given by:

$$F(\sigma) = \int_{-\infty}^\infty f(x)e^{-i2\pi\sigma x}dx \equiv \tilde{f}(x). \qquad \text{[a.u.]} \quad \text{(C.5)}$$

One of the advantages of the FTS is that it is a linear system; the presence of one source excitation does not impact the system response to any other excitations [84]. Furthermore, a factor multiplied to the source signal will identically multiply the response. Providing that the detector response remains linear with respect to incident power, the principle of superposition applies allowing the use of the powerful Fourier relations. Additionally, the FTS response is generally time invariant, which when combined with the linearity, allows the output of the FTS to be described by a convolution of an instrumental function, $O(x)$, with the input signal [84]. This allows the input signal to be easily reconstructed with a knowledge of $O(x)$.

For a real instrument, the mirror travels a finite distance and the system aperture is finite as well. The travel distance of the mirror acts as a rectangular function multiplying an otherwise infinitely wide inteferogram. This transforms to a sinc function convolving the spectrum. Additionally, the finite optical aperture multiplies the spectrum by a recangular function which corresponds to a sinc function convoluting the interferogram [84]. For a monochromatic source with frequency, σ_o, the instrumental line shape function, $O(\sigma)$, convolves with the ideal spectrum. $O(\sigma)$ is the combination of the finite path and aperture:

$$O(\sigma) = \left[\Omega_m \frac{2\pi}{\sigma_o \Omega_m} \Pi\left(\frac{2\pi\sigma}{\sigma_o \Omega_m}\right)\right] * [2L\text{sinc}(2L\sigma)] \qquad [1] \quad \text{(C.6)}$$

where Ω_m is the solid angle projection corresponding to the maximum aperture extent and $2L$ is the maximum travel distance of the mirror. The observed spectrum is then given by: $B_{obs}(\sigma) = B(\sigma) * O(\sigma)$, where $B(\sigma)$ is the ideal spectrum convoluted by the instrumental line shape. See [84] for details of these calculations. The resolving power of the FTS is related to the maximum optical path difference by:

$$R = \frac{\sigma}{\Delta\sigma} = 2L\sigma \qquad [1] \quad \text{(C.7)}$$

where the total travel distance of the mirror is $2L$ [84]. The next section will discuss the program used to process the FTS data.

C.2 Data Processing

The previous section discussed the FT being applied to continuous functions, however, a real signal is a sampled, discrete representation of a continuous signal. Instead of integrating the sinusoid and cosine components as in equation C.5, the discrete signal is described by a summation:

$$F(\sigma_k) = \sum_{j=1}^{N} F(x_j) e^{-i2\pi\sigma_k x_j}, \qquad [\text{a.u.}] \quad \text{(C.8)}$$

where x_j are the sampled points along the interferogram, σ_k are the frequency sampled points, and the summation is over N real data points [84]. The discrete Fourier transform (DFT) calculation requires N^2 computations of the FT, which is a significant time consumption for a high-resolution (large N) instrument. In 1965, a more efficient approach

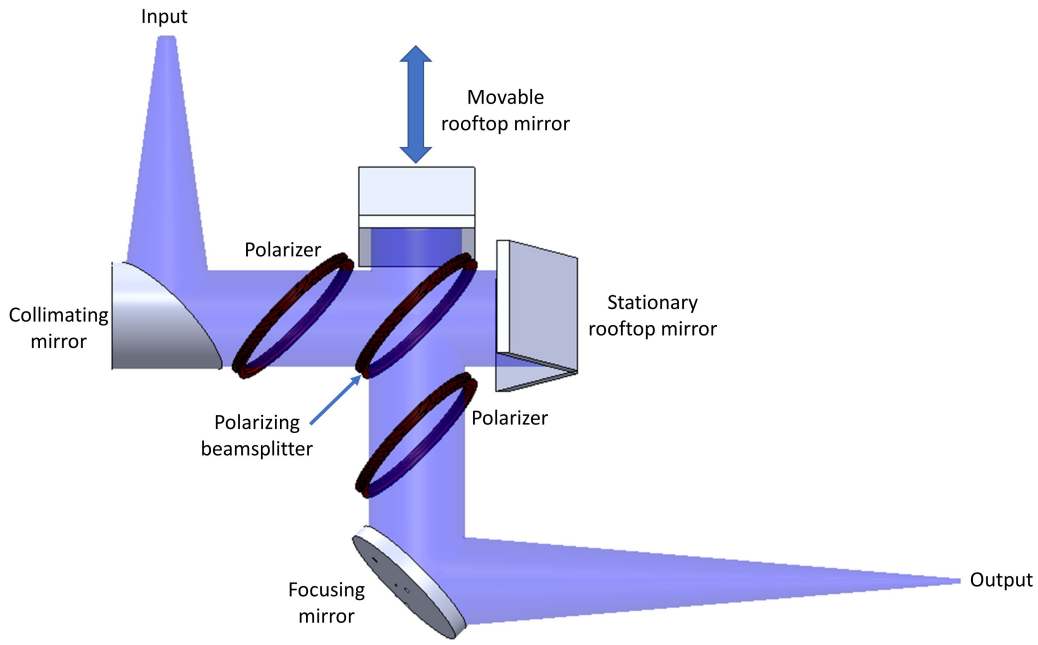

Figure C.2: CAD rendering of the cFTS developed by Blue Sky Spectroscopy Inc. [73] used in this thesis. The optical configuration is a Martin-Puplett interferometer which utilizes polarizers to split the radiation into two beams. The recombined beam then passes through a third polarizer which encodes the polarization of the output signal.

was developed by Cooley and Tukey known as the fast Fourier transform (FFT) which is now a standard library in most modern programming languages [105].

The interferogram data are processed using previous programs written in Interactive Data Language, IDL [106]. The mirror is controlled by an Aerotech high-precision translation stage with a linear encoder [107]. As the mirror translates, a MC 1808X data acquisition device [88] simultaneously records the position of the mirror from the encoder and the signal from the detector. An array of mirror positions and signal measurements is then sent to the computer where a program converts the position to OPD and plots the signal in real-time. The raw interferogram is processed using a modified form of the robust data processing pipeline developed for the Spectral and Photometric Imaging Receiver (SPIRE) imaging FTS flown on the Herschel Space Observatory [108]. For more details on the data processing used specifically for the post-dispersed FTS refer to [95] and [94]. The FTS pipeline used in this thesis locates the position of zero path difference, ZPD, and performs a phase correction routine to eliminate imaginary (asymmetric) components in the signal since we are only interested in the real part of the signal. Once the interferogram is corrected, it is transformed using the FFT algorithm and the spectrum is returned to be analyzed. The next section will discuss the specifications of the calibration FTS (cFTS) provided by Blue Sky Spectroscopy Inc. [73] which was used in the measurements presented in this thesis.

Table C.1: Specifications for the calibration FTS [73].

Parameter	Value
Spectral Range	10 - 333 cm^{-1} (1000 - 30 μm)
Spectral Resolution	0.016 cm^{-1}
Resolving Power	625 - 20,813
Throughput	0.14 cm^2 sr
Vacuum Pressure	$<$10 mTorr

C.3 Calibration FTS Specifications

The cFTS optical configuration is a Martin-Puplett interferometer, MPI, [109] as shown in figure C.2. The specifications of the cFTS are listed in table C.1. The MPI configurations incorporates three wire-grid linear polarizers to further encode the polarization state onto the propagating beams. The first polarizer is configured either horizontal (p-plane) or vertical (s-plane) such that an unpolarized source will lose half of its incident power. The polarized light then travels to the polarizing beamsplitter which is oriented at 45° with respect to the first polarizer which serves to reflect half of the beam and transmit the other half. The last polarizer serves to encode the polarization of the recombined output. Compared to the Michelson interferometer which uses a beamsplitter, the MPI is much more efficient at far-infrared wavelengths [104, 109].